

THE EFFECT OF THE GALAXY CLUSTER ENVIRONMENT ON GALAXIES AND AGN

A LOFAR STUDY

DISSERTATION

ZUR ERLANGUNG DES DOKTORGRADES
AN DER FAKULTÄT FÜR MATHEMATIK, INFORMATIK UND NATURWISSENSCHAFTEN
FACHEREICH PHYSIK
DER UNIVERSITÄT HAMBURG

VORGELEGT VON

HENRIK WILHELM EDLER

HAMBURG
2023

Gutachter der Dissertation:

Prof. Dr. Marcus Brüggem
Prof. Dr. Francesco de Gasperin

Zusammensetzung der Prüfungskommission:

Prof. Dr. Marcus Brüggem
Prof. Dr. Francesco de Gasperin
Prof. Dr. Jochen Liske
Prof. Dr. Dieter Horns
Prof. Dr. Peter Hauschildt

Vorsitzender der Prüfungskommission:

Prof. Dr. Jochen Liske

Datum der Disputation:

16. Januar 2023

Vorsitzender des Fach-Promotionsausschusses PHYSIK:

Prof. Dr. Markus Drescher

Leiter des Fachbereichs PHYSIK:

Prof. Dr. Wolfgang J. Parak

Dekan der Fakultät MIN:

Prof. Dr. Norbert Ritter

Eidesstattliche Versicherung

Hiermit versichere ich an Eides statt, die vorliegende Dissertationsschrift selbst verfasst und keine anderen als die angegebenen Hilfsmittel und Quellen benutzt zu haben.

Hamburg, den 07.11.2023

Henrik Edler

Zusammenfassung

Galaxienhaufen, die massereichsten Bausteine der großräumigen Struktur des Universums, sind mit dem heißen Intracluster-Medium (ICM) gefüllt. Obwohl es sich bei dem ICM um ein extrem dünnes Medium handelt, führen die hohen Geschwindigkeiten der Galaxien und die Bewegungen des ICM zu hydrodynamischen Strömungskräften. Der Staudruck, der vom heißen ICM-Wind ausgeübt wird, kann sich auf sternbildende Galaxien und Radiogalaxien auswirken und damit deren Eigenschaften und Entwicklung beeinflussen. Das Ziel dieser Doktorarbeit ist es, herauszufinden wie Galaxien und ihre Radioemission von der Interaktion mit der Galaxienhaufenumgebung geformt werden. Als wichtigstes Beobachtungsinstrument habe ich das LOw-Frequency Array (LOFAR) verwendet, das hohe Empfindlichkeit und Winkelauflösung mit einem weiten Sichtfeld und einzigartigen Niedrigfrequenzfähigkeiten kombiniert.

Das erste Anschauungsobjekt dieser Arbeit ist der Virgo-Haufen, der nächstgelegene massive Galaxienhaufen und somit ein ideales Beispiel, um Umgebungseffekte in Haufen bei unübertroffener räumlicher Auflösung und Empfindlichkeit zu erforschen. Allerdings stellt die helle zentrale Radioquelle in M 87 eine technische Herausforderung für Radiobeobachtungen des Haufens dar. Um diese Schwierigkeiten zu bewältigen, habe ich eine Kalibrierungsstrategie entwickelt, die es erstmals ermöglichte, M 87 genau zu kalibrieren und den Virgo-Haufen mit dem LOFAR-High Band Antenna (HBA) System zu untersuchen. Diese Himmelsdurchmusterung erreicht eine Empfindlichkeit, die um eine Größenordnung höher ist als bestehende Weitfeld-Himmelsdurchmusterungen in dieser Region, und wird zusammen mit einem Radiokatalog der Virgo-Haufen-Galaxien öffentlich zugänglich gemacht. In diesen Himmelskarten habe ich acht neue Kandidaten für Galaxien mit durch Staudruck abströmenden Radioschweif (ram-pressure stripping, RPS) entdeckt. Durch den Vergleich der Radioeigenschaften einer Gruppe von RPS-Galaxien und einer Kontrollgruppe konnte ich bestätigen, dass die RPS-Galaxien im Virgo-Haufen eine zwei- bis dreimal höhere Radioleuchtkraft aufweisen, als anhand ihrer Sternentstehungsrate zu erwarten wäre. Darüber hinaus fand ich erstmals Hinweise darauf, dass RPS-Galaxien einen steileren Radiospektralindex als ungestörten Objekten derselben Masse aufweisen. Ich habe auch verschiedene umweltbedingte Mechanismen verglichen und eingeschränkt, die sowohl die höhere Radioemission als auch eine spektrale Steigerung erklären können.

Das zweite Anschauungsobject dieser Arbeit ist Abell 1033, ein verschmelzender Galaxienhaufen mittlerer Masse. Er beherbergt eine Radioquelle, die als sanft wiederenergetisierter Schweif (gently re-energized tail, GReET) bekannt ist. Dieser ausgedehnte Radiogalaxienschweif wird vom Staudruck des ICM geformt, wobei die zweite Hälfte des Schweifes besonders spektakuläre Eigenschaften aufweist, darunter ein räumlich gleichmäßiges und extrem steiles Spektrum. Ich erweiterte die Wellenlängenabdeckung dieses Haufens, zu der auch ein Radiophönix und ein riesiger Radiohalo gehören, hin zu Ultratiefstfrequenzen unter Verwendung des LOFAR-Low Band Antenna (LBA) Systems bei einer Frequenz von 54 MHz. Ich habe herausgefunden, dass der GReET ein extrem konvexes Spektrum aufweist. Dies ist im Einklang mit dem Aufrechterhalten einer relativistischen Elektronenpopulation durch einen ineffizienten Wiederenergetisierungsmechanismus. Ein möglicher Beschleunigungsmechanismus ist die stochastische Beschleunigung durch Turbulenzen, die durch Wechselwirkungen mit dem umgebenden ICM in den Schweif eingebracht werden. Darüber hinaus stellte ich fest, dass das riesige Radiohalo in Abell 1033 sowohl ein extrem steiles Spektrum hat, wie es von homogenen

Wiederbeschleunigungsmechanismen erwartet wird, als auch eine überhohe Leuchtkraft aufweist.

Diese Ergebnisse zeigen, dass das Radiofenster im Nieder- und Ultraniederfrequenzbereich entscheidend ist, um ineffiziente Beschleunigungsprozesse und die ältesten Elektronen der kosmischen Strahlung zu erforschen. Der Stand der Technik in diesem Bereich wird durch das LOFAR 2.0-Upgrade weiter vorangetrieben. Dies wird die Möglichkeit zur gleichzeitigen Beobachtung mit dem LBA und HBA-System einführen, wodurch innovative Kalibrierungsstrategien eröffnet werden. Diese können die großen Bandbreite nutzen, um die starken richtungsabhängigen Fehler, die die Ionosphäre im Niederfrequenzbereich erzeugt, genau zu korrigieren. In diesem Zusammenhang habe ich eine simulierte Beobachtung mit dem LOFAR 2.0-System analysiert, die realistische Modelle der relevanten systematischen Effekte enthält. Ich habe die Möglichkeit der gleichzeitigen Bestimmung der ionosphärischen Parameter aus dem LBA und HBA in LOFAR 2.0 untersucht, indem ich systematisch drei verschiedene Kalibrierungsstrategien auf den simulierten Daten verglichen habe.

Zusammenfassend präsentiere ich in dieser Arbeit LOFAR-Studien zu Umgebungseffekten in Galaxienhaufen, am Beispiel von Staudruck-beeinträchtigten Galaxien im Virgo-Haufen und dem GReET in Abell 1033. Dies wurde durch Fortschritte in Kalibrierungs- und Bildgebungstechniken ermöglicht, zu denen dieses Promotionsprojekt beigetragen hat. In naher Zukunft wird das LOFAR 2.0-Upgrade und die neuartigen Kalibrierungsstrategien, die ich in dieser Arbeit untersucht habe, zu einer weiteren erheblichen Verbesserung der Beobachtungsmöglichkeiten im Nieder- und Ultraniederfrequenzbereich führen.

Abstract

Galaxy clusters, the most massive virialized constituents of the large-scale structure of the Universe, are filled with the hot intracluster medium (ICM). Even though the ICM is dilute, the high velocities of cluster member galaxies and the bulk motions of the ICM give rise to hydrodynamical drag forces. The ram pressure exerted by the hot ICM wind can affect star-forming and radio galaxies, thereby shaping their properties and evolution. In this doctoral thesis, my main focus lies on unraveling the connection between cluster galaxies, their radio emission and the environmental mechanisms at play. As primary observational tool, I used the LOw-Frequency Array (LOFAR), which combines high sensitivity and angular resolution with a wide field of view and unique low-frequency capabilities.

The first subject of this thesis is the Virgo Cluster, the closest massive galaxy cluster and thus an ideal laboratory to probe environmental effects in clusters at unmatched spatial resolution and sensitivity. However, the bright central radio source in M 87 presents a technical challenge for radio observations of the cluster. To address these difficulties, I developed a calibration strategy which allowed for the first time to accurately calibrate M 87 and survey the Virgo Cluster with the LOFAR high-band antenna (HBA) system. This survey reaches an order-of-magnitude greater sensitivity than existing blind surveys of that region and is made publicly available to the community together with a radio catalog of Virgo Cluster galaxies. In this survey, I discovered eight new candidate ram pressure stripped (RPS) radio tails. By comparing the radio properties of a sample of RPS galaxies and a control sample, I could confirm that the RPS galaxies in Virgo have two to three times higher radio luminosities than expected, given their star formation rate. Furthermore, for the first time I reported evidence that RPS galaxies show a steeper radio spectral index compared to non-perturbed objects of the same mass. I also compared and constrained different environmental mechanisms which can explain both the excess radio emission and a spectral steepening.

The second subject of this thesis is Abell 1033, a merging galaxy cluster of moderate mass. It hosts a radio source known as gently reenergized tail (GReET). This extended radio galaxy tail is shaped by the ICM ram pressure, the second half of the tail possesses peculiar properties with a spatially uniform and ultra-steep spectrum. I extended the radio coverage of the ultra-steep spectrum emission of this cluster, which also includes a radio phoenix and a giant radio halo, towards ultra-low frequencies using the LOFAR low-band antenna (LBA) system at 54 MHz. I found that the GReET shows extreme spectral curvature, in agreement with a cosmic ray electron population that is maintained by an inefficient reacceleration process. A feasible acceleration mechanism is stochastic reacceleration by turbulence which is driven into the tail through interactions with the surrounding ICM. Furthermore, I found that the giant radio halo in Abell 1033 is both ultra-steep, in line with expectations from homogeneous reacceleration models, and over-luminous.

These findings prove that the low- and ultra-low frequency radio window is crucial to probe inefficient acceleration processes and the oldest cosmic ray electrons. The state of the art in this regime is about to be advanced by the LOFAR 2.0 upgrade. This will introduce the capability of simultaneous observations with the LBA and HBA, thereby allowing for innovative calibration strategies that leverage the large fractional bandwidth to calibrate the direction-dependent errors introduced by the ionosphere, which are a critical limitation in the low-frequency regime. In this context, I analyzed a simulated observation with the LOFAR 2.0 system, which included realistic models of the relevant

systematic effects. I investigated the prospects of the simultaneous inference of ionospheric parameters from the LBA and HBA in LOFAR 2.0 by systematically comparing three different calibration approaches on the simulated data.

In summary, in this thesis I present LOFAR studies of the environmental effect in galaxy clusters, at the example of ram pressure stripped star-forming galaxies in the Virgo cluster and the GReET in Abell 1033. This was enabled by the advances in calibration and imaging techniques, to which this doctoral project contributed. In the near future, the LOFAR 2.0 upgrade and the novel calibration strategies that I investigated in this thesis will lead to a further substantial improvement of the observational capabilities in the low- and ultra-low frequency regime.

List of publications

This thesis is partly based on (but does not include all of) the following publications:

First author publications

- **Edler, H.W.**, Roberts, I. D., Boselli, A., de Gasperin, F., Heesen, V., Brügger, M., Ignesti, A., Gajović, L., 2023. *ViCTORIA project: The LOFAR-view of environmental effects in Virgo Cluster star-forming galaxies*. Submitted to A&A; arXiv:2311.01904. [Edler et al. 2023b]
- **Edler, H.W.**, de Gasperin, F., Shimwell, T.W., Hardcastle, M.J., Boselli, A., Heesen, V., McCall, H., Bomans, D.J., Brügger, M., Bulbul, E. and Chyży, K.T. et al., 2023. *ViCTORIA project: The LOFAR HBA Virgo Cluster Survey*. A&A, 676, p.A24. [Edler et al. 2023a]
- **Edler, H.W.**, de Gasperin, F., Brunetti, G., Botteon, A., Cuciti, V., van Weeren, R.J., Cassano, R., Shimwell, T.W., Brügger, M. and Drabant, A., 2022. *Abell 1033: A Radio Halo and Gently Re-Energized Tail at 54 MHz*. A&A, Volume 666, id.A3, 15 pp. [Edler et al. 2022]
- **Edler, H.W.**, de Gasperin, F. and Rafferty, D., 2021. *Investigating ionospheric calibration for LOFAR 2.0 with simulated observations*. A&A, 652, p.A37. [Edler et al. 2021]

Publications with major contributions

- de Gasperin, F., **Edler, H.W.**, Williams, W.L., Callingham, J.R., Asabere, B., Brügger, M., Brunetti, G., Dijkema, T.J., Hardcastle, M.J., Iacobelli, M. and Offringa, A. et al., 2023. *The LOFAR LBA Sky Survey II. First data release*. A&A, Volume 673, id.A165, 20 pp. [de Gasperin et al. 2023]
- Pasini, T., **Edler, H.W.**, Brügger, M., de Gasperin, F., Botteon, A., Rajpurohit, K., van Weeren, R.J., Gastaldello, F., Gaspari, M., Brunetti, G. and Cuciti, V. et al., 2022. *Particle re-acceleration and diffuse radio sources in the galaxy cluster Abell 1550*. A&A, 663, p.A105. [Pasini et al. 2022]

Co-author publications

- Heesen, V., Schulz, S., Brügger, M., **Edler, H.**, Stein, M., Paladino, R., Boselli, A., Ignesti, A., Fossati, M. and Dettmar, R.J. et al., 2023. *Nearby galaxies in the LOFAR Two-metre Sky Survey III. Influence of cosmic-ray transport on the radio-SFR relation*. Accepted for publication in A&A; arXiv:2309.05732. [Heesen et al. 2023b]
- Geyer, F., Schmidt, K., Kummer, J., Brügger, M., **Edler, H.W.**, Elsässer, D., Griese, F., Poggenpohl, A., Rustige, L. and Rhode, W., 2023. *Deep-learning-based radiointerferometric imaging with GAN-aided training*. A&A, 677, p.A167. [Geyer et al. 2023]
- Boselli, A., Serra, P., de Gasperin, F., Vollmer, B., Amram, P., **Edler, H.W.**, Fossati, M., Consolandi, G., Cote, P., Cuillandre, J.C. and Ferrarese, L. et al., 2023. *ViCTORIA project: MeerKAT HI observations of the ram pressure stripped galaxy NGC 4523*. A&A, 676, id.A92, 24 pp. [Boselli et al. 2023b]

- Cuciti, V., de Gasperin, F., Brügger, M., Vazza, F., Brunetti, G., Shimwell, T.W., **Edler, H.W.**, van Weeren, R.J., Botteon, A., Cassano, R. and Di Gennaro, G. et al., 2022. *Galaxy clusters enveloped by vast volumes of relativistic electrons*. *Nature*, 609(7929), pp.911-914. [Cuciti et al. 2022]
- Shimwell, T.W., Hardcastle, M.J., Tasse, C., Best, P.N., Röttgering, H.J.A., Williams, W.L., Botteon, A., Drabent, A., Mechev, A., Shulevski, A., ..., **Edler, H.W.** et al., 2022. *The LOFAR Two-metre Sky Survey-V. Second data release*. *A&A*, 659, p.A1. [Shimwell et al. 2022]
- Biava, N., De Gasperin, F., Bonafede, A., **Edler, H.W.**, Giacintucci, S., Mazzotta, P., Brunetti, G., Botteon, A., Brügger, M., Cassano, R. and Drabent, A. et al., 2021. *The ultra-steep diffuse radio emission observed in the cool-core cluster RX J1720.1+ 2638 with LOFAR at 54 MHz*. *MNRAS*, 508(3), pp.3995-4007. [Biava et al. 2021]
- de Gasperin, F., Williams, W.L., Best, P., Brügger, M., Brunetti, G., Cuciti, V., Dijkema, T.J., Hardcastle, M.J., Norden, M.J., Offringa, A., ..., **Edler, H.W.** et al., 2021. *The LOFAR LBA Sky Survey-I. Survey description and preliminary data release*. *A&A*, 648, p.A104. [de Gasperin et al. 2021]
- de Gasperin, F., Brunetti, G., Brügger, M., van Weeren, R., Williams, W.L., Botteon, A., Cuciti, V., Dijkema, T.J., **Edler, H.**, Iacobelli, M. and Kang, H. et al., 2020. *Reaching thermal noise at ultra-low radio frequencies-Toothbrush radio relic downstream of the shock front*. *A&A*, 642, p.A85. [de Gasperin et al. 2020]

Contents

1	Introduction	1
1.1	Cosmic ray electrons	2
1.1.1	Acceleration processes	2
1.1.2	Loss processes	4
1.1.3	Fokker-Planck equation	5
1.1.4	Synchrotron emission	6
1.1.5	Spectral aging	7
1.2	Radio emission from galaxies	8
1.2.1	Star-forming galaxies	9
1.2.2	Radio galaxies	11
1.3	Galaxy clusters	12
1.3.1	Diffuse radio emission in galaxy clusters	14
1.3.2	The Virgo cluster	17
1.4	Environmental effects in galaxy clusters	19
1.4.1	RPS of late-type galaxies	21
1.4.2	Environmental effects in radio galaxies	24
1.5	The Low-Frequency Array	26
1.5.1	LOFAR calibration	28
1.5.2	LOFAR surveys	29
1.6	Aims and outline of this thesis	29
2	ViCTORIA project: The LOFAR HBA Virgo Cluster Survey	33
2.1	Introduction	34
2.2	Observations and data reduction	36
2.2.1	Challenges of the Virgo field	36
2.2.2	Data reduction	38
2.2.3	Flux density scale	44
2.3	LOFAR Virgo cluster catalog	47
2.4	Discussion	50
2.4.1	Galaxies	50
2.4.2	Extended emission	56
2.5	Summary	59
3	ViCTORIA project: The LOFAR view of environmental effects in the Virgo Cluster	65
3.1	Introduction	65
3.2	Data and sample	67
3.2.1	RPS sample	67
3.2.2	LOFAR-HRS sample	71

Contents

3.3	Statistical analysis	75
3.3.1	Radio-SFR-relation	75
3.3.2	Mass dependency and radio excess	77
3.3.3	Spectral properties	79
3.4	Spatially resolved radio-SFR analysis	81
3.5	Discussion	82
3.5.1	Radio-SFR relations	82
3.5.2	Spectral index of RPS galaxies	85
3.5.3	Model scenarios	86
3.6	Conclusion	90
4	Abell 1033: Radio halo and gently reenergized tail at 54 MHz	93
4.1	Introduction	94
4.2	Observations and data reduction	95
4.2.1	LOFAR LBA data	95
4.2.2	LOFAR HBA data	97
4.3	Results	99
4.3.1	Spectral index maps	100
4.3.2	Spectral aging analysis	100
4.3.3	Source-subtracted low-resolution images	103
4.3.4	Calculating the radio halo flux	105
4.3.5	Spectral index of the radio halo	106
4.4	Discussion	106
4.4.1	Spectral study of the GReET	106
4.4.2	Turbulent velocity	108
4.4.3	Radio halo	109
4.4.4	Radio phoenix	111
4.5	Conclusion	112
5	Investigating LOFAR 2.0 with Simulations	115
5.1	Introduction	115
5.2	LOFAR and future upgrades	116
5.3	Model corruptions	117
5.3.1	Ionosphere model	118
5.3.2	Primary beam	122
5.3.3	Bandpass response	122
5.3.4	Station based delays	124
5.3.5	Thermal noise	125
5.4	Simulation software	126
5.4.1	Full simulation setup	127
5.5	Calibration	128
5.5.1	Calibrator data reduction	130
5.5.2	Direction-independent calibration	133
5.5.3	Direction-dependent calibration	134
5.5.4	Calibration scenarios for LOFAR 2.0	139
5.5.5	Limitations	140
5.6	Conclusions	141

6 Conclusion and Outlook	143
6.1 Further projects	144
6.2 The next steps	145
7 Acknowledgments	147
8 Bibliography	149
A Images of Virgo cluster galaxies	169
B LOFAR data	207
C Radio-SFR maps	211
D Synchrotron emission model	213
E Uncertainty maps	215
F Spectral aging model	217
G Halo fit results	219

Contents

1 Introduction

The past century marks the epoch of extragalactic astrophysics, where we aim at understanding the universe beyond our Milky Way. The fundamental questions of extragalactic astrophysics are: What is the nature of the objects that we observe, what is their origin and what are their properties? And why are some objects different than others? In this thesis, I address these questions by investigating the influence the large-scale structure of the universe has on the properties of galaxies. In particular, my aim is to understand how the galaxy cluster environment influences the evolution of cluster member galaxies compared to galaxies that exist in more sparse astrophysical surroundings.

Two specific galaxy clusters serve as laboratories for my studies: The Virgo Cluster is the nearest cluster to us, and a considerable amount of our knowledge on the impact of the environment on the evolution of galaxies stems from this cluster. Even though it is among the best studied galaxy clusters, our picture of Virgo is far from complete. This is in particular the case in the radio band, where the extremely bright central radio galaxy M 87 prevented deep wide-field observations of the system up to now. Especially if we are able to open up this new observational window, which so far is only poorly unexplored, we can broaden our understanding of the processes which shape Virgo and its members. The second cluster that is investigated in this thesis is the merging system Abell 1033 (A1033). The merger activity and the environmental interactions in this cluster give rise to puzzling radio sources whose radio emission quickly fades at frequencies above 100 MHz. Thus, to get a deeper understanding of the effects at play, we require observations in the lowest possible frequency range in which we can conduct sensitive observations.

As primary observational tool, I rely on the Low-Frequency Array (LOFAR). This leading radio interferometer effectively combines high sensitivity, high resolution and a large field of view. Thus, it is perfectly suited to provide deep maps of the $> 100 \text{ deg}^2$ Virgo cluster field. Furthermore, its unique capabilities in the low- ($< 1 \text{ GHz}$) and ultra-low ($< 100 \text{ MHz}$) frequency regime allow the detection of the steep-spectrum emission from the radio sources in A1033 and the Virgo cluster. With radio observations, we are able to probe the non-thermal constituents of astrophysical objects - cosmic rays and magnetic fields. These can act as passive tracers for environmental interactions, since they are compressed and advected by the relative motion between galaxies and the ICM. Furthermore, they may also be actively affected by environmental interactions, for example if cosmic rays are accelerated by shocks and turbulence induced by the infall of galaxies on a cluster or, on much larger scales, in mergers between clusters.

In the following chapter, I provide an introduction to my research topics, starting with the fundamental processes involving the radio-emitting cosmic ray electrons Sect. 1.1. Next, in Sect. 1.2 and Sect. 1.3, I discuss star-forming galaxies, active galactic nuclei and galaxy clusters as well as the mechanisms behind their radio emission. The interplay between galaxies and the cluster environment is covered in Sect. 1.4, and LOFAR, as main observational tool is introduced in Sect. 1.5. Lastly, I provide more details on the aims of this thesis and the individual research projects in Sect. 1.6.

1.1 Cosmic ray electrons

The interpretation of radio observations is inevitably linked to the properties of the radio-emitting particles. Thus, this thesis starts with a brief review of the fundamental processes involving cosmic ray electrons (CRE). Cosmic rays (CR) are relativistic particles, such as protons, nuclei or electrons that are of extra-terrestrial origin (Hess 1913). They receive their energy from cosmic particle accelerators, for example in supernove (SN) explosions (as first suggested by Baade & Zwicky 1934), pulsars and pulsar wind nebulae (e.g. Abdo et al. 2010b), strong stellar winds (e.g. Abdo et al. 2010a; Bykov et al. 2020), active galactic nuclei (AGN, Blandford & Znajek 1977) and galaxy clusters (e.g. Willson 1970).

Local CR in the Solar System can be measured directly using space-bound instruments or indirectly using air shower detectors. CR are non-thermal particles, the local energy spectrum dN/dE of hadronic cosmic rays (i.e. protons and nuclei) follows a famous and well-studied power law relation ($dN/dE \propto E^\delta$) with a slope of $\delta \sim -2.7$ (Kotera & Olinto 2011) extending from GeV energies for many orders of magnitude. CRE (which include positrons in this thesis) show a somewhat steeper local spectrum $\delta \sim -3$, that shows a further steepening beyond $E = 1$ TeV. This local CRE spectrum is displayed in Fig. 1.1. Towards low energies, the local CRE spectrum is affected by solar modulation due to the interaction with the solar wind. Due to their charge, CR are deflected by galactic magnetic fields, which means that the spatial information of their origin is lost (except at the highest energies). However, photons and more recently, also neutrinos created in interactions of CR allow us to probe the cosmic laboratories of particle acceleration, the properties of astrophysical magnetic fields and the media in which the CR propagate as well as various feedback processes in which CR contribute to the evolution of stars, galaxies and galaxy clusters (see Ruszkowski & Pfrommer 2023, for a recent and extensive review on CR feedback).

A key difference between hadronic and leptonic CR lies in their interactions: Hadronic CR mainly interact in pp (proton-proton) and p γ (proton-photon) processes, resulting in a range of secondary particles, including gamma rays (I refer to Owen et al. 2023, for a review on CR processes). Those gamma rays can be observed using gamma ray satellites or Cherenkov telescopes, but those methods, while of crucial importance to understand the high-energy universe, suffer from the intrinsically low photon flux at gamma ray energies. Due to their lower mass, CRE, on the other hand, are much more efficient at radiating photons via synchrotron, Bremsstrahlung and inverse Compton processes, making them observable from the low-frequency ionospheric cutoff at $E_\gamma \approx 4 \times 10^{-8}$ eV to the high-energy Klein-Nishina cutoff at $E_\gamma > 10^{13}$ eV, across more than 20 orders of magnitude of photon energies. In this thesis, I focus on the emission of CRE with GeV energies, which are observable in the low-frequency (< 1 GHz) radio regime due to their synchrotron radiation. In the following sections, I provide a brief overview on the acceleration, loss and transport processes relevant for CRE.

1.1.1 Acceleration processes

A common mechanism for the acceleration of CR is diffusive shock acceleration (DSA). In the following, I closely rely on the description of a shock wave that expands into a surrounding medium which is provided in the classical papers of Bell (1978a,b). The shock wave is hereby assumed to be super-Alfvénic, such that the propagation velocity of the shock is larger than the Alfvén velocity v_A of disturbances in the magnetic field of a plasma. In the context of this thesis, this picture is associated with SN in the interstellar medium (ISM) and shock waves in AGN jets or the ICM from galaxy cluster mergers. Due to the low density of the surrounding medium, a shock wave does not directly transfer momentum to the medium via particle-particle collisions, but in a collisionless manner through inter-

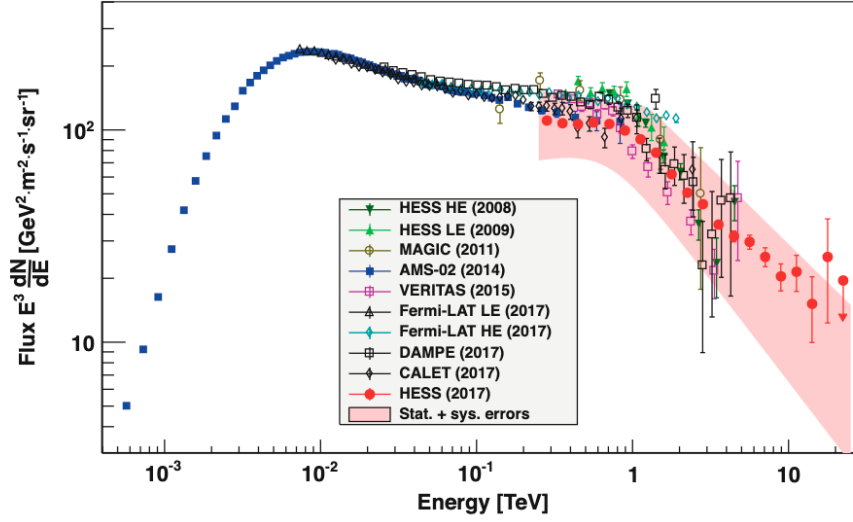


Figure 1.1: The local cosmic ray electron spectrum multiplied by E^3 . The measurements are taken from Aguilar et al. (2014); Abdollahi et al. (2017); Adriani et al. (2017); DAMPE Collaboration et al. (2017); Kerszberg (2017), the figure was adapted from Hofmann & Hinton (2020).

actions of particles with the electromagnetic inhomogeneities in the surrounding plasma. Considering energetic non-thermal electrons, protons or nuclei with gyroradii significantly larger than the width of the shock front which is approximately the gyroradius of a thermal proton (Boyd & Sanderson 1969), such that the particles are able to freely pass between the downstream region – in the direction of the shock’s origin – and upstream region –in the direction of the shock’s propagation. In the upstream region, the energetic electrons (which must also be super-Alfvénic since they overtook the shock) excite Alfvén waves, which in turn scatters them and reduces their streaming velocity to the order of the Alfvén speed, such that they are overtaken by the shock and enter the downstream region. In the downstream vicinity of the shock front, there is a turbulent region powered by the dissipation of the kinetic energy of the upstream plasma, which may again scatter the energetic electrons upstream, repeating the cycle, or diffuse away – hence, *diffusive* shock acceleration. After each crossing, the energetic electrons are effectively isotropized within the respective rest frame, and due to the velocity difference between the frames (the Mach number of the shock), each time there is a net gain of energy $E' = \beta E$. The efficiency of this process is, hence, determined by the Mach number. As derived by Bell (1978a), the fractional energy gain for relativistic particles ($v \approx c$) per up- and downstream crossing depends on the shock velocity u as $\beta = 1 + u/c$ (hence the process is also known as *first-order* Fermi acceleration), and the escape probability is $P = 1 - u/c$. Since both the fractional energy gain β and the escape probability P per crossing are energy independent for electrons of sufficient energy (see Bell 1978a), this process naturally leads to a power-law energy spectrum:

$$N(E) \propto E^{(\ln P / \ln \beta) - 1} = E^{(\ln(1-u/c) / \ln(1+u/c)) - 1} \approx E^{-2}, \quad (1.1)$$

for strong, non-relativistic shocks.

Another group of acceleration mechanisms, which do not require the presence of a shock, are second-order Fermi processes. Those involve energetic charged particles (e.g. electrons) that stochastically scatter with electromagnetic irregularities in a medium, for example those generated by magneto-hydrodynamic turbulence. Particles can either gain energy in head-on collisions or lose energy in fol-

1 Introduction

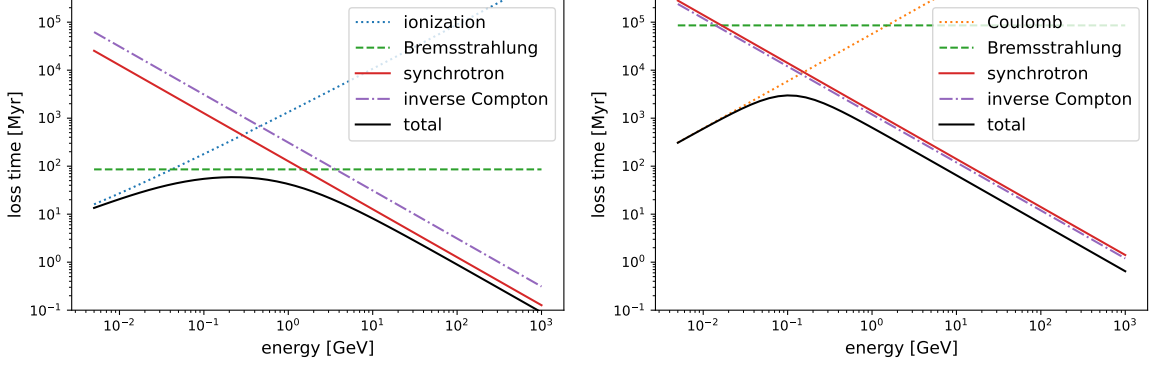


Figure 1.2: CRe energy loss times for different processes in a fiducial ISM (left panel) and ICM (right panel).

lowing collisions. Statistically, head-on collisions are more likely, such that there is a net energy gain $\langle\beta\rangle \propto (u/c)^2$, where u is the velocity of the irregularity (the original argument of Fermi 1949). The resulting volume-averaged electron spectrum for second-order Fermi processes can be approximated by a power-law with exponential cut-off $N(E) \propto E^\delta e^{-E/E_c}$ (Schlickeiser et al. 1987), where E_c is the cut-off energy. Due to its stochastic nature, the process is inefficient, resulting in a steep electron index $\delta \leq -3$ (Schlickeiser et al. 1987).

Further mechanisms capable of creating CRe that are relevant in the context of this thesis are the adiabatic compression of relativistic plasma (Enßlin & Gopal-Krishna 2001; Enßlin & Brüggén 2002) and inelastic collisions of hadronic CRe which create charged pions that subsequently decay into leptons (Dennison 1980; Enßlin et al. 2011). For a more detailed review on the various acceleration mechanisms and the observational implications, I refer to Brunetti & Jones (2014).

1.1.2 Loss processes

CRe are subject to various loss processes which consequently impact their energy spectrum and in the case of radiative losses, also allow us to indirectly probe their properties by observing the emitted photons. In presence of a neutral gas with a number density of N , CRe lose energy due to ionization of the gas. If the neutral medium is in the form of H I, the ionization energy loss rate of CRe with energy E is given by (throughout this section, the equations are based on the ones provided in Longair 2011):

$$-\frac{dE}{dt} = 2.6 \times 10^{-9} \left(\frac{N}{\text{cm}^{-3}} \right) \left[\ln \left(\frac{E}{\text{GeV}} \right) + 9.1 \right] \text{ eV s}^{-1}. \quad (1.2)$$

A similar logarithmic energy dependence is found in the case of Coulomb losses due to collisions with particles of a thermal plasma (Sarazin 1999):

$$-\frac{dE}{dt} = 8.3 \times 10^{-9} \left(\frac{N}{\text{cm}^{-3}} \right) \left[\ln \left(\frac{E/\text{GeV}}{N/\text{cm}^{-3}} \right) + 67 \right] \text{ eV s}^{-1}. \quad (1.3)$$

Since the dependency on the energy loss rate is logarithmic in both cases, the fractional energy losses due to ionization or Coulomb collisions are highest for low-energy CRe. This introduces a low-energy turnover in the electron spectrum. In neutral media such as the cold phases of the ISM, ionization losses are the most important loss process at low energies, while in highly ionized media, such as the ICM, Coulomb collisions are relevant. When propagating in a medium, CRe may further lose energy when being deflected by the electrostatic field of electrons, ions or nuclei, thereby emitting

Bremsstrahlung. For ultra-relativistic electrons and neutral hydrogen as the medium, the energy loss rate is proportional to the energy:

$$-\frac{dE}{dt} = 3.7 \times 10^{-7} \left(\frac{N}{\text{cm}^{-3}} \right) \left(\frac{E}{\text{GeV}} \right) \text{eV s}^{-1}, \quad (1.4)$$

meaning the fractional energy loss is constant and the shape (however, not the normalization) of the CRe energy distribution is unchanged.

Similarly to the deflection in the electrostatic fields of ambient particles, CRe will also lose energy and emit radiation when they are deflected by magnetic fields, this process is called synchrotron radiation (or *Magnetobremsstrahlung*). For CRe that are deflected in a magnetic field B with an isotropic pitch angle distribution, the energy loss rate is given by:

$$-\frac{dE}{dt} = 2.5 \times 10^{-7} \left(\frac{E}{\text{GeV}} \right)^2 \left(\frac{B}{10 \mu\text{G}} \right)^2 \text{eV s}^{-1}. \quad (1.5)$$

Analogously, CRe can scatter with electromagnetic waves in the form of an ambient photon field via the inverse Compton process, which yields a similar description of the loss rate to the synchrotron case:

$$-\frac{dE}{dt} = 1.02 \times 10^{-7} \left(\frac{E}{\text{GeV}} \right)^2 \left(\frac{U_{\text{rad}}}{\text{eV cm}^{-3}} \right) \text{eV s}^{-1}, \quad (1.6)$$

where U_{rad} is the energy density of the photon field. Both synchrotron and inverse Compton losses depend on the square of the CRe energy, meaning they steepen the electron spectrum towards high energies.

In Fig. 1.2, I show the energy loss times $t_{\text{loss}} = \frac{E}{dE/dt}$ for a fiducial ISM and ICM scenario. For the ISM, I assumed $N = 1 \text{ cm}^{-3}$, $B = 10 \mu\text{G}$, $U_{\text{rad}} = 1 \text{ eV cm}^{-3}$ and for the ICM, I used $N = 10^{-3} \text{ cm}^{-3}$, $B = 3 \mu\text{G}$ and $U_{\text{rad}} = U_{\text{CMB}} = 0.26 \text{ eV cm}^{-3}$. In a dilute medium such as the ICM, only synchrotron and inverse Compton losses are relevant for electrons of GeV energies and above. Notably, the only ubiquitous process, fully independent of the surrounding medium, is the inverse Compton scattering of the omnipresent cosmic microwave background (CMB) photons with an energy density of $U_{\text{rad}} = 0.26(1+z)^4 \text{ eV cm}^{-3}$ (Fixsen 2009).

1.1.3 Fokker-Planck equation

The electron energy distribution $N(E)$, governed by aforementioned acceleration and loss processes, is described by the Fokker-Planck partial differential equation. Here, I briefly discuss a simplified isotropic formulation of this equation, assuming no diffusion, advection, compression or rarefaction.

$$\frac{\partial N(E, t)}{\partial t} = \frac{\partial}{\partial E} \left[N(E, t) \left| \frac{dE}{dt} \right| \right] + Q(E, t) \quad (1.7)$$

Where $Q(E, t)$ is the injection term and $\left| \frac{dE}{dt} \right|$ the energy loss due to the processes presented in the previous Sect. 1.1.2.

In the following, I briefly review analytical steady-state solutions of this equation in the case of power-law injection $Q(E) = qE^\delta$ and different loss processes. Given the requirement that the system reached a steady state is equivalent to $\frac{\partial N(E, t)}{\partial t} = 0$, we can thus rearrange and integrate:

$$N(E, t) \left| \frac{dE}{dt} \right| = - \int Q(E, t). \quad (1.8)$$

1 Introduction

This yields

$$N(E) = \frac{qE^{\delta+1}}{(\delta + 1) \left| \frac{dE}{dt} \right|} \quad (1.9)$$

for $\delta \neq -1$. Therefore, if synchrotron and inverse Compton losses are dominant and $\frac{dE}{dt} \propto E^2$, we find that the steady-state electron energy index is steeper by one, i.e. $N(E) \propto E^{\delta-1}$. This realization is of high importance for numerous astrophysical environments where electrons are continuously injected and cooled by synchrotron and inverse Compton emission, and it approximately describes the volume-integrated energy spectrum of electrons in such systems.

In dense astrophysical surroundings, such as cool phases of the ISM, other loss processes may be dominant, in particular for low-energy CRe. In the case of dominant Bremsstrahlung losses ($\frac{dE}{dt} \propto E$), the electron spectral index remains unchanged, and for ionization losses, neglecting the logarithmic energy dependency in Eq. 1.2, we find a flatter electron spectrum of $N(E) \propto E^{\delta+1}$. Aside from a few instructive simplified cases, Eq. 1.7 is solved numerically. Various algorithms exist to solve different formulations of the equation in an efficient manner. In this thesis I employ the method developed by Chang & Cooper (1970).

More general formulations of Eq. 1.7 include advective and diffusive transport processes, energy changes due to expansion and compression and momentum space diffusion. For information on these processes, I refer to Heesen et al. (2018) and Brunetti & Jones (2014).

1.1.4 Synchrotron emission

Via the radiative loss processes presented in the previous section, CRe are capable of emitting across a wide range of photon energies. At low radio frequencies, the only relevant emission is synchrotron radiation. The intensity I at a given frequency ν of a CRe population $N(E, \theta)$ is given by (Harwood et al. 2013)

$$I_\nu = 4\pi B I_0 \int_0^\pi d\theta \sin^2(\theta) \int dE F(x) N(E, B, t, \theta), \quad (1.10)$$

where θ is the pitch angle between the electron velocity and the magnetic field, I_0 a normalization constant and $F(x)$ the following integral of the Bessel function of order 5/3:

$$F(x) = x \int_x^\infty K_{5/3}(z) dz. \quad (1.11)$$

The variable $x = \nu/\nu_c$ is the ratio of the frequency ν and the critical frequency ν_c , which is given by:

$$\nu_c = \frac{3E^2 e B \sin(\theta)}{4\pi m_e^3 c^4}. \quad (1.12)$$

Here, e is the electron charge, m_e the electron rest mass and c the speed of light. An important property of synchrotron emission is that it is polarized if the magnetic field in the emission region are coherent on sufficiently large scales.

For a power law injection electron spectrum $N(E) = N_0 E^\delta$, we can approximate the synchrotron spectrum $J(\nu)$ by summing up the contribution of the individual electrons and assuming that they radiate all their energy at a frequency of $\nu = \gamma^2 \nu_g$, where γ is their Lorentz factor and $\nu_g = eB/2\pi m_e$ their gyro frequency (Longair 2011). We can then directly relate the energy radiated in a frequency interval $d\nu$ to the energy the electron population loses in an energy interval dE :

$$J(\nu) d\nu = -\frac{dE}{dt} N(E) dE \quad (1.13)$$

The electron energy E in the terms of the right-hand side can be expressed as a function of the frequency at which these electrons emit: $E \propto \gamma = \sqrt{v/v_g}$. Taking the derivative of this expression in v and re-arranging, we further obtain $dE \propto dv / \sqrt{vv_g}$. Lastly, $\frac{dE}{dt} \propto E^2 B^2$ is directly given by the energy loss rate Eq. 1.6. Putting these relations into Eq. 1.13, we find

$$J(\nu) \propto v_g^{-1} B^2 E^{2+\delta} \propto B^{(1-\delta)/2} \nu^{(\delta+1)/2}. \quad (1.14)$$

Thus, a power law electron population with an energy index δ emits synchrotron radiation that obeys a power law with a spectral index $\alpha = (\delta+1)/2$. For DSA at a high mach number shock, we consequently obtain a injection spectral index of $\alpha = -0.5$. We can also express the steady-state electron indices found in the previous Sect. 1.1.3 for continuous strong-shock DSA: In the case of synchrotron and inverse Compton losses, we find a volume-integrated spectral index of $\alpha = -1$, whereas for dominant ionization losses, the synchrotron spectrum is approximately constant ($\alpha \approx 0$).

1.1.5 Spectral aging

In reality, CRe in astrophysical systems are, at least locally, not well described by steady-state solutions to Eq. 1.7. If we consider a quasi-instantaneous pulse-injection of CRe, that can be found for example if the source of injection (e.g. a shock) propagates relative to the surrounding medium, clearly there cannot be a local equilibrium between the injection and energy losses. After the injection, the high-energy electrons lose energy due to synchrotron and inverse Compton processes: $\frac{dE}{dt} \propto E^2$ (see Sect. 1.1.2). The energy loss time scale for the CRe is given by

$$t_{\text{sync+IC}} = \frac{E}{\frac{dE}{dt}} \propto E^{-1} \quad (1.15)$$

Thus, more energetic particles are depleted on shorter time scales, causing a steepening of the electron and the corresponding synchrotron emission spectrum in a phenomenon known as *radiative aging*. The energy loss rate $-\frac{dE}{dt}$ of electrons of a certain energy E is determined by the energy density in the ambient magnetic field (if synchrotron losses dominate). Thus, if reacceleration processes can be neglected, there is a causal connection between the observable synchrotron slope, the age of the CRe population and the magnetic field energy density. With certain assumptions, this allows us to infer physical parameters of radio sources. In this model, the initially injected spectrum $N(E) = N_0 E^\delta$ deviates from the power law shape after a time $t > 0$ (Pacholczyk 1970):

$$N(E, \theta, t) = N_0 E^\delta \left(1 - \frac{E}{E_c(t, B, \theta)} \right)^{-\delta-2}. \quad (1.16)$$

Here, E_c is the cutoff energy. Depending on the assumptions regarding the pitch angle θ , different formulations for E_c exist. The original suggestion of Kardashev (1962), which was further popularized by Pacholczyk (1970) (hereafter KP-model), assumes that the pitch angles are isotropic and constant. This yields the following definition:

$$E_{c,\text{KP}} = \frac{3m_e^3 c^7}{2e^4 t B^2 \sin(\theta)^2}. \quad (1.17)$$

Instead, the model of Jaffe & Perola (1973) (hereafter JP model) follows a more physically realistic approach by assuming that the pitch angles are only isotropic on short time scales and using the time average $\langle \sin(\theta)^2 \rangle$

$$E_{c,\text{JP}} = \frac{3m_e^3 c^7}{2e^4 t B^2 \langle \sin(\theta)^2 \rangle}. \quad (1.18)$$

1 Introduction

The formulations here only take the synchrotron losses into account, but considering additional inverse Compton processes is analogous since they behave identically. Further, more complex models were also suggested in the literature, e.g. the one of Tribble (1993) which assumes a Gaussian random magnetic field.

In the JP and the KP model, the resulting electron spectrum increasingly steepens towards the sharp cut-off at E_c . Since $E_c \propto t^{-1}$, the cut-off migrates to lower energies with time. The cut-off is less sharp in the KP case, since for small θ , E_c becomes increasingly high. The corresponding synchrotron spectrum will also feature a steepening, albeit less sharp than in energy – since contrary to what was assumed in the simplified derivation of Eq. 1.14, CRe do not radiate their energy only at a single frequency.

Under the assumption that the spectral aging obeys a certain model, the curvature of the synchrotron spectrum, which can be obtained from multi-frequency radio observations, can constrain the age t and the magnetic field B . There is an ambiguity between the aging rate (the magnetic field) and the radiative age (the spectral curvature). This ambiguity is commonly resolved by assuming that there is an equipartition in the radio source between the energy density in the magnetic field $U_{\text{mag}} = B^2/2\mu_0$ and the cosmic ray energy density (see e.g. Beck & Krause 2005; Harwood et al. 2013). Direct observations of the inverse Compton emission in radio galaxy lobes indicate that the actual magnetic field strength for those sources is rather close to the equipartition assumption (e.g. Croston et al. 2005). An alternative approach is to assume a minimum-aging magnetic field strength B_{min} , which is the magnetic field value that balances the synchrotron and inverse Compton losses such that the losses of the observed electron energies are minimal. Therefore, one can obtain an upper limit on the age of the radio emission. The idea behind this is that for very high values of B , rapid synchrotron losses quickly deplete the CRe. Similarly, for very low values of B , we observe synchrotron emission from highly energetic CRe which suffer rapid inverse Compton losses. In-between these two limits, there exists a global maximum for the CRe lifetime for $B = B_{\text{min}}$. The minimum aging magnetic field strength B_{min} can be calculated from the sum of the synchrotron and inverse Compton losses (in cases where the CMB is the only relevant radiation field). This sum is minimal for $B_{\text{min}} = B_{\text{CMB}}/\sqrt{3}$, where $B_{\text{CMB}} = 3.2 \times (1+z)^2 \mu\text{G}$ is the equivalent magnetic field strength of the CMB at a redshift z (Longair 2011). More detailed information about the spectral aging analysis of radio sources can be found in Hardcastle (2013); Harwood et al. (2013); Harwood et al. (2015); Harwood et al. (2017).

1.2 Radio emission from galaxies

Depending on their optical morphology, galaxies are broadly classified into spiral, irregular, lenticular and elliptical galaxies (Hubble 1926; de Vaucouleurs 1961). A prototypical spiral galaxy like our Milky Way shows spiral arms which are part of a flat disk that contains an ISM with a significant amount of neutral and molecular gas and is actively forming stars. Elliptical galaxies on the other hand typically show no to little star formation and cold gas. The differences between the morphological classes is also apparent in the radio continuum. The radio emission of late-type galaxies (spiral and irregular galaxies) is usually due to star formation, while in early-type galaxies (lenticular and elliptical galaxies), it is due to nuclear activity. In this section, I will briefly introduce these processes which are responsible for the radio emission of galaxies.

1.2.1 Star-forming galaxies

New stars are formed by the gravitational collapse of dense and cold gas clouds in the ISM. This process is most commonly associated with late-type galaxies. When massive and short lived stars are formed, they quickly reach the end of their lives in SN explosions. Those accelerate CRe which emit synchrotron radiation in the presence of galactic magnetic fields. This is the dominant mechanism for the radio continuum emission of normal star forming galaxies at GHz frequencies and below.

The ISM is a multi-phase medium, consisting of a hot-ionized phase with densities $n < 10^{-2} \text{ cm}^{-3}$ and temperatures $T > 10^5 \text{ K}$ and a warm-ionized and warm-neutral phase which have densities $n \approx 0.1 - 1 \text{ cm}^{-3}$ and temperatures $T \sim 10^4 \text{ K}$ (Kennicutt & Evans 2012). Thermal instabilities in the dense neutral gas give rise to the cold neutral medium which has a density of $n > 10 \text{ cm}^{-3}$ and temperatures $T < 100 \text{ K}$ (Field et al. 1969). Observationally, the H I gas in this phase can be probed due to its hyperfine structure transition which gives rise to the 21 cm radio line. The coldest part of the ISM, in which star formation can take place, are molecular clouds ($n > 30 \text{ cm}^{-3}$, $T < 10 \text{ K}$, Kennicutt & Evans 2012). Due to the lack of dipole transitions and its low mass, the molecular hydrogen, that is the dominant component of these clouds, is challenging to observe directly. Thus, it is probed indirectly, usually in CO lines (as first demonstrated by Wilson et al. 1970).

If a molecular gas cloud is sufficiently cold, dense and large, it will depart from hydrostatic equilibrium and undergo runaway gravitational collapse. During the collapse of the cloud, it fragments and produces stars of different masses. The mass-distribution of the newly formed stars is known as initial mass function (IMF). Famously, Salpeter (1955) derived an IMF that is a simple power-law $\frac{dM_\star}{dN} \propto M_\star^{-2.35}$ in the stellar mass M_\star . While later works found IMFs that strongly deviate from this power law below $1 M_\odot$, at higher masses, more recent studies are still in reasonable agreement with the Salpeter slope (e.g. Kroupa 2001; Chabrier 2003). While the IMF varies depending on the metallicity, gas temperature and other environmental parameters, a uniform IMF remains a good approximation for integrated populations of galaxies at low redshifts $z \approx 0$ (Kennicutt & Evans 2012). The IMF is one of the most fundamental astronomical distributions, since the basic properties of stars such as their luminosity, lifetime and color strongly depend on their mass. The luminosity-mass relation for stars is usually expressed as power law of the form $L = L_\odot \left(\frac{M_\star}{M_\odot}\right)^a$ with $a \approx 3.5$, where $L_\odot = 3.8 \times 10^{26} \text{ W}$ is the solar luminosity, M_\star the mass of the star and $M_\odot = 2.0 \times 10^{30} \text{ kg}$ the solar mass. Massive stars can convert mass to radiative energy more effectively, and as a consequence, they are short-lived with a lifetime $\tau_\star \propto M_\star/L_\star \propto M_\star^{-2.5}$. To give an example, a B-star with a mass of $10 M_\odot$ has a lifetime of only 25 Myr (Smartt et al. 2009). Thus, massive stars are indicative of recent star formation, and by inferring their number, we can observationally estimate the star formation rate (SFR). This is a crucial quantity of galaxies and smaller structures, and for the Milky Way, $\text{SFR} \approx M_\odot \text{ yr}^{-1}$ (Chomiuk & Povich 2011). The time scale over which the SFR is averaged in such measurements depends on the lifetime and as a consequence, the mass of the stars that contribute to the observed emission. A star with a photospheric temperature T emits radiation that approximately follows Planck's law

$$B(\nu, T) = \frac{8\pi h \nu^3}{c^3} \frac{1}{e^{\frac{h\nu}{k_B T}} - 1}, \quad (1.19)$$

where B is the spectral radiance, ν the observed frequency, h Planck's constant and k_B Boltzmann's constant. As can be shown with Boltzmann's law and the mass-luminosity and mass-radius relations for main sequence stars, $T \propto M_\star^{\frac{5}{8}}$. So more massive stars have higher temperatures and thus emit more strongly at shorter wavelengths. This stellar ultraviolet (UV) emission can be directly observed by space-bound telescopes and is one of the most direct tracers of star formation (Kennicutt & Evans

1 Introduction

2012). A fraction of the UV photons are capable of ionizing the surrounding medium, which gives rise to ionization lines. Due to its brightness, the most commonly observed ionization line is the Balmer series H α line at $\lambda = 656$ nm. Responsible for the ionization of hydrogen are far-UV photons ($\lambda < 91$ nm) which are mainly emitted by massive O-B stars ($M > 8M_{\odot}$) with main sequence life times of ~ 10 Myr (Boselli et al. 2015). Thus it is one of the most instantaneous star formation tracers available. A fraction of the UV and H α line emission is absorbed and thus contributes to the heating of the surrounding dust in the ISM. This means on the one hand that the infrared (IR) emission of the dust itself is a tracer of the SFR, and on the other hand that the SFR estimates in the optical regime need to be corrected for that dust absorption. This correction requires good multi-wavelength coverage and introduces systematic uncertainties in the SFRs.

An alternative SFR tracer, that is not obscured by dust and thus provides effectively extinction-free estimates of the SFR is the radio continuum emission of galaxies¹. Massive ($M > 8M_{\odot}$) stars quickly end their life in an SN explosion, which are capable of accelerating CRe via DSA (see Sect. 1.1.1). Gyrating in the galactic magnetic fields, these CRe emit synchrotron radiation (see Sect. 1.1.4). In galaxies that do not show strong AGN activity, this emission is the dominant contribution to the radio luminosity below a few GHz. At higher frequencies, the free-free emission from H II regions is another relevant contribution (see Sect. 1.1.2 and Condon 1992). This is also an independent SFR tracer after separating it from the synchrotron component (e.g. Niklas et al. 1997; Murphy et al. 2012). In the low-frequency regime ($\nu < 1$ GHz), the use of synchrotron emissions as widely available SFR tracer that is unaffected by extinction and free-free contamination comes at the cost of a significant lifetime of the CRe of ~ 100 Myr (see Sect. 1.1.2), which can be problematic in the case of quick variations in SFR due to external perturbations (Ignesti et al. 2022c). Also contrary to more direct SFR tracers, the radio-SFR-relation is extremely challenging to derive from first principles due to the high uncertainties of the many relevant processing steps (SN acceleration efficiency, CRe transport, magnetic field configuration, loss processes, escape, contribution of secondary electrons). It is thus usually empirically calibrated against other tracers (e.g. Condon 1992; Murphy et al. 2011), for example using the tight radio-IR correlation (e.g. Bell 2003).

In the calorimetric theory originally proposed by Voelk (1989), it is assumed that all energy of the CRe is lost inside the galaxies via radiative processes. In this model, the total radio emission of star forming galaxies has a rather weak dependence on the magnetic field strength, which leads to a radio-SFR relation (and hence radio-IR relation) that is approximately linear. At a high frequency (in the context of this thesis) of 6 GHz, this appears to hold (e.g. Li et al. 2016; Hindson et al. 2018), while observations show that at lower frequencies, the relation becomes increasingly super-linear (e.g. Basu et al. 2015; Gürkan et al. 2018; Heesen et al. 2022). This super-linearity is thought to be due to the greater life times and transport lengths for the lower-energy CRe emitting at lower frequencies, where CRe escape becomes increasingly important. Gürkan et al. (2018) suggested that the super linearity is explained by the CRe-escape being less effective in larger galaxies, with statistically higher SFR, turning them into more efficient calorimeters. A clear imprint of this is that larger, more massive galaxies show steeper radio spectral indices, corresponding to strong radiative losses (see Sect. 1.1.2), which Heesen et al. (2022) attributed to their higher calorimetric efficiency. In Heesen et al. (2023b), these authors showed that a spectral index-based correction can be applied to linearize the low-frequency radio-SFR relation. In Chap. 3, I present an independent study on the radio-SFR relation of a sample of nearby galaxies in the Virgo cluster and beyond, including their spectral properties.

Observations show that star-forming galaxies have magnetic fields in the order of $10 \mu\text{G}$ (Beck 2015, and references therein). The magnetic field is thought to be amplified by a small-scale dy-

¹At low frequencies, free-free absorption plays a role in some cases (Clemens et al. 2010).

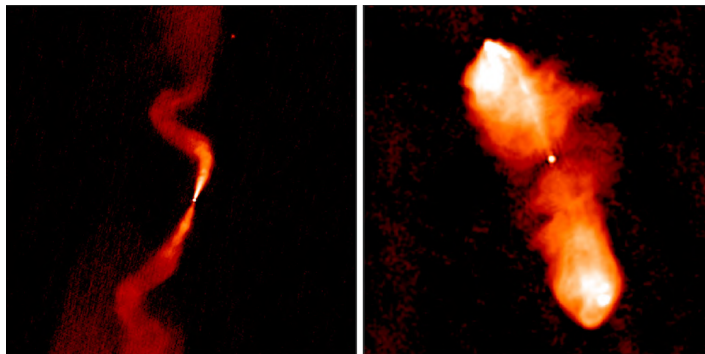


Figure 1.3: Fanaroff-Riley type I (left, 3C 31) and type II (right, 3C 98) radio galaxies. This figure was adopted from Hardcastle & Croston (2020).

nano due to turbulence that is injected into the ISM by SN explosions (Gressel et al. 2008). Thus, star-forming activity enhances the magnetic field, and empirical relations point towards $B \propto \text{SFR}^{0.3}$ (Schleicher & Beck 2013; Tabatabaei et al. 2017). The large-scale ordered magnetic field in star-forming galaxies (Borlaff et al. 2023) is believed to be generated by the α - Ω dynamo (Beck et al. 2020). In this process, the differential rotation of the galaxy disk creates a large-scale ordered magnetic field from turbulent fields. Aforementioned dynamo effects require an initial seed magnetic field, which may be either of primordial origin or due to astrophysical processes (see e.g. the review of Beck 2015).

1.2.2 Radio galaxies

Radio galaxies are energetic and luminous (up to $L_{144\text{MHz}} \sim 10^{27} \text{ W Hz}^{-1}$) radio sources powered by an AGN (Lynden-Bell 1969). They make up the vast majority of the bright sources in the radio sky (e.g. Best et al. 2023). Oftentimes, the relativistic jets launched by the AGN give rise to bi-symmetric lobes of radio emission which may be significantly larger than the optical host galaxy. If those lobes show a smooth surface brightness profile which is gradually fading, they are categorized as Fanaroff-Riley type I (FRI, Fanaroff & Riley 1974) sources. If instead, they terminate in edge-brightened hotspots, they are called Fanaroff-Riley type II (FR II) radio galaxies. In Fig. 1.3, I show two examples for FRI and FR II sources. Historically, a rather clear separation between the radio luminosities of FRI and FR II galaxies was suggested, with FR II objects being more radio-luminous. More recent results with improved samples, however, showed that this dichotomy is not as clear as initially expected (e.g. Best 2009; Mingo et al. 2019). The jets of both FRI and FR II sources are thought to be initially relativistic, but the FRI jets are thought to decelerate quickly and become non-relativistic, while FR II jets are believed to remain relativistic up to the hotspots (Saikia 2022). For general reviews on radio galaxies and their properties, I refer to Hardcastle & Croston (2020); Magliocchetti (2022) and Saikia (2022). The optical hosts of radio galaxies are typically massive early-type galaxies, and there is a strong correlation of their radio luminosity and the stellar mass (e.g. Best et al. 2005). The angle between the jet axis and the line of sight plays an important role for the multi-frequency emission of AGN, this also holds in the radio regime. If the jet axis is closely aligned with the line of sight, relativistic beaming amplifies the observed radio emission. Examples for sources where this effect is apparent are 3C 273, the prototype quasar (Schmidt 1963) in the background of the Virgo cluster, and M 87 at the center of the Virgo cluster. In both sources, only the beamed jet can be observed, leading to a single-jet morphology (Groeneveld et al. 2022; Owen et al. 1989).

1 Introduction

The lobes of radio galaxies are permeated by a relativistic plasma and magnetic fields, which generate the observed synchrotron emission. From the observed synchrotron emission alone, it is not possible to estimate the strength of the magnetic fields, as there is an ambiguity between the energy density of the magnetic field and the CRe. However, for a limited number of nearby powerful radio galaxies, the inverse Compton scattering of the CRe with ambient photon fields could be directly observed. This resolves the degeneracy and allows to determine the magnetic fields in the lobes, which are found to be on the order of $\sim 10 \mu\text{G}$ (e.g. Croston et al. 2005). Furthermore, radio galaxies are oftentimes found to be strongly linearly polarized (Pacholczyk 1970), this is in particular the case for the hotspots of FR II sources, where the magnetic field is thought to be compressed due to the expansion of the lobes. For FRI type radio galaxies, studies of the polarization in the jets point to a parallel orientation between the jets and the magnetic fields (e.g. Laing et al. 2008; Kharb et al. 2012).

The integrated radio spectral index of radio galaxies is $\alpha \sim -0.7$ (Condon et al. 2002), their central core oftentimes shows a flat or even inverted ($\alpha > 0$) spectral index, which is interpreted as the absorption of low-frequency radiation (e.g. O’Dea 1998; Lobanov 1998). The hotspots are typically in agreement with a spectral index from diffusive shock acceleration at a high Mach number shock $\alpha \approx -0.5$, while the diffuse low-surface brightness emission surrounding the hotspots is typically steeper. A resolved analysis of the spectral index distribution of radio galaxy lobes can be used to estimate the radiative age of the plasma in a spectral aging analysis (e.g. Harwood et al. 2013; Harwood et al. 2015). Generally, in FRI radio galaxies, a gradual aging from the core of the radio galaxy along the jets is found (e.g. Laing et al. 2008), while in FR II objects, the plasma ages as it is transported away from the hotspots (e.g. Harwood et al. 2013, 2017; Pinjarkar et al. 2023).

1.3 Galaxy clusters

Galaxy clusters are the most massive ($M \geq 10^{14} M_{\odot}$) structures in the universe that have reached virial equilibrium, and are located at the nodes of the cosmic web. They are composed of hundreds to thousands of galaxies bound together by gravitational attraction, most importantly from the dark matter component, which accounts for approximately 85% of the total mass (e.g. Blumenthal et al. 1984; Gonzalez et al. 2013). At optical wavelengths, galaxy clusters stand out as an overdensity in the number of galaxies. Additionally, they show a faint and diffuse stellar component, the intracluster light, which accounts for $\sim 15\%$ of the total luminosity (e.g. Adami et al. 2005). Clusters typically host a large fraction of elliptical galaxies, in particular in their central regions. A strong correlation is found between the fraction of early type galaxies (meaning ellipticals and lenticulars) and proxies of the cluster mass, such as the velocity dispersion (typically $\geq 1000 \text{ km s}^{-1}$ in massive clusters) and X-ray luminosity. In massive systems, the early type fraction in the central region can exceed 80% (Poggianti et al. 2009). Galaxy clusters oftentimes host one (or in some cases, more) dominant elliptical galaxies, these are referred to as brightest cluster galaxies (BCG) and are usually found at the cluster center.

However, the majority of the baryonic content ($\sim 80\%$, Gonzalez et al. 2013) of galaxy clusters is not in the form of stars, but in the ICM, a hot ($T > 10^7 \text{ K}$), ionized and dilute ($\sim 10^{-3} \text{ particles cm}^{-3}$, see also Fig. 1.5) plasma. The ICM can be probed based on its imprint on the cosmic microwave background (CMB) using the Sunyaev-Zeldovich (SZ, Sunyaev & Zeldovich 1972) effect, which also allows for inference of the cluster mass (e.g. Ade et al. 2016). Due to its high temperature, the thermal electrons in the ICM emit via Bremsstrahlung (also known as free-free radiation) and metal recombination lines. Thus, galaxy clusters are bright and extended X-ray sources. Observations with X-ray telescopes allow us to map the distribution of the ICM at high resolution and to determine

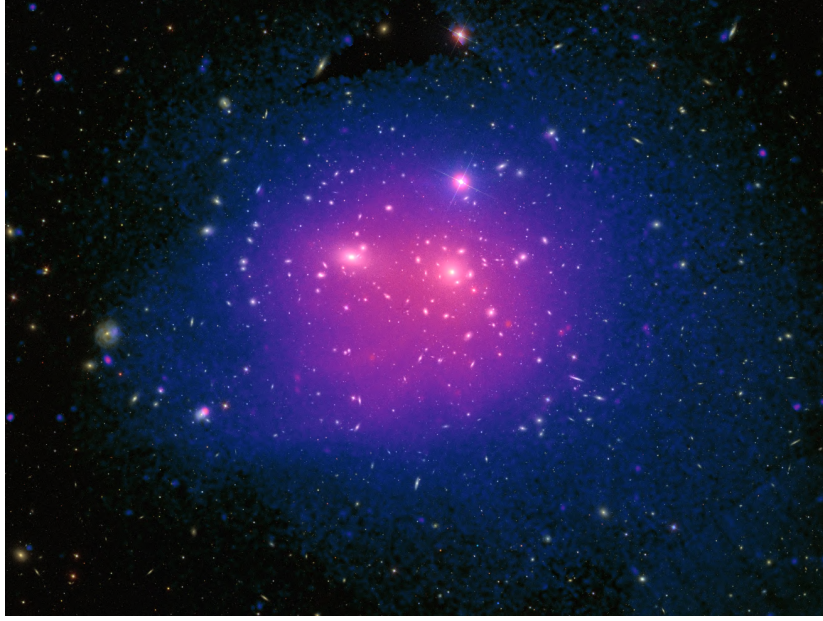


Figure 1.4: The X-ray (blue-purple, from XMM-NEWTON) and optical (white, from the SDSS) view of the Coma cluster. In the optical, a high fraction of elliptical galaxies can be observed, while the X-ray emission traces the hot ICM in the cluster. The size of the image corresponds to approximately $1.5 \times 1.1 \text{ Mpc}^2$ at the redshift of the Coma cluster ($z = 0.023$, Bilton & Pimblet 2018). Image credits: ESA/XMM-Newton/SDSS/Sanders et al. (2020).

ICM properties such as temperature, metallicity and the dynamical state. Common estimates for characteristic radial scales of clusters are also derived from the X-ray brightness distribution, such as R_{200} and R_{500} , which define the radii of spheres encompassing a mean density of 200 and 500 times the critical density ρ_c . In Fig. 1.4, I show the X-ray and optical emission of the massive nearby Coma cluster. The cluster has a high fraction of elliptical galaxies with two BCGs, which are embedded in the X-ray emitting ICM.

In the absence of external perturbations, the ICM is close to kinetic equilibrium, meaning the electrons and the protons both approximately follow Maxwellian distributions of the same temperature. The Bremsstrahlung emissivity ϵ_v^{ff} of the plasma depends on the density n_e and the temperature T (Sarazin 2008, here the simplified case of a hydrogen plasma)

$$\epsilon_v^{\text{ff}} \propto n_e^2 T^{-\frac{1}{2}} e^{-\frac{h\nu}{kT}} g_{\text{ff}}(T, \nu), \quad (1.20)$$

where ν is the emitted frequency, h Planck's constant, k Boltzmann's constant and g_{ff} the Gaunt factor, which varies only slowly. The quadratic dependency on the electron density is a consequence of the Bremsstrahlung process being proportional to both the electron and ion density ($\approx n_e$ in this example). Equivalently, the emission from metal recombination lines, which is dominant at temperatures below $\approx 3 \times 10^7 \text{ K}$ (Sarazin 2008), is also approximately quadratic in the density and additionally depends on the metallicity, which, as the density, is highest in the cluster center. As a consequence, the overall X-ray emission of galaxy clusters is strongly peaked towards the dense central parts, where the gas can efficiently cool via these radiative channels. In the Fig. 1.5, I show the radial profiles of electron density, temperature, pressure and enclosed mass for the nearby Virgo cluster. As can be seen in the top two panels, the central region with a density $n_e \geq 10^{-2} \text{ cm}^{-3}$ corresponds to the cool core of the cluster. The pressure $P \propto \rho T$ of the ICM can approximately be derived from the ideal gas law. In

1 Introduction

hydrostatic equilibrium, the thermal pressure is equal to the gravitational one.

The enormous accumulations of mass that galaxy clusters represent originate via bottom-up mergers of smaller structures over cosmic times (e.g. Voit 2005). Major mergers between clusters are the most energetic events in the present-day universe, releasing gravitational energy in excess of 10^{64} ergs (Sarazin 2008). Part of that energy is dissipated into the ICM through shock waves, which heat the plasma and are also able to accelerate cosmic rays via first- and second-order Fermi processes, giving rise to cluster-scale synchrotron emission which is detected at radio wavelengths in a fraction of merging clusters (see Sect. 1.3.1). The enormous amount of energy released during mergers leads to a departure from the state of hydrostatic equilibrium.

Ongoing and recent mergers can be traced by the spatial and velocity distribution of the galaxies. However, the most important tracer is the X-ray morphology of the ICM (see ZuHone & Su 2022, for a detailed introduction). Large scale shocks and cold fronts, strong deviations from spherical symmetry, and the presence of clear substructure are all indicative of merger activity.

1.3.1 Diffuse radio emission in galaxy clusters

A fraction of the energy released in mergers of galaxy clusters can be converted into the kinetic energy of CRe. The synchrotron emission of these relativistic electrons in the ICM can be observed as diffuse, cluster-scale radio emission. For a detailed review of this topic, I refer to van Weeren et al. (2019). Historically, these cluster radio sources were classified mainly by their morphology and location with respect to the ICM. Diffuse, approximately spherical radio sources which roughly follow the X-ray emission of the ICM are referred to as radio halos. They have sizes of ~ 1 Mpc. The prototype radio halo is located in the nearby Coma cluster (e.g. Large et al. 1959; Ballarati et al. 1981; Bonafede et al. 2022, see Fig. 1.6, left panel). Elongated, arc-like radio sources in the outskirts of galaxy clusters are known as radio relics, they can also reach sizes in excess of 1 Mpc. In Fig. 1.6 (right panel) the famous *Sausage* radio relic in the cluster CIZA J2242.8+5301 is displayed (e.g. Di Gennaro et al. 2018). It has an extension of 2 Mpc and is located 1.5 Mpc from the cluster center. For both source categories, a connection to mergers of galaxy clusters is established. Radio relics trace merger-induced shock waves which are also observable as temperature jumps or surface brightness discontinuities in the X-rays. Diffusive shock-acceleration is possibly responsible for the acceleration of CRe which can then emit synchrotron radiation in the weak magnetic fields of the ICM (e.g. van Weeren et al. 2010). The connection to the merger-shocks also explains the arc-like morphology of many radio relics. The shock waves of cluster mergers are typically low-Mach number $\mathcal{M} \sim 3$, leading to a steep injection spectrum at the shock front ($\alpha \sim -0.7$, see Sect. 1.1.1) which further steepens downstream (towards the cluster center) due to radiative aging. Various statistical studies established a connection between the occurrence of radio halos and merging galaxy clusters, as traced by the X-ray morphological parameters, is also established (e.g. Cassano et al. 2010; Cuciti et al. 2021). In the case of radio halos, it is thought that second-order Fermi processes, related to the turbulent energy dissipated into the ICM during the merger, stochastically accelerate CRe in-situ (e.g. Brunetti et al. 2001; Petrosian 2001). A strong contribution from CRe of secondary origin (i.e. due to collisions involving hadronic cosmic rays) is ruled out by gamma-ray upper limits of the Fermi satellite (e.g. Brunetti et al. 2012, 2017) and by the spectral properties of radio halos. *Classical* radio halos, which were typically detected at frequencies > 1 GHz, show an integrated spectral index of $\alpha \sim -1.3$ (Giovannini et al. 2009). The detection of a growing number of ultra-steep spectrum radio halos (USSRH, Brunetti et al. 2008; Macario et al. 2011; van Weeren et al. 2012; Wilber et al. 2018, see also Sect. 4.3.5) poses a strong challenge for hadronic models, where the electrons are purely of secondary origin. These cannot account for spectral indices $\alpha \leq -1.5$. Turbulent reacceleration models, however, lead to spectra of

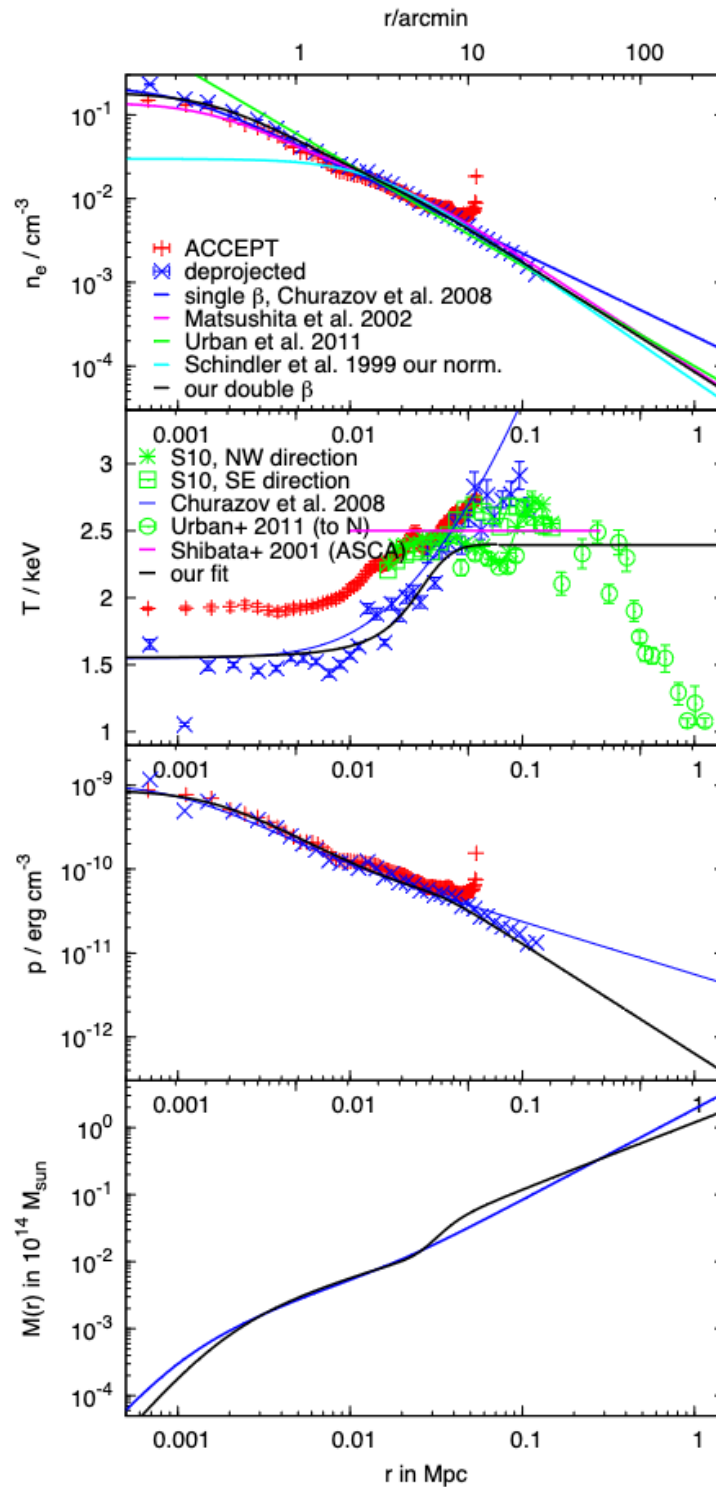


Figure 1.5: Radial profiles of the Virgo cluster. Starting at the top, the panels show the electron density, the temperature, the pressure and the cumulative mass. The figure is taken from Roediger et al. (2014), additional data is from Schindler et al. (1999); Shibata et al. (2001); Matsushita et al. (2002); Churazov et al. (2008); Cavagnolo et al. (2009); Simionescu et al. (2011); Urban et al. (2011).

1 Introduction

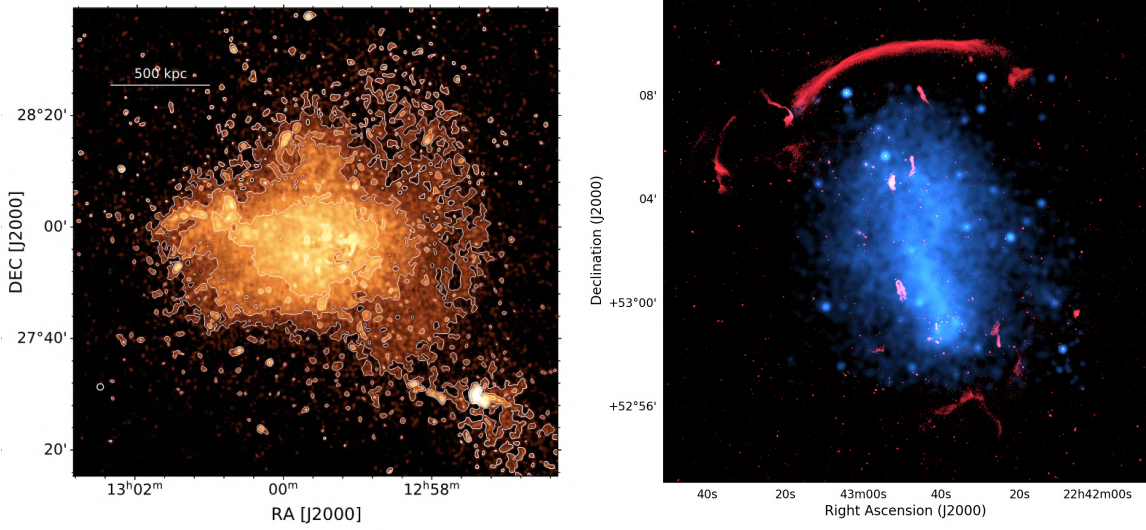


Figure 1.6: Left panel: The radio halo of the Coma cluster which was observed at 144 MHz with LOFAR by Bonafede et al. (2022). The angular resolution is $35'' \times 35''$ and contours are $[3, 6, 12, 24] \times \sigma_{\text{rms}}$. Right panel: The 1.5 GHz JVLA radio (red, Di Gennaro et al. 2018) and Chandra X-ray (blue, Ogorean et al. 2014) emission of the galaxy cluster CIZA J2242.8+5301. The *Sausage* radio relic in the north of the cluster has an extension of ≈ 2 Mpc (image credits: Di Gennaro).

radio halos that feature a cut-off (Brunetti et al. 2001; Cassano et al. 2006) and therefore predict a population of USSRH (Cassano et al. 2012).

Both the DSA of radio relics and the turbulent reacceleration of CRe in radio halos require a population of at least mildly energetic electrons to efficiently accelerate CRe to higher energies. This non-thermal pool could stem from CRe which were initially accelerated by AGN and then mixed with the ICM on large scales and from secondary CRe from hadronic collisions (e.g. Ensslin et al. 1998; Brunetti & Lazarian 2011; Kang et al. 2012; van Weeren et al. 2017; Vazza et al. 2023). Furthermore, the observation of synchrotron emission across Mpc scales clearly implies the existence of magnetic fields in the ICM. These magnetic fields are commonly believed to be the result of an amplification of a seed field by processes involving turbulence and compression (see e.g. Donnert et al. 2018 and references therein). The ICM is a high-conductivity and low-diffusivity plasma, which means that the magnetic field remains essentially frozen into the plasma and can be advected with the ICM bulk motions (Kulsrud & Ostriker 2006). Thus, stretching compression is capable of amplifying the magnetic field. Compression leads to an increased magnetic field B in high-density regions such as galaxy clusters, where $B \propto \rho^{2/3}$ (Donnert et al. 2018). Further amplification of the magnetic field is possible through the repeated turbulent folding and shearing motions, e.g. in the small-scale dynamo process (e.g. Kraichnan & Nagarajan 1967; Goldreich & Sridhar 1997; Vazza et al. 2014). The origin or the required seed field remains unclear, they could either be generated in the early universe as primordial magnetic fields (e.g. Subramanian 2016) or be of astrophysical origin (e.g. Kronberg et al. 1999; Völk & Atoyan 2000).

Observationally, astrophysical magnetic fields, and ICM magnetic fields in particular, are challenging to measure. Nevertheless, Faraday-rotation measurements of polarized background sources (Govoni & Feretti 2004; Clarke 2004; Bonafede et al. 2010; Böhringer et al. 2016), limits on the inverse Compton component (e.g. Bartels et al. 2015), spectral aging analysis of radio relics (e.g. van Weeren et al. 2010; Rajpurohit et al. 2018) or equipartition/minimum energy assumptions (Pfrommer

& Enßlin 2004; Beck & Krause 2005) established the existence of $\sim \mu\text{G}$ magnetic fields in the ICM (see also Brüggén et al. 2012).

The cluster magnetic fields are also responsible for the polarization signature of the diffuse emission. Whenever the magnetic field structure in the emitting region is coherent across sufficiently large scales, in principle, a polarized signal should be detectable. For radio relics, this clearly seems to be the case, as they are strongly polarized, sometimes reaching fractional polarizations $\geq 50\%$ at GHz frequencies, with magnetic field vectors that are mostly tangential to the shock front (e.g. van Weeren et al. 2010; Loi et al. 2017; Kierdorf et al. 2017; Rajpurohit et al. 2020; de Gasperin et al. 2022). This is thought to be the consequence of the shock-compression of the cluster magnetic field, amplifying the magnetic field components parallel to the shock (Enßlin et al. 1998).

In contrast to radio relics, radio halos are generally found to be unpolarized, which is thought to be the consequence of coherence scales that are smaller than the spatial resolution of the radio observations (beam depolarization, van Weeren et al. 2019). The large emitting volume of radio halos also means that reversals of the magnetic field and Faraday rotation along the line of sight further diminish the polarization signal.

Another class of diffuse radio source in galaxy clusters are radio minihalos (Giacintucci et al. 2017, 2019; van Weeren et al. 2019; Biava et al. 2021). These sources share some properties with radio halos, e.g. the central location in the cluster, but they are smaller in size (~ 100 kpc) and are also frequently found in non-merging cool-core clusters.

1.3.2 The Virgo cluster

The Virgo Cluster is the closest galaxy cluster to us ($d = 16.5$ Mpc, Mei et al. 2007; Cantiello et al. 2018), making it the largest cluster in terms of angular extent with a virial radius of 3.3° (≈ 1 Mpc, Simionescu et al. 2017) and the most-massive system within ~ 35 Mpc. The earliest notion of this overdensity of nearby galaxies is attributed to Messier (1781), it is therefore the first known galaxy cluster. Its virial mass is estimated to be around $1.0 - 1.4 \times 10^{14} M_\odot$, which makes it considerably more massive than the Fornax cluster which is located at a similar distance (Ferrarese et al. 2000; Drinkwater et al. 2001), but significantly less massive compared to more distant systems such as Abell 1367 or Coma (Boselli & Gavazzi 2006).

The Virgo Cluster has a complex structure with several subclusters (Binggeli et al. 1987). In Fig. 1.7, I display the SDSS optical image together with the eROSITA X-ray contours (McCall et al. in prep.) In the central region of the cluster, the massive elliptical galaxy M 87 is located, which is one of the brightest radio sources on the sky (Virgo A). This galaxy is surrounded by a cool core (see Fig. 1.5). Less than 400 kpc in projection to the north-west of M 87 lies the massive elliptical galaxy M 86, which is part of a famous arrangement of galaxies that is known as Markarian's Chain. The galaxy is thought to be the dominant galaxy of a group that is in the process of merging with the main cluster from behind, as indicated by its blueshift.

To the south of the main cluster lies cluster *B* with the central massive elliptical galaxy M 49, which is the optically brightest galaxy in the cluster and at a similar distance to M 87 (Mei et al. 2007). This subcluster is the second most massive structure after the M 87 central cluster and appears to be falling into the main cluster in the plain of the sky. To the south-west of cluster *B* lies the *W'-filament*, which is a group of galaxies around the elliptical galaxy NGC 4365 behind Virgo ($d = 23$ Mpc) that is also observable as an extended, elongated source of X-rays. The *W'-filament* lies in-between the southern outskirts of the Virgo cluster and the *W-cloud* in the south-western background of the Virgo cluster at $d \sim 30$ Mpc. In general, the southern region of the cluster is rich in galaxies, many of which are falling into the cluster for the first time. Further notable substructures of Virgo are the cluster *C*

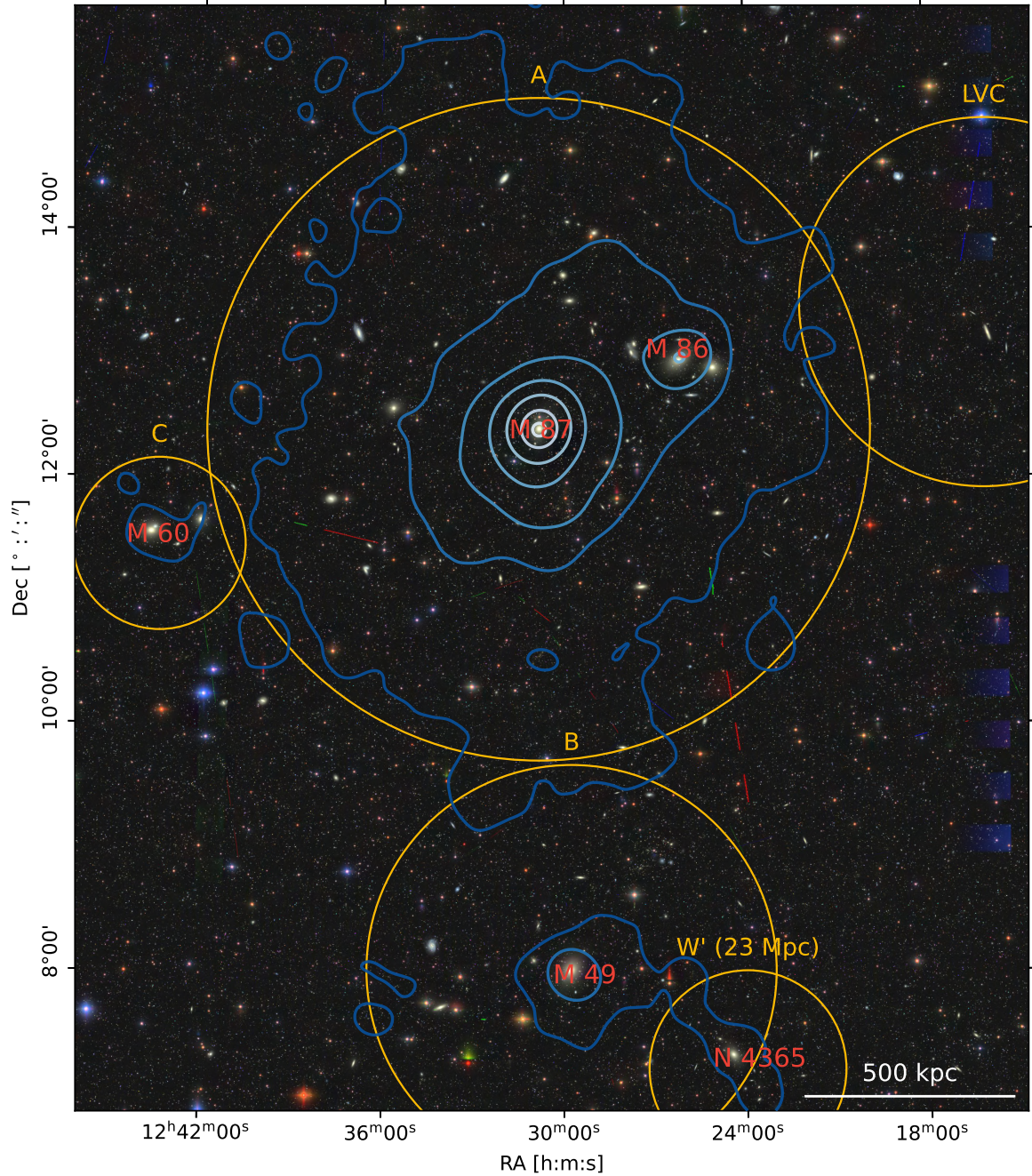


Figure 1.7: Overview of the Virgo Cluster. The background image shows the g , r and z filters of the SDSS (Alam et al. 2015) and the blue contours the 0.3 – 2 keV eROSITA X-ray surface brightness (McCall et al. in prep.). Orange circles highlight substructures of the cluster as defined in Boselli et al. (2014) and red text marks the central elliptical galaxies of these structures.

around the massive elliptical galaxy M 60 in the west of the cluster and the low-velocity cloud (LVC) in the east of the cluster.

The influential optical Virgo Cluster Catalog (VCC) published by Binggeli et al. (1985) lists 1277 galaxies as certain members of the cluster and 574 further galaxies as possible members. The SDSS-based digital Extended Virgo Cluster Catalog (EVCC) of Kim et al. (2014) lists 1589 galaxies, 1024 of which are classified as certain members of the cluster.

1.4 Environmental effects in galaxy clusters

The galaxy cluster environment plays a crucial role in shaping the properties of its member galaxies. As previously noted, the early-type fraction is strongly increased in clusters. Massive early-type galaxies are oftentimes strong radio sources in the form of radio galaxies, showing roughly symmetric lobes of emission (see Fig. 1.3, right panel). However, if they are located within clusters, they commonly exhibit an asymmetric, strongly tailed structure (see the examples in Fig. 1.8, Gavazzi 1978). Furthermore, also the late-type galaxies in clusters show strongly different properties compared to those inhabiting less dense environments. They show a reduced content of atomic hydrogen when compared to isolated objects of similar size and morphological type (e.g. Haynes et al. 1984) and molecular gas (e.g. Fumagalli & Gavazzi 2008; Fumagalli et al. 2009) and as consequence, a reduced SFR (e.g. Gavazzi et al. 1998). They may also feature tails or asymmetries in one or multiple windows of the electromagnetic spectrum, such as those displayed in Fig. 1.9.

Perturbations due to the cluster environment may in principle be of two categories, either of gravitational nature or due to hydrodynamic interactions with the ICM. Gravitational interactions can be due to tidal forces of other cluster member galaxies (Merritt 1984) and/or the clusters gravitational potential (Byrd & Valtonen 1990). The time-integrated effect of gravitational fly-by interactions with other galaxies or the cluster's gravitational potential is referred to as *harassment* (e.g. Moore et al. 1996). Gravitational effects have in common that they affect all kinds of matter equally, and thus, they also perturb the stellar component of galaxies. In the left panel of Fig. 1.9, I show NGC 4438 as an example for a strongly tidally perturbed object (see also Kenney et al. 2008).

As hydrodynamic interaction, the surrounding hot ($T \geq 10^7$ K) ICM deprives galaxies of their ability to accrete cold matter (*starvation*, Larson et al. 1980) and further leads to the *thermal evaporation* of the ISM (Cowie & Songaila 1977). Additionally, due to the rapid motions ($v \sim 1000$ km s⁻¹) of galaxies with respect to the ICM, the ICM ram pressure is capable of displacing parts of the ISM, even though the ICM is a rather dilute medium. This ram-pressure stripping (RPS) depends on the density ρ and the velocity v as $P \propto \rho v^2$, thus, its relevance is strongly increasing in massive clusters where the ICM is denser and the velocity dispersion is higher. Hydrodynamic interactions differ from gravitational interactions since they do not (directly) affect the stellar component. To first order, these effects deplete, convert or remove the ISM without perturbing the stellar component. In the right panel of Fig. 1.9, the Virgo cluster galaxy NGC 4523 is displayed. This object is on its first infall towards the cluster and suffers from RPS, as indicated by the H I tail recently discovered by Boselli et al. (2023b).

To understand how the present day properties of cluster galaxies are formed, it is crucial to disentangle the impact of the various external perturbations under different circumstances and across timescales. Distinguishing between gravitational and hydrodynamic effects is possible since gravitational perturbations cause truncated stellar disks and tidal tails. Thermal evaporation and starvation can be differentiated from RPS since the latter asymmetrically affects the ISM, thereby creating truncated disks at the leading edge of the galaxy (the side in direction of motion with respect to the ICM) and tails of gas at the trailing edge.

1 Introduction

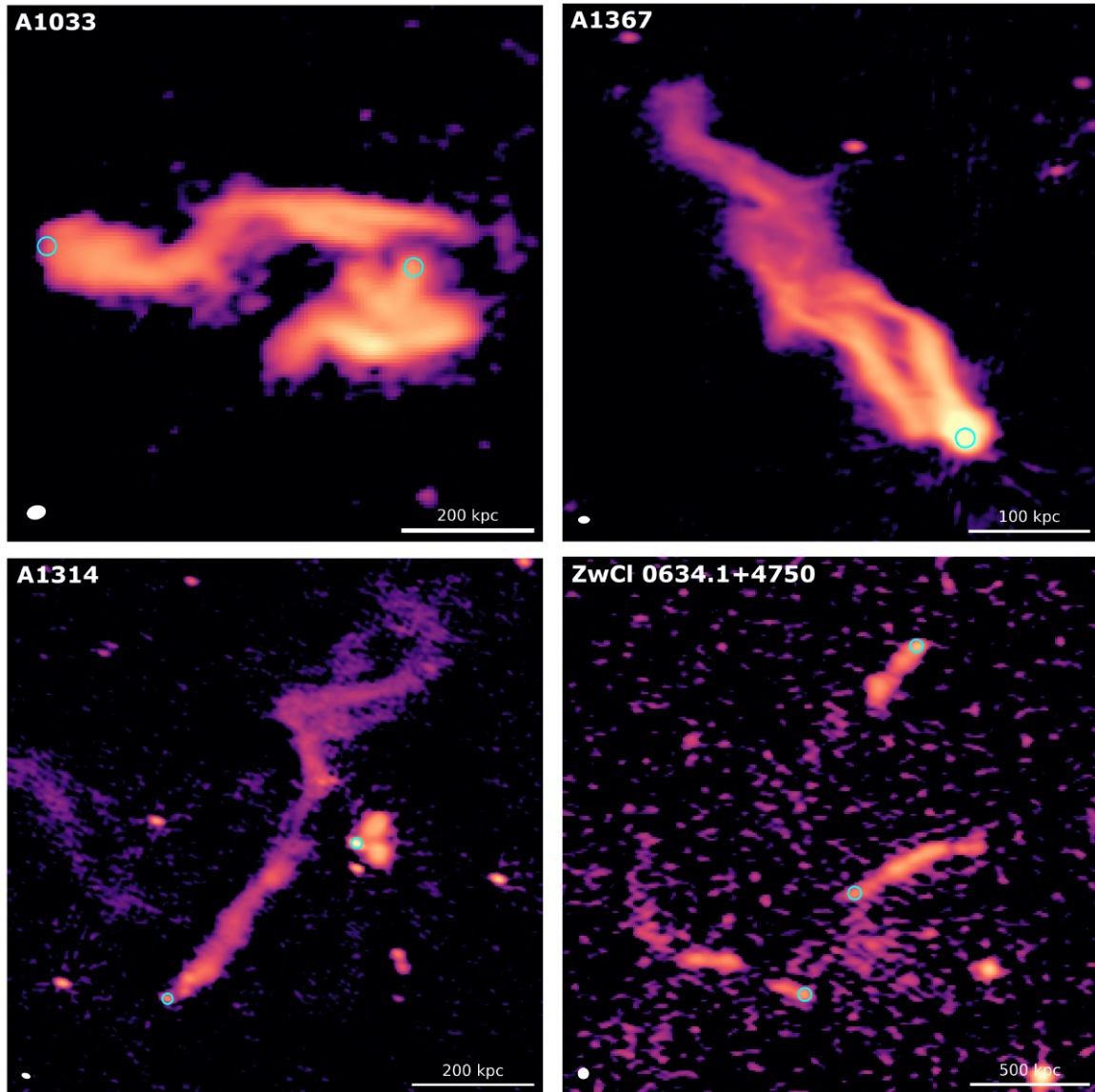


Figure 1.8: LOFAR LBA observations at 54 MHz of tailed radio galaxies in the clusters (top left to bottom right) A1033 (wide-angle tail, this work), A1376 (narrow-angle tail, my work), A1314 (head-tail, recalibrated from LoLSS, de Gasperin et al. 2023), and ZwCl 0634.1+4750 (head-tail, Cuciti et al. 2022). The cyan circles mark the location of the optical hosts of the AGN.

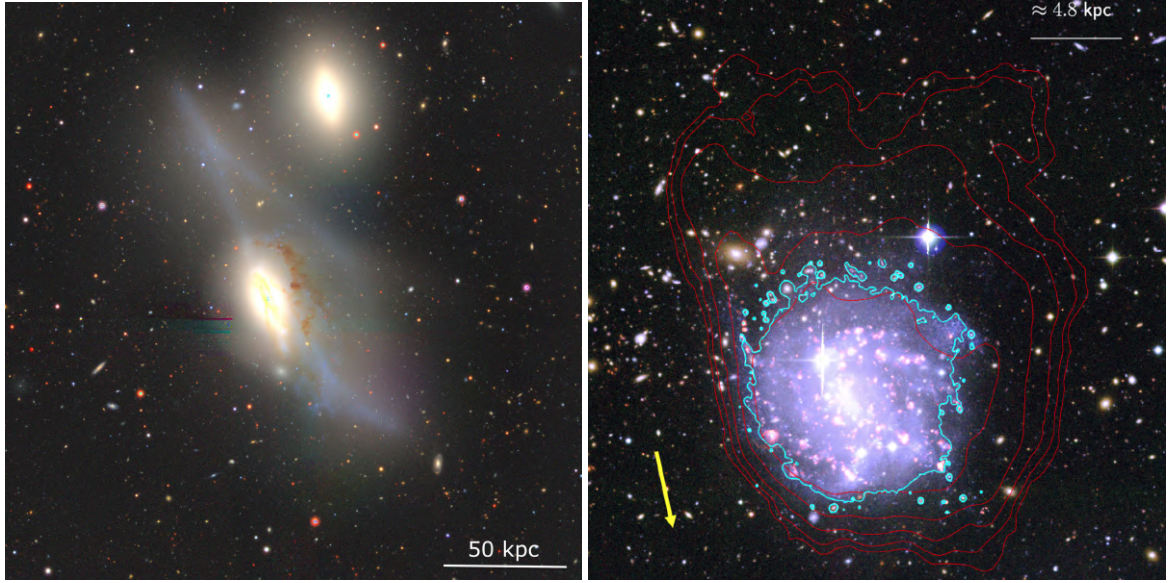


Figure 1.9: Perturbed late-type Virgo cluster galaxies. Left: Optical image of the galaxy NGC 4438 from the DESI Legacy survey (Dey et al. 2019) which shows tidal tails due to an encounter with the giant elliptical galaxy M 60 (Kenney et al. 2008). Right: The ram pressure stripped galaxy NGC 4523. The colors are a composition of the optical continuum and $H\alpha$, the cyan contours is the i -band isophote and the red contours show the MeerKAT H I. The image was published as part of the ViCTORIA project in Boselli et al. (2023b). The yellow arrow indicates the direction of the cluster center. The galaxy shows an H I-tail, while the stellar distribution is symmetric.

1.4.1 RPS of late-type galaxies

It is thought that RPS is the most relevant perturbation in low-redshift galaxy clusters (Boselli et al. 2022, for a recent and detailed review). Historically, RPS as a mechanism that shapes cluster galaxies was first suggested by Gunn & Gott (1972). It is no coincidence that their work followed closely after the discovery that galaxy clusters are extended X-ray sources, which unveiled the existence of the ICM (Meekins et al. 1971; Gursky et al. 1971). Gunn & Gott (1972) noted that if the ICM ram pressure faced by the ISM exceeds the gravitational attraction, the gas in the disk of galaxies will be displaced. The ram pressure of an ICM wind with a density of ρ_{ICM} is given by (Boselli et al. 2022):

$$P_{\text{ram}} = \rho_{\text{ICM}} v_{\perp}^2, \quad (1.21)$$

where v_{\perp} is the velocity component perpendicular to the ISM surface. Assuming a radially symmetric disk, the restoring gravitational force $f_{\text{grav},z}$ per unit area of the gravitational potential Φ is:

$$f_{\text{grav},z} = \frac{\partial \Phi}{\partial z} \Sigma_{\text{gas}}(r), \quad (1.22)$$

where $\Sigma_{\text{gas}}(r)$ is the column density of the ISM gas at a radius r from the center. For the gravitational potential of an infinitesimally thin stellar disk, it can be shown that $f_{\text{grav},z} \leq 2\pi G \Sigma_{\star} \Sigma_{\text{gas}}$ where G is Newton's gravitational constant and $\Sigma_{\star}(r)$ is the column density of stars (for the mathematical derivation, see Boselli et al. 2022). Comparing the ram pressure with the maximum gravitational restoring force per unit area then yields the classical *Gunn & Gott-criterion* (Gunn & Gott 1972) for RPS:

$$\rho_{\text{ICM}} v_{\perp}^2 \geq 2\pi G \Sigma_{\star} \Sigma_{\text{gas}} = \frac{v_{\text{rot}}^2 \Sigma_{\text{gas}}}{R_{\text{gal}}}, \quad (1.23)$$

1 Introduction

where the equality is due to the virial theorem $\Sigma_{\star} = v_{\text{rot}}^2(2\pi GR_{\text{gal}})^{-1}$ and R_{gal} is the effective radius of the disk. So clearly, RPS is more efficient in systems where the gas is only loosely bound (i.e. in low-mass galaxies with a slow rotational velocity v_{rot}) and in massive clusters with high ICM densities and infall velocities.

As an example, if one considers the location of the solar system within the Milky way ($R_{\text{gal}} \approx 8$ kpc), the H I column density perpendicular to the disk is $\Sigma_{\text{gas}} \approx 7 \times 10^{20} \text{ g cm}^{-2}$ (French et al. 2021) and the rotational velocity $v_{\text{rot}} \approx 220 \text{ km s}^{-1}$, yielding $f_{\text{grav},z} \leq 2.3 \times 10^{-11} \text{ g cm}^{-1} \text{ s}^{-2}$. If the Milky Way were to encounter an ICM wind of a fiducial mass density $\rho_{\text{ICM}} = 5 \times 10^{-4} m_p \text{ cm}^{-3}$, where m_p is the proton mass, a velocity of $v \approx 1700 \text{ km s}^{-1}$ would be required to overcome the gravitational attraction of the stellar disk and strip the H I gas in the Gunn & Gott-limit. Velocities of this order are realistically achievable for galaxies falling into a massive galaxy cluster, in particular since the velocity of a galaxy on its orbit will be highest when it is closest to the cluster center, where it also encounters the greatest ICM density. It is also evident from Eq. 1.23 that RPS of disk galaxies is an outside-in process - v_{rot} is approximately constant, whereas the gas surface density will decrease towards the outskirts of the disk. This is also confirmed by stellar population studies, that showed that star formation at the edge of the disks is quenched first (e.g. Fossati et al. 2018). The widespread action of RPS in galaxy clusters is also found in simulations, for example by Yun et al. (2019) who found RPS signatures in 31% of the cluster satellite galaxies in the IllustrisTNG simulations.

Observationally, the most direct way to discover RPS events is by the detection of the stripped H I gas in the 21 cm radio line (e.g. Kenney et al. 2004; Wang et al. 2021; Deb et al. 2022; Serra et al. 2023, see also Fig. 1.9, right panel). However, the presence of H I tails is not a particularly widespread phenomenon. The VLA Imaging of Virgo in Atomic Gas (VIVA, Chung et al. 2009) survey detected only seven objects with H I tails out of a sample of 53 Virgo cluster late type galaxies. This is possibly due to the heating and mixing of the stripped gas with the ICM, which appears to make H I-tails a short-lived phenomenon (Boselli et al. 2022). Further relevant imaging campaigns in H I include for example the Westerbork Coma Survey (Molnár et al. 2022), the WALLABY survey of the Hydra cluster (Wang et al. 2021), the MeerKAT Fornax Survey (Serra et al. 2016) and the MeerKAT H I survey of the Virgo Cluster multi-Telescope Observations in Radio of Interacting galaxies and AGN project (ViCTORIA, Boselli et al. 2023b). The latter is closely related to my work on the Virgo cluster with LOFAR which is presented in Chap. 2 and Chap. 3.

The contact with the ICM ionizes the stripped neutral hydrogen, which can then be observed in ionization lines, most commonly in the H α line. In star-forming galaxies, the ionized gas is usually linked to star-forming activity due to photoionization by the energetic UV emission of young massive stars (see Sect. 1.2.1). Contrary to these H II regions, which are rather compact sources, the RPS tails of ionized gas are diffuse low-surface brightness features (e.g. Boselli et al. 2016), ionized by other processes such as collisional heating (Ferland et al. 2009) or shocks (Fossati et al. 2016). In some cases, the stripped gas can form stars, thus there may also be compact H II regions super-imposed on the diffuse tail of ionized gas (e.g. Hester et al. 2010). In general, RPS tails are more commonly detected in the H α -line than in the H I-line with the current generation of instruments (Boselli et al. 2022). The two most important imaging projects for the studies of tails of ionized gas in H α are the Virgo Environmental Survey Tracing Ionised Gas Emission (VESTIGE, Boselli et al. 2018b) and the GAs-Stripping Phenomena program (GASP, Poggianti et al. 2017).

RPS tails behind late-type galaxies are composed of a multiphase-medium, which, in addition to the cold ($T \leq 10^2$ K) and warm ($T \sim 10^4$ K) gas traced in H I and H α , is also found to contain hot ($T \sim 10^7$ K) phase observable in the X-rays (Sun et al. 2021). Furthermore, RPS also affects the non-thermal components of the ISM, i.e. the cosmic rays and magnetic fields. Stripped CRE give rise to radio continuum tails behind star-forming galaxies. This phenomenon was first reported in UGC 6697

of the A 1367 cluster (Gavazzi 1978), but it is also commonly found in other nearby galaxy clusters (e.g. Murphy et al. 2009; Vollmer et al. 2010, 2013; Chen et al. 2020). The advance of LOFAR surveys strongly accelerated the discovery rate of radio continuum tails in the past few years, with more than 100 tails being detected by the instrument (Roberts et al. 2021a,b; Roberts et al. 2022b; Ignesti et al. 2022c,b; Ignesti et al. 2023, see also Chap. 2 and Chap. 3). Therefore, radio continuum observations are a well-suited and widely available diagnostic tool to detect RPS events. It is thought that once the CRe are stripped from the galactic disk, their spectral shape is dominated by inverse Compton and synchrotron losses and should thus increasingly steepen with distance from the galaxy due to radiative aging. Indeed, this is found in a number of studies (Vollmer et al. 2004; Chen et al. 2020; Müller et al. 2021; Ignesti et al. 2022c; Roberts et al. 2022b, 2023). Possibly, the CRe in the tail could also be re-energized by first or second order Fermi mechanisms, although there is currently no conclusive evidence for this scenario. In low-redshift clusters, where most of the RPS galaxies are discovered, the aging rate in the tail is mostly determined by the magnetic field strength. Currently, the magnetic field strength in the radio tails is not well constrained. In principle, via the magnetic draping mechanism (Dursi & Pfrommer 2008), galaxies are able to sweep up the magnetic field lines in the ICM, thereby amplifying the magnetic field on the leading edge (Pfrommer & Dursi 2010) and also in the tail. Müller et al. (2021) found strong evidence for the magnetic draping scenario in the form of ordered magnetic fields in the tail of a RPS galaxy. The magnetic field strength in the tail of that object was estimated to be at least $B = 4.1 \mu\text{G}$, with comparable values also reported by other studies (Vollmer et al. 2021; Ignesti et al. 2022c; Ignesti et al. 2023), all of them using the equipartition estimate (Beck & Krause 2005).

For late-type galaxies that do not host a strong AGN, the radio luminosity is an accurate tracer of the SFR (see Sect. 1.2.1). Interestingly, it is oftentimes found that the integrated radio luminosity of galaxies that suffer from RPS is in excess of the expectation given the SFR estimated at other wavelengths (e.g. Gavazzi et al. 1991; S. Niklas 1995; Gavazzi & Boselli 1999; Murphy et al. 2009; Roberts et al. 2021b; Ignesti et al. 2022b). This is not due to nuclear activity, so that several mechanisms to explain this radio excess were suggested: Gavazzi & Boselli (1999) proposed that the ram pressure leads to a compression of the magnetic field and consequentially, increased synchrotron luminosity. Alternatively, an enhancement of the magnetic field may also be caused by the magnetic draping mechanisms (Dursi & Pfrommer 2008; Pfrommer & Dursi 2010; Müller et al. 2021). Völk & Xu (1994) and Murphy et al. (2009) instead favored a scenario where the higher radio luminosity is not simply caused by compression, but instead by shocks driven into the ISM by collisions with fragments of cold gas present in the ICM. Diffusive shock acceleration can then accelerate cosmic-ray electrons in the ISM, which should lead to a flatter radio spectral index at the location of the shocks. Another explanation of the radio-excess was brought up more recently in Ignesti et al. (2022c) and Ignesti et al. (2022b) based on the analysis of jellyfish galaxies. The strong radio excess compared to the $\text{H}\alpha$ -emission was interpreted as the consequence of rapid quenching of the star-forming activity due to RPS. While the $\text{H}\alpha$ emission is a nearly instantaneous SF tracer, with a typical delay of only a few Myr, the radio-emitting CRe have a typical lifetime > 100 Myr. Thus, if the star formation is quenched on time scales shorter than the CRe lifetime, there is an apparent excess of radio emission due to the different time scales probed by $\text{H}\alpha$ and the radio observations. If the effect of RPS on the non-thermal ISM is not fully understood, this introduces a systematic error in radio-inferred SFRs, limiting the application of radio as an extinction-free SFR tracer for cluster galaxies.

Further open questions on RPS and environmental interactions of star-forming galaxies in general regard the role of RPS and the other environmental perturbations and their efficiency as a function of the environment, velocity and mass. LOFAR observations by Roberts et al. (2021b) found RPS to be more common in clusters than groups, as expected from Eq. 1.23. There is also evidence that RPS

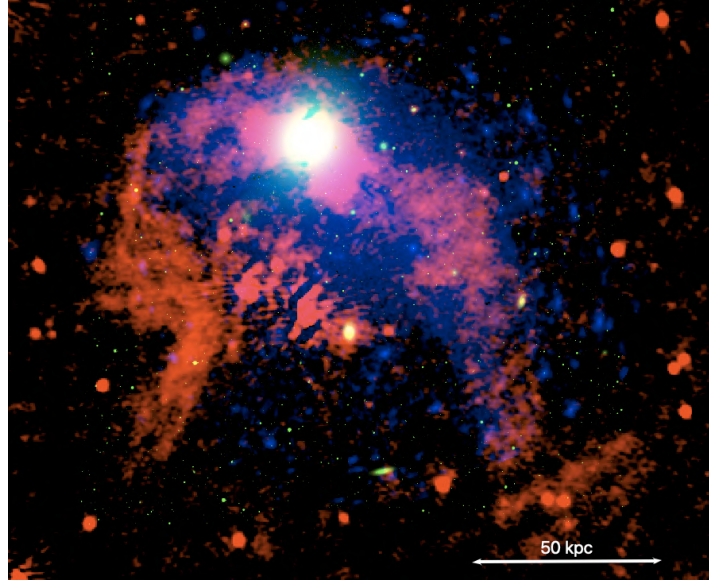


Figure 1.10: Multi-wavelength view of M 49/NGC 4472 in the Virgo cluster. The Legacy survey r -band (green, Dey et al. 2019) shows the optical extent of the galaxy, the XMM-Newton X-ray (blue, Su et al. 2019) the hot plasma with a stripped tail towards the southwest, and the LOFAR 144 MHz continuum (red, this thesis) the bent radio galaxy tails.

affects dwarf galaxies more severely (Steirleithner et al. 2020), although due to their low luminosities, they are challenging to observe. A prime example of a dwarf galaxy suffering from RPS is IC 3418, which is a jellyfish galaxy (i.e. a galaxy with a stripped tail longer than the diameter of its disk, Kenney et al. 2014) in the central parts of the Virgo cluster. This object shows an enhanced SFR, something that was also shown for the GASP sample of jellyfish galaxies (Vulcani et al. 2018). Under some, not yet well-constrained circumstances, RPS is capable of temporarily enhancing the SFR likely due to gas compression (e.g. Gavazzi & Jaffe 1985; Roberts & Parker 2020; Boselli et al. 2021) or RPS-driven mass flows (Zhu et al. 2023), before it eventually leads to a quenching of the SFR. This star formation enhancement can occur in the disk and in some cases, also in the tails. The occurrence of the latter may be modulated by the magnetic fields in the tails (Boselli et al. 2022). The fact that this SFR enhancement in RPS objects is only observed in some (mostly extreme) cases and that it is also not generally observed for RPS populations in simulations (e.g. Göller et al. 2023) suggests that this may be a short-lived transient phenomenon during a fraction of the RPS event.

Due to the complexity of the RPS process, simulations are a critical tool to interpret the observations. They allow us to investigate the dependence of the RPS process on the alignment between the disk and the velocity vector (Vollmer et al. 2001; Roediger & Brüggén 2006; Roediger et al. 2014), the fate of the stripped gas (Roediger & Brüggén 2007), the relevance of RPS across cosmic history (Quilis et al. 2017) and the role of magnetic fields (e.g. Ruszkowski et al. 2014; Tonnesen & Stone 2014).

1.4.2 Environmental effects in radio galaxies

While RPS is extensively studied as a mechanism to quench the star-forming activity in cluster late-type galaxies, its relevance as environmental effect in galaxy clusters was initially suggested by Miley et al. (1972) to explain the properties of peculiar tailed radio galaxies in massive elliptical galaxies.

Radio galaxies in rich environments are more likely to be of FRI morphology (Wing & Blanton 2011; Gendre et al. 2013). It is thought that the higher density of the surrounding medium can more efficiently decelerate and decollimate the jets, favoring an FRI morphology (Saikia 2022). The jets of FRI sources commonly show distorted and asymmetric shapes (see Fig. 1.3, left panel). This is due to the relative motion between the ICM and the plasma in the jets and plumes, which can displace the plasma. FRI radio galaxies where the jets are bent towards the same side, thus forming a tail, are referred to as wide-angle tail (WAT, see top right panel of Fig. 1.8), narrow-angle tail (NAT, see top right panel of Fig. 1.8) or head-tail (HT, see bottom panels of Fig. 1.8) radio galaxies. The distinction between these classes depends on the opening angle of the bent tail Rudnick & Owen 1976; Owen & Rudnick 1976, where HT radio galaxies are the most extreme case where the two bent plumes merge to a single tail (at least in projection). The tailed shapes are created due to the relative motion between the ICM and the radio galaxy. For BCGs which are close to the bottom of the cluster potential well, the dominant effect is likely the dynamics in the ICM, while for satellite galaxies, the ram pressure due to the motion of the galaxy in the cluster shapes the tail (Saikia 2022). The ram pressure origin of the bent tails is also supported by the correlation between the opening angle and the cluster-centric distance for satellites, where galaxies that are closer to the cluster center face stronger ram pressure and show narrower tails (Garon et al. 2019). Ram pressure may not only displace the jets, but it can also strip the hot ISM of the host galaxy, leading to RPS X-ray tails in early-type galaxies. In Fig. 1.10, I display radio and X-ray observations of the Virgo cluster galaxy M 49/NGC 4472. The WAT morphology was unveiled by LOFAR in context of this thesis (see Chap. 2), which makes this object (to the best of my knowledge) the closest tailed radio galaxy to us. The radio tails are coincident with a stripped X-ray tail (Su et al. 2019). The comparison of simulations to observations of stripped X-ray tails in elliptical galaxies also allows to constrain the plasma properties and mixing processes (Roediger et al. 2015a,b; Kraft et al. 2017).

For tailed radio galaxies in clusters, the spectral index along the tails is oftentimes found to be in good agreement with pure radiative aging. However, in a number of cases, peculiar features in the spectral index distribution suggest the presence of reacceleration processes in the tails (e.g. de Gasperin et al. 2017; Cuciti et al. 2018; Srivastava & Singal 2020; Müller et al. 2021). If merger shocks cross the tails, they reaccelerate the relativistic plasma, this is for example observed in the nearby Coma cluster (Bonafede et al. 2021) and further clusters (e.g. Bonafede et al. 2014). In other cases, DSA as the reacceleration mechanism was found to be an unlikely explanation, and second-order Fermi-processes, for example due to turbulence in the tail, were instead favored (e.g. de Gasperin et al. 2017; Wilber et al. 2018; Pasini et al. 2022). An extreme example of this are gently reenergized tails (GReETs), a rare category of sources where the reacceleration mechanism is found to be inefficient, such that it barely compensates the energy losses and leads to ultra-steep spectrum emission. The prototype of this source category is the GReET in the galaxy cluster Abell 1033 (de Gasperin et al. 2017, see also Chap. 4). This source is connected to a WAT radio galaxy and shows an ultra-steep spectral index of $\alpha \approx -4$ between 144 and 323 MHz (de Gasperin et al. 2017), which makes it one of the steepest spectrum sources known.

The interaction between cluster merger shocks and (old) lobes of radio galaxies is also connected to diffuse radio sources which are known as *radio phoenixes* (Enßlin & Gopal-Krishna 2001; Enßlin & Brüggén 2002; van Weeren et al. 2019). These sources, which show an irregular morphology and a steep and curved radio spectrum (e.g. Cohen & Clarke 2011), are thought to be created when a cluster merger shock crosses an aged lobe of a radio galaxy, which contains a low-energy CRe population. If the speed of sound inside the lobe is higher than the propagation velocity of the shock, they are compressed adiabatically and thereby re-energized. An example for a radio phoenix source can be found in the cluster Abell 1033 (de Gasperin et al. 2015, see also Chap. 4).

1 Introduction

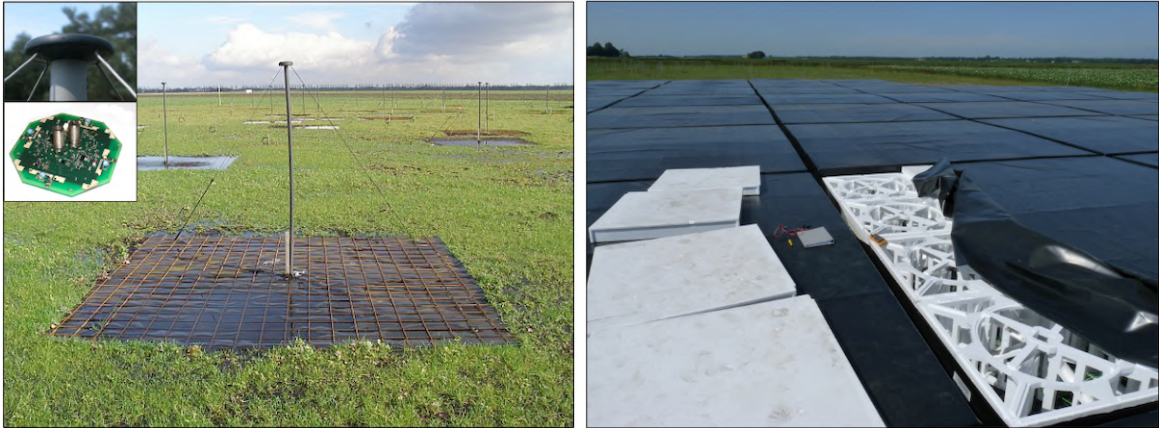


Figure 1.11: A low-band antenna (left) and a set of high-band antenna tiles (right) of LOFAR. Each black rectangular box is an individual HBA tile, consisting of 4×4 dipoles. Image credits: ASTRON.

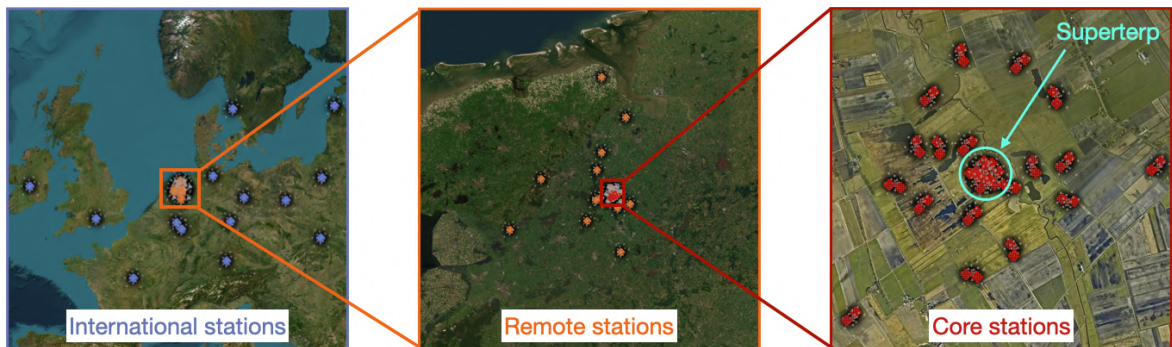


Figure 1.12: Positions of LOFAR stations in Europe. The left panel shows the international stations (blue), the central zoom-in the remote stations (orange) and the right zoom-in the central stations (red). The cyan circle in the right panel marks the central superterp structure. Images adapted from <https://www.astron.nl/lofartools/lofarmap.html>.

A further example for environmental interactions of radio galaxies in dense environments is AGN feedback. This is a process which was suggested as a solution of the cooling flow problem. In the densest central parts of clusters, the ICM should be able to rapidly cool and compresses, which should induce star-formation in the BCG (Fabian 1994). However, this is not observed at the expected magnitude of a scenario of pure radiative cooling of the gas (e.g. Peterson & Fabian 2006), which implies that there are heating processes that balance the cooling. The most important heating process is thought to be AGN feedback – the (usually central) AGN can efficiently accrete the cool ICM and inject radio lobes and jets of plasma into the ICM, thereby heating the surrounding ICM (e.g. Bîrzan et al. 2004; Gaspari et al. 2012).

1.5 The Low-Frequency Array

The Low-Frequency Array (LOFAR, van Haarlem et al. 2013) is a radio interferometer located in Europe and centered in the Netherlands. It operates in the low (<1 GHz) and ultra-low (<100 MHz) frequency range and is the leading instrument in this band in terms of both sensitivity and resolution.

LOFAR follows a phased-array design, which means that the individual dipoles are not physically pointed towards different locations on the sky, but they enhance radiation from a certain direction by introducing phase-delays to the fixed antennas. LOFAR employs two different antenna systems: the low-band antennas (LBA, left panel of Fig. 1.11) are sensitive from 10–90 MHz, they follow a simple and economic design of two perpendicular copper wires that are attached to a PVC rod, with a metal fence ground plate that acts as a reflector. The bandpass response curve of the LBA is strongly peaked, with a maximum at 58 MHz. The high-band antennas (HBA, right panel of Fig. 1.11) are sensitive from 110–240 MHz, although the presence of radio frequency interference in the upper part of the band mostly restricts the operation to the 110–170 MHz range, which is known as the HBA-low band. The HBA follows a design which consists of multiple *tiles* which contain 16 dual-polarized dipole elements each. Every tile effectively acts as phased array and is equipped with a tile-level analog beam former. The gap between the frequency ranges of the LBA and HBA corresponds to the FM broadcast band.

LOFAR consists of different stations, which each host multiple LBAs and HBA tiles. The inner part of the array is made up of the 24 core stations (CS), located in the Northeast of the Netherlands. The six innermost CS form the dense LOFAR Superterp. Each CS consists of 96 LBA and 2×24 HBA tiles. At larger distances from the core, there are 16 remote stations (RS), which are also within the Netherlands. Each RS consists of 96 LBA and 48 HBA tiles. The most distant LOFAR stations are the 14 international stations (IS, two more are under construction) which are spread across Europe and host 96 LBA and 96 HBA each. In Fig. 1.12, the location of the IS, RS, CS and the Superterp within Europe and the Netherlands are displayed.

At each station, the signals of the LBAs and HBA tiles are locally amplified and digitized at a 200 MHz sampling rate in an electromagnetically shielded station cabinet. The digital signal consists of different subbands with 195.3 kHz bandwidth each. Using an 8-bit representation of the signal, 488 subbands can be processed at once in the Dutch stations, the future LOFAR 2.0 upgrade will triple this number, see Sect. 5.2. This gives the system a total bandwidth of 95.3 MHz. The digital signals are beam-formed by introducing time delays that compensate for the geometric delay of the radio waves from the target direction. Due to the phased-array design, it is possible to simultaneously observe with multiple beams in different subbands. In the LBA system, this allows to simultaneously observe e.g. a calibrator and three target sources at a bandwidth of 23.8 MHz each, as it is done in the observation campaign for the LOFAR LBA Sky Survey (LoLSS, de Gasperin et al. 2021; de Gasperin et al. 2023). In the HBA, the analog beam-former at tile-level restricts multi-beam observations to target fields that are in close proximity on the sky ($\sim 10^\circ$ separation). The resulting primary beam (the directional response of the stations) effectively determines the field of view (FoV) of LOFAR. The primary beam, full-width at half-maximum (FWHM) is 3.98° at 144 MHz for observations with the Dutch HBA system (van Haarlem et al. 2013). For the Dutch LBA stations, the current hardware does only allow to operate 48 out of the 96 dipoles per station at once. Multiple dipole selections are possible, either using only the inner half of the dipoles, which maximizes the FoV (FWHM= 10.9°) at the cost of increased dipole cross-talk, or the outer half (FWHM= 4.3°), which minimizes the cross-talk and the FoV. As a compromise, a sparse selection of outer and inner dipoles is also possible, with a FoV of FWHM= 5.9° .

The digitized and beam-formed signals of all stations are subsequently transferred via network to the central processing facility in Groningen (NL), where each combination of stations and polarizations is correlated independently at 1 s time integration and written to disk. In the following, basic on-site processing is possible, in particular to *flag* RFI (Offringa et al. 2012) and remove the signal of extremely bright sources in the side-lobes in a process called *demixing*. The most problematic sources are the so-called *A-team* (Cassiopeia A, Cygnus A, Taurus A and Virgo A de Gasperin et al. 2020),

1 Introduction

which all have fluxe densities above 1 kJy in the frequency range of LOFAR. Finally, after the on-site processing, the data are stored on tape in the LOFAR Long Term Archive.

1.5.1 LOFAR calibration

Radio observations, in particular at low frequencies, are subject to complex systematic effects that need to be corrected for to reconstruct the radio sky. For LOFAR, there are two families of systematic effects: instrumental systematics are connected to the hardware and design of the instrument, whereas ionospheric systematics are due to the direction-, time- and polarization-dependent variations of the ionospheric refraction index. The latter become increasingly severe towards low frequencies and are ultimately responsible for the low-frequency cutoff of the radio window at a frequency of ~ 10 MHz.

For radio interferometers, data is correlated for individual baselines, i.e. for combinations of two different stations (or antennas for other radio telescopes). This means that a telescope with n stations has $n(n - 1)/2$ unique baselines. For the Dutch LOFAR LBA, this amounts to 780 baselines, while the HBA has a total of 2016 baselines since the HBA CS are split into two sub-stations each. Every baseline is defined by a vector \vec{b} which connects the two stations. The directional response function R of a baseline has the form of a *fringe pattern*, that is approximately defined by (see e.g. Thompson et al. 2017):

$$R = \cos\left(2\pi\frac{\vec{b}\hat{s}}{\lambda}\right), \quad (1.24)$$

where \hat{s} is the unity vector in the direction of the source. For a given wavelength λ of the signal, the angular size of the fringes is determined by the baseline length $\|\vec{b}\|$. Short baselines correspond to wide fringes and long baselines to narrow fringes. The angular extent of the fringes determines the angular scale θ to which the baseline is sensitive to:

$$\theta = f_\alpha \frac{\lambda}{b} \text{ rad}, \quad (1.25)$$

where f_α a constant close to unity. The angle of θ is the smallest angular scale that can be resolved by the baseline. Sources that are significantly more extended than θ cover a large number of fringes, which alternately produce a positive and a negative response. As a consequence, the contribution of the source cancels out. This means that long baselines (e.g. the LOFAR baselines involving IS and RS) are required to achieve high angular resolution, but short baselines (the baselines between CS) are necessary to remain sensitive to extended emission. The pointing direction of the baseline is controlled by introduction of a time delay that compensates for the geometrical delay $t_g = \vec{b}\hat{s}/c$.

The radio sky can be described by the brightness matrix \mathbf{B} in terms of components of the (linear polarization basis) electric field vector $\vec{e} = (e_X, e_Y)$, this is directly related to the *Stokes-parameters* I, Q, U, V :

$$\mathbf{B} = 2\langle\vec{e}\vec{e}^\dagger\rangle = 2\begin{pmatrix} \langle e_X e_X^* \rangle & \langle e_X e_Y^* \rangle \\ \langle e_Y e_X^* \rangle & \langle e_Y e_Y^* \rangle \end{pmatrix} = \begin{pmatrix} I + Q & U + iV \\ U - iV & I - Q \end{pmatrix}. \quad (1.26)$$

The aim of radio-interferometry is to reconstruct the emitted sky brightness $\mathbf{B}_{\text{emitted}}$ from the observed one $\mathbf{B}_{\text{measured}}$. This requires us to correct for the systematic effects that occur along the signal paths of the stations i and j . Linear systematic effects can be described as *Jones-matrices* \mathbf{J} (Jones 1941). For a single baseline, the emitted sky brightness distribution can then be obtained from the measured one according to:

$$\mathbf{B}_{\text{measured},ij} = \mathbf{J}_i \mathbf{B}_{\text{emitted}} \mathbf{J}_j^\dagger. \quad (1.27)$$

In radio-interferometric calibration, our aim is to determine the Jones-matrices that correctly describe the systematic effects at play. The generalization of this expression is the radio-interferometer measurement equation which I introduce in Sect. 5.3. There, I also discuss in detail the nature of the Jones-matrices for all relevant systematic effects in LOFAR. For more details on the mathematical basis of radio interferometry, I refer to Hamaker et al. (1996), Smirnov (2011) and Thompson et al. (2017).

1.5.2 LOFAR surveys

The LOFAR Surveys Key Science Project² is conducting two major wide-area surveys, the LOFAR Two-Metre Sky Survey (LoTSS, Shimwell et al. 2017, 2019; Shimwell et al. 2022) with the HBA at 144 MHz, and the LOFAR LBA Sky Survey (LoLSS, de Gasperin et al. 2021; de Gasperin et al. 2023) at 54 MHz with the LBA. In context of these surveys, optimized direction-dependent calibration and imaging strategies were developed. For LoTSS, the `ddf-pipeline`³ Tasse et al. (2021) has become the state of the art for LOFAR calibration. For LoLSS, the Pipeline for LOFAR LBA (PILL) that is part of the Library for Low-Frequencies (LiLF⁴) is the standard approach (de Gasperin et al. 2020). I employ variations of both of these strategies in this thesis.

In the past few years, the LOFAR surveys vastly accelerated discoveries in the field of radio astronomy. Examples relevant for this thesis are the high rate at which new sources of diffuse radio emission in galaxy clusters are discovered (e.g. van Weeren et al. 2021; Botteon et al. 2022) and the more than 100 new ram-pressure stripped tails behind late-type galaxies that were reported by Roberts et al. (2021a,b); Roberts et al. (2022b, 2023); Ignesti et al. (2022c,b); Ignesti et al. (2023).

1.6 Aims and outline of this thesis

During my doctoral research project, I studied environmental interactions of star-forming and radio galaxies in galaxy clusters using LOFAR as well as other radio telescopes and a multitude of further instruments. The main scientific questions that I am addressing in this work are:

- What is the role of RPS in the quenching of the star-formation activity in cluster galaxies?
- Why do galaxies that suffer from RPS follow a different radio-SFR relation?
- How does ICM ram pressure affect the non-thermal components of cluster galaxies?
- How does RPS affect the spectral properties of RPS galaxies?
- What processes are responsible for the gentle reacceleration of radio galaxy plasma in clusters?

Since my work is of observational nature, it furthermore involved the pioneering of technical aspects of LOFAR calibration and imaging.

The work of my thesis project resulted in the following four publications:

Publication I **Edler, H.W.**, de Gasperin, F., Shimwell, T.W., Hardcastle, M.J., Boselli, A., Heesen, V., McCall, H., Bomans, D.J., Brüggén, M., Bulbul, E. and Chyży, K.T. et al., 2023. *VICTORIA project: The LOFAR HBA Virgo Cluster Survey*. *A&A*, 676, p.A24.

²<https://lofar-surveys.org/>

³<https://github.com/mhardcastle/ddf-pipeline>

⁴<https://github.com/revoltek/LiLF>

1 Introduction

Publication II **Edler, H.W.**, Roberts, I. D., Boselli, A., de Gasperin, F., Heesen, V., Brügger, M., Ignesti, A., Gajović, L, 2023. *ViCTORIA project: The LOFAR-view of environmental effects in Virgo Cluster star-forming galaxies*. Submitted to A&A at October 17 2023; arXiv:2311.01904.

Publication III **Edler, H.W.**, de Gasperin, F., Brunetti, G., Botteon, A., Cuciti, V., van Weeren, R.J., Cassano, R., Shimwell, T.W., Brügger, M. and Drabant, A., 2022. *Abell 1033: A Radio Halo and Gently Re-Energized Tail at 54 MHz*. A&A, 666, id.A3, 15 pp.

Publication IV **Edler, H.W.**, de Gasperin, F. and Rafferty, D., 2021. *Investigating ionospheric calibration for LOFAR 2.0 with simulated observations*. A&A, 652, p.A37.

The content of these publications is presented in the following chapters of this thesis. The order of the chapters does not reflect the chronological order of publication.

To investigate how RPS affects star-forming galaxies in the Virgo cluster, I carried out a deep wide-field (135 deg^2) survey of the system at 144 MHz using the LOFAR HBA. I developed a custom calibration strategy to mitigate the dynamic range limitations introduced by the extremely bright central source M 87, which allowed me to carry out a full direction-dependent calibration of the cluster. This work was published in article I: Edler et al. (2023a) and is presented in Chap. 2. I am the lead author of this work and I was responsible for the manuscript, the development of the custom calibration strategy, the full data reduction and the composition of the survey mosaics and Virgo cluster catalog. H. McCall provided the eROSITA X-ray data of the Virgo cluster, and M. Hardcastle kindly created the website where we provide the Virgo cluster survey data products to the public. The other co-authors assisted with preparation of the manuscript and/or acted as scientific consultants.

The analysis of the RPS galaxies in the LOFAR HBA Virgo cluster survey is presented in Chap. 3 (publication II: Edler et al. 2023b). In this work, I analyzed a sample of RPS galaxies in the cluster and compared their properties to a control sample of LOFAR-detected nearby galaxies. I am the lead author of this work and I was responsible for the scientific analysis and the manuscript. I. D. Roberts kindly provided the maps of the star-formation rate surface density of the RPS sample. The other co-authors assisted with preparation of the manuscript and acted as scientific consultants. Publications I and II are part of the project *Virgo Cluster multi-Telescope Observations in Radio of Interacting Galaxies and AGN*, a joint LOFAR-MeerKAT imaging campaign of the Virgo cluster that is revolutionizing the radio coverage of the system across five octaves in frequency.

To investigate the gentle reacceleration of radio galaxy plasma in galaxy clusters, I analyzed a 54 MHz LOFAR LBA observation of the cluster A 1033. This study, which also uses further multi-frequency data, is presented in Chap. 4. It also contains an analyses of the peculiar radio halo in the cluster, which is enigmatic since it is hosted in a moderately massive cluster, over-luminous and has an and ultra-steep spectrum. The corresponding publication is III: Edler et al. (2022). I am the lead author of this work and I was responsible for the calibration of the LOFAR LBA data, the scientific analysis and the manuscript. F. de Gasperin developed the calibration strategy for the LBA system, in which I assisted. A. Botteon and T. W. Shimwell calibrated the LOFAR HBA data and F. de Gasperin calibrated the GMRT data of the system, both of which were presented in previous publications.

The progress in our understanding of the impact of the environment on the evolution of radio and star-forming galaxies is inevitably linked to the expansion of our observational capabilities. If we are able to observe fainter sources or processes on smaller scales, we will be able to investigate how environmental effects shape galaxies at lower mass and luminosity and in more distant systems. Fortunately, the future is bright for low-frequency radio astronomy: The LOFAR 2.0 upgrade will lead to an increased sensitivity and allow for novel strategies to correct the ionospheric systematic effects.

1.6 Aims and outline of this thesis

In Chap. 5, I present an analysis of a simulated LOFAR 2.0 observation, in which I compare novel calibration strategies for the upcoming LOFAR 2.0 system. This work was published in IV: Edler et al. (2021). I am the lead author of this work and I was responsible for the analysis of the calibration strategies for LOFAR 2.0 and the manuscript. The tool to create the simulated LOFAR observations was developed jointly with D. Rafferty prior to my doctoral studies as part of my Master's thesis project. The simulation of the data and the data reduction of the simulation using a serial direction-dependent calibration algorithm is my original work and part of my doctoral research project. Both co-authors assisted with the preparation of the manuscript.

I finally summarize and contextualize my results in Chap. 6. In this section, I also briefly highlight connected publications to which I contributed during my doctoral research and provide an outlook on ongoing and future projects.

1 Introduction

2 ViCTORIA project: The LOFAR HBA Virgo Cluster Survey

H. W. Edler, F. de Gasperin, T. W. Shimwell, M. J. Hardcastle, A. Boselli, V. Heesen, H. McCall, D. J. Bomans, M. Brüggen, E. Bulbul, K. T. Chyży, A. Ignesti, A. Merloni, F. Pacaud, T. H. Reiprich, I. D. Roberts, H. J. A. Rottgering, R. J. van Weeren. *Astronomy & Astrophysics*, 676, p.A24 (2023)

Abstract

Context. The Virgo cluster is the nearest ($d = 16.5$ Mpc) massive ($M \geq 10^{14} M_{\odot}$) galaxy cluster and is therefore a prime target for studying astrophysical processes in dense large-scale environments. In the radio band, we can probe the nonthermal components of the interstellar medium (ISM), the intracluster medium (ICM), and of active galactic nuclei (AGN). This allows an investigation of the impact of the environment on the evolution of galaxies and the contribution of AGN to ICM heating. With the ViCTORIA (VIrgo Cluster multi-Telescope Observations in Radio of Interacting galaxies and AGN) project, we are carrying out multiple wide-field surveys of the Virgo cluster at different frequencies.

Aims. We aim to investigate the impact of the environment on the evolution of galaxies and the contribution of AGN to ICM heating—from the inner cluster regions out to beyond the virial radius.

Methods. We performed a survey of the cluster at 120 – 168 MHz using the LOw-Frequency ARray (LOFAR). We imaged a 132 deg^2 region of the cluster, reaching an order-of-magnitude greater sensitivity than existing wide-field radio surveys of this field at three times higher spatial resolution compared to other low-frequency observations. We developed a tailored data processing strategy to subtract the bright central radio galaxy M 87 from the data. This allowed us to correct for systematic effects due to ionospheric variation as a function of time and direction.

Results. In the final mosaic, which has a resolution of $9'' \times 5''$, we reach a median noise level of $140 \mu\text{Jy beam}^{-1}$ inside the virial radius and $280 \mu\text{Jy beam}^{-1}$ for the full area. We detect 112 Virgo member galaxies and 114 background galaxies. In at least 18 cases, the radio morphology of the cluster member galaxies shows clear signs of ram-pressure stripping. This includes three previously unreported candidates. In addition, we reveal previously undiscovered tails of 150 kpc in length from a previous epoch of AGN activity for NGC 4472 (M 49). While no cluster-scale diffuse radio sources are discovered, we find the presence of an extended radio signature of the W' group. This feature is coincident with an X-ray filament detected with SRG/eROSITA in the outskirts of the cluster. We speculate that this emission is synchrotron radiation, which could be related to shocks or turbulence from accretion processes.

Conclusions. The data published in this paper serve as a valuable resource for future studies. In the follow-up work of the ViCTORIA project, we will use these data for an analysis of environmental effects on the radio properties of star-forming galaxies in Virgo.

2.1 Introduction

The Virgo cluster, referred to hereafter as “Virgo”, is the nearest galaxy cluster to us; its center is coincident with the bright radio galaxy M 87 (Virgo A, NGC 4486, e.g., Owen et al. 2000; de Gasperin et al. 2012) at a distance of 16.5 Mpc (Gavazzi et al. 1998; Mei et al. 2007; Cantiello et al. 2018). Due to its proximity, the cluster spans an enormous angular size with a virial radius of 3.3° (974 kpc) (Simionescu et al. 2017). Estimates of the virial mass M_{vir} ($\approx M_{200}$) of the cluster span the range of $M_{\text{vir}} \approx 1.0\text{--}1.4 \times 10^{14} M_\odot$ (Urban et al. 2011; Ferrarese et al. 2012; Simionescu et al. 2017). The system is considered to be dynamically young and in the process of formation, as indicated by the high fraction of spiral galaxies, the significant deviation from spherical symmetry (Binggeli et al. 1987), and the properties of the intracluster stars (Aguerri et al. 2005; Arnaboldi et al. 2005). A further indication of the young age of the cluster is the presence of pronounced substructure in the galaxy distribution as well as in the X-rays, such as the subclusters and subgroups associated with the massive ellipticals M 49, M 60, and M 86 (Böhringer et al. 1994). All of these features mean that Virgo is an exceptional target for studies of the evolution of clusters and their member galaxies.

An example of a phenomenon that can be studied in rich and dynamic environments such as Virgo is ram-pressure stripping, a perturbation that affects galaxies that move at high velocity with respect to the intracluster medium (ICM). This effect removes part of the interstellar medium (ISM) of star-forming galaxies, eventually causing a quenching of star formation, whereafter they are referred to as quiescent (e.g., Gunn & Gott 1972; Sarazin 1986; Boselli et al. 2022). The synchrotron-emitting cosmic rays in the ISM of star-forming galaxies are accelerated in the supernovae of short-lived massive stars, which gives rise to the particularly tight radio–SFR relation (van der Kruit et al. 1971, 1973; Calistro Rivera et al. 2017; Gürkan et al. 2018). For galaxies that experience ram-pressure stripping, an excess of radio emission can often be found (Gavazzi et al. 1991; Gavazzi & Boselli 1999; Miller & Owen 2001; Murphy et al. 2009; Ignesti et al. 2022b). Integrated flux density measurements and high-resolution studies of individual cluster galaxies can help us to understand the cause of this excess. Cosmic-ray electrons in the stripped ISM of galaxies likely show a steep spectrum due to radiative aging. Low-frequency ($\lesssim 1$ GHz) observations are required to detect the oldest and most distant parts of those stripped tails. Indeed, a number of studies utilizing 144 MHz observations with the Low-Frequency Array High-band Antenna (LOFAR HBA) recently demonstrated that low-frequency observations are well suited to discover ram-pressure-stripped tails (Ignesti et al. 2022c,b; Roberts et al. 2021a,b; Roberts et al. 2022b).

Contrary to star-forming galaxies, where the radio luminosity is dominated by the aforementioned star formation, in early-type galaxies, active galactic nuclei (AGN) are responsible for the radio emission. The relativistic plasma supplied by AGN can halt the star formation of the host galaxy (Gaspari et al. 2012) and in clusters it can even influence the thermodynamical properties of the ICM via AGN feedback (Fabian 2012). For Virgo, interactions between the AGN jets and the surrounding ICM have previously been observed for M 87 (Forman et al. 2007; Million et al. 2010) as well as for numerous other systems at the centers of the less massive substructures (Kraft et al. 2011; Dunn et al. 2010; Paggi et al. 2014; Su et al. 2019) or in noncentral galaxies (Finoguenov et al. 2008; Bîrzan et al. 2008; Kraft et al. 2011; Million et al. 2010; Paggi et al. 2014; Su et al. 2019). As the relativistic electrons accelerated by the AGN lose energy over time, their radio spectrum also becomes steeper.

Therefore, observations at low frequencies are required in order to unveil the emission of past phases of nuclear activity.

Furthermore, in the radio band, the nonthermal component of the ICM can generate radio halos and radio relics if there is sufficient particle acceleration and magnetic field strength (Brunetti & Jones 2014; van Weeren et al. 2019). Such emission is prominent in nearby clusters like Coma and Abell 1367. Contrary to these clusters of higher richness, Virgo is not known to host cluster-scale diffuse radio emission. Nevertheless, deeper observations may provide the means to reveal (or put stringent limits on) the presence of such a source, which could possibly be linked to merging subsystems. Again, observations at low frequency are critical because of the steep-spectrum nature of diffuse radio sources. This is the case for Virgo in particular, given that clusters of lower mass are expected to host steeper radio halos (Cassano 2010).

Until now, the most sensitive wide-field surveys that cover Virgo are the TIFR GMRT Sky-Survey (TGSS, Intema et al. 2017), the NRAO VLA Sky Survey (NVSS, Condon et al. 1998), and, more recently, the Rapid ASKAP Continuum Sky Survey (RACS, McConnell et al. 2020) and the Karl G. Jansky Very Large Array Sky Survey (Lacy et al. 2020). All of these are subject to strong imaging and calibration artifacts in proximity to M 87, and only TGSS is a low-frequency survey, at 150 MHz. In addition to the wide-field surveys, there have been a number of radio studies of samples of Virgo galaxies (Vollmer et al. 2007, 2010, 2013; Weżgowiec et al. 2007, 2012; Murphy et al. 2009; Capetti et al. 2009). However, those are limited to a small number of objects (<20).

We aim to significantly increase the radio coverage of Virgo with the ViCTORIA (Virgo Cluster multi-Telescope Observations in Radio of Interacting galaxies and AGN) project. The project includes data from the low- and high-band systems of LOFAR as well as MeerKAT and will greatly improve the sensitivity and resolution of the wide-field coverage in radio continuum between 42 and 1700 MHz and in the 21 cm line. Polarization data from the L-band observations will also be included. This work represents the first data release of ViCTORIA, and presents data taken with the LOFAR HBA at 144 MHz. LOFAR (van Haarlem et al. 2013) is a radio interferometer based in the Netherlands and operating at frequencies of between 10 and 240 MHz. The LOFAR Surveys Key Science Project is currently carrying out the LOFAR Two-metre Sky Survey (LoTSS, Shimwell et al. 2017, 2019; Shimwell et al. 2022), imaging the Northern Sky at more than an order of magnitude greater sensitivity and significantly higher resolution than previous large sky surveys. Due to its low declination and the presence of the extremely bright source M 87 (1250 Jy at 144 MHz), which severely complicates calibration and imaging of the field, Virgo is not yet included in the published footprint of LoTSS. With this work, we take advantage of significant advances in low-frequency radio interferometric calibration techniques developed for LoTSS (Tasse et al. 2021) to extend the coverage of sensitive LOFAR surveys to the Virgo region by employing a partly custom-developed calibration strategy to address the severe image fidelity issues associated with M 87.

A wealth of multiwavelength data exists on Virgo, which is complemented by the LOFAR observations presented in this paper and the further releases of the ViCTORIA project. For example, the classical reference for galaxies in the Virgo field is Binggeli et al. (1985), who carried out optical observations and published the photographic Virgo Cluster Catalog (VCC), which includes 2096 galaxies in an area of 140 deg². A digital successor to the VCC is the Extended Virgo Cluster Catalog (EVCC) (Kim et al. 2014), which is based on SDSS Data Release 7 photometric and spectroscopic data (Abazajian et al. 2009) and provides an updated cluster membership and morphology categorization of galaxies residing in a five times larger area than the VCC. The deepest optical survey of the cluster is the Next Generation Virgo Cluster Survey (NGVS, Ferrarese et al. 2012) conducted with the MegaCam instrument at the CFHT. Other auxiliary data include the Virgo Environmental Survey Tracing Ionised Gas Emission (VESTIGE, Boselli et al. 2018b), which mapped the cluster in H α + [N II]

also using MegaCam and following the NGVS footprint. In the far-infrared, data of the Herschel Reference Survey (HRS, Boselli et al. 2010) and the Herschel Virgo Cluster Survey (HeViCS, Davies et al. 2010) exists. In the near- and far-ultraviolet, the cluster was observed by the GALEX Ultraviolet Virgo Cluster Survey (GUViCS, Boselli et al. 2011). Combined, these data give an outstanding repertoire of star-formation tracers over the entire cluster region. Other data include the sample from the ACS Virgo Cluster Survey (ACSVCS, Cote et al. 2004) of 100 early-type Virgo galaxies. In infrared and X-rays, this sample has also been studied with Spitzer and Chandra (Gallo et al. 2010). Samples of late-type galaxies were the subject of dedicated studies with Chandra in X-rays (Soria et al. 2022), ALMA in molecular gas (Brown et al. 2021) and with the VLA in atomic gas (H I, Chung et al. 2009). The properties of the ICM were analyzed based on X-ray observations with ROSAT (Böhringer et al. 1994), XMM-Newton (Urban et al. 2011), and Suzaku (Simionescu et al. 2017). An study beyond the virial radius is currently being conducted with the extended ROentgen Survey with an Imaging Telescope Array (eROSITA, (Merloni et al. 2012; Predehl et al. 2021, McCall et al. in prep.).

With this paper, we extend the multiwavelength coverage of Virgo by providing wide-field images of the cluster and radio measurements of all LOFAR-detected Virgo galaxies. A detailed scientific interpretation of the radio data will follow in upcoming publications, where we will analyze the environmental impact on galaxy evolution and the radio galaxy population in the Virgo cluster.

Throughout this paper, we assume a flat Λ CDM cosmology with $\Omega_m=0.3$ and $H_0=70$ km/s/Mpc. At the distance of M 87, for which we adopt a value of 16.5 Mpc (Mei et al. 2007; Cantiello et al. 2018), one arcsecond corresponds to 80 pc. This paper is arranged as follows: In Sect. 2.2, we present the observations and the data reduction strategy of the survey. In Sect. 2.3, we report details of the catalog of Virgo galaxies we provide, and in Sect. 2.4, we highlight individual objects and findings in the LOFAR maps. We conclude in Sect. 2.5.

2.2 Observations and data reduction

The LOFAR HBA Virgo Cluster Survey covers a 132 deg^2 region of the Virgo cluster between a declination of 3° and 18° . The survey footprint displayed in Fig. 2.1 is composed of the nine different pointings listed in Tab. 2.1. In total, eight observations of 8 h each were conducted (project: LC11.010) between March 18, 2019, and April 2, 2019, book-ended by 10 min calibrator scans of 3C 196 and 3C 295. The observations were taken in dual-beam mode, with one beam always pointing toward M 87, and the other toward one of the eight outer fields. The outer fields lie on the grid of LoTSS. The total observation time of M 87 is only 56h rather than 64h because the observation parallel to field 1 is missing in the LOFAR Long-Term Archive (LTA). Data were taken with the LOFAR HBA in a setup identical to observations taken for LoTSS with a nearly continuous frequency range from 120 to 168 MHz, a frequency resolution of 3.07 kHz, and a time resolution of 1 s. After initial flagging of the raw data, the data are averaged to a resolution of 12.2 kHz in frequency and stored in the LTA.

2.2.1 Challenges of the Virgo field

The presence of M 87 in the cluster center makes radio calibration and imaging of the Virgo field particularly challenging. It is not only one of the brightest sources on the radio sky (1.25 kJy at 144 MHz, Scaife & Heald 2012), but is also highly extended with an angular size of $15'$. This complex morphology makes an accurate deconvolution of the source hard to achieve, and the large extent means that the primary beam variation across M 87 is non-negligible; indeed it is $> 20\%$ for some pointings.

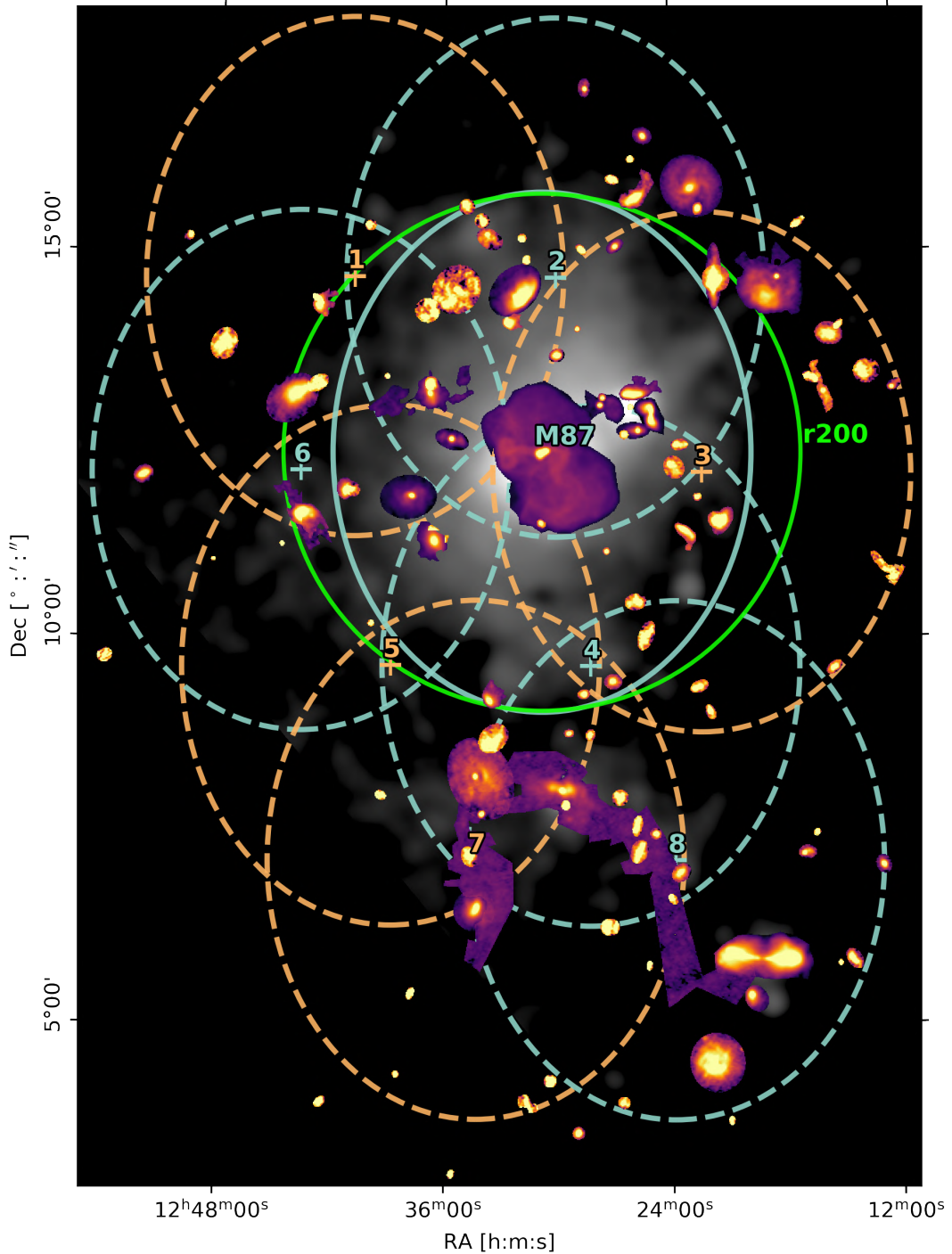


Figure 2.1: Overview of the LOFAR HBA Virgo cluster survey. As cutouts, we show the radio-detected galaxies from the 20' mosaic; for better visualization, their sizes are magnified by a factor of six and their color mappings adjusted individually. The central points and the half-maximum primary beam ellipses of the nine survey pointings are displayed in alternating colors (orange/blue). The green circle marks r_{200} and the grayscale background image is the eROSITA X-ray map in the 0.3 – 2 keV band (McCall et al. in prep.) where we mask the southeastern emission in the direction of the NPS.

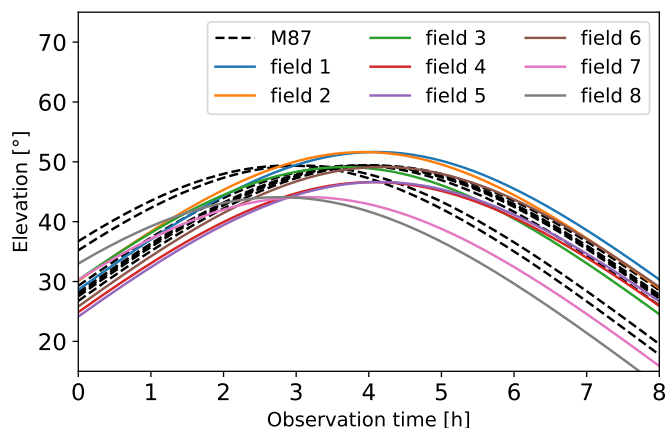


Figure 2.2: Elevation as a function of observation time for the Virgo cluster observations.

Table 2.1: Virgo cluster pointings.

field	RA _{J2000} [h:m:s]	DEC _{J2000} [°:′:″]	exposure [h]	comments
M87	12:30:49.42	+12:23:28.0	56	
1	12:40:47.46	+14:39:45.5	8	severe ionosphere, high noise level
2	12:30:05.30	+14:38:54.9	8	
3	12:22:22.72	+12:07:42.3	8	
4	12:28:16.58	+09:37:33.7	8	
5	12:38:46.71	+09:38:23.2	8	
6	12:43:33.66	+12:09:22.3	8	dynamic ionosphere
7	12:34:18.36	+07:07:25.6	8	bright sources
8	12:23:52.29	+07:06:36.4	8	bright sources

Another difference in comparison to observations of LoTSS-DR2 is the declination of the LOFAR Virgo field, which is between $+3^\circ$ and $+18^\circ$; this translates to rather low-elevation observations in the range of $\sim 25^\circ$ – 50° (see Fig. 2.2). This causes an elongated primary beam shape, an increased thermal noise level due to the reduced sensitivity of the dipoles, and greater susceptibility to ionospheric disturbances caused by the higher air mass compared to observations at more favorable declinations. Furthermore, the LOFAR primary beam model is expected to be less accurate at lower elevations, which affects the accuracy of the flux density scale. Finally, the majority of the Virgo cluster galaxies are extended objects with a low radio-continuum surface brightness and as such, are difficult to fully deconvolve.

2.2.2 Data reduction

To address the aforementioned difficulties, we developed a strategy specifically tailored to the Virgo cluster field and the targets of interest. The main difference from the default calibration approach for LOFAR HBA, which is used, for example, for LoTSS-DR2, is an additional step in which we accurately subtract M 87 from the uv -data. Subsequently, direction-dependent calibration can mostly

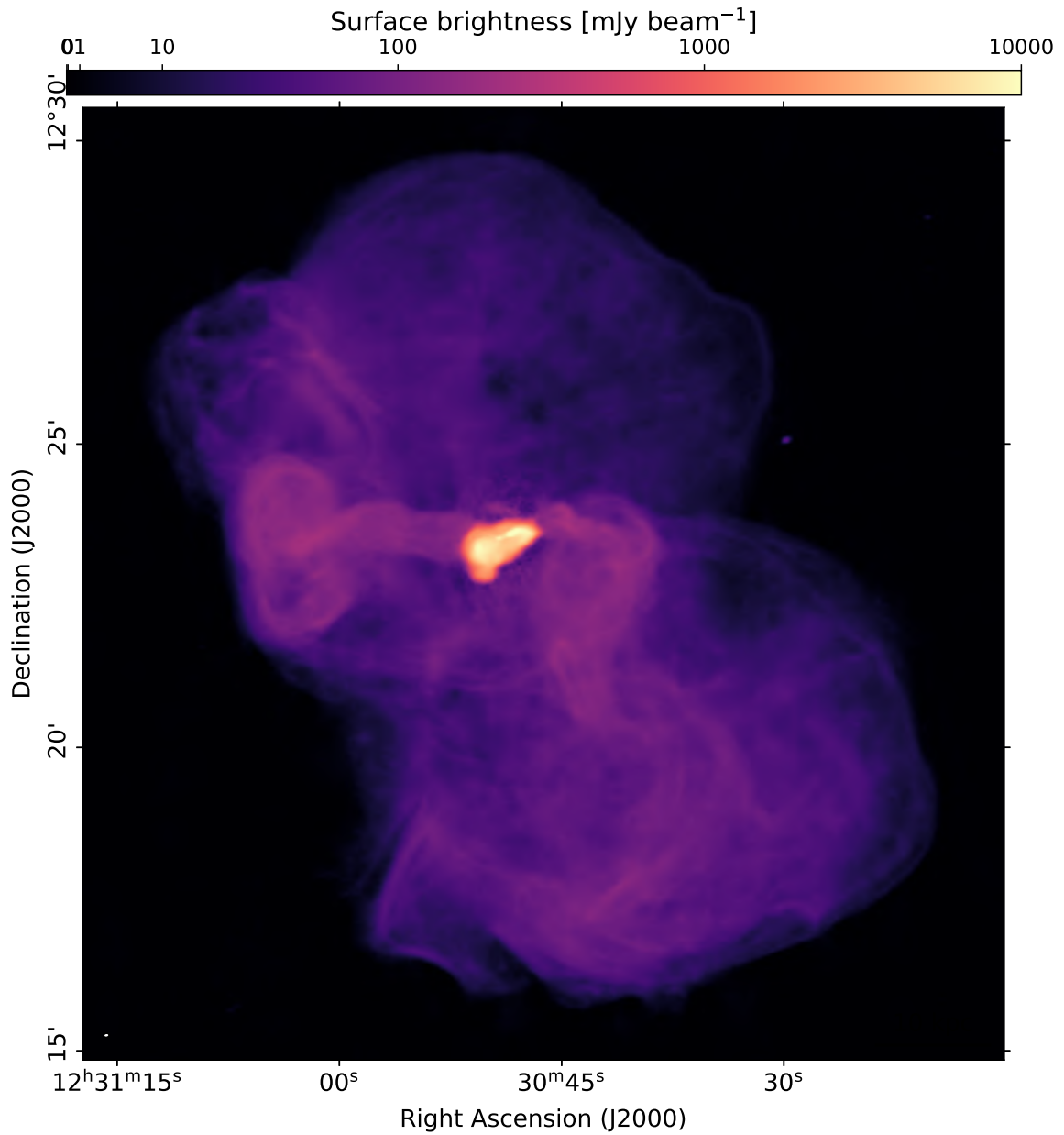


Figure 2.3: LOFAR image of M87 at 144 MHz. The ellipse in the bottom left corner indicates the primary beam size of $5.6'' \times 4.1''$. The noise level is $350 \mu\text{Jy beam}^{-1}$, corresponding to a dynamic range of 44000.

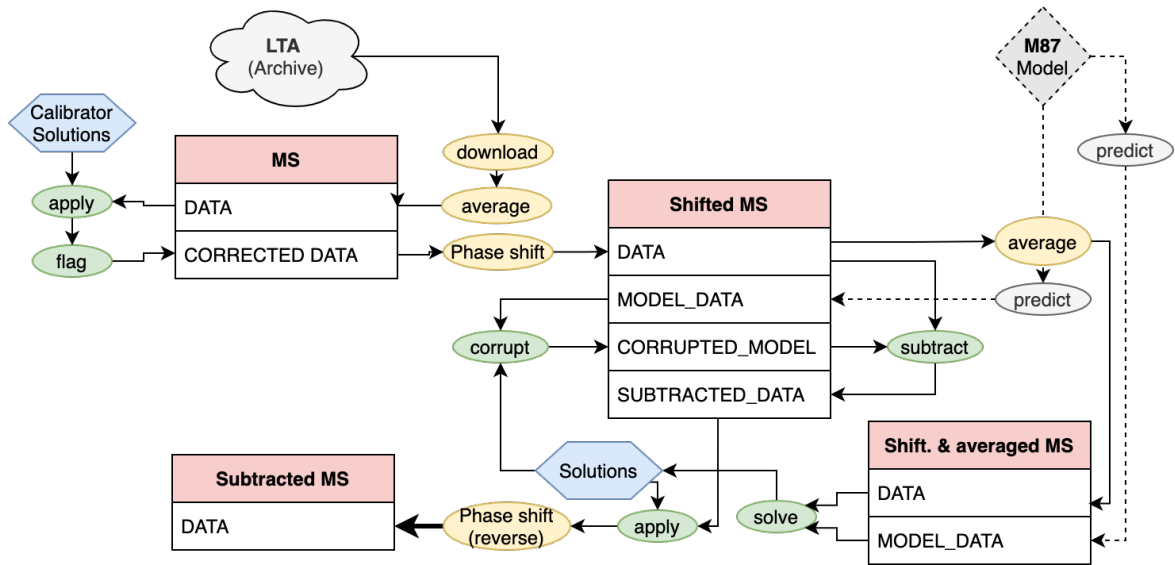


Figure 2.4: Scheme of the peeling strategy.

be carried out in a similar way to LOFAR HBA observations of normal fields.

The data reduction is split into a series of steps, which are implemented in various pipelines: The first step is pre-processing, the second is to reduce the data of the calibrator scans, the third is to subtract M 87 from the data, and the last step is a full direction-dependent calibration. Subsequently, an extraction and re-calibration procedure can be applied for selected targets (see van Weeren et al. 2021). For the first three steps, we make use of the Library for Low Frequencies (LiLF¹), and for the direction-dependent calibration and extraction, we use the ddf-pipeline²(Tasse et al. 2021).

In the pre-processing step, the data of all calibrator and target observations were downloaded from the LTA. Subsequently, all baselines containing international LOFAR stations were removed and the data were averaged down to 48.8 kHz in frequency (four channels per sub-band) and 4 s in time. The strategy used to find the calibrator solutions is described in detail in de Gasperin et al. (2019); nevertheless, we briefly summarize the key steps below. The pipeline derived the polarization alignment delays as well as the Faraday rotation and bandpass solutions. These were then applied to the data in physical order together with the primary beam model. Finally, we solved for scalar phases, which describe the ionospheric and clock delays.

Peeling pipeline

The purpose of this pipeline is to subtract M 87 from the uv -data of each observation of the Virgo field. A key requirement for this is a high-quality model of the source, which did not exist at 144 MHz prior to this project. Starting from the $21'' \times 15''$ image of de Gasperin et al. (2012), we performed multiple rounds of self-calibration using an 8 h observation with M 87 at the phase center. In each iteration, we solved for scalar phases at full time- and frequency resolution and for full-Jones matrices at a resolution of 64 s and 0.49 MHz using DP3³. For imaging, we used the multi-scale and multi-frequency deconvolution mode of WSCLEAN (Offringa et al. 2014; Offringa & Smirnov 2016). As

¹<https://github.com/revoltek/LiLF>

²<https://github.com/mhardcastle/ddf-pipeline>

³<https://github.com/lofar-astron/DP3>

M 87 is extremely bright, highly resolved, and of complex morphology, deconvolution is particularly delicate. With improving solutions during self-calibration, less conservative deconvolution parameters can be used. A high-resolution image of a single 8 h observation was created using a *Briggs*-value of -1.2 —shown in Fig. 2.3—and the final model of M 87 used for the peeling is created with a *Briggs*-weighting of -0.6 .

The following peeling procedure was carried out for each observation. The first step of the peeling pipeline is to apply the polarization alignment, bandpass, and scalar-phase solutions from the calibrator together with the primary beam model at the phase center to the target field. Here, we used the corresponding calibrator observation with the least amount of flagged data. Next, we perform ‘A-Team clipping’. The purpose of this procedure is to flag the parts of the data where the bright sources Cassiopeia A, Cygnus A, and Taurus A (which form the infamous ‘‘A-team’’ together with ‘‘Virgo A’’) reside in a side-lobe of the primary beam. If their predicted amplitude is above 5 Jy for any time, frequency, or polarization, this part of the data is flagged. In addition, we flag the parts of the data affected by radio-frequency interference using AOFLAGGER (Offringa et al. 2012) as well as all data taken below 20° elevation. Afterwards, time steps that contain more than 50% flagged data are discarded.

Next, the data are phase-shifted toward the location of M 87, that is, if they are not already centered on the source, and are corrected for the difference between the primary beam at the original phase center and M 87. From this phase-shifted data set, a smaller data set is created by averaging down to a resolution of 16 s in time and 0.39 MHz in frequency. This speeds up computation and suppresses the contribution of sources away from M 87 by time- and frequency-smearing them. The model-*uv*-data of this small data set is populated with the M 87 source model using WSCLEAN together with the image domain gridded (*idg*, van der Tol et al. 2019). Due to a large angular size of $15'$, the primary beam variations across M 87 are non-negligible, especially for the pointings where M 87 is close to the edge of the primary beam. Therefore, we find that it is important to adjust the predicted visibilities with the direction-dependent component of the primary beam during prediction. Then, complex scalar gain solutions are derived by solving against the model data on the full time resolution of the averaged data set. In the solver, the solutions are smoothed in frequency with a 1 MHz kernel. From the resulting calibration solutions, we only apply those phases to the data that encompass the ionospheric delays. However, the amplitudes are used to identify bad parts of the data by flagging all time and frequency intervals where the amplitudes are more than a factor of five from unity. We perform a second, slow full-Jones calibration on timescales of 256 s. In this solve step, we smooth the calibration solutions with a 2 MHz kernel in frequency. After deriving the solutions towards M 87 from the small data set, we predict the *uv*-data corresponding to the M 87 model to the large data set at 48.8 kHz bandwidth and 4 s time resolution, again using *idg* to include the direction-dependent component of the primary beam. The predicted visibilities are then corrupted with the phase and slow full-Jones solutions. We create a new data set by subtracting the corrupted M 87 model from the data. We then correct the subtracted data using the scalar phases towards M 87, which is intended to correct the clock delays as well as to pre-correct the ionospheric delays in the direction of Virgo. The pre-corrected subtracted data column is then phase-shifted back to the original phase center, averaged to a resolution of 8 s in time and 98 kHz in frequency, and is concatenated into frequency blocks of 1.95 MHz. Finally, we correct for the difference of the primary beam at the phase center and at the location of M 87. The resulting measurement sets now have M 87 subtracted and are therefore prepared in a format that is suitable for the following direction-dependent calibration. A schematic overview of the peeling strategy is presented in Fig. 2.4.

For the observations centered on M 87, the subtraction procedure was slightly altered. The phase-shifting and additional beam-correction steps are not necessary due to the greater apparent brightness.

Furthermore, the calibration solutions are derived at a higher time resolution of 4 s for the Jones scalar, and 64 s for the full-Jones matrix.

For field 8, the subtraction of M 87 is particularly challenging due to the presence of NGC 4261 (\approx 3C 270; $S_{144} = 73$ Jy) in the center of the field. To obtain robust solutions for this pointing, we used a parallel solve on both NGC 4261 and M 87, where we employed a model of two Gaussian components obtained from the TGSS for NGC 4261. In addition, we solved for a diagonal instead of a full-Jones matrix and used a 4 MHz kernel to smooth the solutions in frequency to reduce the effective number of free parameters. The solutions for M 87 were used for subtraction and to pre-calibrate the phases; the solutions for NGC 4261 were discarded. Stable calibration solutions were not obtained for all time- and frequency windows, which lead to a high ratio of flagged data for this field (55%).

Direction-dependent calibration

For direction-dependent calibration, the `ddf-pipeline` (Shimwell et al. 2019; Tasse et al. 2021) is used, which is a framework that is based on the `DDFacet` imager (Tasse et al. 2018) and the `killMS` solver (Tasse 2014a,b). The `ddf-pipeline` algorithm was also used for the second data release of LoTSS. As it is described in detail in Tasse et al. (2021), only a very brief summary is provided here, mainly focusing on the differences in processing compared to LoTSS-DR2. The algorithm starts with a sparse selection of the data, taking every fourth frequency sub-band. In a series of direction-independent and direction-dependent calibration steps, a sky model of a $8.3^\circ \times 8.3^\circ$ square region of the target field is obtained. Using this model, calibration is carried out on all sub-bands, again in a series of direction-independent and direction-dependent self-calibration cycles. The direction-dependent steps are carried out in a facet-based approach; that is, the sky model is split into 45 discrete directions, which are solved in parallel. An important difference from the LoTSS-calibration is that no amplitude solutions are applied to the data; this is because we experienced divergent amplitude solutions in a small number of facets with a low flux density. This divergence is likely caused by the reduced quality of the data because of residuals of M 87 and/or a low signal-to-noise ratio due to the low elevation of the observations. As a consequence of the missing amplitude corrections, artifacts exist around a number of bright sources, mainly further away from the phase center, suggesting that they may be at least partly caused by errors in the primary beam model. However, this does not notably affect the science quality of the images regarding studies of Virgo cluster objects, because the vast majority of these sources are of low-surface brightness. During the various imaging steps, it is challenging but also critical to accurately deconvolve faint and extended structures in order to obtain a complete sky model for calibration and accurate surface brightness values. The `ddf-pipeline` strongly optimizes deconvolution for these targets using multiple CLEAN iterations with progressively improved masks. Using a mask based on lower resolution images for the deep high-resolution deconvolution, it is possible to further improve deconvolution for extended structures. Nevertheless, a number of faint Virgo galaxies are not fully picked up in the masking procedure and are therefore not accurately deconvolved. To address this, we manually add all detected galaxies of the optical VCC and EVCC catalogs to the masks created by the `ddf-pipeline` and perform one additional deep CLEAN iteration for both the low- and high-resolution images. For the seven observations pointed on M 87, we follow the procedure used for the LoTSS deep fields (Tasse et al. 2021). A single 8 h observation is fully calibrated to derive an accurate sky model. This model is then used to jointly calibrate and deconvolve all 56 h of data.

For three of the eight outer fields, a slightly different strategy was necessary: Field 6 is affected by the presence of 3C 275.1 outside of the 8.3° square region used for imaging and calibration. We

address this by carrying out an additional initial imaging step with a larger field of view (FoV) to subtract sources outside of the square normally used for calibration. Calibration of the two southern pointings on fields 7 and 8 is particularly challenging, as they have a bright source in the FoV (NGC 4261), and the bright quasar 3C 273 (116 Jy, Jacobs et al. 2011) in the side-lobes. The subtraction of sources outside the primary beam, which was used for field 6, did not yield satisfactory results for fields 7 and 8. Instead, the image size used for direction-dependent calibration of these two fields was increased to allow for direction-dependent solutions towards 3C 273. As this strongly increased memory requirements and computation time, the data set was phase-shifted beforehand such that the image size is only increased so as to cover 3C 270, without increasing the coverage in the opposite direction. The size of the square region used for calibration of fields 7 and 8 is 9.5° .

Per field, a number of wide-field imaging products are created from the calibrated data sets: We image Stokes I at angular resolutions of $9'' \times 5''$, $20''$, and $1'$; hereafter, we refer to these resolutions as high, low, and very low. Compact source-subtracted images were created at $1'$ and $4'$ resolution. In addition, we produced Stokes Q and U “dirty” images in a frequency spacing of 97.6 kHz at $20''$ and $4'$ resolution and Stokes V dirty images at $20''$ resolution. No flux-density-scale correction was applied to the per-field data products.

Flux-scale alignment and mosaicing

Uncertainties on the beam model of LOFAR HBA currently limit the accuracy of the flux density scale when it is directly transferred from a calibrator source by introducing a per-field flux density scaling $f_i \neq 1$. Therefore, Shimwell et al. (2022) correct the flux density scale in a post-processing step. By cross-matching sources between LOFAR and the 151 MHz sixth Cambridge survey of radio sources (6C Hales et al. 1988) and between LOFAR and the 1.4 GHz NVSS, these latter authors derive the median flux density ratios $F_{6C,i}$ and $F_{NVSS,i}$ of each field i and both surveys. Under the assumption that the flux-density-scale offsets are direction-independent for a given field, both median ratios should be equally offset by a factor of f_i from the value found for a perfectly accurate flux density scale. Therefore, the ratio of the median flux density ratios per field $F_{6C,i}/F_{NVSS,i}$ should be approximately independent of the offset f_i and also therefore constant between the fields if there is no spatial variation in the NVSS and 6C scales. Considering the median of the median ratios found across all fields, a value of $F_{6C}/F_{NVSS} = 5.724$ was found in Shimwell et al. (2022). Taking into account the frequency difference between LOFAR and 6C, and using the median spectral index of sources in 6C and NVSS of $\alpha = -0.783$, the LOFAR observations are aligned with the 6C flux density scale if the median flux density ratio equals $F_{NVSS} = 5.724 \times (144/151)^{-0.783} = 5.936$. Consequently, the flux-density-scale correction factors f_i^{-1} can be determined from the measured median flux-density-scale ratio $F_{NVSS,i}$ of each field as $f_i^{-1} = 5.936/F_{NVSS,i}$. We followed the procedure developed in Shimwell et al. (2022) with two minor modifications: First, as a flux cut of 30 mJy is applied in the cross-matching with NVSS prior to the re-scaling, and given that we found correction factors strongly different from unity for some fields, we iteratively repeated the calculation of the correction factors f_i , updating the flux cut to $30 \text{ mJy} \times f_i^{-1}$ each time. Second, we estimated the correction factors from the $20''$ -resolution maps, because in the high-resolution maps, ionospheric smearing leads to a systematic over-correction of 10% – 20% for the fields where we have lower quality (fields 1, 6, 7, 8). For the remaining fields with good image quality, the difference between the correction factors estimated from the high- and low-resolution maps is between 1% and 8%. To derive these factors, we created a LOFAR source catalog for each Virgo field using the Python Blob Detector and Source Finder (PyBDSF, Mohan & Rafferty 2015) and only considered sources with: no neighbor within $30''$; a major axis of less than $25''$; and a significance of at least 5σ . The final correction factors we found

Table 2.2: Imaging parameters

resolution	subtracted	beam [$'' \times ''$]	robust weighting	min. uv [km]	max. uv [km]
high		9×5	-0.5	0.1	120.6
low		20×20	-0.25	0.1	25.8
very low		60×60	-0.2	0.04	7.0
very low	yes	60×60	-0.2	0.04	~ 7.0 (1'-taper)

were applied to the fields during mosaicing, ultimately placing our survey on the scale of the 6C survey, which in turn is aligned with the flux density scale of Roger et al. (1973). In the mosaicing procedure, pixels were weighted according to the primary beam response as well as the central noise level of the corresponding field. We also excluded all areas with a primary beam attenuation factor of below 0.3. In the final mosaic, we restore the clean components of M 87 that were subtracted in the peeling pipeline. Wide-field mosaics are created for the high-, low-, and very-low-resolution Stokes I maps as well as for the source-subtracted images. The image parameters of all Virgo field mosaics are presented in Tab. 2.2; the image files are available online in fits format⁴.

A map of the root mean square (RMS) noise level of the high-resolution Stokes I mosaic is displayed in Fig. 2.5; the median noise level is $140 \mu\text{Jy beam}^{-1}$ within the virial radius and $280 \mu\text{Jy beam}^{-1}$ across the full footprint. In the vicinity of M 87, the noise level is $\sim 170 \mu\text{Jy beam}^{-1}$, only 40% deeper than what we find for a single 8 h observation, which indicates that we are limited by dynamic range in the central few square degrees. Beyond 2° separation from M 87, the sensitivity ratio between 8 h and 56 h of data approaches the expected ratio of $\sqrt{56 \text{ h} / 8 \text{ h}} \approx 2.65$. Remaining artifacts related to M 87 manifest themselves as wave-like patterns, the most dominant of those originate from M 87 and cross the image towards the north and south, extending for multiple degrees. In some of the outer regions of the survey, the noise level is strongly increased. This is most apparent in the northeast, where the observation of field 1 was affected by particularly unfortunate ionospheric conditions with rapid high-amplitude variations of the ionospheric parameters. The noise level for the region that is exclusively covered by this pointing is $\sim 800 \mu\text{Jy beam}^{-1}$. Fortunately, only very few Virgo cluster galaxies populate that area. Similarly, the eastern field 6 to the south of field 1 was also affected by a dynamic ionosphere, which increased the noise level to $250 \mu\text{Jy beam}^{-1}$. Another region where the image quality is reduced is the southwestern field 8, where the presence of the bright sources 3C 270 and 3C 273, as well as a high flag ratio and low elevation, increase the noise level to $\sim 400 \mu\text{Jy beam}^{-1}$. In the lower-resolution mosaics in particular, this area also shows the presence of larger-scale calibration artifacts.

In Fig. 2.6, we compare the noise level of the LOFAR HBA Virgo cluster survey to that of other surveys and targeted observations of the Virgo field. The quoted noise level of $\sim 150 \mu\text{Jy beam}^{-1}$ corresponds to the region just inside the area covered by the deeper M 87 pointing, which approximately coincides with the Virgo cluster virial radius.

2.2.3 Flux density scale

For LoTSS-DR2, the global uncertainty of the flux density scale was estimated to be 10%, with an additional positional variation of 10% (Shimwell et al. 2022). For a number of reasons, we expect the uncertainty to be higher for the Virgo field: first, due to the low declination of Virgo, the LOFAR

⁴<https://lofar-surveys.org>

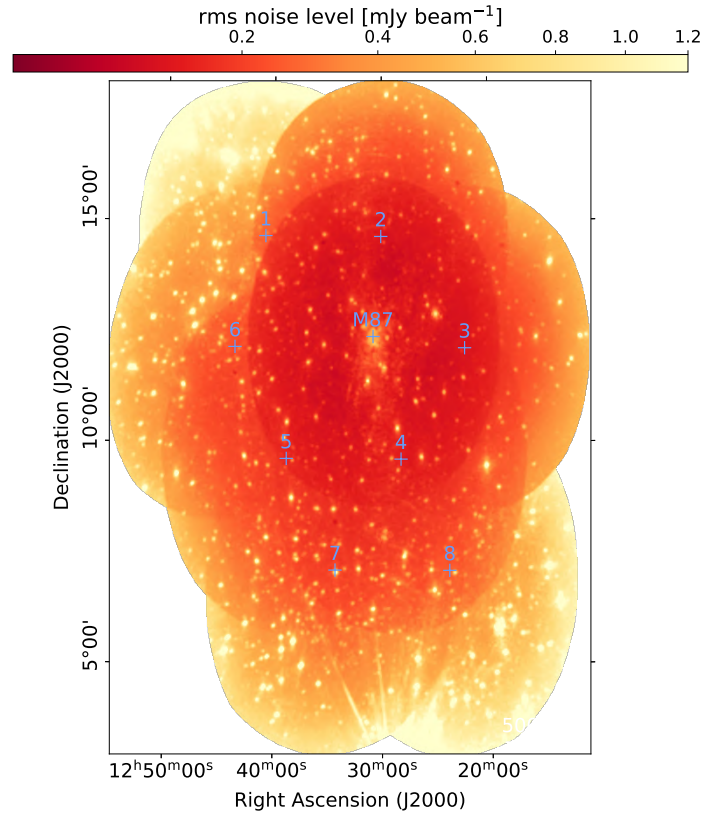


Figure 2.5: RMS noise map of the $9'' \times 5''$ mosaic. Blue annotations indicate the pointing centers of the nine LOFAR fields.

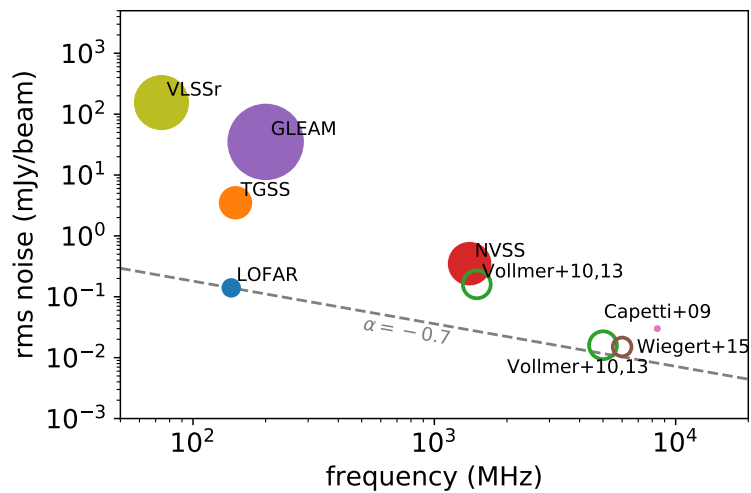


Figure 2.6: Noise-level comparison of different Virgo cluster surveys. The circles show different wide-field surveys (filled circles) and targeted observations of samples of Virgo galaxies (hollow circles). The marker size is proportional to the angular resolution of the corresponding survey. The quoted noise level for LOFAR refers to the median noise inside the virial radius. The dashed line shows an interpolation of this noise level assuming a spectral index of -0.7 .

2 *ViCTORIA project: The LOFAR HBA Virgo Cluster Survey*

beam model should be less accurate, which translates to a higher systematic uncertainty on the flux densities. Indeed, Shimwell et al. (2022) found a declination dependency of the flux density scale that becomes increasingly severe at lower declination. Second, the presence of M 87 in the field not only causes image artifacts in our LOFAR data, but also —and even more severely— in the NVSS and other all-sky surveys, where no tailored strategy was used to address this bright source. This decreases the quality of reference radio catalogs within a few degrees around M 87. Finally, the direction-dependent variation of the flux density scale should be higher for simple statistical reasons; since our survey consists of only nine pointings, the degree of overlap is lower than in LoTSS, where the mosaicing of multiple pointings was shown to reduce the scatter of flux density measurements (Shimwell et al. 2022).

To assess the systematic uncertainty of the flux density scale of the LOFAR HBA Virgo cluster survey, we created a source catalog of the final low-resolution mosaic using PyBDSF. We first compared the LOFAR catalog to NVSS, which was also used for the flux density scale alignment. Repeating the source selection and matching as described in Sect. 2.2.2, we find a median ratio of $S_{\text{LOFAR}}/S_{\text{NVSS}} = 5.42$, which differs by 9% from the value of 5.94 we used for the alignment.

We then cross-matched the LOFAR catalog with sources of the TGSS and the Galactic and extragalactic all-sky MWA survey (GLEAM Hurley-Walker et al. 2017), which are at almost the same frequency as LOFAR HBA. We searched for unique matches inside a radius of 10'' for TGSS and 50'' for GLEAM. To avoid complex sources, where the flux density measurements might not be accurate, we only kept the LOFAR sources that have no other source within 30'' for TGSS and within 2' for GLEAM. Furthermore, we removed sources with an extension above 25'' or a signal-to-noise ratio below five. This resulted in 576 matched sources with TGSS and 68 with GLEAM. We extrapolated the TGSS 150 MHz flux densities to 144 MHz using a factor of $(144/150)^{-0.783} = 1.03$. For GLEAM, we used the 143 MHz catalog and neglected the frequency difference as well as the 3% systematic uncertainty arising due to the Baars flux density scale (Baars et al. 1977) of GLEAM (Hurley-Walker et al. 2017; Perley & Butler 2017). Compared to TGSS, the median flux scale ratio is 1.05 with a standard deviation of 0.23, and for GLEAM, it is 1.02 with a standard deviation of 0.19. This independent test shows that the flux density scale is aligned accurately, albeit with considerable scatter. This scatter is partly caused by the direction-dependent flux scale uncertainty in the LOFAR maps; another contribution stems from outliers in the cross-matching procedure. Additionally, the reference surveys also add considerably to the scatter. By cross-matching 211 sources in the Virgo field between TGSS and GLEAM, we find that the flux densities of those two surveys show a median flux ratio of 1.01 (expected: $(143/150)^{-0.78} = 1.04$) with a standard deviation of 0.29. Given the comparison with both TGSS and GLEAM, we assume that the systematic uncertainty on the flux density scale of our LOFAR HBA survey of the Virgo cluster is $f_{\text{sys}} = 20\%$, which includes both the uncertainty of the absolute flux density scale and the direction-dependent variation.

During the flux-scale alignment, we used the low-resolution mosaic, because it is less affected by poor ionospheric conditions. Indeed, repeating the procedure for the high-resolution images, we find that the median flux density is significantly lower for the observations with poor ionospheric conditions. The most extreme case is field 1, where the difference in median flux between the high-resolution and the low-resolution image is 28%. A significant difference of $\sim 20\%$ is also observed for the southern fields 7 and 8, where bright sources limit the quality of the calibration. This indicates that for regions close to the edge of the survey footprint, which are exclusively covered by one of those fields, particular care must be taken when working with the high-resolution images.

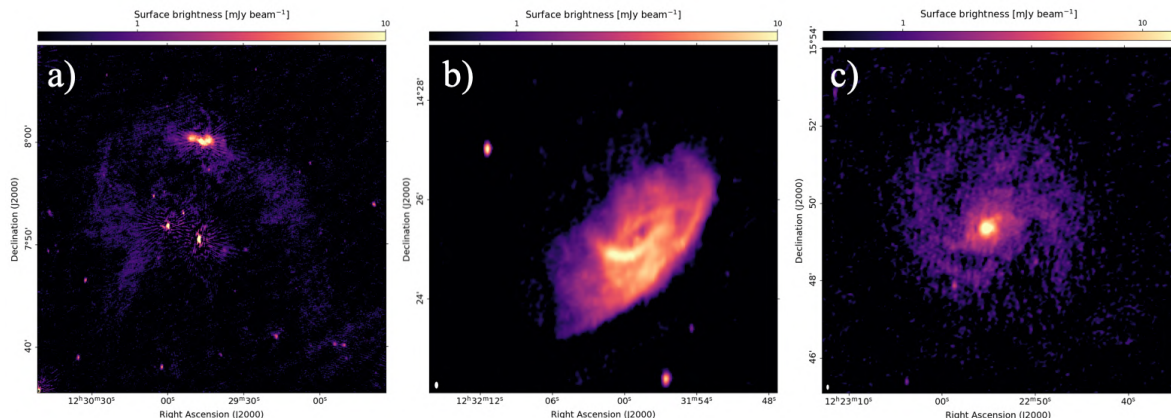


Figure 2.7: LOFAR maps of selected Virgo cluster galaxies. The panels show (a) NGC 4472 (M 49), (b) NGC 4501 (M 88), and (c) NGC 4321 (M 100). The ellipse in the bottom left corner of the panels indicates the synthesized beam size of $9'' \times 5''$.

2.3 LOFAR Virgo cluster catalog

To create the catalog of all Virgo cluster galaxies that are detected in the 144 MHz LOFAR Virgo cluster survey, we considered all galaxies in the EVCC, which fully covers our LOFAR footprint. For the EVCC, a radial velocity cut of $v < 3000 \text{ km s}^{-1}$ is employed to select possible cluster members, and a redshift-based infall model is used to identify certain cluster members (Kim et al. 2014). Of the 1589 galaxies, 991 are in the footprint of our LOFAR survey. The classical VCC includes a high number of background objects that do not fall into the radial velocity cut. As the VCC is still used as a common reference for galaxies in the Virgo field, we also compiled a radio catalog of the background VCC galaxies that are not part of the Virgo cluster.

As the radio continuum emission of the galaxies is mostly faint, extended, and often not well described by a Gaussian profile (see Fig. 2.7), it is challenging to accurately identify all emission attributed to galaxies using an automatized source finder. We therefore measured the flux densities manually. We visually inspected the high- and low-resolution images of every galaxy in the EVCC and VCC with a z -band magnitude of 16 or below in the footprint of the LOFAR Virgo field. If emission is detected, we manually determine an elliptical region around the emission, if possible fully enclosing the 3σ contours in the low-resolution mosaic. In cases where the radio morphology is particularly complex or background sources are superimposed on the emission, we instead use a more complex polygon region to trace the emission. To check for misidentifications, the optical images of the DESI Legacy Imaging Survey DR9 (Dey et al. 2019) were inspected together with the radio contours.

We measure the integrated flux density in the regions, and the corresponding uncertainty σ_S is calculated according to:

$$\sigma_S = \sqrt{\sigma_{\text{rms}}^2 N_{\text{beam}} + (f_{\text{sys}} S)^2}, \quad (2.1)$$

where $f_{\text{sys}} = 0.2$ is the systematic uncertainty of the flux density scale, N_{beam} the number of synthesized beams covering the region, and σ_{rms} the local statistical uncertainty as measured from the RMS of the residual maps. We only consider sources with a statistical significance above 4σ in the low-resolution mosaic. This results in 112 Virgo cluster galaxies that are detected in the LOFAR maps out of the 991 EVCC galaxies in the survey footprint. The detection fraction strongly depends on the optical brightness; it is above 50% for the 171 galaxies brighter than a z -band magnitude of 12.

In contrast, none of the objects fainter than a z-band magnitude of 14.6 are radio-detected, although those constitute more than half of the EVCC objects in the LOFAR footprint. The optically bright objects that are not detected in LOFAR are mostly ellipticals and lenticulars without strong AGN. Additionally, we detect 114 background galaxies that are listed in the VCC.

As the galaxies are mostly low-surface-brightness extended sources, particular care must be taken during the deconvolution. If sources are not fully deconvolved, emission coming from the side-lobes of the point-spread function may remain and their flux density will be overestimated. This problem mostly affects the high-resolution mosaic, where the objects are more strongly resolved. To assess the completeness of the deconvolution, we compare the flux densities of the sources in the high- and low-resolution images using identical regions. This comparison is presented in Fig. 2.8. Particularly for fainter sources, the flux density estimated from the high-resolution image is systematically above the measurement at low resolution, even after we perform an additional round of deep deconvolution with manual clean-masks for all objects in the catalog (see Sect. 2.2.2). A further measure of the completeness of the deconvolution is the integrated flux density measured from the residual images using the source regions. If a source is not or barely deconvolved, the flux density in the residual image will be close or equal to the flux density in the restored image, while for a perfect deconvolution in the absence of noise and systematic errors, the integrated flux in the residual image should be zero. In Fig. 2.9, we show the flux density ratio between the residual and restored mosaics for the Virgo cluster galaxies as a function of the mean surface brightness and mark the galaxies where the difference between the high- and low-resolution images is larger than 20%. At high resolution, for 13 out of 112 galaxies, the residual flux ratio is at least 50%, and for all but one of these cases, there is a difference of above 20% between the integrated flux densities at the different resolutions. On the contrary, at low resolution, the residual flux density ratio is always below 50%. We therefore decided to report the flux density measurements of the low-resolution images. Two galaxies in Fig. 2.9 show a residual flux density ratio of < -0.5 . The orange cross marks VCC 144, which is located in a high-noise region and is not significantly detected in the high-resolution map, causing this fluctuation. The blue cross is VCC 758, which is located directly next to an extended radio feature that we discuss in Sect. 2.4.2. Around this feature, a bowl of negative surface brightness is present, which is caused by the incomplete deconvolution of the large-scale emission. Tab. 2.3 lists the measured flux densities of the LOFAR-detected Virgo cluster member galaxies together with the position, morphological classification, and r -band magnitude as provided in Kim et al. (2014). Additionally, we specify the area of the region used for the flux-density measurements as well as redshift independent distance measurements. We assume the distances of the galaxies to be identical to the mean distance of the substructure they belong to. We follow the substructure distances and membership criteria defined in (Boselli et al. 2014), which report the clusters *A* and *C* and the low-velocity cloud (LVC) at $d = 17$ Mpc, the cluster *B* and *W'* cloud at 23 Mpc and the *W* and *M* clouds at 32 Mpc. However, for consistency with the VESTIGE (Boselli et al. 2018b) and NGVS (Ferrarese et al. 2012) projects, we assume a distance of $d = 16.5$ Mpc instead of 17 Mpc for clusters *A*, *B*, and the LVC. Based on these distances, we also calculated the radio luminosity for all galaxies in the catalog. The catalog is made available online at the CDS together with cutout images of all detected galaxies, and is also available at the LOFAR Surveys web page⁵. We report the LOFAR flux density measurements and the auxiliary data for the LOFAR-detected VCC background galaxies, which can be found in Tab. 2.4. Furthermore, while not suitable for the analysis of nearby galaxies, the full wide-field source catalog obtained with PyBDSF from the low-resolution mosaic is still highly valuable for studies of background objects, and so we also provide this catalog online.

⁵https://lofar-surveys.org/virgo_survey.html

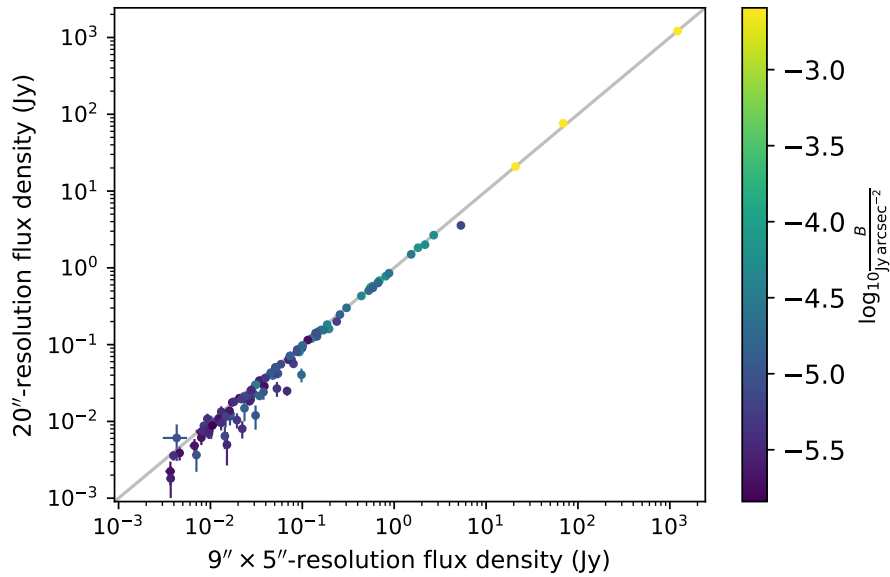


Figure 2.8: Flux densities of Virgo cluster members measured from the high-resolution ($9'' \times 5''$, x -axis) and low-resolution ($20'' \times 20''$, y -axis) mosaics using identical regions. The color scale corresponds to the logarithm of the average surface brightness.

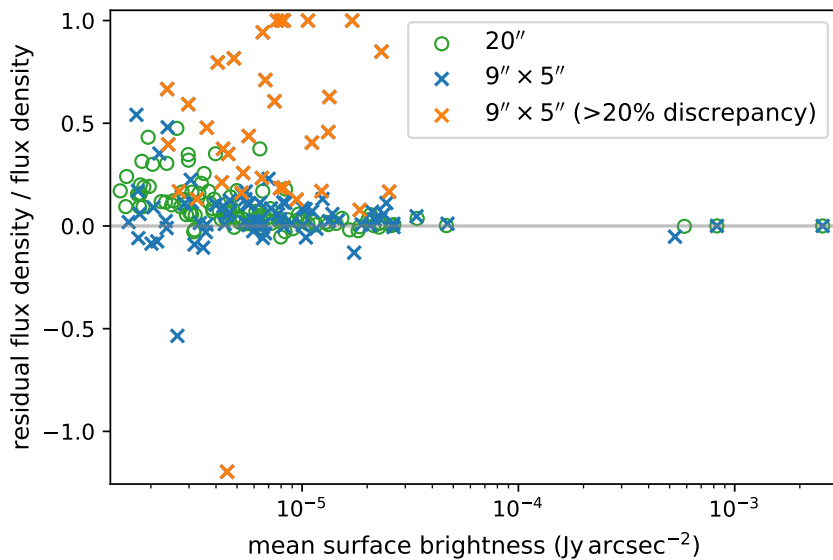


Figure 2.9: Ratio between the flux density measured from the residual and the restored images (y -axis) as a function of mean surface brightness (x -axis). Circles and crosses mark measurements from the low-resolution and high-resolution mosaic, respectively. For the orange crosses, the difference between the flux density in the low- and high-resolution measurements is above 20%.

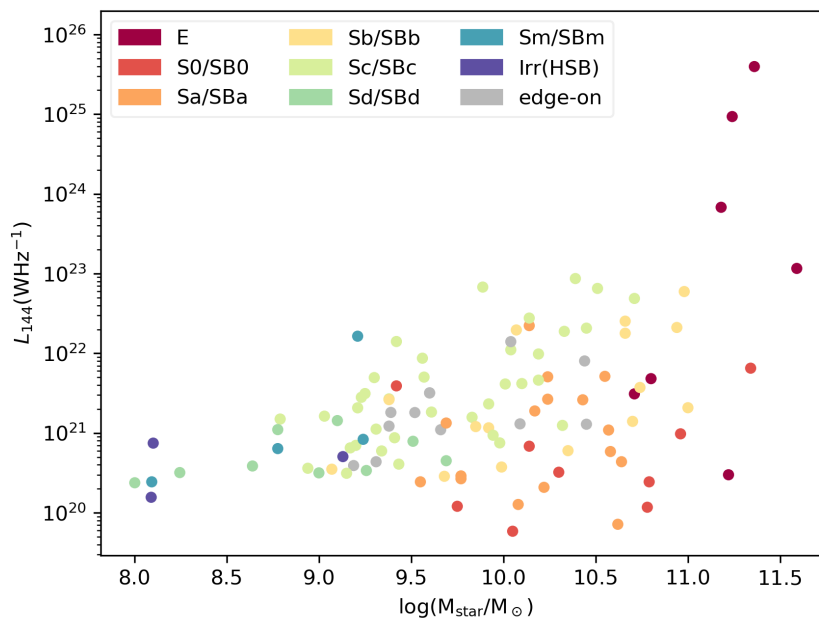


Figure 2.10: Stellar mass (x -axis) vs. 144 MHz radio luminosity (y -axis) for galaxies in the LOFAR Virgo cluster catalog. The marker color corresponds to the Hubble-type.

The Hubble morphological classification is shown together with the stellar masses and radio-luminosities of the LOFAR Virgo cluster catalog galaxies in Fig. 2.10. Stellar masses were taken from Boselli et al. (2015), or, if not available, from (Boselli et al. 2014). In both cases, we used the calibration of Zibetti et al. (2009) based on the Chabrier initial mass function (Chabrier 2003). The most radio-bright and most massive objects are radio galaxies in giant ellipticals. For spiral galaxies, later-type objects are on average brighter than earlier-type spirals of similar mass.

2.4 Discussion

A dedicated scientific analysis of the radio data presented here will be the subject of follow-up work by our team, including a study of the radio–star formation rate (SFR) relation and the ram-pressure stripped objects in Virgo. However, here we present highlights and a brief initial discussion of radio sources that are noteworthy either due to their environmental interaction or because they otherwise belong to a class of objects that is of particular interest in the radio continuum, such as giant ellipticals or dwarf galaxies. See Appendix A for an image atlas of all the galaxies.

2.4.1 Galaxies

VCC 144

VCC 144 is discussed in Brosch et al. (1998) as a blue compact dwarf galaxy with an extended H I envelop currently undergoing an intense starburst. These authors propose it to be an example of galaxy formation currently taking place in the southern extension of the Virgo cluster. In the optical

wavelengths, VCC 144 is the faintest galaxy in our radio catalog. It is also part of the HERSCHEL far-infrared-selected star-forming dwarf galaxy survey of Grossi et al. (2016)

VCC 241 (IC 3105)

This irregular galaxy shows low-surface brightness emission in our LOFAR maps. In the south of the galaxy, the radio emission appears to extend towards the west. This feature is coincident with extra-planar H II regions traced by VESTIGE (Boselli priv. comm.). It is therefore likely that the low-frequency radio continuum emission distribution traces cosmic-ray electrons advected due to ram pressure and/or tracing the star formation in the stripped gas.

VCC 307 (NGC 4254, M 99)

M 99 is the most radio-bright late-type galaxy in the Virgo cluster and is oriented close to face-on. The high SFR, the disturbed morphology, with a peculiar spiral arm in the west, and the long H I tail (Haynes et al. 2007) are thought to originate from an encounter with another massive cluster member in the past (Vollmer et al. 2005; Chyzy et al. 2007; Duc & Bournaud 2008; Chyzy 2008; Boselli et al. 2018a). However, even though the galaxy is located in the cluster outskirts at a distance of ≈ 1 Mpc to M 87, ram-pressure stripping also appears to play a role (Murphy et al. 2009). In the LOFAR images and previous low-frequency studies (Kantharia et al. 2008), the radio emission extends beyond the optical disk towards the north for at least 10 kpc; this, together with the steep surface brightness gradient toward the south, is interpreted as a sign of interaction with the ICM while the galaxy is moving rapidly toward the cluster center.

VCC 345 (NGC 4261, 3C 270)

This bright Fanaroff-Riley type I radio galaxy sits at the center of a poor group located ~ 12 Mpc behind the Virgo cluster core in a structure known as the *W*-cloud (de Vaucouleurs 1961). It is well studied at radio wavelengths (Dunn et al. 2010; Kolokythas et al. 2015; Grossová et al. 2022) and shows clear signs of interaction between the AGN and the surrounding medium (O’Sullivan et al. 2011).

VCC 596 (NGC 4321, M 100)

M 100 is another grand-design spiral galaxy in the outskirts of the Virgo cluster. In the high-resolution LOFAR map, the supernova SN1979C (Urbanik et al. 1986) is visible in the southeast of the galaxy as a faint point source with a background-subtracted flux density of 3.9 ± 0.5 mJy. The galaxy does not show particularly asymmetric radio emission or other clear signs of perturbation, and is therefore currently unlikely to be undergoing significant ram-pressure stripping.

VCC 630 (NGC 4330)

The radio emission of this edge-on galaxy shows the presence of a tail in the southwest that is caused by ram-pressure stripping (Murphy et al. 2009; Vollmer et al. 2012) and also visible in the LOFAR maps. Tails in the same region are also present in atomic hydrogen (Chung et al. 2007, 2009) and H α (Fossati et al. 2018; Sardaneta et al. 2022).

VCC 664 (IC 3258)

To our knowledge, we detect this late-type spiral galaxy for the first time in the radio continuum. It is among the faintest Virgo cluster members at optical wavelengths in our catalog. The 3σ contours in the low-resolution map are elongated towards the west. The orientation of the tail opposite to the cluster center and the lack of any associated stellar component in the optical image suggest that the galaxy is suffering a ram-pressure stripping event. This could also explain the H I deficiency of the object (Köppen et al. 2018).

VCC 699 (IC 3268)

This galaxy is another Virgo star-forming dwarf galaxy from the Grossi et al. (2016) sample. The LOFAR detection is slightly offset from the optical image but is toward the projected center of the Virgo cluster. If real, this would imply an orbit moving away from the cluster center. In view of the relatively small mass and very high SFR, interpretation of the offset as a galactic outflow would be even more compelling.

VCC 763 (NGC 4374, M 84)

The radio galaxy M 84 is the second-brightest radio source in the central Virgo cluster after M 87 and is a well-studied example of AGN-feedback in noncentral galaxies (Finoguenov & Jones 2001; Bîrzan et al. 2004; Finoguenov et al. 2008; Laing et al. 2011; Bambic et al. 2023). The radio lobes/tails are deflected after 5 kpc, a clear sign of interaction with the ICM. They coincide with Chandra-detected X-ray cavities (Finoguenov & Jones 2001; Finoguenov et al. 2008; Bambic et al. 2023). In the 144 MHz LOFAR images, the source is not significantly more extended than at GHz frequencies.

VCC 836 (NGC 4388)

This object hosts a Seyfert 2-type nucleus and is the only spiral galaxy in the Virgo cluster where an AGN contributes a large fraction of the total radio emission. The subparsec nuclear jets are oriented perpendicular to the disk (Giroletti & Panessa 2009) and give rise to a biconical outflow (Damas-Segovia et al. 2016) that is barely resolved even in our high-resolution maps. Furthermore, the galaxy, which is believed to be post-core passage and moving to the southwest, is undergoing a ram-pressure stripping event (Murphy et al. 2009) that generates a spectacular H I tail (Oosterloo & van Gorkom 2005), which can also be partly traced in H α (Yoshida et al. 2002). In the LOFAR maps, this manifests as a strong intensity gradient on the leading side and an extension of the emission beyond the stellar component toward the trailing side of the galaxy. Still, Damas-Segovia et al. (2016) found that the leading-edge polarized outflow is able to resist the ram pressure.

VCC 865 (NGC 4396)

The presence of a tail in neutral hydrogen (Chung et al. 2007) is a sign of ram-pressure stripping also acting on this galaxy. However, a lack of compression in the H I contours (Chung et al. 2009) and a radio-to-infrared deficit (Murphy et al. 2009) on the leading edge make this interpretation somewhat uncertain. In the low-resolution LOFAR map, the radio emission shows a strong gradient toward the southeast, with a tail-like extension in the opposite direction, which favors the scenario that the galaxy is suffering from ram-pressure stripping while falling into the cluster center. Within the optical disk, the LOFAR images reveal enhanced radio emission in the leading half of the galaxy, coincident with a

blue region of current or recent star formation in the optical. This may be an example of ram-pressure-induced star-formation due to gas compression on the leading edge (e.g., Boselli et al. 2021; Roberts et al. 2022a)

VCC 873 (NGC 4402)

This edge-on spiral is located at a distance of ≈ 700 kpc from M 87 and shows a truncated radio profile to the southeast with an extension in the opposite direction (see also Murphy et al. 2009). Furthermore, signs of ram-pressure stripping are also visible in the H I and the dust components of the galaxy (Crowl et al. 2005). We speculate that in the LOFAR images, a low-surface-brightness patch to the northwest of the galaxy might constitute part of a radio continuum tail, which has not previously been observed.

VCC 881 (NGC 4406, M 86)

While close in projection, the massive elliptical galaxy and its surrounding group, which is extended in the X-rays (Böhringer et al. 1994), likely lie around 2 Mpc behind M 87 (Cantiello et al. 2018). M 86 is rapidly falling towards the cluster center from behind, as indicated by the blueshifted spectrum. The galaxy was first discovered in the radio continuum at 4.9 GHz as a faint point source in Dunn et al. (2010), and was recently also detected at 1.5 GHz by Grossová et al. (2022). These latter authors concluded that the radio emission could be dominated by star formation instead of nuclear activity; furthermore, no signs of X-ray cavities were observed.

VCC 1043 (NGC 4438)

NGC 4438 is a unique object in the Virgo cluster, which shows strong disruption of the stellar component. This was caused by a gravitational interaction with NGC 4435 and NGC 4406 (M 86), to which it is connected by filaments visible in H α emission (Kenney et al. 2008). NGC 4438 shows peculiar radio emission; a central point source corresponds to the LINER-type AGN (Decarli et al. 2007) and unresolved inner lobes (Hota et al. 2007), with an accompanying radio bubble to the west (Weżgowiec et al. 2007; Vollmer et al. 2009).

VCC 1226 (NGC 4472, M 49)

Being optically brighter than M 87, M 49 is the BCG of a southern subcluster falling into the Virgo core almost perpendicular to the line of sight (Mei et al. 2007). It lies at a projected distance of 1.3 Mpc ($1.3r_{\text{vir}}$) from the cluster center. At GHz frequencies, it hosts a slightly extended, double-lobed radio source of low power (e.g., Dunn et al. 2010). X-ray observations with the XMM-Newton and Chandra satellites (Kraft et al. 2011; Gendron-Marsolais et al. 2017; Su et al. 2019) revealed the presence of cavities in the thermal plasma, which have been excavated by the AGN. These inner cavities connect to X-ray filaments of ~ 30 kpc in length. These are thought to originate from a previous nuclear outbreak, which can only be revealed in the radio by deep, low-frequency observations. With our LOFAR survey, we report the discovery of radio tails that correspond to the X-ray features. The tails extend far beyond the X-ray cavities for a projected distance of 150 kpc ($\hat{=}0.52^\circ$) and are detected at a surface-brightness significance of $2 - 4\sigma$ even in the high-resolution image (panel a) of Fig. 2.7). Due to the ram pressure they experience from the Virgo ICM, they are bent southwards, giving rise to a wide-angle tail morphology. Follow-up studies of the spectral aging along the tails using 54 MHz

observations of LOFAR LBA will allow us to constrain both the duty cycle of the AGN and the infall-history of the M49 subcluster.

VCC 1316 (NGC 4486, M 87)

M 87 is the famous radio galaxy at the center of the Virgo cluster and is among the brightest radio sources on the sky. It consists of an inner pair of jets also visible in the X-ray and optical and forming a cocoon with an extension of ~ 6 kpc (see Fig. 2.3). This emission is embedded in a highly extended halo with a size of ~ 75 kpc, which contains the outer jets with a prominent smoking-gun morphology. The extended emission was studied in detail in Owen et al. (2000) at 300 MHz using the VLA, which for the past 20 years remained the highest quality published image of the large-scale structure of M 87. In the early commissioning stage of LOFAR, the source was studied from 20 to 160 MHz, although with limited resolution and image fidelity owing to the incompleteness of the instrument and the lack of sophisticated calibration strategies (de Gasperin et al. 2012). A high-fidelity LOFAR LBA image is provided in de Gasperin et al. (2020). M 87 and the filaments permeating the extended halo of the source will be the subject of a dedicated multifrequency study combining our LOFAR data with unpublished VLA and MeerKAT observations (de Gasperin et al. in prep.).

VCC 1401 (NGC 4501, M 88)

The radio map Fig. 2.7 b) of this bright, highly inclined spiral galaxy shows significant asymmetry with a strong gradient toward the southwest. This asymmetry is caused by the ram-pressure stripping the galaxy experiences during the infall onto the central Virgo cluster. In our LOFAR 144 MHz image, the radio emission in the northeast extends further from the optical disk than at 1.4 GHz (Vollmer et al. 2010), which is in agreement with the greater age of the advected cosmic-ray electrons.

VCC 1450 (IC 3476)

Boselli et al. (2021) reported the presence of ionized gas tails for VCC 1450 caused by a recent onset of ram-pressure stripping. This is in agreement with the LOFAR images, where a strong gradient on the leading (eastern) side and a tail on the trailing side are visible. To the best of our knowledge, this is the first time this tail is reported in the radio continuum.

VCC 1516 (NGC 4522)

This galaxy is observed at high inclination and shows strongly asymmetric radio emission with a tail toward the northwest (Vollmer et al. 2004; Murphy et al. 2009). It is undergoing active ram-pressure stripping and also shows extraplanar and UV emission (Kenney & Koopmann 1999; Kenney et al. 2004; Vollmer et al. 2012).

VCC 1532 (IC 800)

The LOFAR maps of VCC 1532 reveal a gradient of radio emission at the edge of the galaxy facing the cluster center, and a tail in the opposite direction. To the best of our knowledge, the galaxy has not previously been reported to show signs of ram-pressure stripping. We therefore note it as a new candidate for ongoing ram-pressure stripping.

VCC 1575 (IC 3521)

This is another Virgo star-forming dwarf galaxy from the Grossi et al. (2016) sample. The LOFAR emission appears to extend beyond the optical image of the galaxy, which implies a galactic outflow, consistent with the high SFR of this low-mass galaxy.

VCC 1632 (NGC 4552, M 89)

M 89 hosts a nuclear point source surrounded by two lobes reminiscent of ears, each of 5 kpc in extent. Those ears correspond to X-ray cavities revealed by Chandra studies (Machacek et al. 2006; Allen et al. 2006; Kraft et al. 2017).

VCC 1686 (IC 3583)

VCC 1686 has a projected location very close to VCC 1690, but both galaxies differ by more than 1300 km s^{-1} in radial velocity, making a tidal interaction between the two galaxies very unlikely. Still, there is a spur of LOFAR emission in the south of VCC 1686 pointing toward VCC 1690. This feature also has a counterpart in at least two independent $H\alpha$ maps of VCC 1686. The origin of the $H\alpha$ feature is unclear, but the radio emission is more extended than the optical image of the galaxies over the whole quadrant, and so this may be a large-scale outflow. This would be consistent with the high SFR of this dwarf galaxy. We note that the two relatively bright radio sources are likely background and not physically connected to VCC 1686. VCC 1686 also belongs to the Grossi et al. (2016) sample.

VCC 1690 (NGC 4569, M 90)

M 90 is one of the brightest spiral galaxies in the Virgo cluster. As traced by tails of ionized gas to the east (Boselli et al. 2016), it is currently undergoing a ram-pressure stripping event. Observations in the radio continuum revealed symmetric bubbles extending up to 24 kpc perpendicular to the disk (Chyzy et al. 2006). Our LOFAR map detects both radio lobes and the southwestern ridge of the emission connected to the star-forming disk. The southwestern ridge likely results from gas and magnetic field compression by the ambient ICM. As M 90 does not show signs of strong nuclear activity, it was concluded that the lobes are likely powered by a nuclear starburst event. A detailed analysis of the stellar emission in the innermost region by Gabel & Bruhweiler (2002) using spectral synthesis led the authors to propose an age for the starburst of 5 – 6 Myr and 5×10^4 O and B stars, which would be sufficient to create a large-scale outflow or wind.

VCC 1727 (NGC 4579, M 58)

The massive barred spiral galaxy M 58 hosts a Seyfert 2-type low-luminosity AGN (Contini 2004). Despite its significant $H\text{I}$ deficiency, it was found to have the radio properties of a normal star-forming galaxy by Vollmer et al. (2013), even after subtracting the AGN contribution. In the LOFAR images, a central point source can be observed, with swirling features extending over 5 kpc; as their direction is counterclockwise, opposite to the spiral arms, they most likely correspond to the AGN jets. The central structure is embedded in low-surface brightness emission covering a region that is similar in size to the optical disk that traces the star formation activity.

VCC 1791 (IC 3617)

VCC 1791 also belongs to the Grossi et al. (2016) sample. It has a relatively high SFR (but lower than that of VCC 1686) but also a relatively low mass. Therefore, the extent of the radio emission beyond the optical body of the galaxy is suggestive of an outflow. The brightest peak of the radio emission coincides with three very blue compact knots.

VCC 1932 (NGC 4634)

The low-resolution LOFAR map of this edge-on spiral galaxy, which forms a close pair with NGC 4633, shows extra-planar radio emission to the west, which could be interpreted as a radio tail. In the same direction, a star forming object can be seen that was likely created from material stripped (or tidally ejected) from VCC 1932 (Stein et al. 2018). However, the galaxy is not known to show a tail at any other wavelength, and therefore interpretation of the radio morphology remains somewhat difficult.

VCC 1972 (NGC 4647)

The spiral galaxy VCC 1972 lies close to M 60 in an eastern subcluster of Virgo. The radio surface brightness and the molecular gas distribution (Young et al. 2006) of this galaxy are asymmetric, which is likely due to ram pressure exerted by the ICM around M 60 and/or a disturbance of the gravitational well.

VCC 1978 (NGC 4649, M 60)

This giant elliptical galaxy is the most massive galaxy in the Virgo cluster and dominates a small, X-ray-bright subcluster (Böhringer et al. 1994). Deep Chandra and VLA observations revealed the presence of X-ray cavities coincident with the radio jets of the central AGN (Shurkin et al. 2007; Dunn et al. 2010; Paggi et al. 2014; Grossová et al. 2022), placing it among the Virgo galaxies that are prime examples of AGN feedback in noncentral galaxies. In the 144 MHz LOFAR images, the inner radio source of 5 kpc in extension, which is also visible at GHz frequencies, is embedded in an area of low-surface brightness diffuse emission of 75 kpc in size.

2.4.2 Extended emission

For the following discussion of emission on large angular scales, it must be considered that radio interferometers have a reduced sensitivity to features beyond a certain extent; for LOFAR, the flux density loss at a scale of 18' is around 20% (Bruno et al. 2023), and more extended sources will be attenuated more drastically. Fig. 2.11 shows the very low-resolution source-subtracted mosaic that is sensitive to large-scale diffuse radio emission in the Virgo cluster environment. Among the most prominent large-scale features are at least four sets of diagonal stripes that extend from the northeast toward the southwest and are marked by black dashed lines. Given their location and orientation, they are certainly associated with the North Polar Spur (Loop I), a Galactic spherical structure which is thought to either be local ($d \sim 100$ pc Salter 1983) or originating from the Galactic center, as indicated by studies of the coincident X-ray emission (see also Fig. 2.1, Sofue 2000; Predehl et al. 2020). Further large-scale emission with an extent of $\approx 1^\circ$ is marked in Fig. 2.11 by two dashed ellipses. The emission in the SW follows a similar orientation to the tails of M 49, which might indicate that it is part of those. However, the emission does not show a clear connection to M 49. Furthermore, if the emission were indeed due to a tail of this giant elliptical galaxy, it would follow a

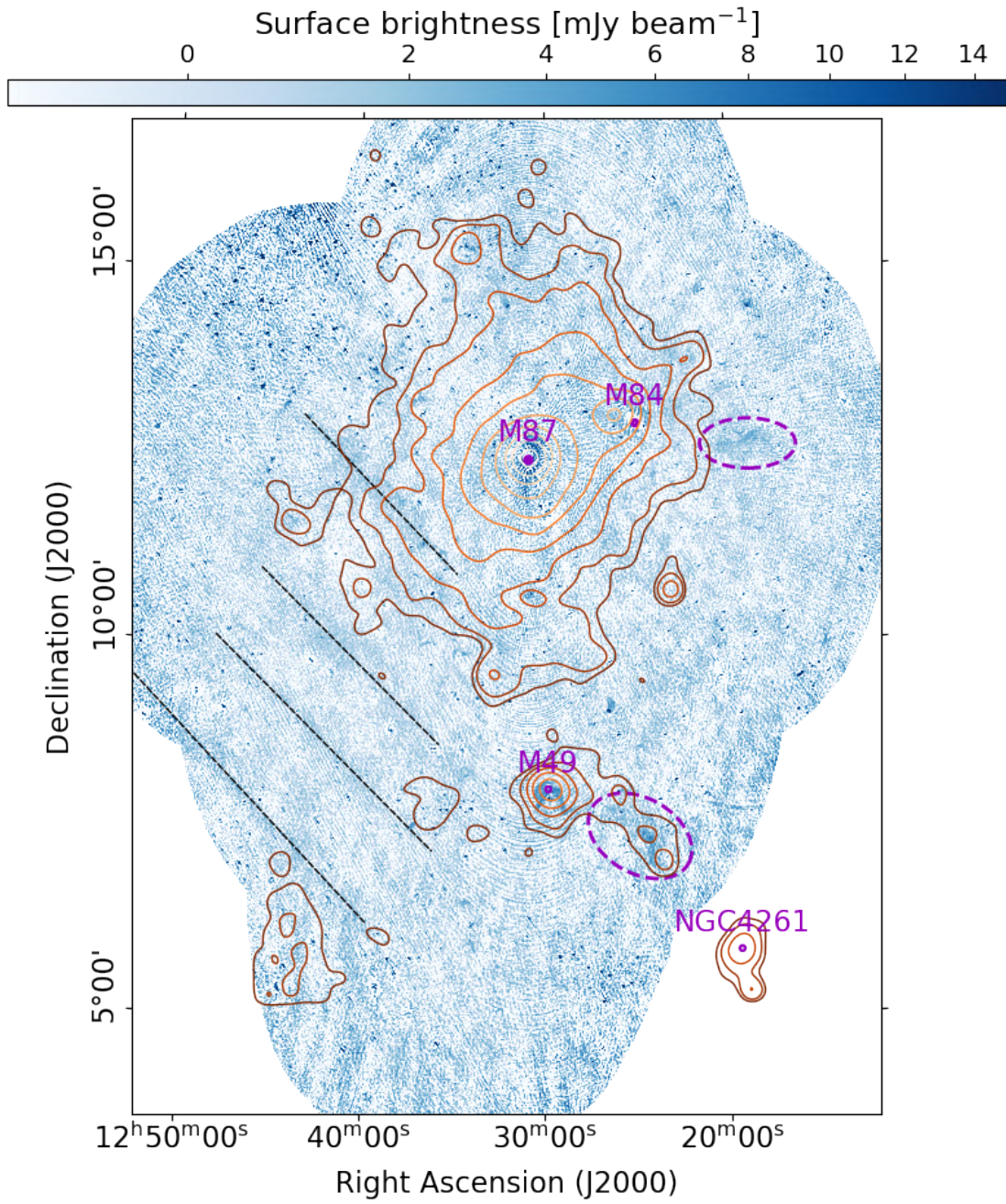


Figure 2.11: Compact source-subtracted mosaic at 1' resolution. Due to the poor quality of the very low-resolution images, field 1 and 8 are excluded. Black dashed lines correspond to large-scale Galactic emission of the North Polar Spur (NPS), purple circles mark the position of the giant elliptical galaxies M 49 (NGC 4472), M 84 (NGC 4374), and M 87 (NGC 4486). The dashed purple ellipses highlight candidate extragalactic emission, which could be related to the wider Virgo environment, and orange contours mark the eROSITA compact source-subtracted X-ray surface brightness (McCall et al. in prep.).

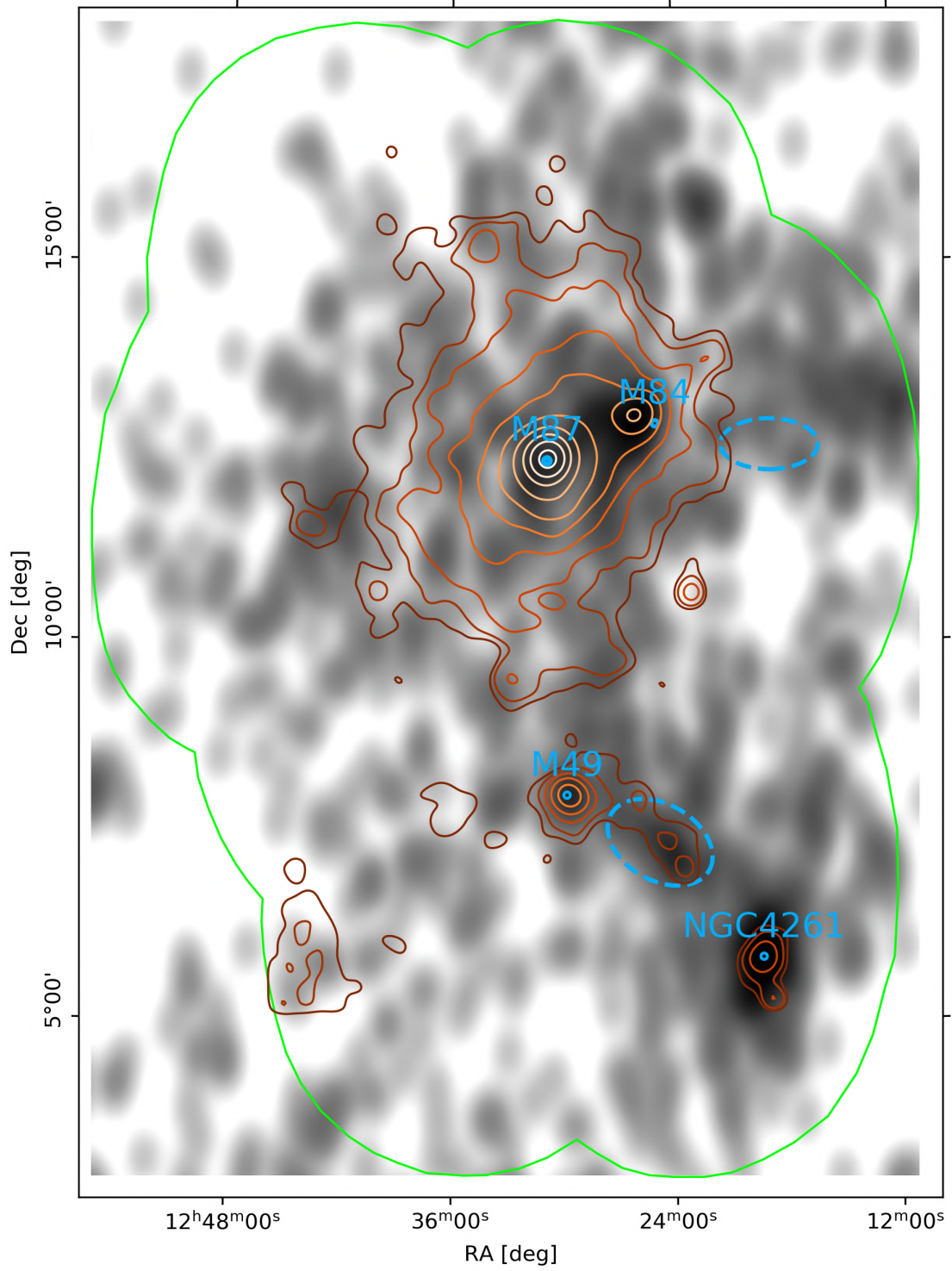


Figure 2.12: Projected galaxy density of the EVCC. Orange contours show the eROSITA source-subtracted X-ray surface brightness (McCall et al. in prep.), the green contour outlines the footprint of the LOFAR observations, and the blue circles and dotted ellipses mark individual galaxies and the extended emission as in Fig. 2.11.

highly unexpected surface brightness trend with a complete fainting and a subsequent rebrightening. While this is not fully unheard of for cluster radio galaxies (de Gasperin 2017; Cuciti et al. 2018; Edler et al. 2022), it is a rare phenomenon. Thus, we consider it unlikely that the southwestern extended feature is causally connected to the AGN in M 49. However, we note that directly coincident with the radio emission is the W' cloud (de Vaucouleurs 1961), a group of galaxies ~ 5.5 Mpc behind M 49 and located in a filament connecting the cluster to the background W cloud (Binggeli et al. 1993; Mei et al. 2007). In Fig. 2.12, we show that the elongated structure of the filament is apparent both in the galaxy density distribution and the eROSITA (McCall et al. in prep.) X-ray surface brightness distribution and has a similar morphology and location to the radio emission. The displayed galaxy density was obtained from the EVCC by smoothing the galaxy distribution with a Gaussian kernel of $\sigma = 14'$ in width. These aspects combined suggest that the emission originates from phenomena related to the ICM or intragroup medium, that is, either turbulent reacceleration processes or accretion shocks. This could explain the similar morphology of the X-ray and radio signals. An alternative explanation is that the radio emission traces a past phase of nuclear activity of a galaxy in the group, such as the dominant elliptical NGC 4365. However, at present, NGC 4365 is not associated with a compact radio source. The only radio-detected galaxy nearby is NGC 4370, although there is no clear connection to the diffuse emission. The extended radio source coincident with the W' group or filament will be the subject of a forthcoming multifrequency follow-up study. The second extended and elongated feature in the northeast is of similar size, but does not directly coincide with an overdensity of galaxies in the EVCC or with an increase in surface brightness in the ROSAT (Böhringer et al. 1994) or eROSITA (McCall et al. in prep.) X-ray images. However, it is located between the Virgo core and the M cloud of galaxies, which is another concentration of galaxies in the wider Virgo environment (de Vaucouleurs 1961; Mei et al. 2007).

The three small circles in Fig. 2.11 mark the location of extended emission possibly associated with giant elliptical galaxies in the cluster. The extended tails of M 49 are discussed in Sect. 2.4.1. Around M 87, there is extended emission on a scale of $\sim 1^\circ$ (four times larger than M 87). Given the cool-core nature of the Virgo cluster and the 200 – 300 kpc extent of the candidate diffuse emission, a tentative possibility is that this emission is caused by a radio mini-halo (Gitti et al. 2004; Giacintucci et al. 2017, 2019; van Weeren et al. 2019) caused by the sloshing of gas in the Virgo core (Gatzuz et al. 2018). However, due to the presence of strong systematic uncertainties directly next to M 87, we cannot conclude with certainty that the emission is physical. Around the bright (21 Jy) radio galaxy M 84, a circular halo of emission with an embedded negative hole is most likely a calibration or imaging artifact.

2.5 Summary

In this work, we present the LOFAR HBA Virgo cluster survey, which is the first data release of the ViCTORIA project and represents the deepest wide-field radio survey of the Virgo cluster field published to date. This advance was made possible by the general progress in low-frequency radio calibration techniques and the development of a specifically tailored subtraction procedure introduced in this work, which mitigates dynamic range limitations due to the extremely bright source M 87. Within the virial radius of the cluster, where we have increased exposure time and pointing overlap, we reach a median noise level of $140 \mu\text{Jy beam}^{-1}$ at a resolution of $9'' \times 5''$, while across the full survey area, the median noise is twice as high. We use this data to create a catalog of the radio properties of 112 LOFAR-detected certain and possible Virgo cluster galaxies ($v_{\text{rad}} < 3000 \text{ km s}^{-1}$). The detected objects include at least 18 cases of galaxies exhibiting a radio morphology indicative

2 *ViCTORIA project: The LOFAR HBA Virgo Cluster Survey*

of ongoing ram-pressure stripping. Of those, we report VCC 664 (IC 3258), VCC 1532 (IC 800), and VCC 1932 (NGC 4632) as new ram-pressure-stripping candidates. Further, for the giant elliptical galaxy VCC 1226 (NGC 4472, M 49), we reveal the presence of old radio tails of $0.5^\circ/150$ kpc in extent. Due to the interaction with the ICM, the tails are bent toward the south and assume a wide-angle tail morphology. The image cutouts, the catalog of the Virgo galaxies, and the full mosaics are made available online⁶.

We also investigated the presence of large-scale diffuse emission in the Virgo cluster. While no radio emission attributable to the radio halo or radio relic phenomena is found, we detect extended emission coincident with the W' group in a filament between Virgo and the background W cloud. The scale of this feature is ≈ 1 deg and emission with a similar extent and orientation is also present in the eROSITA/SRG X-ray map of the cluster. We therefore speculate that this radio emission may be caused by accretion processes due to shocks or turbulence.

This work is the first part of ViCTORIA, a project designed to drastically improve the multi-frequency radio coverage of the Virgo cluster. Further planned radio surveys are being conducted at 54 MHz with the LOFAR low-band antenna system as well as in the L-band using MeerKAT, including the 21 cm line. In a forthcoming work of the ViCTORIA project, we will use the LOFAR data presented here to analyze the impact of the cluster environment on the evolution of star-forming galaxies in Virgo. Further, we will employ the multifrequency data provided by ViCTORIA for detailed spectral studies of the interacting radio tail we unveil for VCC 1226 and the extended emission coincident with the W' filament.

Acknowledgements

HE acknowledges support by the Deutsche Forschungsgemeinschaft (DFG, German Research Foundation) under project number 427771150. MB acknowledges support from the Deutsche Forschungsgemeinschaft under Germany's Excellence Strategy - EXC 2121 "Quantum Universe" - 390833306. AI acknowledges financial support from the European Research Council (ERC) programme (grant agreement No. 833824). DJB acknowledges funding from the German Science Foundation DFG, via the Collaborative Research Center SFB1491 'Cosmic Interacting Matters - From Source to Signal'. AI acknowledges the INAF founding program 'Ricerca Fondamentale 2022' (PI A. Iagnesi). RJvW acknowledges support from the ERC Starting Grant ClusterWeb 804208. E.B. acknowledges financial support from the European Research Council (ERC) Consolidator Grant under the European Union's Horizon 2020 research and innovation programme (grant agreement CoG DarkQuest No 101002585). LOFAR is the Low Frequency Array designed and constructed by ASTRON. It has observing, data processing, and data storage facilities in several countries, which are owned by various parties (each with their own funding sources), and which are collectively operated by the ILT foundation under a joint scientific policy. The ILT resources have benefited from the following recent major funding sources: CNRS-INSU, Observatoire de Paris and Université d'Orléans, France; BMBF, MIWF-NRW, MPG, Germany; Science Foundation Ireland (SFI), Department of Business, Enterprise and Innovation (DBEI), Ireland; NWO, The Netherlands; The Science and Technology Facilities Council, UK; Ministry of Science and Higher Education, Poland; The Istituto Nazionale di Astrofisica (INAF), Italy. This research made use of the Dutch national e-infrastructure with support of the SURF Cooperative (e-infra 180169) and NWO (grant 2019.056). The Jülich LOFAR Long Term Archive and the German LOFAR network are both coordinated and operated by the Jülich Supercomputing Centre (JSC), and computing resources on the supercomputer JUWELS at JSC were provided by the Gauss Centre for Supercomputing e.V. (grant CHTB00) through the John von Neumann Institute for Computing (NIC). This research made use of the University of Hertfordshire high-performance computing facility and the LOFAR-UK computing facility located at the University of Hertfordshire and supported by STFC [ST/P000096/1], and of the Italian LOFAR IT computing infrastructure supported and operated by INAF, and by the Physics Department of Turin

⁶https://lofar-surveys.org/virgo_survey.html

2.5 Summary

university (under an agreement with Consorzio Interuniversitario per la Fisica Spaziale) at the C3S Supercomputing Centre, Italy. The data are published via the SURF Data Repository service which is supported by the EU funded DICE project (H2020-INFRAEOSC-2018-2020 under Grant Agreement no. 101017207). This work is based on data from eROSITA, the soft X-ray instrument aboard SRG, a joint Russian-German science mission supported by the Russian Space Agency (Roskosmos), in the interests of the Russian Academy of Sciences represented by its Space Research Institute (IKI), and the Deutsches Zentrum für Luft und Raumfahrt (DLR). The SRG spacecraft was built by Lavochkin Association (NPOL) and its subcontractors and is operated by NPOL with support from the Max Planck Institute for Extraterrestrial Physics (MPE). The development and construction of the eROSITA X-ray instrument was led by MPE, with contributions from the Dr. Karl Remeis Observatory Bamberg & ECAP (FAU Erlangen-Nuernberg), the University of Hamburg Observatory, the Leibniz Institute for Astrophysics Potsdam (AIP), and the Institute for Astronomy and Astrophysics of the University of Tübingen, with the support of DLR and the Max Planck Society. The Argelander Institute for Astronomy of the University of Bonn and the Ludwig Maximilians Universität Munich also participated in the science preparation for eROSITA. The eROSITA data shown here were processed using the eSASS software system developed by the German eROSITA consortium.

Table 2.3: LOFAR catalog of Virgo cluster galaxies.

VCC	NGC	IC	RA J2000 [h:m:s]	Dec J2000 [°:′:″]	Type	m_r [mag]	S [Jy]	A [″×″]	d [Mpc]	L_{144} [W Hz ⁻¹]
(1)	(2)	(3)	(4)	(5)	(6)	(7)	(8)	(9)	(10)	(11)
49	4168		12:12:17.2	+13:12:19	E	11.00	(2.5±0.5)e-2	4291	32.0	(3.1±0.7)e+21
66	4178	3042	12:12:46.1	+10:51:55	SbC	11.24	(5.6±1.2)e-2	14149	16.5	(1.8±0.4)e+21
73	4180		12:13:03.0	+07:02:20	Sb	12.23	(1.6±0.3)e-1	7735	32.0	(2.0±0.4)e+22
89	4189	3050	12:13:47.4	+13:25:34	SbC	11.51	(9.0±1.8)e-2	17831	32.0	(1.1±0.2)e+22
120	4197		12:14:38.6	+05:48:23	Sc	12.65	(7.1±1.5)e-2	8902	32.0	(8.7±1.8)e+21

Notes. This table is available in its entirety at the CDS and contains the following information. The first three columns list the index of the galaxies in the VCC, NGC, and IC. Columns 4-7 list the optical coordinates, the morphological classification, and the r -band magnitude of the galaxies as in Kim et al. (2014). Column 8 shows the integrated flux density as measured from the 20″-resolution mosaics, column 9 quotes the source area, column 10 the distance, and column 11 the 144 MHz radio luminosity.

Table 2.4: LOFAR catalog of VCC galaxies in the background of the Virgo cluster.

VCC	NGC	IC	RA J2000 [h:m:s]	Dec J2000 [°:':"]	Type	m_r [mag]	S [Jy]	A ["x'"]	d [Mpc]	L_{144} [W Hz ⁻¹]
(1)	(2)	(3)	(4)	(5)	(6)	(7)	(8)	(9)	(10)	(11)
76		3046	12:13:07.8	+12:55:05	Sc(s)I	14.16	(1.3±0.3)e-2	3420	119	(2.2±0.5)e+22
121			12:14:42.5	+12:59:24	E7/S017	14.87	(3.5±1.1)e-3	1463	267	(3.0±0.9)e+22
123			12:14:45.7	+13:19:35	Sa	14.57	(7.1±1.6)e-3	1346	306	(8.0±1.8)e+22
129		3060	12:15:02.0	+12:32:49	Sab	14.39	(4.9±1.5)e-3	2544	86	(4.3±1.3)e+21
134		3062	12:15:05.3	+13:35:42	ScI	14.00	(4.2±1.3)e-3	1852	116	(6.8±2.1)e+21

Notes. This table is available in its entirety at the CDS and contains the following information. The first, second, and third column list the indices of the galaxies in the VCC, NGC, and IC. The fourth to seventh columns list the optical coordinates, the morphological classification, and the r -band magnitude of the galaxies as reported in Binggeli et al. (1985). Column 8 shows the integrated flux density as measured from the low-resolution mosaics. Column 9 quotes the source area, column 10 the radial-velocity-inferred distance, and column 11 the resulting radio luminosity.

2 ViCTORIA project: The LOFAR HBA Virgo Cluster Survey

3 ViCTORIA project: The LOFAR view of environmental effects in the Virgo Cluster

H. W. Edler, I. D. Roberts, A. Boselli, F. de Gasperin, V. Heesen, M. Brüggen, A. Ignesti, L. Gajović.
Submitted to A&A, arXiv:2311.01904

Abstract

Context. Environmental effects such as ram-pressure stripping (RPS) shape the evolution of galaxies in dense regions.

Aims. We use the nearby Virgo cluster as a laboratory to study environmental effects on the non-thermal components of star-forming galaxies.

Methods. We constructed a sample of 17 RPS galaxies in the Virgo cluster and a statistical control sample of 119 nearby galaxies from the Herschel Reference Survey. All objects in these samples are detected in LOFAR 144 MHz observations and come with H α and/or far-UV star formation rate (SFR) estimates.

Results. We derived the radio-SFR relations, confirming a clearly super-linear slope of ≈ 1.4 . We found that Virgo cluster RPS galaxies have radio luminosities that are a factor of 2-3 larger than galaxies in our control sample. We also investigated the total mass-spectral index relation, where we found a relation for the Virgo cluster RPS galaxies that is shifted to steeper spectral index values by 0.17 ± 0.06 . Analyzing the spatially resolved ratio between the observed and the expected radio emission based on the hybrid near-UV + 100 μm SFR surface density, we generally observe excess radio emission all across the disk with the exception of a few leading-edge radio-deficient regions.

Conclusion. The radio excess and the spectral steepening for the RPS sample could be explained by an increased magnetic field strength if the disk-wide radio enhancement is due to projection effects. For the galaxies that show the strongest radio excesses (NGC 4330, NGC 4396, NGC 4522), a rapid decline of the SFR ($t_{\text{quench}} \leq 100$ Myr) could be an alternative explanation. We disfavor shock acceleration of electrons as cause for the radio excess since it cannot easily explain the spectral steepening and radio morphology.

3.1 Introduction

Galaxies that inhabit dense environments such as galaxy clusters show a lower cold gas content (e.g. Catinella et al. 2013; Boselli et al. 2014b) and a reduced star-forming (SF) activity (e.g. Kennicutt 1983; Boselli et al. 2014; Boselli et al. 2016) compared to those located in poorer environments.

3 Environmental effects in the Virgo Cluster

It is thought that those differences are caused by environmental processes, i.e. perturbations due to interactions with other galaxies or the intra-cluster medium (ICM). The process which is often thought to be the dominant perturbation affecting galaxies in massive ($>10^{14} M_{\odot}$), low-redshift clusters is ram-pressure stripping (RPS; see Cortese et al. 2021; Boselli et al. 2022, for recent reviews). RPS is the removal of the interstellar medium (ISM) of a galaxy moving at high velocity v relative to the ICM. The ram-pressure scales as $P \propto \rho v^2$ where ρ is the ICM density. Consequently, it is most effective in massive clusters where the galaxy velocities and the ICM densities are high.

RPS impacts the diffuse atomic phase of the ISM due to the advection of the loosely bound neutral hydrogen (H I) which can give rise to tails that can be traced by 21 cm line observations (e.g. Chung et al. 2007). This can also explain the truncated radial H I-profiles (e.g. Chung et al. 2009) and the statistical H I-deficiency (e.g. Boselli & Gavazzi 2006) of galaxies in clusters. Subsequent ionization of the stripped H I due to interactions with the ICM creates tails of ionized gas that are most commonly observed in the H α line (e.g. Gavazzi et al. 2001; Yagi et al. 2010; Boselli et al. 2016); as those recently observed during the GAs Stripping Phenomena in galaxies with MUSE (GASP; Poggianti et al. 2017) program and the Virgo Environmental Survey Tracing Ionised Gas Emission (VESTIGE; Boselli et al. 2018b). In some cases, RPS may also affect the dense molecular gas, which is fueling star formation, either indirectly by displacing the atomic gas or directly by displacing the molecular gas from the stellar disk (e.g. Cramer et al. 2020; Watts et al. 2023); this will in turn reduce the star formation rate (SFR). The time-scale on which the star formation is quenched may depend on a number of parameters such as galaxy mass, orientation and velocity with respect to the ICM as well as the ICM density and dynamical state. Observational evidence points to quenching times of ≤ 1 Gyr (e.g. Boselli et al. 2006, 2016; Ciesla et al. 2016; Fossati et al. 2018).

Current RPS events in star-forming galaxies show tails in the atomic or ionized hydrogen distribution, as well as in the radio continuum (e.g. Gavazzi 1978; Gavazzi et al. 1995). The radio continuum emission of star-forming galaxies is caused by cosmic-ray electrons (CRe) that were shock-accelerated in supernovae gyrating in weak magnetic fields (i.e. synchrotron radiation). Thus, it is a tracer of the SFR (Condon 1992; Gürkan et al. 2018; Heesen et al. 2019; Heesen et al. 2022). The CRe are transported by diffusion processes in the galactic magnetic fields, but may also be subject to advection through ram pressure, creating asymmetric or tailed radio continuum profiles. The advance of sensitive radio surveys, such as those undertaken with the LOw-Frequency ARray (LOFAR; van Haarlem et al. 2013), allowed the identification of >100 ongoing RPS events in the past few years (Roberts et al. 2021a,b; Roberts et al. 2022b; Ignesti et al. 2022b; Ignesti et al. 2023; Edler et al. 2023a).

Observations in the radio continuum are well suited to identify RPS events and trace galaxy SFR. They also allow us to probe the non-thermal phase of the ISM, i.e. the CRe and the magnetic fields via their synchrotron emission. The radio emission of RPS galaxies often appears to be in excess of what is expected given their SFR inferred from observations at other wavelengths (e.g. Gavazzi et al. 1991; Murphy et al. 2009; Vollmer et al. 2010; Chen et al. 2020; Ignesti et al. 2022c,b). Several explanations for the radio-excess of cluster SF-galaxies have been discussed in the literature: Gavazzi & Boselli (1999) proposed that the ram-pressure leads to a compression of the magnetic field and consequentially, increased synchrotron luminosity. Völk & Xu (1994) and Murphy et al. (2009) favored a scenario where the higher radio luminosity is not simply caused by compression, but instead due to shocks driven into the ISM by collisions with fragments of cold gas present in the ICM. Diffusive shock acceleration can then accelerate CRe in the ISM, which should result in a flatter radio spectral index. A third explanation of the radio-excess was brought up more recently in Ignesti et al. (2022b) and Ignesti et al. (2022c) based on the analysis of so-called jellyfish galaxies which are the most extreme examples of galaxies undergoing strong RPS events. The strong radio-

excess compared to the H α -emission was interpreted as the consequence of a rapid quenching of the star-forming activity due to RPS. While the H α -emission is a nearly instantaneous SF-tracer, with a typical delay of only a few Myr, the radio-emitting CRe have a typical lifetime > 100 Myr. Thus, if the star formation is quenched on time-scales shorter than the CRe lifetime, we will observe an apparent excess of radio emission simply due to the different time-scales probed by H α and the radio observations. As a consequence, the spectral index of those objects should be rather steep owing to spectral aging.

This work is part of the Virgo Cluster multi-Telescope Observations in Radio of Interacting galaxies and AGN (ViCTORIA) project, a broadband radio imaging campaign of the Virgo cluster (de Gasperin et al. in prep.). In Edler et al. (2023a), we recently published a 144 MHz survey of the Virgo cluster region using the LOFAR high-band antenna system as first data release of ViCTORIA. The survey led to the radio detection of 112 cluster members, with 19 objects that show signs of RPS in their radio morphology. We will use this data set to study the RPS phenomenon in the Virgo cluster.

In this work, we assume a flat Λ CDM cosmology with $\Omega_m = 0.3$ and $H_0 = 70 \text{ km s}^{-1} \text{ Mpc}^{-1}$. At the distance of M 87, for which we adopt a value of 16.5 Mpc (Mei et al. 2007; Cantiello et al. 2018), one arcsecond corresponds to 80 pc. This paper is arranged as follows: In Sect. 3.2, we report the data used for this work and our samples. In Sect. 3.3, we present a statistical study of the radio and star-forming properties and in Sect. 3.4, we carry out a spatially resolved analysis of the LOFAR maps. Finally, our conclusions are outlined in Sect. 3.6.

3.2 Data and sample

This paper builds primarily on the LOFAR HBA Virgo Cluster Survey (Edler et al. 2023a) published as part of the ViCTORIA-project. This 144 MHz-survey covers a 132 deg^2 field around the Virgo cluster and is to date the deepest blind radio continuum survey of this particular region.

3.2.1 RPS sample

For our LOFAR-study of star-forming galaxies in the Virgo cluster, we composed a sample of objects detected in Edler et al. (2023a) that show signs of RPS in the radio-continuum. As criteria, we require an asymmetric radio morphology in combination with an undisturbed optical appearance. The latter is to exclude cases where the dominant perturbing mechanism is tidal interaction. If the available literature clearly shows that an object suffers both from tidal interactions and RPS, we include it in our sample. This is the case for NGC 4254 (Vollmer et al. 2005), NGC 4438 (Vollmer et al. 2005) and NGC 4654 (Vollmer 2003). The Virgo cluster has been the target of several multi-frequency surveys and dedicated studies of individual objects. Out of the 19 galaxies with evident tails in radio continuum, 15 were already identified as suffering a RPS event in these detailed studies, as summarized in Boselli et al. (2022). They show tails of stripped atomic or ionized gas, have truncated gaseous and star-forming discs, and have been identified as suffering a RPS event from tuned models and hydrodynamic simulations. Four of the objects are for the first time reported to be RPS candidates based on our LOFAR data: IC 800 shows a radio tail to the northeast, in agreement with being on a radial orbit towards the cluster center, and is strongly H I deficient. IC 3258 is a dwarf galaxy with a radio tail that is also in agreement with a highly radial orbit. NGC 4607 shows a mild asymmetry with an extension of the radio contours towards the northeast and a strong gradient in the opposite direction, it is also highly deficient in neutral hydrogen. Lastly, NGC 4634 shows a radio tail towards the west and is slightly deficient in H I, a star-forming object is coincident with the radio tail (Stein et al. 2018).

3 Environmental effects in the Virgo Cluster

Table 3.1: LOFAR sample of ram-pressure stripped galaxies in the Virgo cluster.

VCC	NGC	IC	Morphology	$\log M_*$ [$\log M_\odot$]	H I-def.	$\Delta v_{\text{rad}, M87}$ [km/s]	Literature	Comment
(1)	(2)	(3)	(4)	(5)	(6)	(7)	(8)	(9)
241		3105	SW tail	7.89	0.41	-1439	B22	new radio tail, H α tail
307	4254		N tail	10.39	0.06	1124	V05, H07, V12b, B18a, M09	RPS + tidal interaction
497	4302		light N tail	10.44	0.50	-153	C07, V13, W12	new radio tail, H I tail
630	4330		S tail	9.52	0.92	321	C07, M09, V12a, V12b, V13, F18	H I tail, H α tail
664		3258	W tail	8.20	0.57	-1713		new candidate
865	4396		NW tail	9.25	0.20	-1398	C07, V07, V10, M09	H I tail
873	4402		NW tail	10.04	0.83	-1049	CR05, V07, M09, V10, V12b	H I tail, stripped dust
979	4424		small S tail	10.17	0.98	-842	C07, V13, B18b	H I tail, H α tail/outflow, radio deficient
1401	4501		NE tail	10.98	0.58	999	W07, V07, V10, V12b	new radio tail, H α tail
1450		3476	long W tail	9.02	0.66	-1112	B21	M87 side-lobes
1516	4522		long NW tail	9.38	0.68	1037	V04, M09, V12b	new candidate
1532		800	NE tail	9.07	1.00	1051		old stripping event
1615	4548		N-S asymmetry	10.74	0.94	-802	V99, W07	H α tail
1690	4569		SW tail, outflows	10.66	1.05	-1503	M09, V12b, B16	new candidate
1868	4607		asymmetry	9.60	1.20	973		new candidate, star-forming
1932	4634		SW tail	9.57	0.45	-1163	S18	object in the tail (S18)
1987	4654		asymmetry	10.14	-0.05	-240	V03, V07, C07, W07, V10	H I tail, RPS and tidal interaction

Notes. Columns 1 to 3 list the identifiers of the galaxies in the VCC, NGC and IC. Column 4 comments on the LOFAR morphology of the sources and columns 5 to 7 show the stellar mass (from Boselli et al. 2015), H I-deficiency (from Boselli et al. 2014a and Köppen et al. 2018) and the radial velocity relative to M87, taken from HyperLeda^a). In columns 8 and 9, we list the relevant literature and additional comments.

References. V99 – Vollmer et al. (1999); – Vollmer (2003); Vollmer et al. (2004) – V04; CR05 – Crowl et al. (2005); V05 – Vollmer et al. (2005); C07 – Chung et al. (2007); H07 – Haynes et al. (2007); W07 – Weżgowiec et al. (2007); V07 – Vollmer et al. (2007); M09 – Murphy et al. (2009); V10 – Vollmer et al. (2010), V12a – Vollmer et al. (2012); V12b – Vollmer et al. (2012), W12 – Weżgowiec et al. (2012); V13 – Vollmer et al. (2013); B16 – Boselli et al. (2016); B18a – Boselli et al. (2018a); B18b – Boselli et al. (2018); S18 – Stein et al. (2018); B21 – Boselli et al. (2021); B22 – Boselli et al. (2022).

^a<https://leda.univ-lyon1.fr/>

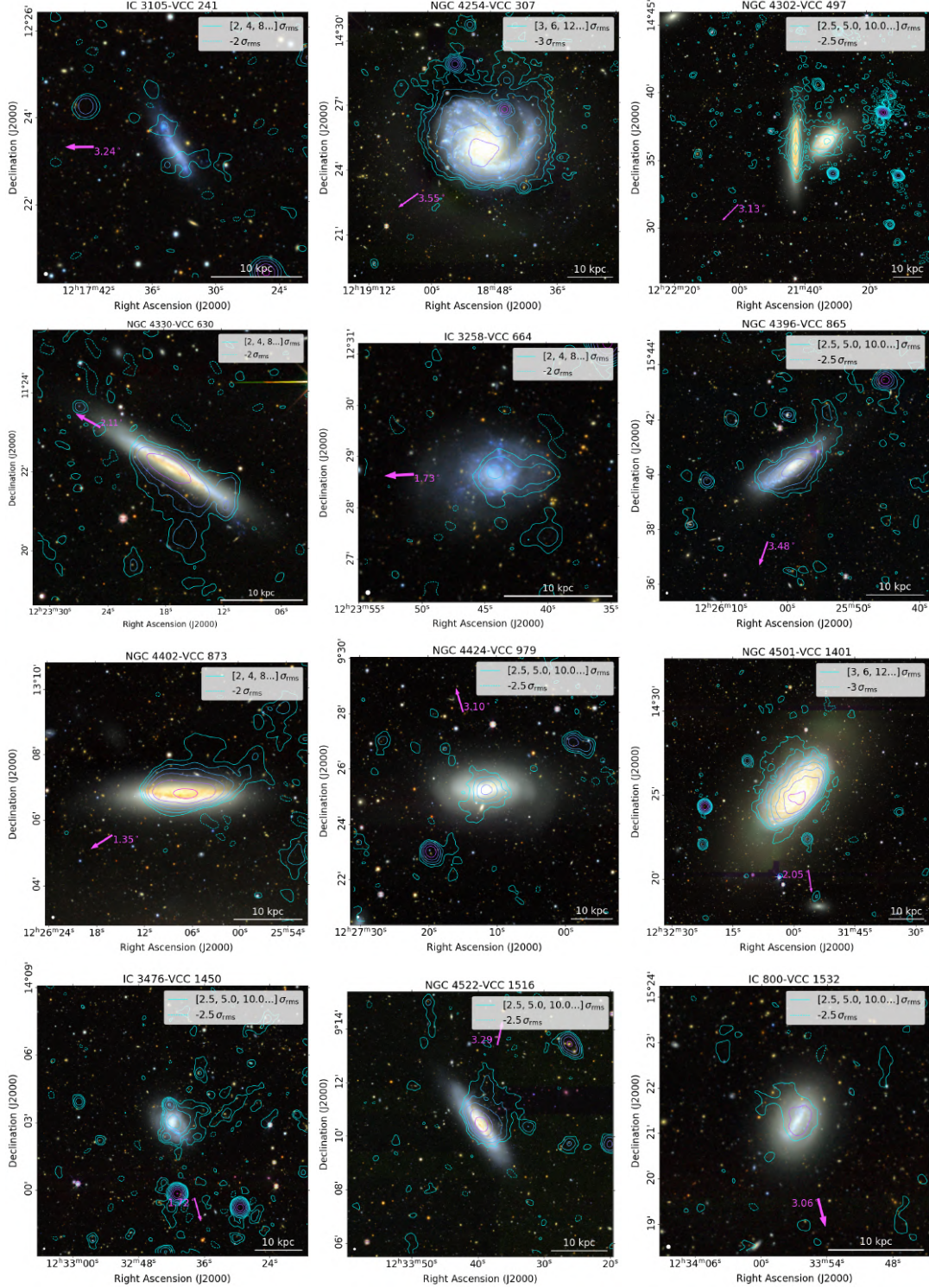


Figure 3.1: Radio continuum emission in galaxies with a radio-morphology indicative of RPS. We show LO-FAR radio continuum intensity contours at 144 MHz from the 20''-resolution maps overlaid on top of optical images from the DESI Legacy Survey. Contour-levels increase in increments of powers of two and pink arrows indicate the direction and angular distance (in units of degree) to the center of the Virgo cluster.

3 Environmental effects in the Virgo Cluster

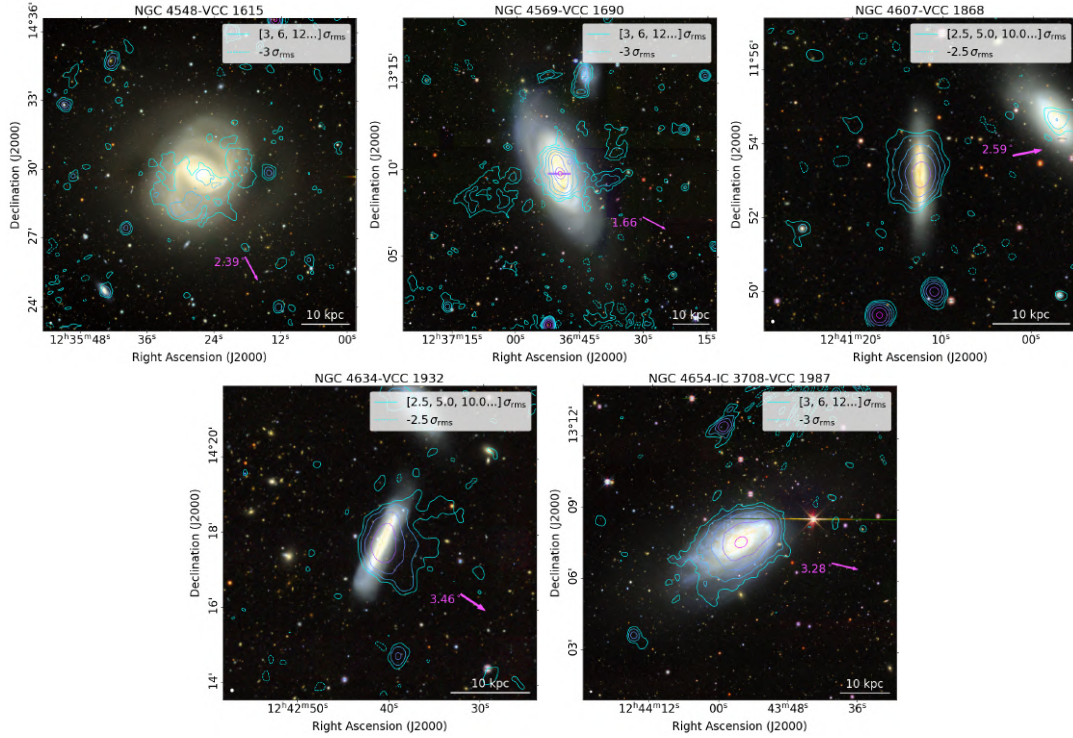


Figure 3.1: Continued.

Preliminary images from the ViCTORIA MeerKAT Survey confirm the morphological peculiarities found in LOFAR for all four objects. For four other galaxies in our RPS sample (IC 3105, IC 3476, NGC 4302 and NGC 4424), the impact of RPS was previously observed at other wavelengths (Chung et al. 2007; Boselli et al. 2021, 2022) but not in the radio continuum.

Since our analysis focuses on the star-forming properties, radio emission due to active galactic nucleus (AGN) activity is a strong contamination. Thus, we investigate the possible contribution of AGN-emission for the galaxies that show signs of ram-pressure stripping in the radio continuum. Three of those objects, NGC 4388, NGC 4438 and NGC 4501 are Seyfert-galaxies. The first two have a radio-morphology that is clearly dominated by nuclear emission (Hummel & Saikia 1991). However, in NGC 4501, the nuclear point-source accounts for only 1% of the total radio emission. The other galaxies mostly host H II-nuclei in the BPT (Baldwin, Phillips & Terlevich; Baldwin et al. 1981) and WHAN ($W_{\text{H}\alpha}$ versus $N_{\text{II}}/\text{H}\alpha$; Cid Fernandes et al. 2011) diagrams according to Gavazzi et al. (2018). Exceptions are NGC 4302, NGC 4548 and NGC 4569 and which have a nuclear WHAN classification as AGN and an inconclusive nuclear BPT classification. NGC 4607 is also classified as AGN in the WHAN diagram and as LINER (Low Ionization Nuclear Emission-line Region; Heckman 1980) or transition object in the BPT, but has an integrated classification as an H II-galaxy. Of those, only NGC 4569 shows a compact nuclear source in the LOFAR maps. While a minor contribution of an AGN cannot be ruled out for this object, this central source is dominantly fueled by nuclear star formation giving rise to prominent outflows (Boselli et al. 2016). Thus, the only AGN we remove from our sample are NGC 4388 and NGC 4438.

We are left with a sample of 17 RPS galaxies (see Tab. 3.1). Their 20''-resolution LOFAR contours on top of the optical images of the Dark Energy Spectroscopic Instrument (DESI) Legacy Survey data release 10 (Dey et al. 2019) are displayed in Fig. 3.1. They range from galaxies with clear

and prominent 144 MHz tails, such as NGC 4330, NGC 4396, NGC 4522 or IGC 3476 to objects with only mild asymmetry like NGC 4548 and NGC 4607. With the availability of high-sensitivity images of the nearby Virgo cluster, we start probing the regime of dwarf galaxies with radio continuum tails by detecting lower mass systems, down to a stellar mass of $M_{\star} = 7.8 \times 10^7 M_{\odot}$. Previous studies of more distant clusters and groups are limited to objects with masses $M_{\star} \geq 10^9 M_{\odot}$ (Roberts et al. 2021a,b; Roberts et al. 2022b; Ignesti et al. 2022b).

A number of galaxies that were reported in the literature to suffer from RPS (Boselli et al. 2022) are not part of our LOFAR RPS sample. Of those, IC 3412, IC 3418, NGC 4506 and UGC 7636 are non-detections in LOFAR at 4σ . Others, mostly galaxies which have tails in H I, are radio-detected but show a symmetric radio morphology. Those objects are NGC 4294, NGC 4299, NGC 4469, NGC 4470, NGC 4491 and NGC 4523 (Chung et al. 2007; Boselli et al. 2023b). For these objects, we speculate that they experience rather mild ram-pressure, which mostly affects the outskirts of the ISM, such that a tail in radio continuum is below our sensitivity threshold. Alternatively, the peculiar H I morphology of these objects could be due to other process than RPS. In the case of NGC 4470, the non-detection of a continuum tail is due to local dynamic range limitations in the LOFAR map, indeed preliminary images of our ViCTORIA MeerKAT survey reveal a prominent tail at 1.3 GHz. For NGC 4523, a continuum counterpart to the H I tail which we reported in Boselli et al. (2023b) is also observed in the preliminary MeerKAT maps, although at low significance.

3.2.2 LOFAR-HRS sample

To assess how the non-thermal properties of galaxies in the Virgo cluster are shaped by their local surroundings, we compile a comparison sample of nearby galaxies with high-quality star formation tracer data available. For this, the Herschel Reference Survey (HRS; Boselli et al. 2010), which also contains all but two of the galaxies in our RPS sample, is well suited. This survey consists of a statistically complete, *K*-band limited sample of 323 nearby (15–25 Mpc distance) galaxies. Around a quarter of those galaxies reside in the Virgo sub-clusters around either M 87 or M 49, another quarter is located in other sub-structures of the Virgo cluster or its outskirts. The remaining objects are in less dense environments such as groups and pairs or are isolated galaxies. This allows us to compare the properties of galaxies in the Virgo cluster with those that are inhabiting poorer surroundings.

We construct a sample of the 144 MHz LOFAR-detected star-forming galaxies in the HRS. For this, we use data of the LOFAR HBA Virgo Cluster Survey (Edler et al. 2023a), which covers the majority of the galaxies in the Virgo Cluster. In addition, all the HRS galaxies at declinations of $\delta > 30^{\circ}$ are covered by the second data release of the LOFAR Two-metre Sky Survey (LoTSS-DR2; Shimwell et al. 2022). Further galaxies were observed by more recent, previously unpublished observations of LoTSS, processed by the LOFAR Surveys Key Science Project¹. All LOFAR HBA observations were taken with identical observational settings and processed using the *ddf-pipeline* algorithm (Tasse et al. 2021). For the Virgo cluster observations, additional pre-processing was necessary due to the close proximity to the extremely luminous radio galaxy M 87 (Virgo A), those steps are described in Edler et al. (2023a).

For the HRS galaxies in the footprint of the LOFAR HBA Virgo Cluster Survey, we use the 144 MHz measurements reported in Edler et al. (2023a) based on the 20''-resolution LOFAR-maps. In this paper, all HRS galaxies within the survey area were considered. We extend this sample also to the HRS galaxies covered by LoTSS-DR2 as well as to those which are within 1.97° angular distance of unpublished LoTSS-observations processed before August 2023. We manually inspect all HRS

¹<https://lofar-surveys.org/>

3 Environmental effects in the Virgo Cluster

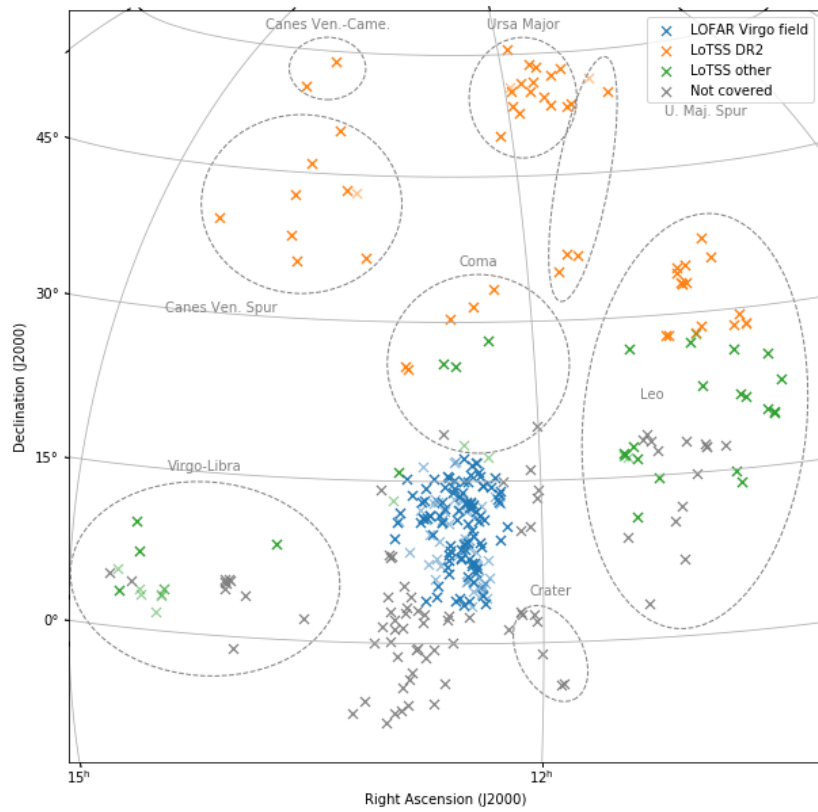


Figure 3.2: LOFAR-coverage of the HRS. The galaxies are either in the LOFAR Virgo Cluster Survey (blue), in LoTSS-DR2 (orange) or covered in further LoTSS observations (green). Grey crosses are not covered by LoTSS, and colored but partially transparent points are covered but not detected. Dashed regions mark structures of galaxies other than the Virgo cluster.

galaxies in the LoTSS 20''-maps and, if they are visible in the radio images, we measure the flux density in a region encompassing the 3σ -contours as it was done in Edler et al. (2022) for the Virgo objects. For observations outside of LoTSS-DR2, we use the pointing closest to the galaxy of interest and we take into account a field-dependent factor to align the flux density scale with the one of the 6 C-survey (Hales et al. 1988) and NRAO VLA Sky Survey (NVSS; Condon et al. 1998). This factor was calculated as described in Shimwell et al. (2022). We consider all galaxies with an integrated signal-to-noise ratio above four as radio-detected. While we use the 10% systematic uncertainty of the flux density scale for LoTSS-DR2 as reported in (Shimwell et al. 2022), a larger uncertainty of 20% is assumed for the other LOFAR maps due to the reduced overlap and statistics, the higher uncertainty of the primary beam model for low declinations, and the presence of bright sources such as M 87 (for sources in the Virgo field, Edler et al. (2023a)). In Fig. 3.2, we show the sky distribution of the HRS galaxies and their coverage by the different LOFAR projects. In total, out of the 261 late-type galaxies in the statistically complete sample of the HRS (excluding ellipticals and lenticulars), 193 are in the footprint of our LOFAR observations. Of those, 141 galaxies are detected, 76 are in the LOFAR Virgo field, 44 are from LoTSS-DR2, and 21 are in LoTSS-fields outside of the LoTSS-DR2 footprint.

Since we are interested in radio emission as tracer of the SFR, we need to exclude objects where a significant fraction of the radio emission is due to an active galactic nucleus (AGN). By excluding elliptical and lenticular galaxies, we remove most objects with strong AGN contamination. In Gavazzi et al. (2018), nuclear spectroscopy-based BPT and WHAN classifications for the HRS galaxies were presented. Eleven of the LOFAR-detected objects were classified as either strong or weak AGN in the WHAN diagram and as Seyfert galaxy in the BPT diagram. Visually inspecting the radio maps of those revealed that for six of them the nuclear point-like sources contribute $>15\%$ to the flux density. These objects (NGC 3227, NGC 4313, NGC 4419, NGC 4586) were removed from our sample. All galaxies in the RPS sample described in Sect. 3.2.1 except for IC 3105 and IC 3258, which are fainter than the limiting K -band magnitude of 12, are also part of the HRS. Those two objects will also be part of our analysis but are excluded from any fitting since they do not meet the selection criteria of the HRS. In the following, we will refer to the objects in our LOFAR-HRS sample minus the objects in our RPS sample for simplicity as the non-RPS sample.

In Appendix B, we display the 144 MHz measurements of the 137 LOFAR-detected star-forming galaxies used in this work. The spectral luminosity L_{144} at 144 MHz is calculated from the measured flux densities S according to $L_{144} = 4\pi d^2 S$; since our sample only consists of nearby galaxies at $v < 1750 \text{ km s}^{-1}$, we neglect k -correction. We employed distances d following the HRS (Boselli et al. 2010), with the difference that we set the distance to objects in the Virgo cluster to 16.5 Mpc instead of 17 Mpc to be consistent with what was assumed in the NGVS (Ferrarese et al. 2012) and VESTIGE (Boselli et al. 2018b).

Star formation tracers

The integrated radio luminosities serve as a tracer of the SFR of the individual galaxies in the sample. A key advantage of radio-inferred SFR is that it is not affected by dust-attenuation (Condon 1992; Murphy et al. 2011). Thus, no extinction-correction is required. While at low radio frequencies, the radio emission is almost free from the Bremsstrahlung-contribution of thermal electrons, the synchrotron lifetime of CRE in a magnetic field B (Beck & Krause 2005):

$$t_{\text{syn}} = 88 \text{ Myr} \left(\frac{B}{10 \mu\text{G}} \right)^{-3/2} \left(\frac{\nu}{144 \text{ MHz}} \right)^{-1/2} \quad (3.1)$$

3 Environmental effects in the Virgo Cluster

is longer compared to CRE probed at higher frequencies. So an underlying assumption of SFRs derived from low frequency observations is that the SFR is constant on timescales of ≈ 100 Myr.

To compare the radio luminosity to further tracers of the star-forming activity, we consider SFRs based on far-UV (FUV) and H α . The SFRs obtained from H α and FUV were reported in Boselli et al. (2015) for the HRS star-forming galaxies based on the Salpeter initial mass function (IMF) and the calibration of Kennicutt (1998). We converted the SFR to a Chabrier IMF (Chabrier 2003) by applying a factor of 0.63 to the SFRs (Madau & Dickinson 2014). The SFRs also need to be corrected for dust attenuation. For the UV-based SFR, Boselli et al. (2015) employed a correction based on the 24 μ m emission. For the H α -inferred SFR, two approaches were compared in Boselli et al. (2015) – a correction based on the Balmer-decrement using spectroscopic data (Boselli et al. 2013) and a method relying on the 24 μ m dust emission. The authors found that the correction with the Balmer decrement $C(H\beta)$ as defined in Lequeux et al. (1981) is only accurate if the fractional uncertainty is $\sigma[C(H\beta)] < 0.1$; on the other hand, the correction using the 24 μ m emission can be biased for systems with a particularly low specific SFR due to the contribution of the old stellar population to the dust heating (Cortese et al. 2008; Boselli et al. 2015). Thus, we use the values corrected with the Balmer-decrement if $\sigma[C(H\beta)] < 0.1$, and with the 24 μ m emission otherwise.

No uncertainty estimates are available for the SFRs published in Boselli et al. (2015). In the following, we assume a systematic uncertainty of 15% for the GALEX UV measurements (Gil de Paz et al. 2007) and the H α photometry with the San Pedro Martir telescopes (Boselli et al. 2015; Boselli et al. 2023a). We neglect the photometric uncertainty of the Spitzer 24 μ m measurements used for a dust correction as they have a uncertainty of only 2% (Engelbracht et al. 2007). We note that those estimates are only a rough first-order approximation of the true uncertainties, which also would require us to take into account the complex and hardly quantifiable dependencies on the dust and N II-line corrections and the SFR conversion (for discussions of those, see e.g. Boselli et al. 2015; Boselli et al. 2016, 2023a). We ensure that the SFRs are based on the same distances as the radio luminosities by re-scaling the SFRs by $(d/d_{\text{HRS}})^2$.

Another common SFR-tracer is the infrared-emission which traces the dust heated by the young stellar population. As already mentioned, in systems with low specific SFR, older stellar populations also contribute to the dust heating. Low specific SFR systems are systematically more common in our sample which includes relatively quenched galaxies in the Virgo cluster (Boselli et al. 2016). For this reason, we do not consider SFRs based purely on the infrared emission.

Sample properties

The stellar masses of our sample were obtained from Cortese et al. (2012) who used the Chabrier IMF and span a large regime, ranging from $3.0 \times 10^8 M_{\odot}$ to $1.3 \times 10^{11} M_{\odot}$. The two additional RPS galaxies outside of the HRS, IC 3105 and IC 3258, are of even lower mass with $M_{\star} = 7.8 \times 10^7 M_{\odot}$ and $M_{\star} = 8.3 \times 10^7 M_{\odot}$, respectively. In Fig. 3.3, the mean of the H α and UV-based SFR is shown as a function of the stellar mass. We also display the star-forming main sequence relation for Virgo cluster galaxies with normal H I-content (Boselli et al. 2023a). As RPS generally reduces the SFR, RPS galaxies are expected to mostly lie below this relation. In some cases, RPS galaxies can show a high specific SFR due to a temporary enhancement of SFR (Bothun & Dressler 1986; Vulcani et al. 2018; Roberts & Parker 2020). Since our sample is limited to 144 MHz detected objects, we are biased towards high-SFR objects, in particular at the low-mass end of the distribution.

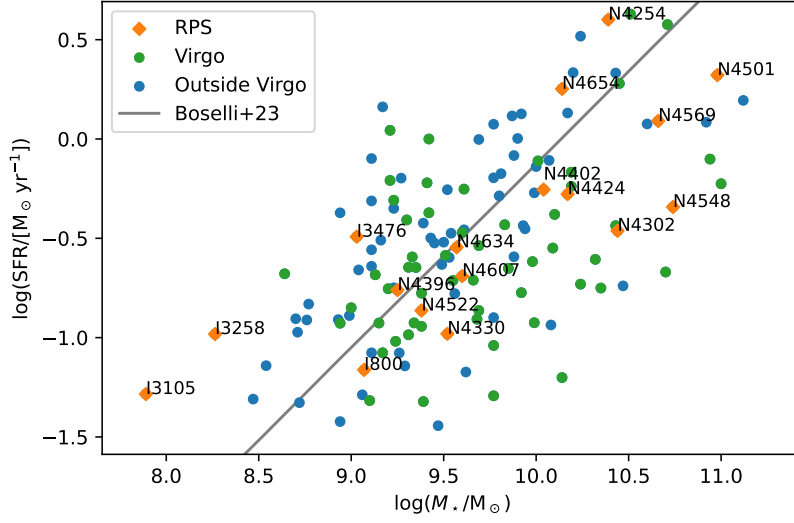


Figure 3.3: SFR (mean of H α and UV-based values) as function of stellar mass for galaxies in the RPS sample (orange diamonds), galaxies in the Virgo cluster region (within 10° from M 87, green circles) and galaxies outside of the cluster (blue circles). For comparison, we show the star-forming main sequence for Virgo cluster galaxies with normal H I-content (Boselli et al. 2023a, grey line).

3.3 Statistical analysis

3.3.1 Radio-SFR-relation

The availability of radio and other SFR-tracers for our data allows us to investigate the radio-SFR-relation for our samples. Particularly at low radio-frequencies, this radio-SFR-relation is known to deviate from the linear scenario (Heesen et al. 2022). Thus, we fit a power-law relation of the form:

$$\left(\frac{L_{144}}{\text{W Hz}^{-1}} \right) = N_0 \left(\frac{\text{SFR}}{\text{M}_\odot \text{ yr}^{-1}} \right)^\beta. \quad (3.2)$$

Fitting is performed in log-log space, where the expression assumes a linear form. We use the orthogonal method of the *bivariate errors and intrinsic scatter* (BCES) regression algorithm (Akritas & Bershady 1996; Nemmen et al. 2012) for the minimization.

We fitted Eq. 3.2 for the H α and UV inferred SFRs and for the HRS galaxies in the RPS sample and those not in the RPS sample independently. The scatter σ_{raw} of the data points around the fit is calculated as:

$$\sigma_{\text{raw}}^2 = (n - 2)^{-1} \sum_i (\log L_{144,i} - \beta \log \text{SFR}_i - \log N_0)^2, \quad (3.3)$$

where n is the sample size. The best-fitting parameters are reported in Tab. 3.2 and we display the fit results together with the data points in Fig. 3.4.

For both SFR tracers, the relation for the radio continuum luminosity derived for the RPS sample is a factor of 2–3 above the one found for the non-RPS galaxies. This is expected given the reports of enhanced radio-to-SFR ratios for RPS galaxies in the literature (Murphy et al. 2009; Vollmer et al. 2010, 2013; Roberts et al. 2021a; Ignesti et al. 2022b). In Fig. 3.4, we also display the relations derived from LOFAR observations of SF-galaxies in other works: Heesen et al. (2022) analyzed a sample of 45 nearby galaxies, Gürkan et al. (2018) studied a sample of > 2000 SF-galaxies across

3 Environmental effects in the Virgo Cluster

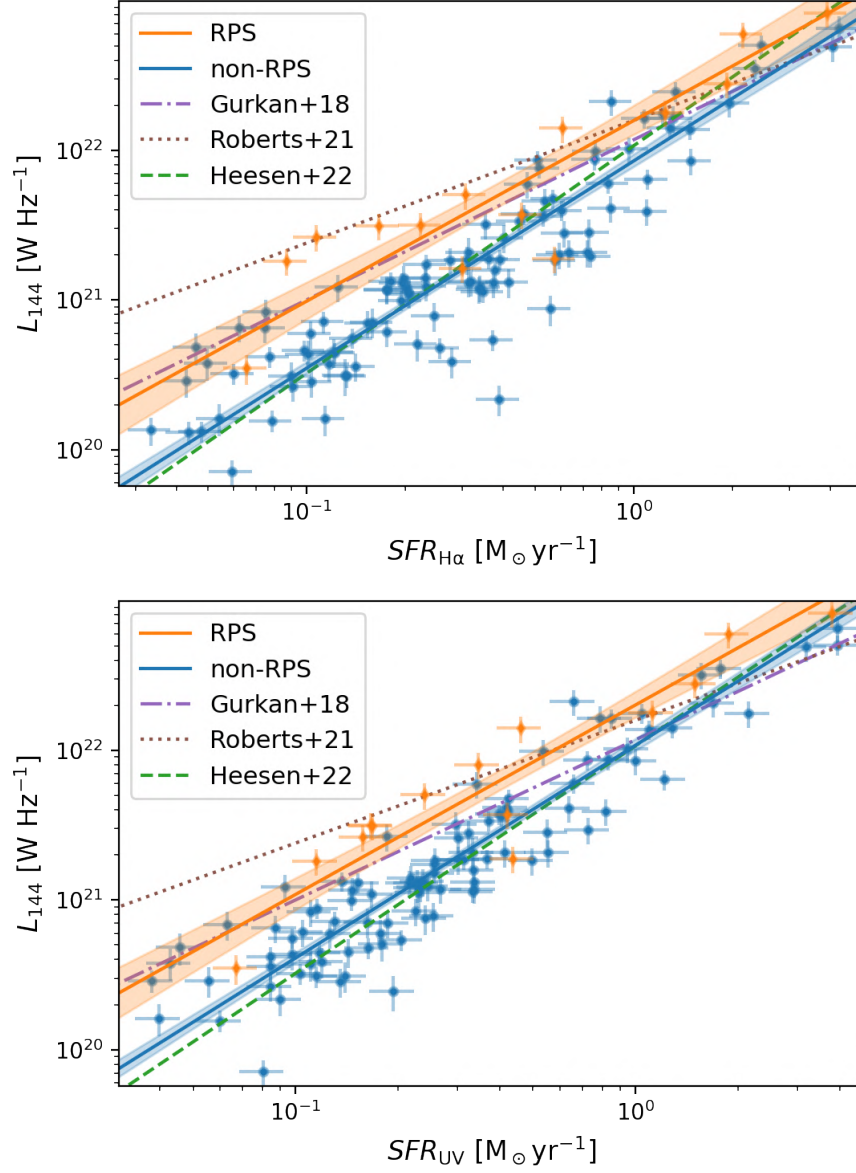


Figure 3.4: Radio-SFR relations. Top panel: $\text{H}\alpha$ -inferred SFRs against radio luminosity for galaxies in the RPS sample (orange data points) and other galaxies in the LOFAR HRS sample (blue data points). The orange and blue lines represent the best-fitting power-law fits and the corresponding 1σ uncertainty bands for those samples. The green, purple and brown lines are fits taken from the literature. Bottom panel: Same as above but for the UV-based SFRs.

Table 3.2: Best-fitting parameters for different parametrizations of the radio-SFR relation.

Tracer	Sample	$N_0 [10^{21}]$	β	γ	σ_{raw}	n
H α	RPS	15.8 ± 2.1	1.21 ± 0.11	–	0.28	14
H α	others	8.5 ± 0.67	1.39 ± 0.06	–	0.28	103
UV	RPS	20.0 ± 2.6	1.27 ± 0.11	–	0.23	14
UV	others	10.8 ± 0.8	1.42 ± 0.06	–	0.24	102
H α	RPS	13.7 ± 2.5	–	0.08 ± 0.13	0.29	14
H α	others	7.2 ± 0.6	–	0.23 ± 0.05	0.27	103
UV	RPS	16.0 ± 2.5	–	0.08 ± 0.12	0.26	14
UV	others	7.8 ± 0.5	–	0.21 ± 0.04	0.25	102
H α	RPS	14.1 ± 3.6	1.05 ± 0.25	0.05 ± 0.21	0.29	14
H α	others	8.3 ± 0.7	1.22 ± 0.06	0.12 ± 0.06	0.26	103
UV	RPS	20.3 ± 5.2	1.26 ± 0.23	0.09 ± 0.19	0.25	14
UV	others	9.9 ± 0.8	1.28 ± 0.06	0.08 ± 0.05	0.24	102

a wide range of redshifts and Roberts et al. (2021a) published a relation for a sample of 95 jellyfish galaxies in low-redshift clusters.

3.3.2 Mass dependency and radio excess

The resulting power-law fits for our samples are super-linear with $\beta \approx 1.4$. This super-linearity is thought to originate from a mass-dependence in the calorimetric efficiency $\eta = \eta(M)$, which is the ratio of CRE energy that is radiated within galaxy. In larger galaxies with a higher mass M , CRE have longer escape times t_{esc} in relation to their lifetime t_{syn} , thus, they lose a greater fraction of their energy inside the galaxy before escaping into regions with low magnetic field strengths.

We use the following parametrization to enforce a linear radio-SFR relation while taking into account a mass-dependent calorimetric efficiency (see e.g. Heesen et al. 2022):

$$L_{144} = N_0 \left(\frac{\text{SFR}}{\text{M}_\odot \text{ yr}^{-1}} \right) \left(\frac{M_\star}{10^{10} \text{M}_\odot} \right)^\gamma. \quad (3.4)$$

Here, γ describes the dependency on the stellar mass M_\star . We repeat the fitting for the RPS and non-RPS galaxies for both SFR-tracers. The best-fitting model-parameters are reported in Tab. 3.2, and the data points and fits are shown in Fig. 3.5. For the galaxies that do not show a RPS-morphology, we can reproduce the systematic increase of L_{144}/SFR as a function of mass, finding a positive mass-exponent of $\gamma \approx 0.2$.

Again, the population of RPS galaxies has a clear radio-excess with 12/14 galaxies above the relation for non-RPS galaxies. However, for them, the mass-dependency is less clear. This could be either due to an increased scatter in L_{144}/SFR for this population, indirectly connected to the ram-pressure stripping, or due to the small sample size.

We further investigate a relation with an additional free parameter, which is a power-law in both mass and SFR (see Gürkan et al. 2018):

$$\left(\frac{L_{144}}{\text{W Hz}^{-1}} \right) = N_0 \left(\frac{\text{SFR}}{\text{M}_\odot \text{ yr}^{-1}} \right)^\beta \left(\frac{M_\star}{10^{10} \text{M}_\odot} \right)^\gamma. \quad (3.5)$$

The best-fitting results for this parametrization are displayed in Tab. 3.2. For the non-RPS galaxies, we find a mass-exponent of $\gamma \approx 0.1$ and an SFR-exponent of $\beta \approx 1.25$. Those results can be compared

3 Environmental effects in the Virgo Cluster

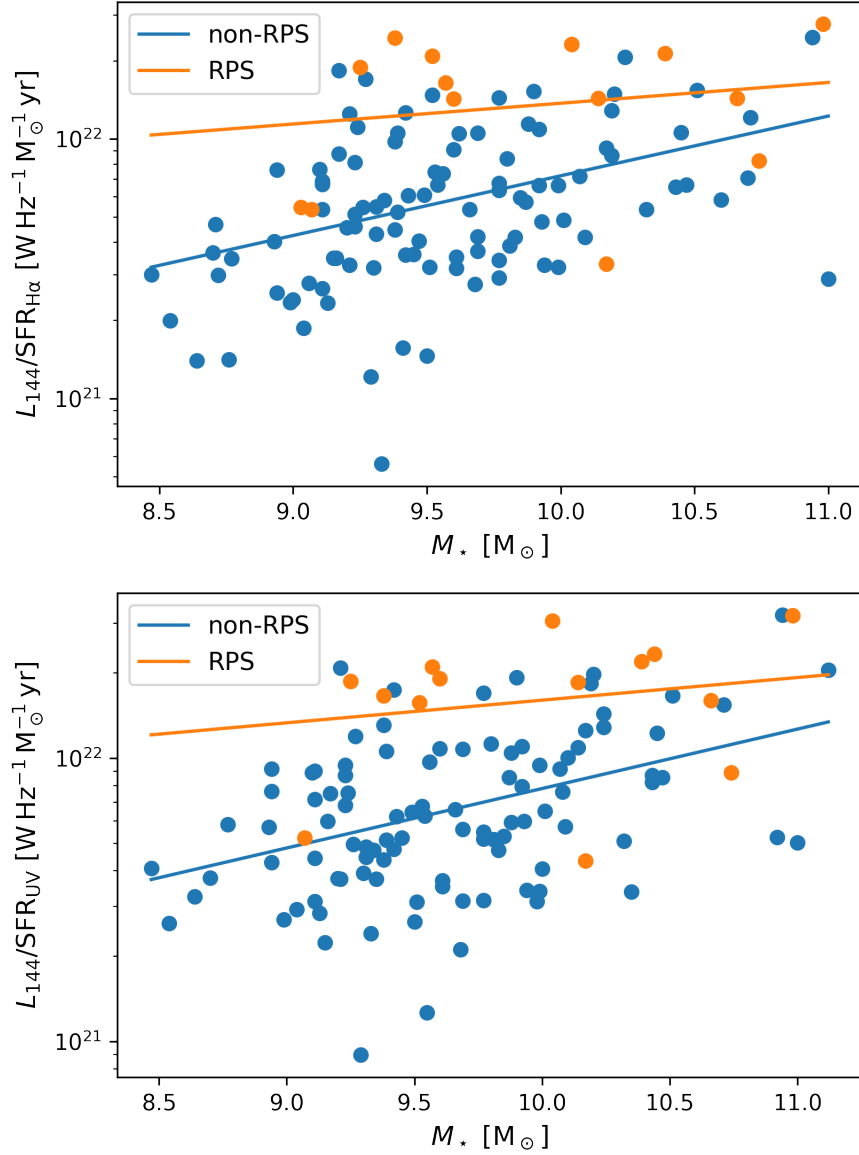


Figure 3.5: Top panel: Ratio of L_{144} to $\text{SFR}_{\text{H}\alpha}$ as a function of M_{\star} . The orange data points mark the galaxies in the RPS sample, the blue ones the galaxies outside the RPS sample. The orange and blue lines are the corresponding fits. Bottom panel: Same but for the UV-inferred SFR.

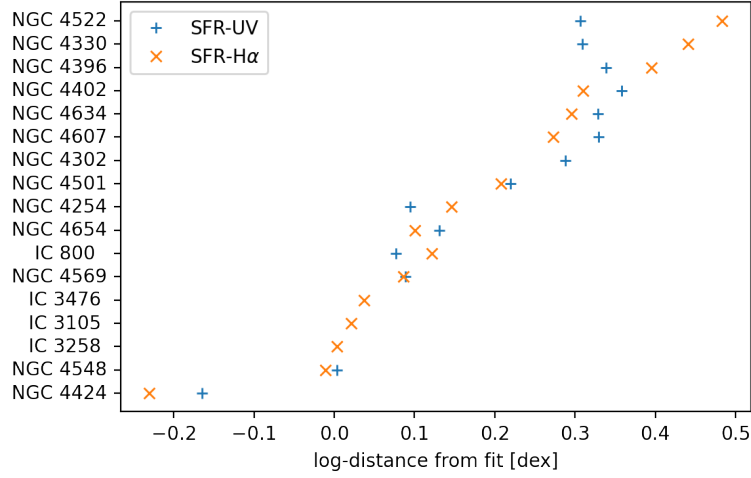


Figure 3.6: Distance of the RPS galaxies to the best-fitting L_{144} -SFR- M_{\star} -plane for the non-RPS galaxies in log-space. The galaxies are sorted by the mean of the SFR_{UV} and $\text{SFR}_{\text{H}\alpha}$ based log-distances.

to the ones from Gürkan et al. (2018), who found a flatter relation with SFR ($\beta = 0.77$) but a steeper exponent in mass ($\gamma = 0.44$).

To quantify the radio-excess (or deficit) compared to the best fit of Eq. 3.5 for the non-RPS sample, we calculate the distance of the RPS-galaxies to the best-fitting plane in log-space according to:

$$d_{3D} = \frac{\log\left(\frac{L_{144}}{\text{W Hz}^{-1}}\right) - \beta \log\left(\frac{\text{SFR}}{\text{M}_{\odot} \text{yr}^{-1}}\right) - \gamma \log\left(\frac{M_{\star}}{10^{10} \text{M}_{\odot}}\right)}{\sqrt{\beta^2 + \gamma^2 + 1}}. \quad (3.6)$$

We display those distances in Fig. 3.6. In general, there is a good agreement between the distances based on the UV and $\text{H}\alpha$ -inferred SFR. The only object with a strong radio-deficit is the peculiar galaxy NGC 4424, which is thought to be a merger remnant and shows outflows of ionized gas (Boselli et al. 2018). Similarly, the galaxies with a clear RPS morphology in radio show the strongest radio-excesses, those are NGC 4522, NGC 4330, NGC 4396, NGC 4402 and NGC 4634. Qualitatively, there appears to be a connection between the asymmetry of the radio emission and the strength of the radio excess. The only exception being IC 3476, which shows a strong tail but only a mild excess of $\approx 10\%$. Possibly, the radio emission of this source is underestimated due to masked background sources and side-lobes of M 87 which unfortunately cover parts of the tail of this source .

3.3.3 Spectral properties

To probe if the spectral properties of the galaxies in the ram-pressure stripped sample differ from the ones of unperturbed galaxies, we determined the integrated spectral index α^2 for all objects which have radio-measurements also at 1.4 GHz available in the literature. The spectral index α between two frequencies ν_1, ν_2 with flux density measurements S_1, S_2 is calculated as: $\alpha = \ln(S_1/S_2)/\ln(\nu_1/\nu_2)$. We estimate the corresponding uncertainties following Gaussian propagation of uncertainty. The 1.4 GHz flux densities or upper limits were collected from Murphy et al. (2009), Chung et al. (2009) (re-measured in cases where the maps were provided by the authors), Vollmer et al. (2010) and Boselli et al. (2015). For the two RPS objects which are not in the HRS, we derived the 4σ upper limits from

²Defined as $S \propto \nu \alpha$.

3 Environmental effects in the Virgo Cluster

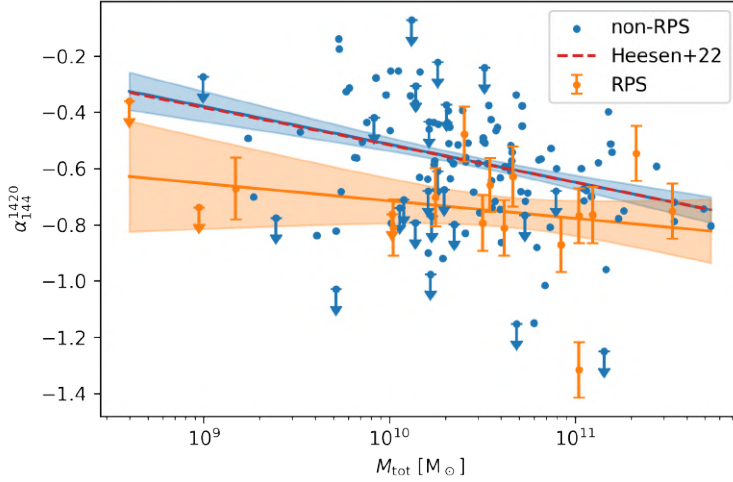


Figure 3.7: Total mass against spectral index for the RPS sample (orange markers) and the other galaxies in the sample (blue markers). For clarity, uncertainties are only displayed for the RPS sample, they are of comparable size ($\sigma_\alpha \sim 0.1$) for the other galaxies. Downward pointing arrows correspond to 4σ upper limits. The orange and blue line show the corresponding best-fitting relations, and the red dashed line shows the fit from Heesen et al. (2022).

the NVSS (Condon et al. 1998). To allow for comparison with the work of Heesen et al. (2022), we estimated the total masses of the galaxies in our sample. For this, we employed the dynamical data derived from H α (Gómez-López et al. 2019) or H I (Boselli et al. 2014a) observations according to $M_{\text{tot}} = r_{\text{SF}} v_{\text{rot}}^2 / G$, where G is the gravitational constant, v_{rot} the rotation velocity and r_{SF} the size of the star-forming disk, estimated from $D24$ or $D25$ as described in Gómez-López et al. (2019).

In Fig. 3.7, we display the total mass-spectral index-distribution of the 114 galaxies with available 1.4 GHz measurements, for the 26 objects without detection, we provide an upper limit. We also show the best-fitting log-linear relation of the form $\alpha = A \log(M_{\text{tot}}/M_\odot) + B$. For the galaxies outside of our RPS sample, we find $A = -0.13 \pm 0.02$ and $B = 0.83 \pm 0.20$, in excellent agreement with the parameters derived by Heesen et al. 2022 ($A = -0.13$ and $B = 0.81$). However, for the RPS sample, we find evidence that the relation is shifted towards steeper spectral index values with $A = -0.06 \pm 0.05$ and $B = 0.09 \pm 0.52$. Evaluated at $M_{\text{tot}} = 3 \times 10^{10} M_\odot$, the relations differ by $\Delta\alpha = 0.17 \pm 0.06$. We cross check that this finding is not simply caused by a systematic underestimation in the dynamical estimates of M_{tot} due to truncated gas disks in RPS galaxies by repeating the fitting using M_\star , where we find $\Delta\alpha = 0.13 \pm 0.07$ at $M_\star = 4 \times 10^9 M_\odot$. A strong outlier from the relation is NGC 4548 with a particularly steep spectral index of $\alpha = -1.3 \pm 0.1$ measured from the VIVA (Chung et al. 2009) map with low image fidelity. However, the 4σ upper limit from the NVSS map (Condon et al. 1998) agrees with a steep spectrum $\alpha \leq -1.0$. Our finding with a best-fitting relation for the RPS galaxies that is shifted to lower values of α holds when repeating the analysis without NGC 4548 ($\Delta\alpha = 0.13 \pm 0.04$ at $M_{\text{tot}} = 3 \times 10^{10} M_\odot$).

We also investigated if there is a correlation between the spectral index and the log-distance from the best-fitting L_{144} -SFR- M_\star plane for the RPS sample. We find a slightly positive Pearson’s correlation coefficient of 0.30 using SFR_{UV} and 0.377 $\text{SFR}_{\text{H}\alpha}$, however, both are not significant (p -value > 0.23), the slightly positive relation is due to the low luminosity steep spectrum source NGC 4548.

3.4 Spatially resolved radio-SFR analysis

In Sect. 3.3.2, we showed that the radio emission of our Virgo RPS sample is enhanced up to a factor of 3 compared to the H α and UV-inferred SFR. The localization of this excess allows to constrain the origin of the surplus radio emission. So could a leading-edge enhancement point towards compression of the magnetic field lines or to ram-pressure driven shocks as additional source of CRE. To investigate this, we created maps of the ratio between the observed radio surface brightness B_{obs} and the expected radio surface brightness B_{model} based on the SFR-surface density Σ_{SFR} . A similar analysis was carried in Murphy et al. (2009) for six of the galaxies in our sample using 1.4 GHz VLA observations and *Spitzer* far-infrared emission as SFR-tracer. For our analysis, we derived the SFR-surface density from *GALEX* NUV (Martin et al. 2005) following the calibration of Leroy et al. (2019). We employed a dust-correction based on Herschel 100 μm measurements obtained from the HRS (Cortese et al. 2014) and HeVICS (Davies et al. 2010) according to Kennicutt & Evans (2012). Foreground and background sources in the Σ_{SFR} and LOFAR maps were manually masked and the maps were gridded to the same pixel layout. We convolved the Σ_{SFR} -maps to match the resolution of our LOFAR maps (either $9'' \times 9''$ or $20'' \times 20''$) using the `convolve` method implemented in `astropy` (Astropy Collaboration et al. 2022). We obtained the model for the radio emission using Eq. 3.4 and our best-fitting parameters ($N_0 = 7.7 \times 10^{21}$ and $\gamma = 0.21$) for the non-RPS sample to convert Σ_{SFR} to the radio surface brightness B :

$$\frac{B_{\text{model}}}{\text{Jy beam}^{-1}} = \frac{N_0}{4\pi \times 10^{-26}} \left(\frac{\Sigma_{\text{SFR}}}{\text{M}_{\odot} \text{ yr}^{-1} \text{ kpc}^2} \right) \left(\frac{M_{\star}}{10^{10} \text{M}_{\odot}} \right)^{\gamma} \left(\frac{A_{\text{beam}}}{\text{kpc}^2} \right)^{-1} \left(\frac{d}{\text{m}} \right)^{-2}. \quad (3.7)$$

Since the CRE have lifetimes of ~ 100 Myr and are subject to CR-transport, the synchrotron emission of an undisturbed galaxy should be a smoothed version of SFR-surface density (e.g. Heesen et al. 2023a), this can be expressed in terms of the CRE-transport length l_{CRE} . The shape of the smoothing kernel used to model the CR-transport depends on the transport process. We assume as a benchmark the case of pure diffusion modeled by a Gaussian kernel. The width σ of the Gaussian kernel used for the smoothing is related to l_{CRE} according to $\sigma = (2\ln 2)^{-0.5} l_{\text{CRE}}$.

Since CRE diffuse away from the star-forming regions into regions with low or no star-forming activity, the resolved B - Σ_{SFR} -relation is sub-linear, opposite to the global radio-SFR-relation. Taking into account CRE diffusion with an appropriate choice of l_{CRE} , the relation can be linearized (Murphy et al. 2009; Berkhuijsen et al. 2013; Heesen et al. 2023a). To linearize this relation, we fit the convolution kernel size σ . For each σ , we determine the slope a of the relation by fitting the pixels that are above a signal-to-noise ratio of 5 in both maps. Due to their low surface brightness, we instead require a S/N of 3 for IC 800 and IC 3105 and 4 for NGC 4548. The optimal σ is found once the slope reaches unity. We carried out the smoothing procedure based on maps at $9''$ resolution (for sources with sufficient surface brightness) and at $20''$ resolution. The resulting transport lengths are listed in Tab. 3.3, there is decent agreement between the values derived at different resolutions. Two notable outliers with a large transport length are NGC 4254 and NGC 4548 with $l_{\text{CRE}} > 5$ kpc. Those values are larger than the values ≤ 3.8 found for field galaxies at 144 MHz in Heesen et al. (2023b). This is likely due to the significant contribution of the external perturbations to the CRE-transport, a scenario also suggested by Ignesti et al. (2022c).

We then convolved the maps of the model surface brightness using a Gaussian kernel with the corresponding width σ . In Fig. 3.8, we display the log-ratio $R = \log_{10}(B_{\text{obs}}/B_{\text{model}})$ between the observed and the modeled radio emission for all pixels with a signal-to-noise ratio above 3 (above 2 in the case of IC 3105). We also mark the 5σ contours of the SFR-surface density and radio surface brightness. For sufficiently bright sources, we used the $9''$ -resolution maps to derive the ratios, otherwise the $20''$ -resolution ones. For the former, we present the $20''$ maps, which are more sensitive to

3 Environmental effects in the Virgo Cluster

the faint tails, in Appendix C.

In general, the radio excess is a global phenomenon and all galaxies but NGC 4424, NGC 4548 and IC 3258 show enhanced radio emission across the disk. As expected, the excess is strongest at the trailing edge or in the tail, where all objects show some form of enhanced radio emission or radio contours that extend asymmetrically beyond the SFR contours at the trailing edge. This is most pronounced in NGC 4330, NGC 4522 and NGC 4634, while NGC 4548 shows only a mild enhancement in parts of the trailing half of the disk. The reason for the excess radio emission in the tails is the advection of CRe from the disk due to RPS to regions with low star-forming activity (e.g. Murphy et al. 2009; Ignesti et al. 2022b). At the same time, many galaxies show a deficit of radio emission at the leading edge (i.e. Σ_{SFR} contours that extend beyond the radio contours) - e.g. in NGC 4330, NGC 4396, NGC 4402, NGC 4522, NGC 4548 and IC 3476 (see also Murphy et al. (2009)). However, the leading-edge deficit is not omnipresent. Most notably, in NGC 4501, we instead observe an enhancement of radio emission at the leading edge – likely connected to a local compression of magnetic fields (Vollmer et al. 2008).

Table 3.3: CRe transport length and spectral indices of the RPS sample.

Name	$l_{\text{CRe}}^{9''}$ [kpc]	$l_{\text{CRe}}^{20''}$ [kpc]	$\alpha_{144\text{MHz}}^{1.4\text{GHz}}$
IC 3105	–	2.3	$< -0.36^a$
NGC 4254	5.2	5.4	-0.77 ± 0.10^b
NGC 4302	4.4	3.9	-0.77 ± 0.10^c
NGC 4330	1.9	1.1	-0.63 ± 0.11^c
IC 3258	–	1.8	$< -0.74^a$
NGC 4396	2.3	1.3	-0.79 ± 0.10^c
NGC 4402	1.4	1.6	-0.81 ± 0.10^c
NGC 4424	1.9	1.4	-0.67 ± 0.11^c
NGC 4501	1.3	0.9	-0.75 ± 0.10^c
IC 3476	1.7	1.8	-0.81 ± 0.1^a
NGC 4522	1.0	1.6	-0.48 ± 0.10^b
IC 800	–	2.2	$< -0.76^a$
NGC 4548	–	5.5	-1.32 ± 0.10^d
NGC 4569	2.5	2.0	-0.55 ± 0.10^b
NGC 4607	1.6	1.5	-0.70 ± 0.10^d
NGC 4634	2.0	1.8	-0.66 ± 0.10^e
NGC 4654	3.0	3.0	-0.87 ± 0.10^d

Notes. The 1.4 GHz flux densities for the spectral index estimation are taken from: ^aNVSS (4σ upper limits Condon et al. 1998); ^bMurphy et al. (2009), ^cVollmer et al. (2010); ^d measured from the maps provided by Chung et al. (2009) and ^eBoselli et al. (2015).

3.5 Discussion

3.5.1 Radio-SFR relations

In Fig. 3.4, our best-fitting radio SFR relations are displayed. As expected, our result for the non-interacting galaxies is in good agreement with Heesen et al. (2022), who worked on galaxies which

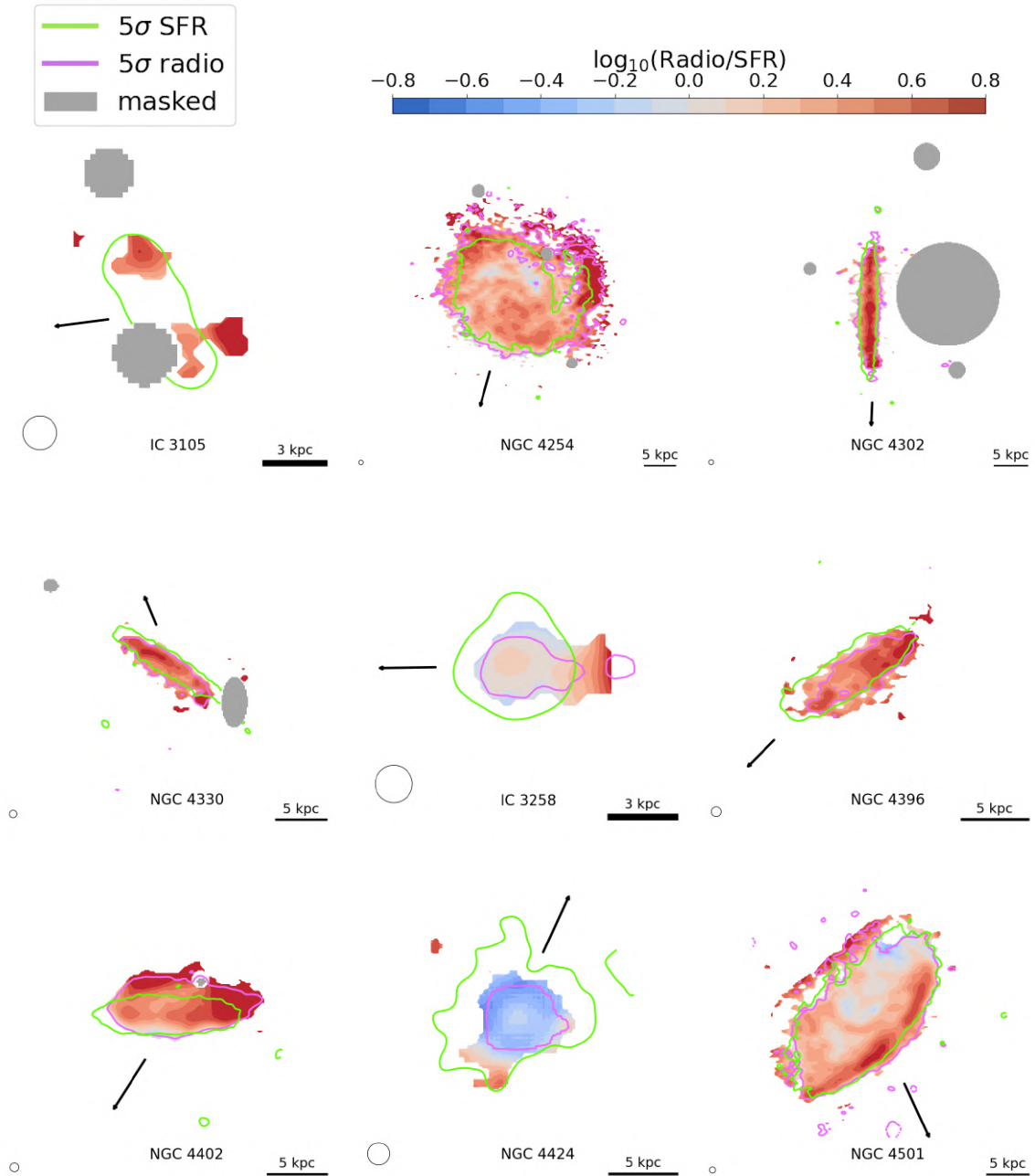


Figure 3.8: Logarithmic ratio between the observed and modeled radio emission. The color-scale is symmetric and increases in increments of 0.1 dex, red colors indicate a local radio excess, blue colors a radio deficit and gray areas are masked background sources. Magenta and green lines are the 5σ contours of B_{obs} and Σ_{SFR} , respectively. The black arrow indicates the approximate orbit of the galaxy as inferred from the direction of the tail. The circles in the bottom left correspond to the angular resolution of the radio data, which is $9''$, except for IC 3105, IC 3258, NGC 4424, IC 800 and NGC 4654 where we used maps at $20''$ resolution.

3 Environmental effects in the Virgo Cluster

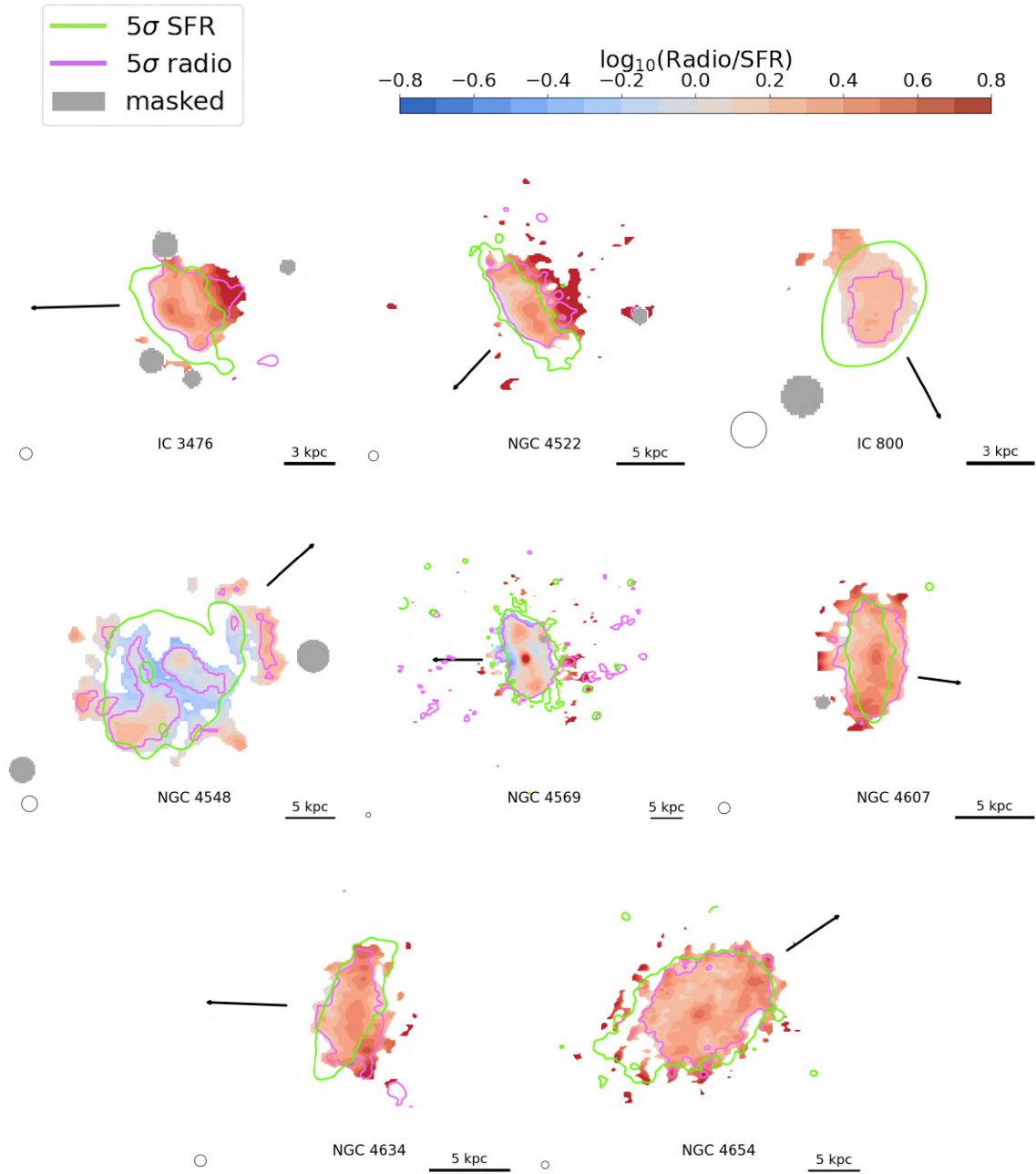


Figure 3.8: Continued.

are nearby and are not members of a cluster. Comparison of our relation for the non-RPS objects with the work of Gürkan et al. (2018) shows that their relation is shifted towards higher radio luminosity, in particular towards the low SFRs. These authors also used LOFAR data, but their sample extends to significantly larger redshifts and has a mean stellar mass that is 2.5 times higher than in our work. We argue that the mass-dependency can mitigate the discrepancy between the various relations, taking into account the mean stellar mass of the samples can account for a discrepancy of ≈ 0.1 dex in Fig. 3.4. Roberts et al. (2021a) on the other hand studied a sample of 95 jellyfish galaxies in low-redshift clusters and found a relation even above our RPS sample. In agreement with the picture that RPS increases the radio-SFR ratio, this relation is closest to the ones for our RPS sample. Indeed, the fact that the relation of Roberts et al. (2021a) is offset to higher radio luminosities compared to our relations for the RPS sample could be explained by the more efficient RPS for the objects in the Roberts et al. (2021a) sample, since they are mostly in clusters that are more massive than Virgo. It was also previously reported that Coma and A1367, more massive nearby clusters, show a greater radio excess compared to Virgo (see Boselli & Gavazzi 2006, and references therein).

That galaxies suffering from RPS do not follow the radio-SFR relation of normal star-forming galaxies but show a higher radio luminosity is well established now due to observations in nearby galaxy clusters. In our RPS sample, this radio excess is widespread ($\sim 14/17$ objects) and ranges from 0.1 to 0.5 dex (Murphy et al. 2009), in line with previous radio continuum studies of the cluster (e.g. S. Niklas 1995; Murphy et al. 2009).

3.5.2 Spectral index of RPS galaxies

We additionally report for the first time tentative evidence for a spectral index-mass relation for RPS galaxies that is shifted to steeper spectral index values compared to normal star-forming galaxies (Fig. 3.7). While the significance of this result is currently limited by the availability of uniform, high-fidelity continuum data at 1.4 GHz, it is noteworthy that also other studies reported steep spectral indices for a number of objects suffering from RPS (Chen et al. 2020; Müller et al. 2021; Ignesti et al. 2022c). The spectral steepening is indicative of a CRe population that is of higher radiative age.

Little is known about the spectral indices of RPS galaxies, with studies mostly limited to a few or individual object (Vollmer et al. 2013; Chen et al. 2020; Müller et al. 2021; Ignesti et al. 2022c; Lal et al. 2022; Roberts et al. 2022b). A multitude of effects that could explain the enhanced radio luminosity of RPS galaxies are also able to influence the spectral properties of this population. Particle (re-)acceleration due to ISM-ICM shocks could introduce an additional source of CRe (Murphy et al. 2009) with an injection spectral index that may differ from acceleration at supernova shocks associated with star-forming activity. In front of a galaxy moving at a velocity greater than the speed of sound c_s through the ICM, a bow shock is expected to form (Stevens et al. 1999). In principle, particle acceleration may occur at this bow shock, or at reverse shocks launched into the ISM. The bow shock should be ~ 1.5 kpc in front of the galaxy depending on its size of the galaxy and velocity (Farris & Russell 1994). Due to high speed of sound ($c_s \sim 500 \text{ km s}^{-1}$, e.g. Simionescu et al. (2017)) in the ICM, the shock acceleration will take place in the low Mach number regime. That means that the injection spectral index of the shock (Drury 1983):

$$\alpha_{\text{inj}}(\mathcal{M}) = -\frac{\mathcal{M}^2 + 1}{\mathcal{M}^2 - 1} + 0.5 \quad (3.8)$$

will be steeper than the ~ -0.5 in high Mach-number SN explosions. While a significant contribution of CRe accelerated at the bow shock to the total radio emission of RPS galaxies could thus explain both the radio excess and the steeper spectral indices for this population, we do not consider this scenario

3 Environmental effects in the Virgo Cluster

since we do not observe radio emission $\sim 1 - 2$ kpc in advance of the leading edges of the galaxies, the only exceptions are NGC 4607 and NGC 4634. Conversely, these regions are oftentimes deficient in radio emission, as already reported by Murphy et al. (2009). As alternative to the acceleration at the bow-shock, CRe could instead be accelerated at reverse shocks launched into the ISM. However, due to the lower temperature of the ISM and the correspondingly slow speed of sound, these shocks would then again be in the high Mach-number regime resulting in $\alpha_{\text{inj}} \sim -0.5$, such that they would not lead to a steepening of the synchrotron spectrum. Thus, we do not consider acceleration due to ISM-ICM shocks as mechanism that can explain steeper radio spectral indices for RPS galaxies.

Another scenario is that of an enhanced magnetic field strength due to compression of the ISM magnetic field (Boselli & Gavazzi 2006) or the magnetic draping mechanism (Dursi & Pfrommer 2008; Pfrommer & Dursi 2010). This effect would cause a steepening of the synchrotron spectrum, since the loss time t_{sync} would decrease compared to the escape time t_{esc} , meaning that more spectral aging can occur before the CRe escape the galaxy. In this scenario, the enhancement of the radio emission should also be localized at the leading edge, where the magnetic field compression takes place. This mechanism is supported by the detection of asymmetric polarized ridges in some of the Virgo cluster RPS galaxies (e.g. Vollmer et al. 2008; Pfrommer & Dursi 2010). If the magnetic fields are enhanced due to leading-edge compression of the ISM, the corresponding gas compression could possibly introduce relevant ionization capture losses for low-energy electrons. Those compete with the fast radiative losses at high electron energy due to the accelerated radiative aging in shaping the observed synchrotron spectral index.

As third scenario, Ignesi et al. (2022c) suggested a rapid quenching of the SFR due to the environmental interaction as explanation for the radio excess. This would translate to a strong reduction of $\text{SFR}_{\text{H}\alpha}$ after a delay of only few Myr but would only affect L_{144} at later times due to the lifetime of the massive O-B stars and the cosmic rays that contribute to the 144 MHz synchrotron emission. The availability of UV data presents us with the opportunity to constrain the quenching scenario, since it probes time scales in between the H α and 144 MHz continuum emission (Kennicutt & Evans 2012; Leroy et al. 2012). This scenario would also lead to a steeper radio spectrum for the RPS galaxies due to the declining injection of fresh CRe, resulting in an increased average radiative age of the CRe.

3.5.3 Model scenarios

In the following, we will analyze the phenomenology of simple homogeneous models for the third and second scenario mentioned above. We consider the following version of the momentum-space Fokker-Planck-equation (ignoring diffusion and re-acceleration processes) to describe the evolution of the electron spectrum $N(E, t)$ as a function of time t and energy E :

$$\frac{\partial N(E, t)}{\partial t} = \frac{\partial}{\partial E} [N(E, t)b(E)] - \frac{N(E, t)}{t_{\text{esc}}} + Q(E, t). \quad (3.9)$$

Here, t_{esc} is the CRe escape time for which we employ a value of 50 Myr (see e.g. Dörner et al. 2023) and $b(E)$ describes the energy losses. In the case of synchrotron and inverse Compton losses, $b(E) = b_0 E^2$ with:

$$b_0 = 3.2 \times 10^{-6} \left(B^2 / 2\mu_0 + u_{\text{rad}} \right) \text{ m}^3 \text{ MeV}^{-2} \text{ Myr}^{-1}, \quad (3.10)$$

where we assume a photon field of energy density $u_{\text{rad}} = 6 \times 10^5 \text{ eV m}^{-3}$ and synchrotron radiation in a magnetic field $B = 10 \mu\text{G}$ (Sarazin 1999). For the source term $Q(E, t) = qE^{-\delta}$ we consider the injection of electrons with an power-law shock-acceleration spectrum with an exponent of $\delta = -2$ and a normalization factor q . The full model and numerical solution of Eq. 3.9 and the calculation of the radio, FUV and H α emission are described in Appendix D.

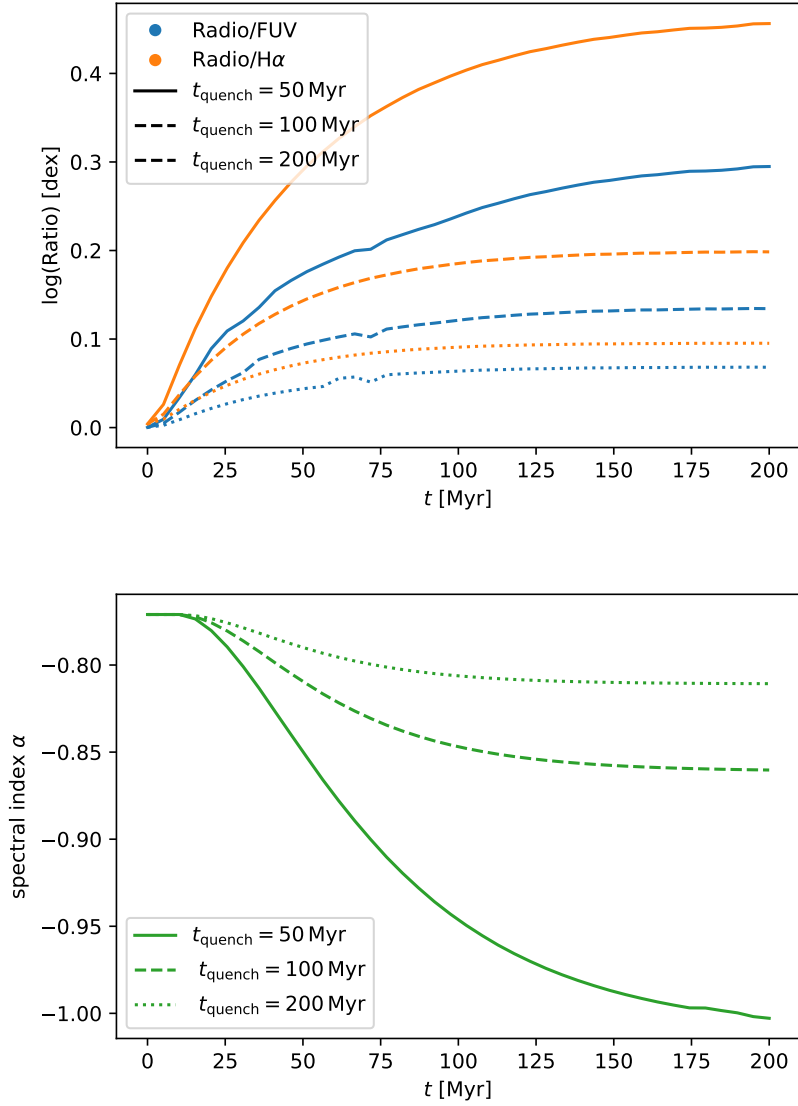


Figure 3.9: Scenario (1) – quenched star formation model. *Top panel:* Log-ratio of the 144 MHz to FUV emission (blue) and H α emission (orange) for a quenching time of 50 Myr (solid lines), 100 Myr (dashed lines) and 200 Myr (dotted lines) as a function of time since the onset of SFR-quenching. The ratios are relative to $t = 0$. *Bottom panel:* Evolution of the 144 MHz to 1.4 GHz spectral index for the two models.

3 Environmental effects in the Virgo Cluster

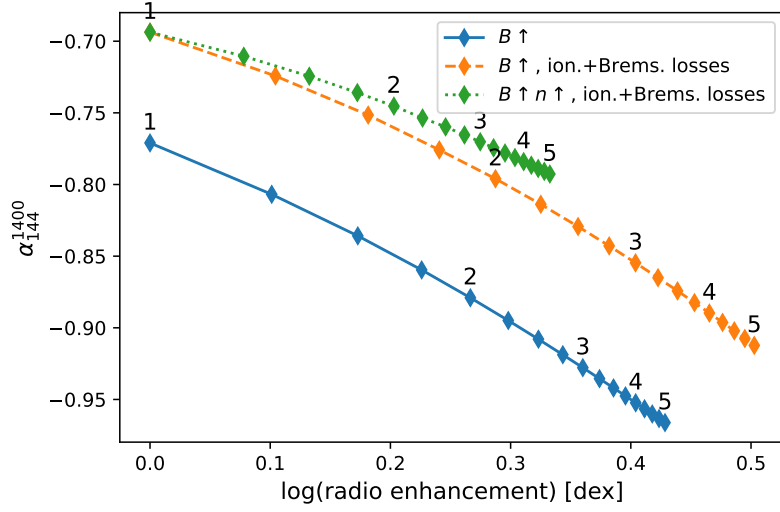


Figure 3.10: Scenario (2) – compression model. Effect of an increase of the initial $10 \mu\text{G}$ magnetic field on the radio excess and synchrotron spectrum (blue continuous line). Diamond symbols mark the fractional increase of the magnetic field in increments of 0.25, integer values are highlighted. The orange dashed line shows the same model when including ionization and Bremsstrahlung losses. The green dotted line shows the same model when also increasing the gas density by the same amount as the magnetic field.

We start from the equilibrium state electron spectrum, which corresponds to a spectral index of $\alpha = -0.77$. We then consider two scenarios: (1) the RPS causes a quenching of the SFR, modeled by an exponential decay of the source term $Q(E)$ with an e-folding time scale of t_{quench} by a factor $\exp(-t/t_{\text{quench}})$; and (2) compression of the ISM magnetic field enhances the magnetic field of a galaxy by a factor of f_B .

For scenario (1), the exponential SFR history is of course a simplification valid only for the recent star-forming history (\sim few 100 Myr). However, this parametrization with only one free parameter allows us to describe the basic effects of a declining SFR due to RPS. In Fig. 3.9, we show the time evolution of the observed radio-FUV and radio- $H\alpha$ ratio (normalized to 1 at $t = 0$) and the radio spectral index for this scenario with quenching time scales of 50, 100 and 200 Myr. In the model with $t_{\text{quench}} = 50$ Myr, we can reproduce the observed enhancement of ~ 0.4 dex in the radio- $H\alpha$ ratio and a significant steepening of the radio spectral index of $\Delta\alpha \approx 0.2$, in agreement with our tentative evidence of steeper spectral indices for RPS galaxies. Higher values of t_{quench} cause a less severe steepening and radio excess. A property of this model is that, due to the longer life time of the stars responsible for the FUV emission, the radio-FUV ratio should be less enhanced compared to the radio- $H\alpha$ ratio. Indeed for three of the objects with the highest radio excesses (NGC 4330, NGC 4501 and NGC 4522) we find that the distance to the best-fitting relation is stronger relative to $\text{SFR}_{H\alpha}$ and weaker relative to SFR_{FUV} (see Fig. 3.6). However, for the remaining objects, no trend can be identified and we also find no significant difference in the $\text{SFR}_{\text{UV}}/\text{SFR}_{H\alpha}$ ratios for the RPS and non-RPS sample. For the quenching scenario (1) to fully explain the radio excess and the steep radio spectra of RPS galaxies, violent quenching of the star formation activity with $t_{\text{quench}} \leq 100$ Myr would need to be a widespread phenomenon and should also imprint in a systematic excess of UV to $H\alpha$ emission, which we only observe for NGC 4330, NGC 4330 and NGC 4522. Spectral energy density fitting of Virgo cluster galaxies yields similarly short quenching time scales for NGC 4330 and NGC 4522 (Boselli et al. 2016). Less violent quenching will still yield some contribution to the

radio excess and spectral steepening, but cannot fully explain the observations.

In scenario (2), we model the effect of an increase of the magnetic field strength by a factor of f_B . This boosts the synchrotron emission and also steepens the spectral index. In the limit $t_{\text{syn}} \gg t_{\text{esc}}$, the electron spectrum is escape-dominated and the corresponding radio slope approaches $\alpha = (\delta - 1)/2 = -0.5$. In the opposite case of high magnetic field strength ($t_{\text{esc}} \gg t_{\text{syn}}$), it is loss-dominated and the radio slope is close to $\alpha = \delta/2 = -1$. For the initial state with $B = 10 \mu\text{G}$, the spectral index is $\alpha = -0.77$. The blue line in Fig. 3.10 shows the change in radio emission and spectral index for different values of f_B . An increase of the magnetic field by $f_B = 1.5$ steepens the spectral index to $\alpha = -0.84$ and increases the synchrotron emission by 0.17 dex, for $f_B = 2$, we find a spectral index of $\alpha = -0.88$ with a radio enhancement of 0.27 dex. To explain the galaxies with the strongest excesses of ≥ 0.4 dex, we would require an increase in the magnetic field strength by $f_b > 4$ (corresponding to a factor of 16 in energy). The quoted values represent the equilibrium states, but we note that during the ramp-up phase of the magnetic field, the radio emission will be higher and the spectral index may be steeper while the ‘surplus’ electrons (compared to the new equilibrium state) are being depleted. Also, less drastic increases of the magnetic field can be required to explain the enhanced radio emission if the electron distribution is strongly dominated by other processes than synchrotron radiation, i.e. in the case of strong Bremsstrahlung and ionization losses (see e.g. Basu et al. 2015). If we extend our model by ionization and Bremsstrahlung losses with a gas number density of $N_{\text{gas}} = 10^6 \text{ m}^{-3}$ (orange line in Fig. 3.10), we still find a significant steepening ($\alpha = -0.64$ to $\alpha = -0.73$) and increased radio emission (by 0.3 dex) in the case $f_B = 2$. The main effect of ionization losses is that for the same magnetic field strength, the observed radio spectrum is flattened towards low frequencies (thus also explaining why the spectral indices in the model without ionization losses are mostly steeper than the observed ones). A much weaker steepening and radio enhancement is predicted by our model if we assume that the gas density n_{gas} is compressed by the same factor as the magnetic field due to the strong ionization losses in such a scenario (green dotted line in Fig. 3.10). To model the relative importance of gas and magnetic field compression and cosmic ray transport, refined simulations are required.

An important open question in scenario (2) is the nature of physical mechanism that is able to increase the magnetic field in RPS galaxies. With simulations, Farber et al. (2022) were able to reproduce a magnetic field enhancement due to compression in the range $f_B \leq 3$, however, Tonnesen & Stone (2014) found that increase to only last a short time (~ 25 Myr). An alternative to the adiabatic compression of the ISM magnetic fields is the magnetic draping mechanism, where the galaxy sweeps up ICM magnetic field lines at the leading edge (Dursi & Pfrommer 2008). It was proposed to explain the asymmetric polarized radio emission for a number of Virgo cluster galaxies (Pfrommer & Dursi 2010). The main difficulty of both mechanisms is that they generate a magnetic field enhancement localized at the leading edge. This is only clearly the case in NGC 4501, where the leading edge radio excess (see Fig. 3.8) corresponds well with the asymmetric polarized radio emission (e.g. Vollmer et al. 2007; Vollmer et al. 2008). Many other galaxies in the RPS sample (e.g. NGC 4330, NGC 4396, NGC 4402, NGC 4522, IC 3476) even show a deficit of radio continuum emission in that region, likely due to the fast advection of CRe or locally efficient ionization losses, amplified by the ISM compression. The compression or magnetic draping scenario can also not easily explain the enhanced radio emission across the disk that is observed for most galaxies. However, the limited angular resolution of our maps, the varying alignment between the galaxy disks and the velocity vector combined with projection effects (the line of sight velocity relative to M 87 is commonly ~ 1000 km/s, indicating significant radial stripping, see Tab. 3.1) complicate the identification of such local signatures. Tuned simulations may be required to investigate if the observed disk-wide radio enhancement can be generated by magnetic field enhancement and projection effects alone.

3.6 Conclusion

In this paper, we analyzed a sample of 17 Virgo cluster galaxies with a radio morphology indicative of RPS. This sample contains galaxies with masses as low as $7.8 \times 10^7 M_{\odot}$. Our LOFAR observations allowed the identification of four new RPS candidates (NGC 4607, NGC 4634, IC 800, IC 3258) and four new objects with radio continuum tails (NGC 4302, NGC 4424, IC 3105, IC 3476) in the cluster. We compare them to a statistical sample of 120 nearby star-forming galaxies in the HRS. Using 144 MHz observations of the LOFAR HBA Virgo Cluster Survey and LoTSS together with the multi-wavelength data of the HRS, our findings are:

- The galaxies in the statistical sample without signs of environmental perturbation in LOFAR follow a super-linear radio-SFR relation with a slope of 1.39 ± 0.06 and 1.42 ± 0.06 compared to H α and FUV-based SFRs, in good agreement with previous low-frequency studies of nearby galaxies.
- Considering the stellar mass as additional parameter in the radio-SFR relation results in fits with comparable scatter (≥ 0.25 dex), supporting a mass-dependent calorimetric efficiency of star-forming galaxies.
- We find a clear radio-excess for the RPS sample, with radio luminosities that are a factor of 2-3 higher compared to the radio-SFR relation for normal star-forming galaxies. Qualitatively, we find the strongest radio excess in galaxies with pronounced radio tails.
- We derived a radio spectral index-total mass relation of the non-RPS galaxies that is in excellent agreement with the literature. For the RPS sample, we find a relation that is shifted towards lower spectral index values by $\Delta\alpha \approx 0.15$.
- We model the expected radio emission based on a pure diffusion scenario and hybrid NUV+100 μm SFR surface densities. Comparing the observed to the expected emission, we find that the radio excess is of global nature and mostly extends across the disks. In a number of cases, we can confirm leading-edge radio-deficit regions as a signature of RPS. Only for NGC 4501 we find a leading-edge radio enhancement.
- The radio excess and spectral steepening can be explained by variations in SF history only for NGC 4330, NGC 4396 and NGC 4522 which show the highest radio excesses, which are also accompanied by FUV excesses. This explanation would require rapid quenching with e-folding times ≤ 100 Myr.
- Alternatively, an increased magnetic field due to RPS is also able to generate both enhanced radio emission and a steeper synchrotron spectrum. A doubling of the magnetic field strength can explain a moderate enhancement of the radio luminosity (≤ 0.27 dex) and steepening ($\Delta\alpha \approx 0.1$). To explain the highest radio excesses with magnetic field increase only, a strong enhancement of more than a factor of four would be required.

This study allowed us for the first time to test different models for the radio excess, with the emerging picture that there are multiple realistic channels which can contribute to anomalous radio continuum properties of RPS galaxies. In extreme RPS galaxies, a rapid quenching of the star-forming activity may be a relevant mechanism to explain excess radio emission, however, for the broad population of objects suffering from RPS, magnetic field enhancement likely dominates. In the near future, our Virgo Cluster multi-Telescope Observations on Radio of Interacting galaxies and AGN (ViCTORIA)

project will allow to further constrain the non-thermal physical mechanisms at play in RPS galaxies with deep, polarized L-band observations by MeerKAT and ultra-low frequency measurements with the LOFAR Low-Band Antenna. Crucially, with the homogeneous multi-frequency data, we will be able to definitely confirm or reject the claim presented in this paper that RPS galaxies in the Virgo cluster show steeper radio spectral indices than normal SF galaxies. Further, we will be able to perform high-fidelity spatially resolved studies of the spectral index and to probe the magnetic field structure using polarization information.

Acknowledgements

HE acknowledges support by the Deutsche Forschungsgemeinschaft (DFG, German Research Foundation) under project number 427771150. MB acknowledges funding by the Deutsche Forschungsgemeinschaft under Germany's Excellence Strategy – EXC 2121 “Quantum Universe” – 390833306. FdG acknowledges support from the ERC Consolidator Grant ULU 101086378. AI acknowledges funding from the European Research Council (ERC) under the European Union's Horizon 2020 research and innovation programme (grant agreement No. 833824, PI Poggianti) and the INAF funding program 'Ricerca Fondamentale 2022' (PI A. Igesti). LOFAR (van Haarlem et al. 2013) is the Low Frequency Array designed and constructed by ASTRON. It has observing, data processing, and data storage facilities in several countries, which are owned by various parties (each with their own funding sources), and that are collectively operated by the ILT foundation under a joint scientific policy. The ILT resources have benefited from the following recent major funding sources: CNRS-INSU, Observatoire de Paris and Université d'Orléans, France; BMBF, MIWF-NRW, MPG, Germany; Science Foundation Ireland (SFI), Department of Business, Enterprise and Innovation (DBEI), Ireland; NWO, The Netherlands; The Science and Technology Facilities Council, UK; Ministry of Science and Higher Education, Poland; The Istituto Nazionale di Astrofisica (INAF), Italy. This research made use of the Dutch national e-infrastructure with support of the SURF Cooperative (e-infra 180169) and the LOFAR e-infra group. The Jülich LOFAR Long Term Archive and the German LOFAR network are both coordinated and operated by the Jülich Supercomputing Centre (JSC), and computing resources on the supercomputer JUWELS at JSC were provided by the Gauss Centre for Supercomputing e.V. (grant CHTB00) through the John von Neumann Institute for Computing (NIC). This research made use of the University of Hertfordshire high-performance computing facility and the LOFAR-UK computing facility located at the University of Hertfordshire and supported by STFC [ST/P000096/1], and of the Italian LOFAR IT computing infrastructure supported and operated by INAF, and by the Physics Department of Turin university (under an agreement with Consorzio Interuniversitario per la Fisica Spaziale) at the C3S Supercomputing Centre, Italy.

3 Environmental effects in the Virgo Cluster

4 Abell 1033: Radio halo and gently reenergized tail at 54 MHz

H. W. Edler, F. de Gasperin, G. Brunetti, A. Botteon, V. Cuciti, R. J. van Weeren, R. Cassano, T. W. Shimwell, M. Brüggén, A. Drabent. *Astronomy & Astrophysics*, 666, id.A3, 15 pp. (2022)

Abstract

Context. Abell 1033 is a merging galaxy cluster of moderate mass ($M_{500} = 3.24 \times 10^{14} M_{\odot}$). It hosts a broad variety of diffuse radio sources that are linked to different astrophysical phenomena. The most peculiar phenomenon is an elongated feature with an ultra-steep spectrum that is the prototype of the category of gently reenergized tails (GReET). Furthermore, the cluster hosts sources that were previously classified as a radio phoenix and a radio halo.

Aims. We aim to improve the understanding of the cosmic-ray acceleration mechanisms in galaxy clusters in a frequency and mass range that has been poorly explored so far.

Methods. To investigate the ultra-steep synchrotron emission in the cluster, we performed a full direction-dependent calibration of a LOFAR observation centered at 54 MHz. We analyzed this observation together with recalibrated data of the LOFAR Two-meter Sky Survey at 144 MHz and an archival GMRT observation at 323 MHz. We performed a spectral study of the radio galaxy tail that is connected to the GReET to test whether the current interpretation of the source agrees with observational evidence below 100 MHz. Additionally, we employed a Markov chain Monte Carlo code to fit the halo surface brightness profile at different frequencies.

Results. We report an extreme spectral curvature for the GReET. The spectral index flattens from $\alpha_{144\text{MHz}}^{323\text{MHz}} \approx -4$ to $\alpha_{54\text{MHz}}^{144\text{MHz}} \approx -2$. This indicates the presence of a cutoff in the electron energy spectrum. At the cluster center, we detect the radio halo at 54, 144, and at lower significance at 323 MHz. We categorize it as an ultra-steep spectrum radio halo with a low-frequency spectral index $\alpha = -1.65 \pm 0.17$. Additionally, with a radio power of $P_{150\text{MHz}} = 1.22 \pm 0.13 \times 10^{25} \text{ W Hz}^{-1}$, it is found to be significantly above the correlations of radio power to cluster mass reported in the literature. Furthermore, the synchrotron spectrum of the halo is found to further steepen between 144 and 323 MHz, in agreement with the presence of a break in the electron spectrum, which is a prediction of homogeneous reacceleration models.

4.1 Introduction

Galaxy clusters are the building blocks of the large-scale structures of the Universe. When observed at radio wavelengths, we can detect synchrotron emission that traces the nonthermal plasma in the cluster volume (for a review, we refer to van Weeren et al. 2019). Different phenomena are associated with this emission. There is consensus that diffuse cluster-scale sources such as radio halos develop in the intracluster medium (ICM) as a consequence of mergers between clusters (Brunetti & Jones 2014). Radio halos are megaparsec-scale sources with a steep spectral index of $\alpha \lesssim -1.2$ ¹ that are located in the central region of clusters, approximately following the thermal ICM brightness distribution as observed in the X-rays. The turbulent reacceleration model (Brunetti et al. 2001; Petrosian 2001; Brunetti & Lazarian 2007; Miniati 2015; Brunetti & Lazarian 2016) is the favored scenario to explain the mechanism that generates radio halos. In this model, turbulence injected in the ICM by a merger event reaccelerates cosmic-ray electrons (CRE) from a population of at least mildly relativistic primary (e.g., accelerated by active galactic nuclei) or secondary (generated in proton-proton collisions) seed electrons. (Brunetti & Lazarian 2011; Pinzke et al. 2017). This is supported by the observed connection between the dynamic state of galaxy clusters and radio halos (Cassano et al. 2010, 2013; Cuciti et al. 2015, 2021). Another important expectation of this model is a cutoff in the electron spectrum that depends on the energetics of the merger event and translates into a gradual steepening in the observed synchrotron spectrum. This implies that at a frequency of ~ 1 GHz, we would in general be able to detect radio halos that were generated during very energetic merger events, while at lower frequency, we might be sensitive to a population of radio halos that is characterized by very steep radio spectra ($\alpha < -1.5$), which are in general referred to as ultra-steep spectrum radio halos (USSRH; Cassano et al. 2006; Brunetti et al. 2008). Such sources have been observed in only a small number of clusters so far (Brunetti et al. 2008; Macario et al. 2011; van Weeren et al. 2012; Wilber et al. 2018; Duchesne et al. 2021; Di Gennaro et al. 2021).

Other extended radio sources in galaxy clusters, such as gently reenergized tails (GReETs; de Gasperin et al. 2017) and radio phoenixes (Kale & Dwarakanath 2011; Cohen & Clarke 2011; Duchesne et al. 2021), are thought to trace ancient tails and lobes of radio galaxies that have been reaccelerated. They are smaller sources (~ 100 kpc) and are directly connected to individual radio galaxies. The observational difference between radio phoenixes and GReETs lies in the morphology, the spectral properties, and in the presence of a shock in the ICM. These differences can be explained by a difference in the underlying reacceleration mechanism. Phoenixes are mostly irregular sources with a steep spectrum without clear spatial trends, and they are thought to be accelerated by the adiabatic compression of old radio lobes through a shock wave (Enßlin & Gopal-Krishna 2001; Enßlin & Brügggen 2002). In contrast, GReETs are elongated tails of radio galaxies with highly unusual properties. Starting from the host radio galaxy, spectral aging causes an increasing steepening of the observed synchrotron emission, but at some point, the tail shows an unexpected rebrightening that coincides with a constant or even flattening spectral index. This is thought to be explained by a gentle energetization mechanism that is probably connected to microturbulence in the tail that is induced by interactions with the ICM (de Gasperin et al. 2017; van Weeren et al. 2021). The exact nature of the mechanism remains unclear because only a small number of such sources or candidates have been reported in the literature so far, with very limited spectral information (de Gasperin et al. 2017; Cuciti et al. 2018; Wilber et al. 2018; Botteon et al. 2021b; Ignesti et al. 2022a).

Observations at low radio frequencies (< 1 GHz) are essential for studying ultra-steep sources such as USSRHs and GReETs because these sources remain undetectable at higher frequencies, which

¹We follow the $S \propto \nu^\alpha$ spectral index convention.

Table 4.1: Observations.

Telescope	Obs. date	Time [h]	Freq. [MHz]	Bandwidth [MHz]
LBA	30 June 2018	8	54	48
LOFAR HBA	24 Nov. 2015 ^a	8	144	48
	24 Dec. 2018	8	144	48
GMRT	02 Nov. 2014 ^a	5.5	323	32

^a Originally published in de Gasperin et al. (2017).

is due to their spectral properties. The LOW-Frequency Array (LOFAR; van Haarlem et al. 2013) is the largest and most sensitive radio-interferometer operating at low frequencies. It is therefore perfectly suited for studying diffuse radio emission in clusters of galaxies.

Abell 1033 (PSZ2 G189.31+59.24, hereafter A1033) is a moderately massive ($M_{500} = 3.24^{+0.30}_{-0.32} \times 10^{14} M_{\odot}$) galaxy cluster at a redshift of $z = 0.126$ (Ade et al. 2016) that shows recent merger activity and hosts a steep spectrum source previously classified as a radio phoenix (de Gasperin et al. 2015). In addition, the cluster contains an elongated ultra-steep ($\alpha \approx -4.0$) source connected to a wide-angle tail radio galaxy (WAT). Gentle reacceleration has been suggested to explain the peculiar spectral properties (de Gasperin et al. 2017). This source is the prototype of the GReET category, and it remains the most extreme of the reported cases of radio galaxy tails that show signs of reacceleration. Observations in the ultra-low frequency regime (< 100 MHz) are necessary for a more detailed study of this source. Furthermore, a radio halo in the cluster has recently been reported in Botteon et al. (2022) based on 144 MHz LOFAR observations.

We analyze a LOFAR low-band antenna (LBA) observation of A1033 and data of the LOFAR Two-Meter Sky-Survey (Shimwell et al. 2017, 2019; Shimwell et al. 2022, LoTSS,) to study the properties and spectral behavior of the peculiar radio sources of this cluster. Throughout this work, we assume a fiducial flat Λ CDM cosmology with $\Omega_m = 0.3$ and $H_0 = 70 \text{ km s}^{-1} \text{ Mpc}^{-1}$. All spatial distances are given with respect to a redshift of $z = 0.126$, at which one arcsecond corresponds to 2.53 kpc.

4.2 Observations and data reduction

For the ultra-low frequency study of A1033, we reduced and analyzed a dedicated LOFAR LBA observation (project LC10-008, PI: de Gasperin) between 30 and 78 MHz. Furthermore, we used data of two 8 h LOFAR HBA pointings from the LOFAR Two-metre Sky Survey (Shimwell et al. 2017, 2019; Shimwell et al. 2022) centered at 144 MHz, as well as archival data of a 5.5 h GMRT observation at 323 MHz and of a 64 ks Chandra X-ray observation in the energy band 0.5-7 keV. The data reduction and analysis of the Chandra observation is described in de Gasperin et al. (2015), and for the reduction of the GMRT data we refer to de Gasperin et al. (2017). We summarize information about the radio observations in Tab. 4.1.

4.2.1 LOFAR LBA data

The LOFAR LBA observation was conducted in observation mode LBA_OUTER, where the outer half of the station dipoles are used to minimize electromagnetic crosstalk. During the preprocessing,

the data were flagged at a resolution of 1 s and 3 kHz to mitigate radio frequency interference. The data were subsequently averaged in time and frequency to 4 s and 49 kHz. The multibeam capability of LOFAR LBA allowed it to continuously point one beam toward the calibrator source *3C196* during the observation. This source is a well-behaved standard calibrator for the low band (Heald et al. 2015). The calibrator data were reduced with the LOFAR LBA calibrator pipeline described in de Gasperin et al. (2019). This pipeline is used to find solutions for station-based direction-independent effects as well as an initial estimate for the ionospheric phase errors. The calibrator solutions revealed a poor data quality for the station CS031LBA, and therefore, we excluded this station from further processing. The calibrator solutions were applied to the target field dataset. Additionally, we corrected the data for the primary beam toward the phase center. Next, we performed direction-independent self-calibration of the target field to find solutions for the average ionospheric effects. We employed the self-calibration pipeline presented in de Gasperin et al. (2020). Starting from an initial model based on a collection of radio surveys (Intema et al. TGSS 2017, Condon et al. NVSS 1998, Rengelink et al. WENNS 1997, Lane et al. VLSSr 2014), solutions for the direction-independent ionospheric total electron content (TEC), Faraday rotation, and second-order primary beam effect were derived in two rounds of self-calibration. The root mean square (rms) background noise of the self-calibrated image is $2.5 \text{ mJy beam}^{-1}$ at a resolution of $35''$, the image quality is limited by significant direction-dependent ionospheric errors still present in the data. These errors were addressed in direction-dependent calibration, where we employed the calibration pipeline that is being developed for the LOFAR LBA Sky Survey (LoLSS; de Gasperin et al. 2021) and based on the facet calibration strategy outlined in van Weeren et al. (2016). For the next processing steps, we reduced the data volume by averaging the data to a resolution of 8 s in time. We used the direction-independently calibrated image to isolate suitable direction-dependent calibrators. We employed the Python blob detector and source finder (PyBDSF; Mohan & Rafferty 2015) as source finder, and selected bright and compact sources by thresholding based on flux density and source area. Compact sources in a proximity of $6'$ at most were merged by a grouping algorithm. We selected all sources and groups of sources with a flux density above $S_{\min} > 1.0 \text{ Jy} \times (\nu/60 \text{ MHz})^{-0.8}$ at $\nu = 30 \text{ MHz}$ or $\nu = 54 \text{ MHz}$. The reason for this is that spectral variation, mainly of the primary beam, can make it hard to identify all bright sources at a single frequency. This yielded 29 calibrator directions for the first of two major iterations of our strategy. To prepare the data for further calibration, we subtracted the model obtained after direction-independent calibration to create a dataset that was empty up to model inaccuracies. Then, we looped through the calibrators ordered by their flux density at 30 MHz and repeated the following steps. First, the model of the calibrator was readded to the empty data. Second, the data were phase shifted to the calibrator direction and subsequently averaged further to a resolution of 16 s (if $S_{54} > 10 \text{ Jy}$) or 32 s (otherwise) in time and 0.39 MHz in frequency. This averaging was possible because we only imaged the single calibrator and not the whole field of view (FoV), so that we were not limited by time or frequency smearing. Third, we corrected this averaged dataset for the primary beam in the new phase center. Then, we self-calibrated on this dataset: By imaging a small field around the calibrator, we obtained a model of the calibrator source(s). The data were smoothed in time and frequency with a baseline-dependent kernel size. Here, shorter baselines were smoothed with a larger kernel to increase the signal-to-noise ratio. We solved on the smoothed data for scalar phases against the model. The frequency interval of this solve step was 0.39 MHz, the time interval varied from 64/128 s in the first iteration down to 16/32 s in the following minor cycles. These solutions were then applied to the data, and the calibrator direction was imaged again to obtain an improved model for the next self-calibration iteration. For sources brighter than 10 Jy, we performed two additional diagonal amplitude calibration steps: one step that enforced constant solutions between stations to capture beam model errors, and a subsequent step solved to correct for remaining errors. If the rms noise of the image did

Table 4.2: Parameters of the images displayed in Fig. 4.1. The Briggs value is the parameter for the baseline-dependent weighting of the visibility data during imaging.

Label	Telescope	Freq. [MHz]	Briggs	Resolution ["×"]	Noise [$\frac{\text{mJy}}{\text{beam}}$]
Fig.4.1a	LBA	54	−0.3	21 × 14	1.4
Fig.4.1b	LBA	54	−1.0	12 × 9	1.7
Fig.4.1c	HBA	144	−0.3	12 × 6	0.11
Fig.4.1d	GMRT	323	−0.3	10 × 6	0.034

not improve by more than 1% during a self-calibration iteration and the noise level was lower than the initial value, we considered this direction to be converged. Otherwise, it was not further used as a calibrator direction. In this case, the solutions were discarded and the direction was divided between the neighboring calibrators. We resubtracted the converged calibrator model that was corrupted with the final solutions in that direction from the data to obtain a cleaner empty dataset. Artifacts in the image around the calibrator related to direction-dependent errors were now strongly reduced. This procedure was repeated for all 29 calibrator directions.

We then started again with the averaged data after direction-independent calibration. From these data, we peeled all calibrator sources outside of a 2.3° region around the pointing center, meaning that we subtracted the model after corrupting it with the corresponding direction-dependent solutions without readding it to the data at any point. This strongly reduced the impact of bright sources outside of the primary beam. These data were then imaged using DDFacet (Tasse et al. 2018). This imager simultaneously applied calibration solutions for the remaining 22 calibrator directions based on Voronoi-tesselated facets around the calibrators. The resulting image and model are the products of the first major iteration of our direction-dependent calibration pipeline. We performed a second major iteration using the improved model as input. This time, we searched for calibrators on the DDE-calibrated image and went 20% lower (to 0.8 Jy) in terms of minimum calibrator flux. We found 25 suitable directions for the second iteration, which were now all inside the primary beam main lobe. Again we looped over these sources ordered according to their brightness and repeated the individual self-calibration cycles as described above. Since A1033 is a somewhat special source because it is both very bright (>10 Jy at 54 MHz) and extended (around $5'$), our default algorithm had problems in correctly detecting all emission associated with A1033 as a calibrator direction. For this target, we therefore employed an LBA-specific implementation of the extraction-pipeline described in van Weeren et al. (2021). This pipeline subtracted all sources outside of a 0.2° radius around A1033 from the data using the model and calibration solutions from the direction-dependent pipeline. Then, it performed multiple rounds of self-calibration solving for TEC and a constant phase in each time interval. This tecandphase-constraint reduces the number of free parameters compared to the phase-solve used in direction-dependent calibration. We imaged the final target-extracted dataset using a robust weighting of -0.3 and -1.0 . The images have a background noise of 1.4 and 1.7 mJy beam $^{-1}$ at a resolution of $21'' \times 13''$ and $12'' \times 9''$. They are displayed in Fig. 4.1.

4.2.2 LOFAR HBA data

A1033 was covered by the pointings P155+27 and P157+35 observed in the context of LoTSS (Shimwell et al. 2017, 2019; Shimwell et al. 2022). The analysis of P157+35 has been presented in de Gasperin et al. (2017). Here, we exploit both datasets, taking advantage of the latest develop-

4 A1033: Radio halo and GReET

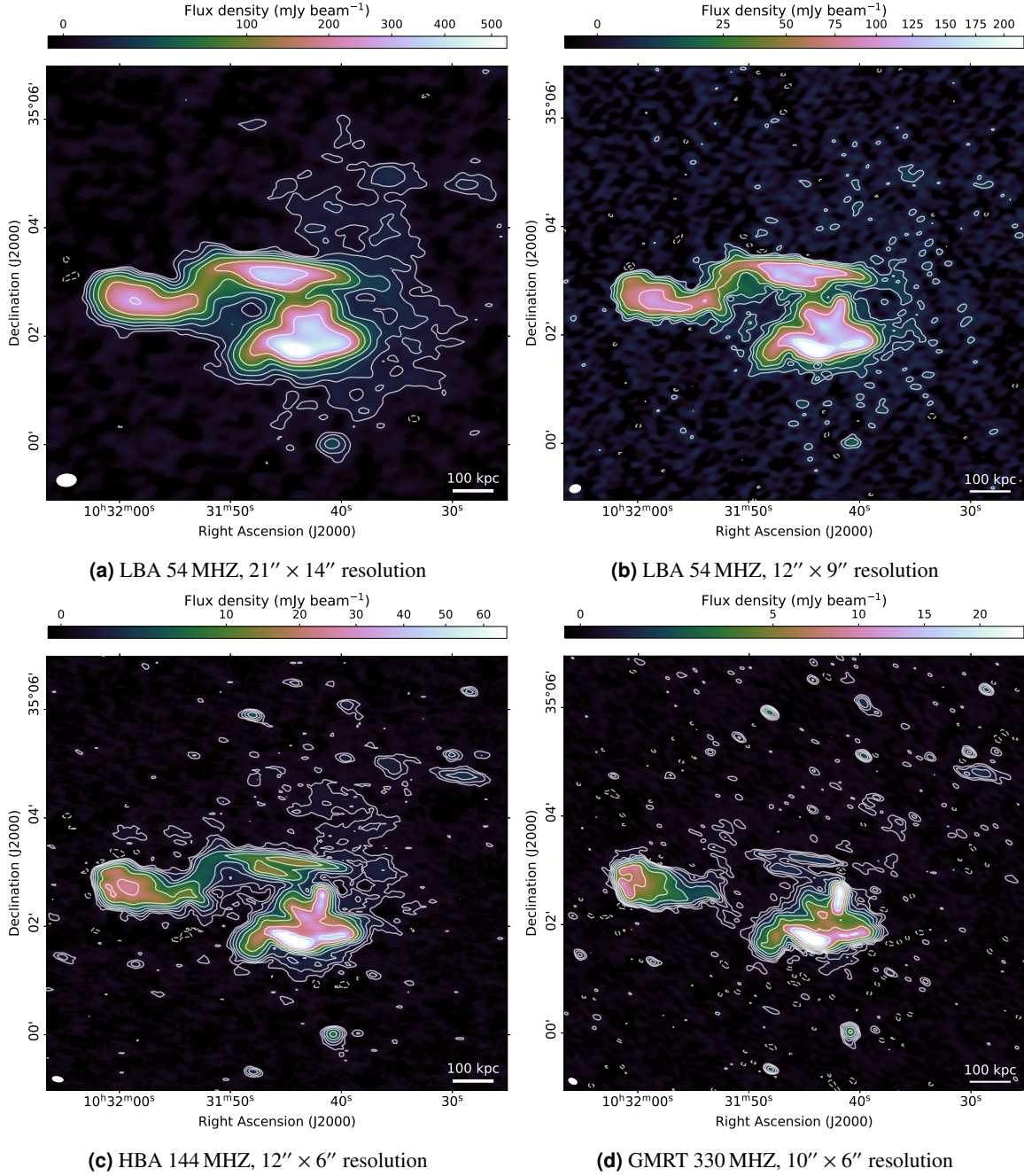


Figure 4.1: Four images (a) to (d) showing A1033 at different frequencies and resolutions. Contours start from 3σ and increase in powers of two. Dashed contours correspond to -3σ . The white ellipse in the bottom left corner of each image corresponds to the beam size as reported in Tab. 4.2. Image (d) was produced using archival GMRT data from de Gasperin et al. (2017).

ments in the processing pipelines, to increase the sensitivity of the images toward the cluster. LoTSS is observing the entire northern sky with 8 h observations per pointing, covering the frequency range 120-168 MHz. LoTSS pointings are processed by the LOFAR Surveys Key Science Project using the automated direction-independent and -dependent calibration pipelines described in van Weeren

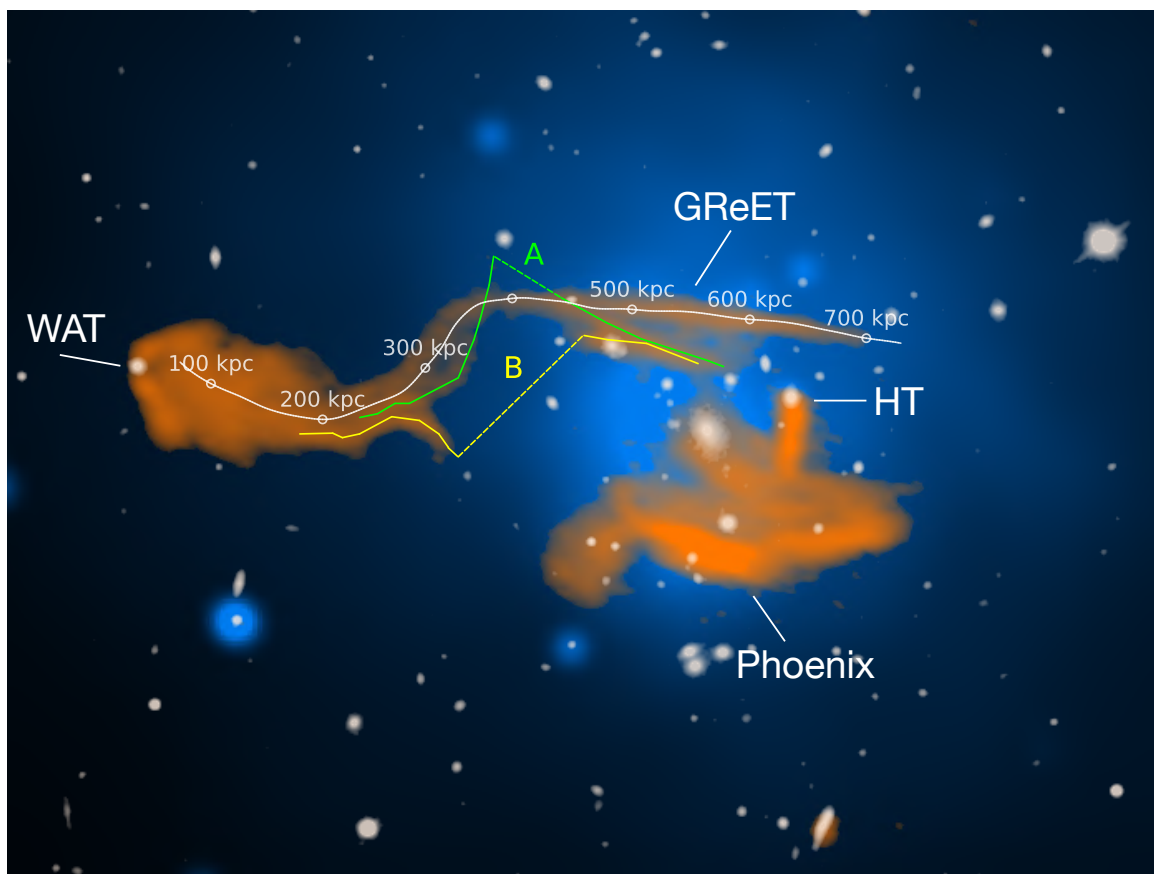


Figure 4.2: Color-composite of the high-resolution LOFAR HBA (orange), the Chandra X-ray (blue) and the SDSS g (white, Alam et al. 2015) images. The white line corresponds to the path that is used to analyze the spectral properties of the GReET, and the dots mark the distance from the starting point in increments of 100 kpc. Paths A (green) and B (yellow) highlight the location of possible interrupted structures. The dashed section shows the discontinuity.

et al. (2016), Williams et al. (2016), de Gasperin et al. (2019), Tasse et al. (2018), and Tasse et al. (2021). A1033 is located within the newly released area of LoTSS Data Release 2 (DR2; Shimwell et al. 2022), and because a cluster in the PSZ2 catalog (Ade et al. 2016), it is also included in the sample of PSZ2/LoTSS-DR2 clusters recently analyzed by Botteon et al. (2022). Here, we used the reprocessed dataset presented in Botteon et al. (2022), in which the data quality has been improved using the extraction and self-calibration procedure described in van Weeren et al. (2021). We used WSCLEAN (Offringa et al. 2014; Offringa & Smirnov 2016) to reimage the data and study the properties of the diffuse emission in the cluster. The final HBA image is shown in Fig. 4.1c. It has a resolution of 12×6 , and with a noise level of $110 \mu\text{Jy beam}^{-1}$, it is about 40% deeper than the image previously presented in de Gasperin et al. (2017).

4.3 Results

In Tab. 4.2 we summarize the medium- and high-resolution LBA as well as the HBA and GMRT images of A1033 displayed in Fig. 4.1. In Fig. 4.2, the radio sources in the cluster are labeled. A

connection between the WAT radio galaxy east of the cluster and the GReET is visible at 54 and 144 MHz. A second radio galaxy with a head-tail morphology is marked HT in the figure.

For our analysis, we assumed a systematic flux scale uncertainty of 10% for the LOFAR LBA, LOFAR HBA, and the GMRT (de Gasperin et al. 2021; Shimwell et al. 2022; Chandra et al. 2004). For all radio images, a common lower uv -cut of 100λ was used during imaging, and all imaging was carried out using WSCLEAN. When information from multiple frequencies is combined for spectral index mapping or spectral shape-modeling, a number of preprocessing steps are required to ensure that the images are comparable. For each image, a point-source catalog was created using PyBDSF, and the images were aligned by cross-matching point sources to account for potential astrometric errors at a level below $5''$. Next, all images were convolved to the smallest common circular beam. Last, they were regridded on the same pixel layout.

4.3.1 Spectral index maps

We created spectral index maps in the ranges 54-144 MHz and 144-323 MHz. For this, we discarded all pixels with a surface brightness significance below $3\sigma_{\text{rms}}$ in at least one of the two relevant images. We used the linear least-squares method in log-space to determine the spectral index values. The uncertainties were estimated according to Gaussian propagation of uncertainty. To investigate the spectral shape, we created a curvature map from the spectral index maps. The curvature is defined as $\Delta_\alpha = \alpha_{54}^{144} - \alpha_{144}^{325}$. The high-resolution spectral index and curvature maps are displayed in Fig. 4.3, and the corresponding uncertainty maps are provided in Fig. E.1. At the position of the WAT host galaxy, we measure a spectral index of $\alpha = -0.65$ in both frequency intervals. Along the tail, the spectral index gradually steepens. The steepening is stronger at higher frequency. At the location of the bend in the tail, the spectral index does not steepen further and remains approximately constant along the GReET for both frequency ranges. For this section of the tail, we measure an extremely steep spectral index of -3.8 ± 0.18 between 144 and 325 MHz, which is fairly uniform for a projected distance of 300 kpc. Toward ultra-low frequencies, the spectrum of this region shows extreme curvature ($\Delta_\alpha = 1.8 \pm 0.23$).

4.3.2 Spectral aging analysis

In absence of acceleration mechanisms, the electron population in a radio galaxy tail is subject to aging due to synchrotron and inverse Compton losses. This causes a spatial evolution of the spectral shape along the tail depending on the magnetic field, injection history, and injection spectral index of the active galactic nucleus (AGN) as well as the projected velocity of the radio galaxy. In the following, we consider this pure-aging scenario for the WAT and examine whether it agrees with our multifrequency observations. This is the expected scenario when no acceleration mechanisms, usually related to ICM shocks, are present in the tail. For our spectral aging model, we probed a path along the brightest part of the tail where we measured the flux densities at 54, 144, and 323 MHz and the spectral indices between 54-144 and 144-323 MHz in 23 different $12.5''$ beam-sized regions that were separated by the beam FWHM. This path is shown in Fig. 4.2, and the flux density and spectral index evolution as a function of distance is shown in Fig. 4.4. We considered the Jaffe-Perola (JP) plasma aging model (Jaffe & Perola 1973), which is the most commonly used model for the aging of radio galaxies, to describe the spectral distribution for the first 300 kpc of the tail, before the brightness of the tail increases again (de Gasperin et al. 2017). We performed a nonlinear least-squares fit of the JP model to the spectral index points, assuming that the projected velocity v_\perp of the galaxy along the path is constant.

From the spectral index maps, we estimate the injection index to be $\alpha_{\text{inj}} = -0.65$. The aging

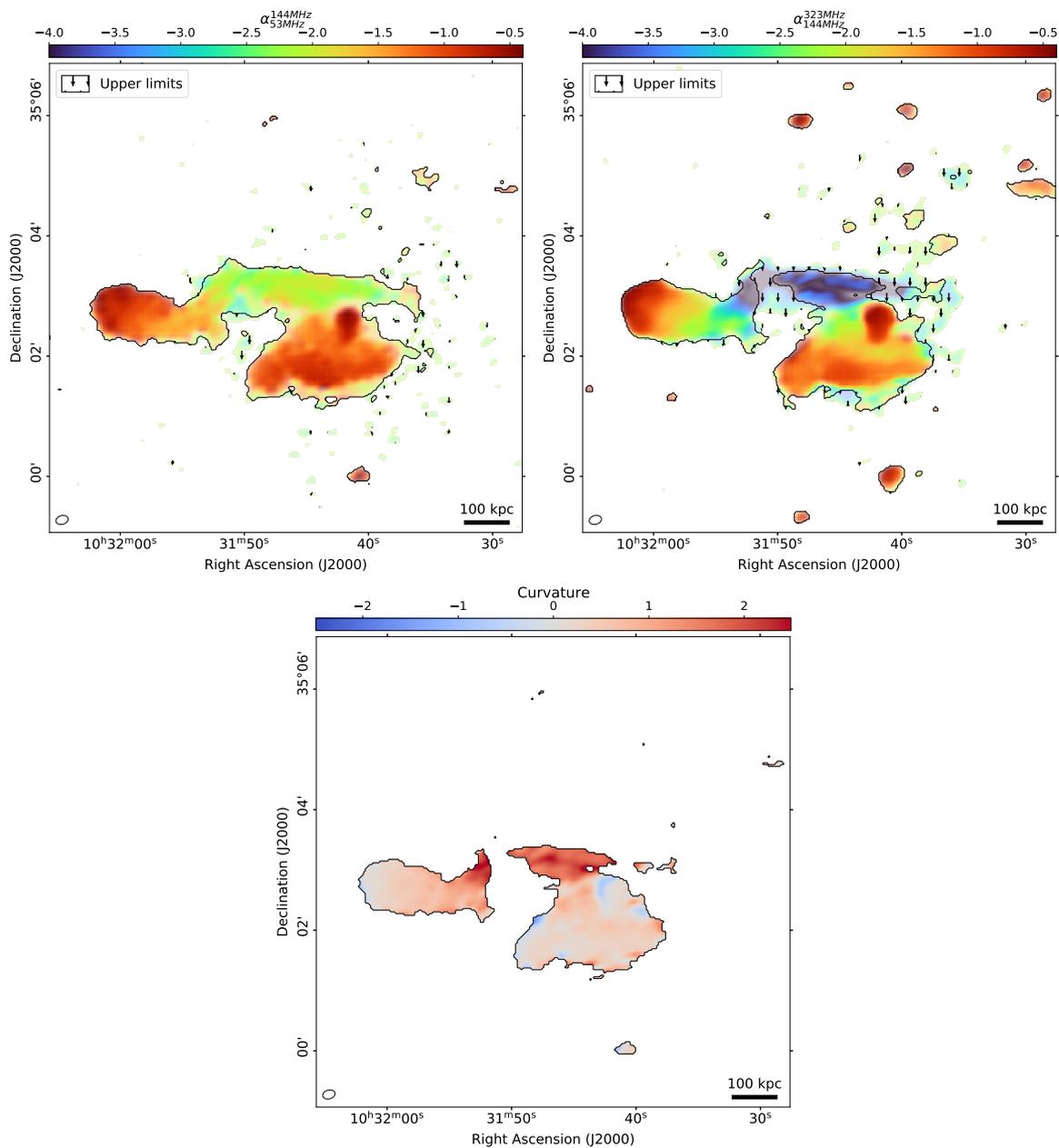


Figure 4.3: High-resolution spectral index map of A1033. The top left image shows the spectral index between 54 and 144 MHz, and the top right image shows the same between 144 and 323 MHz. The images are on the same color scale and have an angular resolution of $12'' \times 9''$. Upper limits below -1.6 are outside the black contours and marked by arrows. The saturation scales inversely with the uncertainty on the spectral index. The bottom image shows the corresponding curvature map, defined as the difference $\Delta_\alpha = \alpha_{54}^{144} - \alpha_{144}^{325}$.

4 A1033: Radio halo and GReET

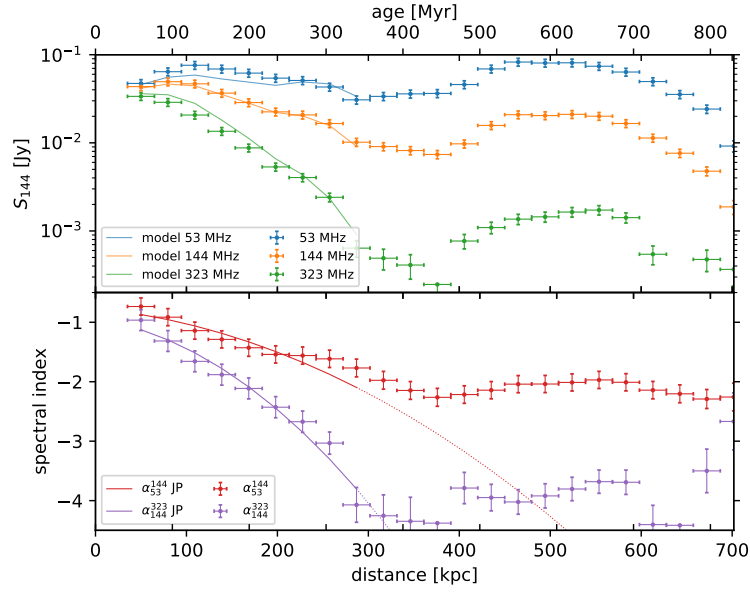


Figure 4.4: Flux density (top) and spectral index (bottom) measured in the $12.5''$ beam-sized regions shown in Fig. 4.2 as a function of distance and estimated age. The continuous lines show the best-fitting model ($\chi^2/\text{d.o.f.} = 29.5/17$) assuming minimum aging ($B = 2.3 \mu\text{G}$) with a projected velocity of 780 km/s. The dotted lines show an extrapolation of this model.

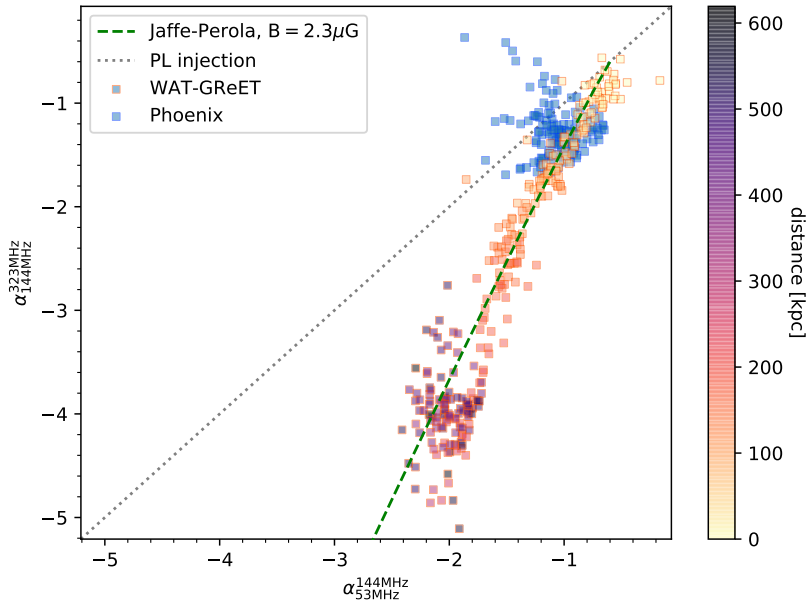


Figure 4.5: Color-color plot of A1033. Each square represents a $5'' \times 5''$ region of the WAT/GReET (orange edges) or phoenix (blue). For the WAT/GReET area, the square faces are color-coded according to their approximate distance from the injection point. Additionally, two lines show the spectral properties for a power-law injection (dotted gray) and for a JP aging model with $B = 2.3 \mu\text{G}$ (dashed green).

history of our model then depends on the magnetic field B and the velocity v_{\perp} . Unfortunately, the magnetic field and the projected velocity are strongly correlated, implying that it is not possible to distinguish between a scenario with a magnetic field close to the minimum aging field strength and a lower velocity and a scenario with more rapid losses and a higher velocity of the WAT galaxy (as illustrated in Fig. F.1). Therefore, we considered a scenario that maximizes the lifetime of the electrons, which provides an upper limit on the radiative age of the plasma. The lifetime of the CRe in the relevant energy regime depends on the magnetic field B as $\tau_{\text{age}} \propto \sqrt{B}/(B^2 + B_{\text{CMB}}^2)$ (Stroe et al. 2014), where $B_{\text{CMB}} = 3.2 \times (1+z)^2 \mu\text{G}$ (Longair 2011) is the magnetic field strength equivalent to the cosmic microwave background (CMB) energy density at redshift z . The expression for τ_{age} takes its maximum value at the minimum loss magnetic field $B = B_{\text{min}}$, where the loss rates due to synchrotron radiation and inverse Compton scattering with the CMB are equal. This is given by $B_{\text{min}} = B_{\text{CMB}}/\sqrt{3}$ at the redshift of A1033, $B_{\text{min}} = 2.3 \mu\text{G}$. We used the nonlinear least-squares method to fit a JP model to the spectral index data points (see Appendix F). By fitting the model to the spectral index points and not the flux densities, we can eliminate the normalization factors and thereby reduce dependences on the injection history of the AGN. The best-fitting model has a projected velocity of $v_{\perp} = 780 \text{ km/s}$ with a reduced χ^2 statistic of $\chi^2/\text{d.o.f.} = 29.5/17$, which agrees reasonably well with the $\approx 730 \text{ km/s}$ found in de Gasperin et al. (2017). This corresponds to a maximum age of the GReET of 800 Myr. The spectral index and flux density data points as well as the best-fitting model are shown in Fig. 4.4. For the flux density models, the flux normalization was fit in log-space independently as a free parameter for each beam-sized region.

To complement the spectral analysis, we created a color-color map. To do this, we calculated the 54-144 and 144-323 MHz spectral indices in $5''$ square boxes in a region covering the WAT and GReET and a second region covering the radio phoenix. We considered all boxes within the two regions with a significance above $3\sigma_{\text{rms}}$ at all three frequencies. For comparison, we also show the spectral trajectory of a power-law injection and the JP aging model discussed above. For points along the WAT and GReET, we additionally color-code the distance from the injection point along the tail. The resulting diagram is shown in Fig. 4.5. The boxes associated with the radio phoenix occupy a rather confined region in the spectral index space without clear trends. In contrast, along the WAT, there is a clear steepening with increased distance from the injection point. The spectral index points depart from the PL-injection spectrum along a trajectory that agrees with a JP model with increased distance. After 300 kpc, the steepening between 54-144 and 144-323 MHz stops and the boxes corresponding to the following part of the GReET scatter around $\alpha_{144}^{323} = -4$ and $\alpha_{54}^{144} = -2$.

4.3.3 Source-subtracted low-resolution images

The medium-resolution images Fig. 4.1a and Fig. 4.1c show an extended diffuse radio emission superimposed on the bright sources associated with individual radio galaxies, the GReET and the radio phoenix. In the LOFAR images, emission with an extension of several 100 kpc is visible at 54 MHz as well as at 144 MHz. This emission is associated with the radio halo detected in A1033 (Botteon et al. 2022). To isolate the emission of the radio halo from the foreground sources, we obtained a model for the compact sources based on high-resolution (Briggs = -1.0) images at 54 MHz, 144 MHz, and 323 MHz. This model is restricted to the clean components in a region that only includes the sources in the high-resolution images (e.g., the radio galaxies, GReET, and phoenix), and subtracted from the data, identical regions are used at all three frequencies. We reimaged the subtracted data using baselines in the range $100\text{-}20000 \lambda$ and tapering the imaging weights to a resolution of $25''$ to enhance the extended emission. The resulting images are displayed in Fig. 4.6 together with the regions we used to restrict our subtraction- model. In the LOFAR maps at 54 and 144 MHz in Fig. 4.6, the

4 A1033: Radio halo and GR_{ET}

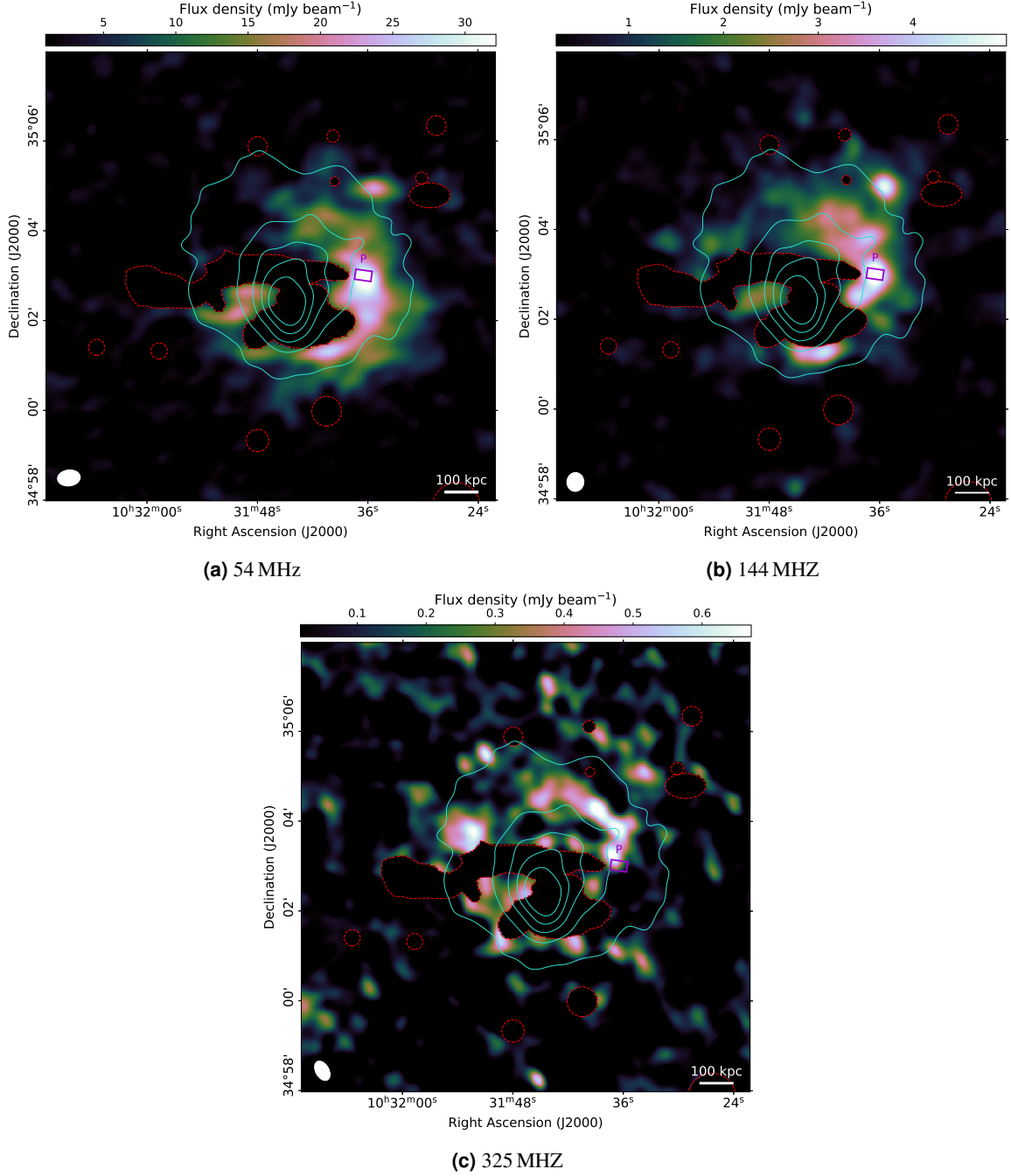


Figure 4.6: Source-subtracted low-resolution images. The image weights are tapered to a resolution of 25". Red contours indicate sources that were subtracted from the data, and cyan contours are smoothed Chandra X-ray contours in the energy band 0.5-7 keV (de Gasperin et al. 2015), linearly spaced between 10-100 σ , where 1 σ = 6.6×10^{-6} photons s⁻¹ cm⁻² arcmin⁻². The purple rectangle labeled *P* marks the brightest part of the visible halo.

extended emission is significantly detected at a surface brightness above $5\sigma_{\text{rms}}$ for a region with a diameter of ≈ 700 kpc except for the subtracted regions. The shape is approximately circular in both frequencies, but some morphological differences exist. At 54 MHz, the halo appears to extend further to the southwest, while a hole in the emission is visible in the northeast. Given the complex procedure of the calibration of a bright, extended source with complex morphology superimposed on the faint, even more extended halo emission together with the source subtraction, we cannot exclude the possibility that these differences in morphology in the lower-significance regime are not physical, but rather artifacts in the data. At 323 MHz, the detected emission appears more patchy, probably because of artifacts caused by calibration errors or radio frequency interference in the GMRT map. In the low-resolution images, we also display the point-source-subtracted Chandra X-ray contours from de Gasperin et al. (2015). The shape of the radio emission is approximately circular and mostly confined within the X-ray contours.

4.3.4 Calculating the radio halo flux

To estimate the total flux density of the halo, we employed the halo flux density calculator HaLo-FDCA (Boxelaar et al. 2021), an MCMC code for estimating halo flux densities with reduced human bias. The code can handle masks to exclude image regions from the analysis. This allowed us to exclude the subtracted regions that do not contain reliable emission. We used the code to fit a spherically symmetric exponential surface-brightness profile described by

$$I(r) = I_0 e^{-\frac{r}{r_e}} \quad (4.1)$$

to the data. Here, $I(r)$ is the surface brightness at a distance r from the profile center, I_0 is the peak surface brightness, and r_e is the e-folding radius (Murgia et al. 2009). This empirical model has frequently been found to describe radio halos accurately (e.g., Vacca et al. 2014; Osinga et al. 2021; Botteon et al. 2021a,b) and it comes with a minimum number of free parameters, which is beneficial for the halo in A1033, which is partly obscured by other sources. A similar analysis for A1033 in LOFAR HBA is presented in Botteon et al. (2022). To allow a consistent analysis of the LBA and HBA data specifically tailored to A1033, we repeated the source subtraction, imaging, and fitting procedures also for the HBA data.

The result of the halo flux calculation is a 1.46 ± 0.15 Jy at 54 MHz and 0.29 ± 0.03 Jy at 144 MHz. The detailed parameters are listed in Tab. 4.3, and plots of the halo fit result and fit residual are shown in Fig. G.1. The location and extension of the best-fitting models at 54 MHz and 144 MHz agree well with e-folding radii of 154 ± 2 and 165 ± 3 kpc, respectively. The LBA model is slightly farther south and the radius is smaller by 7%. We also manually measured the flux density within the respective $3\sigma_{\text{rms}}$ contours $F_{3\sigma}$ of the halo in Fig. G.1, obtaining $F_{54\text{MHz}}^{3\sigma} = 0.87 \pm 0.09$ and $F_{144\text{MHz}}^{3\sigma} = 0.15 \pm 0.02$. Due to the missing extrapolation of the emission in the masked regions, the manually measured flux is a lower limit for the total flux of the halo. The ratio of the manually measured and the fitted flux density is different between LBA and HBA (0.6 and 0.52). We attribute this to a small difference in the location and size of the fitted surface brightness profile. We estimate the total radio power at 150 MHz of the halo based on the HaLo-FDCA results. The resulting value is $P_{150\text{MHz}} = 1.22 \pm 0.13 \times 10^{25} \text{ W Hz}^{-1}$, where a spectral index of $\alpha = -1.65$ was used for extrapolation and k -correction, as we justify in the following Sect. 4.3.5. The independent estimate of the radio power in Botteon et al. (2022) ($P_{150} = 1.09 \pm 0.28 \times 10^{25} \text{ W Hz}^{-1}$) is consistent with ours (at about 1σ), but their reconstructed morphology differs significantly ($r_e = 165 \pm 3$ to $r_e = 103 \pm 1$). We interpret this to mean that the halo morphology is more susceptible to differences in masking and fitting than the flux density of the halo. In general, the fitted parameters of the halo model are subject

to a systematic uncertainty connected to the masking and subtraction procedure, which is hard to assess and was therefore not accounted for in our uncertainties.

Table 4.3: Halo fit results. The total flux density F_{FDCA} includes an extrapolation of the model in the masked region.

ν [MHz]	I_0 [$\mu\text{Jy arcsec}^{-2}$]	r_e [kpc]	F_{FDCA} [Jy]	$F_{3\sigma}$ [Jy]	P_ν [$10^{25} \text{ W Hz}^{-1}$]
54	50.33 ± 5.14	154 ± 2	1.46 ± 0.15	0.87 ± 0.09	6.56 ± 0.67
144	8.63 ± 0.90	165 ± 3	0.29 ± 0.03	0.15 ± 0.02	1.30 ± 0.13

4.3.5 Spectral index of the radio halo

We used the source-subtracted images presented in Fig. 4.6 to create maps of the low-resolution spectral index and to study the spatial variation of the spectral index within the radio halo. The spectral index maps were created as described in Sect. 4.3.1. We excluded the regions that were used to subtract the compact sources. These maps are displayed in Fig. 4.7, and the uncertainty maps are shown in Fig. E.2. In the range of 54-144 MHz, the spectral index of the halo could be determined significantly across a large area. The northern part of the halo is less steep with a spectral index of about $\alpha = -1.5$, and the southwestern region is steeper than $\alpha = -2$. The same trend extends to the ultra-steep upper limits in the southwest and to the flat-spectrum features expressed by lower limits in the northeast. As stated in Sect. 4.3.3, we cannot exclude the possibility that these features are at least partly a consequence of systematic errors in the calibration. Because only a part of the radio halo is detected above a significance of 3σ in the 323 MHz GMRT map, we can constrain the spectral index in the range 144-323 MHz only in a comparatively small area. In this region northwest of the GReET, the spectral index is $\alpha_{144}^{323} = -2.15 \pm 0.19$. For the majority of the remaining halo area, we can constrain the spectrum to be steeper than $\alpha = -2$. This suggests that the spectrum of the halo is curved.

To estimate the integrated halo spectral index between 54 and 144 MHz, we compared different methods. Using the halo fits, we derive a spectral index of $\alpha_{\text{FDCA}} = -1.65 \pm 0.17$ based on the integrated surface brightness. If the flux density is measured manually in the region where we have $> 5\sigma$ significance at both frequencies, the corresponding integrated spectral index is $\alpha_{\text{man}}^{5\sigma} = -1.74 \pm 0.14$. A more conservative estimation using only the area above $10\sigma_{\text{rms}}$ in both images yields $\alpha_{\text{man}}^{10\sigma} = -1.69 \pm 0.15$. We adopted the value based on the HaLo-FDCA fluxes as reference value for the halo because it does not depend on the sensitivity of the observations.

4.4 Discussion

4.4.1 Spectral study of the GReET

In Fig. 4.4 we show the flux density and spectral index evolution along the tail together with the best-fitting JP model as described in Sect. 4.3.2. After about 200 kpc from the injection point, the spectral index appears to be systematically flatter than the best-fitting model. To some degree, this deviation might be caused by a change in velocity of the WAT. Presumably, the galaxy reached a maximum velocity at the minimum of its trajectory in the cluster potential well and slowed down afterward. This is not accounted for in our constant-velocity assumption. However, at about ≈ 350 kpc from

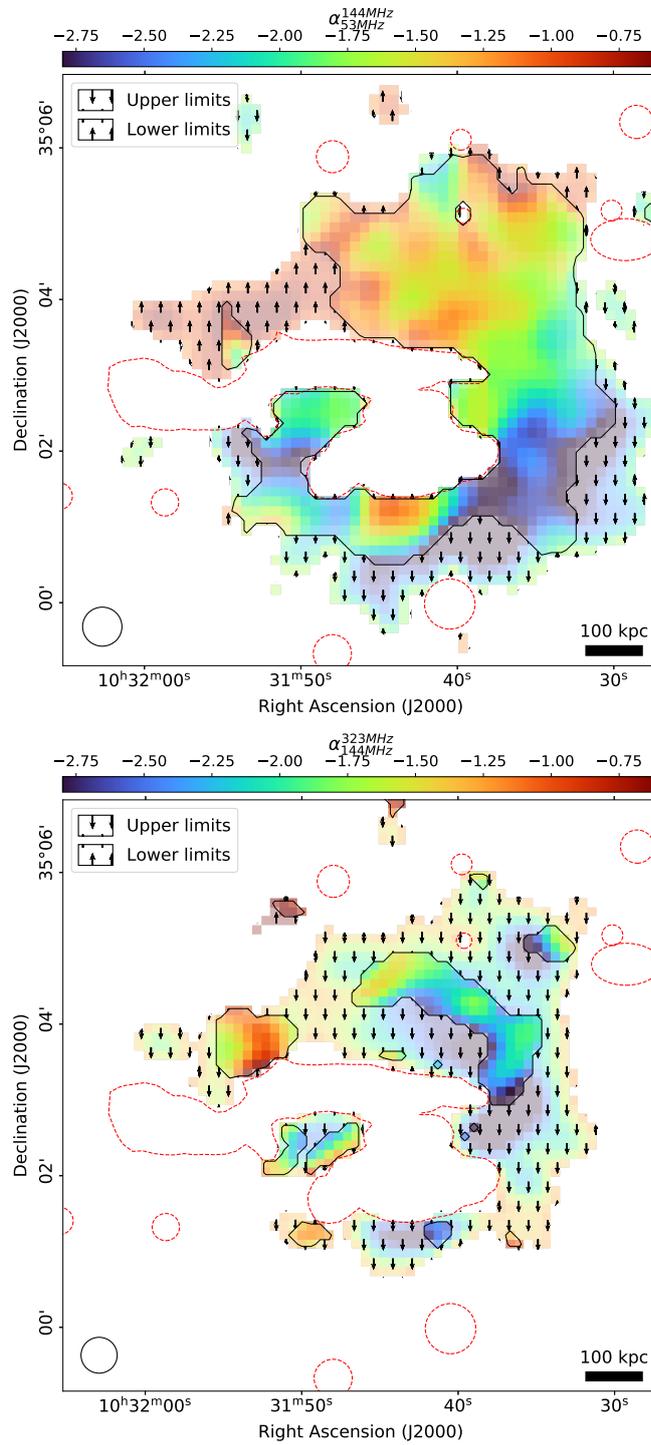


Figure 4.7: Source-subtracted spectral index maps at a spatial resolution of $30''$. The top panel shows the spectral index between 54 MHz and 144 MHz, and the bottom panel shows the same between 144 MHz and 325 MHz. The 3σ upper and lower limits are indicated by arrows. Dashed red lines highlight the regions from which sources were subtracted.

the injection point, the spectrum does not steepen further and a plateau in spectral index associated with the GReET is reached. This constant and even flattening spectral index cannot be explained with the extrapolation of a pure aging model, even when a change in the WAT velocity is considered. The same stalling in the spectral index trend can also be observed in the color-color diagram in Fig. 4.5, where after initial JP-like aging, the spectral evolution stops and appears frozen for several 100 kpc. Consequently, an additional energization mechanism is required. This mechanism needs to be just efficient enough to compensate for the radiation losses, but not so strong that the spectral shape is significantly flattened.

This was previously concluded in de Gasperin et al. (2017), where turbulent reacceleration of the electrons in the tail by magnetic pumping was proposed as a possible mechanism. The suggested scenario is that turbulence is forced into the tail by interactions with the surrounding ICM, which can provide mild acceleration that acts for sufficiently long timescales to explain the homogeneous nature of the GReET. The extreme curvature we detect fully supports the scenario outlined in the previous work: it is a consequence of a cutoff in the electron energy spectrum caused by the balance between the very gentle acceleration and the cooling of CRe, with an acceleration time of the radio-emitting electrons comparable to their cooling time (e.g., Brunetti & Jones 2014).

4.4.2 Turbulent velocity

In the high-resolution map shown in Fig. 4.2, the tail of the WAT shows disrupted features. We suggest that these can be attributed to large-scale shear flows and turbulent motions in the ICM. The tail of the WAT appears to be split into three filaments after about 250 kpc from the injection point. The brightest filament directly connects to the GReET, and the fainter filaments, labeled in Fig. 4.2 as A and B, are discontinuous. Because the GReET is clearly bifurcated, where one of the two parts has no clear connection to the WAT, we consider the possibility that a shear motion in the ICM, at a scale close to the injection scale of the turbulence, caused either A or B to disconnect from the southern segment of the GReET. This then allows us to constrain the large-scale turbulent velocity in the ICM: In the diffusion regime, CRs are displaced a distance d after a time t according to $d \sim \sqrt{tD}$, where D is the spatial diffusion coefficient. For super-Alfvénic turbulence, we can approximate $D \sim v_L L$, where v_L is the turbulent velocity at scale L . If the displacement $d \sim L$, the velocity of large-scale motions can be estimated as $v_L \sim d/t$, where t can be constrained from the age of the plasma from our limit on the velocity of the WAT. We estimate the age at the discontinuities of path A and B to be $t_A < 380$ Myr and $t_B < 310$ Myr using the distance of the discontinuities A and B from the injection point (300 kpc and 250 kpc, respectively) as well as our limit on the WAT velocity of ≈ 780 km s⁻¹. The corresponding projected length scales of the discontinuity are $d_A = 65$ kpc and $d_B = 144$ kpc. This means that we can constrain the turbulent velocity to $v_A \geq 167$ km s⁻¹ and $v_B \geq 464$ km s⁻¹. These values fall within the typical range found for large-scale turbulent motions in simulations of cluster mergers, which are several 100 km s⁻¹ (Vazza et al. 2018). This velocity can also be compared to the sound speed c_s derived from the ICM temperature $kT_{\text{ICM}} = 6.15_{-0.88}^{+1.14}$ keV found in the Chandra X-ray analysis of de Gasperin et al. (2015), which yields

$$c_s = 1480 \left(\frac{T_{\text{ICM}}}{10^8 \text{ K}} \right)^{1/2} \text{ km s}^{-1} = 1250_{-92}^{+111} \text{ km s}^{-1}. \quad (4.2)$$

This implies that the turbulent motions estimated above are likely subsonic, in agreement with expectations in the ICM (e.g., Brunetti & Jones 2014).

This consideration raises the question of how the tail can resist turbulent diffusion for a timescale of several 100 Myr. When we assume a Kolmogorov cascade, the turbulent velocity at a scale L de-

depends on the size of the scale as $v_L \propto L^{1/3}$. Thus, at a scale equal to the thickness of the filaments, the velocity derived from our estimate should be $v_A(10 \text{ kpc}) \geq 89 \text{ km s}^{-1}$ or $v_B(10 \text{ kpc}) \geq 190 \text{ km s}^{-1}$. If this value is below the Alfvén velocity $v_{\text{Alfvén}}$, which is typically in the range $\sim 100 \text{ km s}^{-1}$ (Brunetti & Jones 2014), Reynolds and Maxwell stresses of magnetic fields may stabilize the narrow tails. Similar considerations have been put forward to explain the stability of radio filaments in AGN bubbles (Brienza et al. 2021). From the Navier-Stokes equation, the term corresponding to matter motions on a scale k : $\rho dv^2 k$ competes against magnetic field line tension on the same scale: $B^2 k / (4\pi)$. Thus, for the line tension to dominate, we require

$$B \geq v \sqrt{4\pi\rho}. \quad (4.3)$$

For a reference density 100 kpc from the cluster center (at the projected distance to the GReET) of $\rho \approx 10^{-23} \text{ kg m}^{-3}$, which is a typical value for clusters similar to A1033, and a velocity in the range derived above from $v_A(10 \text{ kpc}) \geq 89 \text{ km s}^{-1}$ to $v_B(10 \text{ kpc}) \geq 190 \text{ km s}^{-1}$, a magnetic field of at least 3.1 - 6.7 μG is required. For the upper half of this range, the magnetic field in the GReET would be greater than what is usually considered for magnetic fields in the ICM even for significantly more massive clusters (e.g., Bonafede et al. 2010), which would imply that it must be seeded from the WAT and sustained for the life time of the GReET. Lower values for the magnetic field in the tail are possible if the distance between the cluster center and the GReET is significantly larger than the projected distance, such that the density ρ entering Eq. 4.3 is lower.

Furthermore, we tried to quantify the conditions under which the electrons can be confined in the GReET for 800 Myr: In general, diffusion perpendicular to magnetic filaments is small, which allows an efficient trapping of the electrons. However, if the magnetic field in the GReET is turbulent, that is, sub-Alfvénic as we require to explain the stability, perpendicular diffusion of electrons may be driven by stochastic diffusion of field lines. The perpendicular diffusion length of the CRE $l_{\perp, \text{cr}}^2$ after a time t can be estimated as (Lazarian & Yan 2014)

$$l_{\perp, \text{cr}}^2 \sim \frac{(Dt)^{3/2}}{27L} M_A^4, \quad (4.4)$$

where in this case, the Alfvénic Mach-number $M_A \sim 1$ and the injection scale $L \sim L_{\perp} = 10 \text{ kpc}$ is the traverse scale of the GReET. We define the lifetime of the electrons in the GReET as the time when the perpendicular diffusion is comparable to the traverse size $l_{\perp, \text{cr}} \sim L_{\perp}$,

$$t \sim 9L_{\perp}^2 / D. \quad (4.5)$$

To be stable for 800 Myr, a diffusion coefficient below $D = 3.4 \times 10^{29} \text{ cm}^2 \text{ s}^{-1}$ is required, which agrees well with the previous estimate of de Gasperin et al. (2017) and observational results for other clusters based on studies of the metallicity profiles (Rebusco et al. 2005, 2006).

4.4.3 Radio halo

The spectral index of $\alpha = -1.65 \pm 0.17$ between 54 and 144 MHz places the radio halo in A1033 in the USSRH category. Together with the further steepening of the spectrum toward higher frequencies, this agrees with a cutoff in the electron spectrum as predicted by the turbulent acceleration model (Brunetti et al. 2001; Petrosian 2001; Kuo et al. 2003; Cassano et al. 2006; Brunetti et al. 2008). It is well known that radio halos in more massive clusters are more powerful (Cassano et al. 2013; van Weeren et al. 2021; Cuciti et al. 2021). Because the mass of A1033 is considerably lower than that of the vast majority of clusters that are known to host a radio halo, the cluster is expected to have a

lower radio power. In Fig. 4.8 we compare the 150 MHz radio power of the A1033 halo to the radio halos and to the correlations of halo power to cluster mass presented in van Weeren et al. (2021). Furthermore, we show the two halos detected in the LOFAR deep fields Osinga et al. (2021) and the low-power halos discovered in Hoang et al. (2021) and Botteon et al. (2021a). All these radio halos are detected close to 150 MHz and are hosted by clusters in the PSZ2 catalog. This comparison shows that while A1033 is one of the lowest-mass clusters hosting a radio halo, the halo is quite powerful. It lies considerably above the low-frequency correlations. Compared to the 150 MHz correlations from van Weeren et al. (2021), it is overluminous by a factor in the range of 7 - 55. This is much larger than the intrinsic scatter of the correlations, which is ~ 3 .

The relatively large radio power is notable given the ultra-steep spectrum nature of the A1033 halo because in general, USSRH are expected to be less powerful (Cassano et al. 2010; Cuciti et al. 2021). We investigated whether the power estimate of the halo might be contaminated by other sources. We found that while the region we used to subtract the GReET indeed contains the significant emission in the HBA high-resolution map, images at lower resolution indicate a less confined feature with a ten times lower surface brightness in extension of the GReET. This patch of emission is coincident with the brightest region of the unobscured part of the radio halo, labeled *P* in Fig. 4.6. To ensure that patch *P* does not contaminate our radio power estimate significantly in case it is not related to the halo, we repeated the flux density calculation, this time with a more conservative mask. The resulting radio power estimate is lower by only 1.3%. Consequently, contamination from embedded sources cannot explain the large observed power.

A radio halo with a power above the correlation should correspond to an energetic merger event and/or a merger in an evolutionary phase close to the peak power. In both cases, the X-ray surface brightness distribution should show strong signs of disruption. The X-ray morphological parameters for the cluster were determined in the Chandra analysis in de Gasperin et al. (2015). While the X-ray concentration parameter *c* (defined, e.g., in Cassano et al. 2013) does not unambiguously qualify the cluster as a merging one ($c = 0.200 \pm 0.004$), the centroid shift $w = 0.086 \pm 0.006$, the high differential velocity of the brightest cluster galaxy (BCG), and a distinct bimodality in the redshift distribution indicate a clear and possibly strong merger scenario (de Gasperin et al. 2015). The strong merger might not fully show in the X-ray morphology parameters because it is likely occurring with a significant line-of-sight component, as also concluded in de Gasperin et al. (2015) based on the BCG dynamics and redshift bimodality. Cuciti et al. (2021) found a trend of the distance from the correlation of radio power to cluster mass and the X-ray morphological disturbance. Following their definition of the disturbance $d_{X\text{-ray}}$, we have $d_{X\text{-ray}} = 0.86 \pm 0.03$, which places A1033 in the region of disturbed clusters. While a more energetic merger should lead to a flatter spectral index, the relatively low cluster mass might be the dominant factor determining the spectral properties. An increasing number of spectral studies of halos in low- and intermediate-mass clusters will help to constrain the spectral properties of halos in this mass regime.

A further reason for the comparatively high power and the steep spectrum of the halo in A1033 could lie in a greater abundance of seed electrons in the cluster, possibly accumulated by the various other bright radio sources. The synchrotron luminosity in reacceleration models is given by (e.g., Brunetti & Vazza 2020; Di Gennaro et al. 2021)

$$P \propto F\eta \frac{B^2}{B^2 + B_{\text{cmb}}^2}, \quad (4.6)$$

where η is the (re-)acceleration efficiency, and $F = \rho v_{L_{\text{inj}}}^3 / L_{\text{inj}}$ is the turbulent energy flux in the emitting volume, which depends on the ICM density ρ as well as the injection scale L_{inj} and turbulent

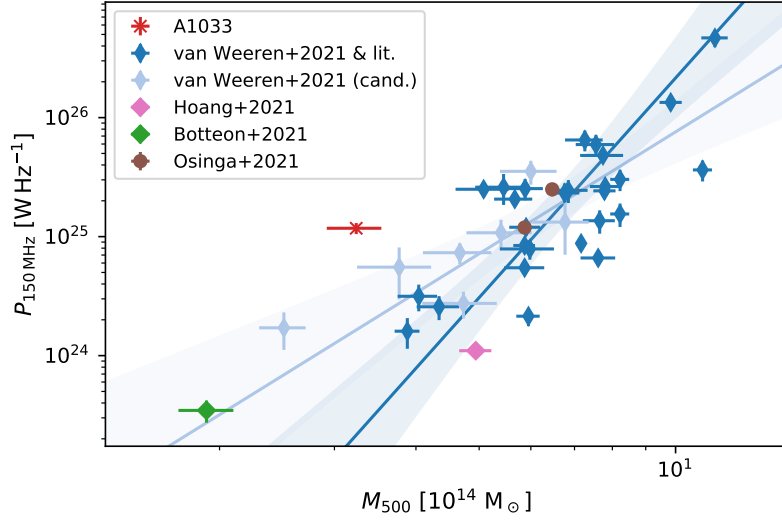


Figure 4.8: Radio power at 150 MHz of low-frequency radio halos as a function of the PSZ2 mass. The lines indicate the extreme cases of the correlations of radio power to cluster mass reported in van Weeren et al. (2021), which were derived using different fitting methods and samples. The dark blue line shows the steepest (orthogonal method) and the light blue line shows the flattest (including candidate halos, Y—X method) correlation. The shaded regions show the 95% confidence interval. The halos reported as ‘van Weeren+21 & lit.’ include a literature radio halo sample (de Gasperin et al. 2015; Cordey 1985; Botteon et al. 2019; Bîrzan et al. 2019; Wilber et al. 2018; Savini et al. 2018, 2019; Bonafede et al. 2018; Hoang et al. 2019b,a; Macario et al. 2013; George et al. 2017; Duchesne et al. 2021).

velocity $v_{L_{\text{inj}}}$. The efficiency η is the fraction of the turbulent energy flux contributing to CRe acceleration and proportional to the CRe energy density u_{CR} : $\eta \propto u_{\text{CR}}$ (Brunetti & Lazarian 2007; Bonafede et al. 2022). Following from Eq. 4.6, for the same CRe energy spectrum, a higher electron density would accordingly increase the halo power while not causing a spectral flattening. We speculate that at the low surface brightness patch in extension of the GReET (marked P in Fig. 4.6) with spectral properties in between those of the GReET and the halo, we might witness electrons that were conserved by the GReET entering the CRe population associated with the halo. A similar connection was proposed in Wilber et al. (2018), for example.

Because only a very small number of halos are detected in clusters with masses similar to or lower than A1033, the shape and scatter of the correlation in this mass range is not yet well determined. The detailed analysis of the largest sample of radio halos so far, based on the second data release of LoTSS (Botteon et al. 2022), will provide strongly improved constraints in the near future (Cuciti et al. in prep.).

4.4.4 Radio phoenix

The bright extended source 150 kpc south of the cluster center was previously studied in de Gasperin et al. (2015) and was categorized as a radio phoenix. A connection to a bright elliptical galaxy (marked S in Fig. 4.2) that coincides with a radio point source at 1.4 GHz was proposed. The radio phoenix has an irregular and elongated shape with a largest linear size of ~ 380 kpc. Toward the south, it shows a steep gradient, while toward the cluster center, the source is fading more slowly, and at

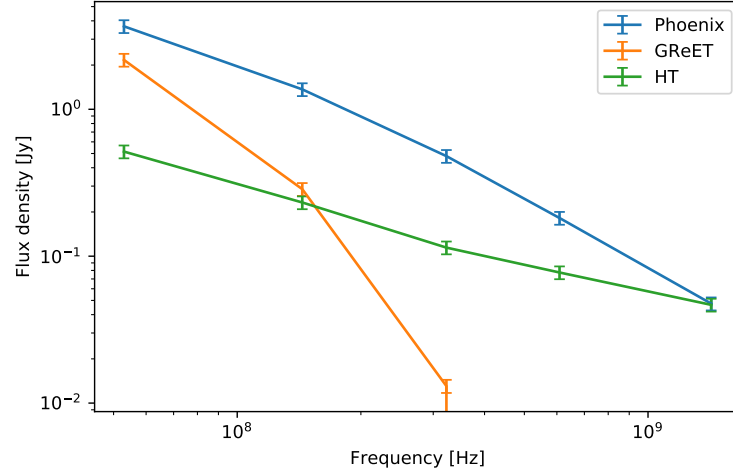


Figure 4.9: Flux densities as a function of frequency. Additional GMRT and VLA data at 609 MHz and 1.4 GHz are taken from de Gasperin et al. (2015, 2017).

lower frequencies, it extends toward the head-tail galaxy and the BCG. In Fig. 4.9, its flux density is compared to the head-tail radio galaxy and the GReET between 54 and 1400 MHz. The source shows spectral curvature. The spectral index flattens from $\alpha_{609}^{1425} = -1.58 \pm 0.17$ (de Gasperin et al. 2015) to $\alpha_{54}^{144} = -0.99 \pm 0.14$. The spatial variation of the spectral properties (Fig. 4.3) does not reveal a clear trend. The spectral curvature we observe is a characteristic feature of radio phoenixes (Enßlin & Gopal-Krishna 2001). Therefore, the ultra-low frequency picture of the source is in line with the phoenix classification. The source differs from the GReET in the spectral shape, its spectrum is significantly less curved between 54 and 323 MHz ($\Delta_\alpha \approx 0.3$ to $\Delta_\alpha \approx 2.0$), and furthermore, its morphology is more irregular and not clearly connected to a radio galaxy.

4.5 Conclusion

We presented an analysis of the galaxy cluster Abell 1033 based on new ultra-low frequency data taken with LOFAR LBA at 54 MHz and on existing data at higher frequencies (LOFAR HBA data at 144 MHz and GMRT data at 323 MHz). The cluster is an especially interesting target because despite its comparatively low mass, it hosts a variety of strong and extended radio sources such as a GReET, a radio phoenix, interacting AGN, and a radio halo, which show very heterogeneous properties. Our findings are listed below.

- For the GReET, we detected extreme spectral curvature. The spectrum steepens from $\alpha \approx -4$ between 144 and 323 MHz to $\alpha \approx -2$ between 54 and 144 MHz. This finding is in line with the emission being generated by strongly aged electrons that are reaccelerated by a mechanism with a very low acceleration efficiency.
- Assuming a maximum lifetime scenario, we found a lower limit for the projected velocity of the WAT of 780 km/s; this agrees with earlier findings. This corresponds to a maximum age of the tail of ~ 800 Myr.
- We investigated the properties of the radio halo in A1033. We found a radio power of $P_{150\text{MHz}} \approx 1.22 \times 10^{25} \text{ W Hz}^{-1}$. This power is higher than the correlations of radio power to cluster mass

by a factor > 7 . At the same time, we found the spectrum of the halo to be ultra-steep between 54 and 144 MHz ($\alpha \approx -1.69$), with a further steepening at higher frequencies.

- We presented possible reasons for both the high luminosity and the ultra-steep spectrum of the halo: The halo power might be explained by an energetic merger that does not fully reveal itself in the X-ray morphology parameters due to a significant line-of-sight component of the merger axis. This scenario is supported by the redshift bimodality and the high radial velocity of the BCG. This requires that the spectral properties are dominantly controlled by the cluster mass. Alternatively, a particularly high density of CRes, possibly accumulated by the various bright radio sources in the cluster, can explain an increased radio power without spectral flattening. Simulations could be used to investigate whether a significant per-cluster variation of seed electrons can be caused by sources such as the GReET and radio phoenix.
- We detected two candidate disrupted filaments in the GReET. We speculated that large-scale turbulent motions are responsible for the disruption. With the lower limit on the WAT velocity we derived, we constrained the turbulent velocity to be greater than 167 km s^{-1} and 464 km s^{-1} , which is within the typical range found in simulations. The thin tail itself could be stabilized by magnetic fields if the turbulence at these small scales becomes sub-Alfvénic.
- We found that the spectrum of the radio phoenix flattens from $\alpha \approx -1.6$ to $\alpha \approx -1.0$ between 1.4 GHz and 54 MHz. A curved synchrotron spectrum is a characteristic property of radio phoenixes.

With the further advance of low-frequency radio surveys such as LoTSS and LoLSS, it will be possible to perform spectral analyses for a rapidly growing number of cluster radio sources. These will show whether the GReET in A1033 is representative for a greater category of sources or if it is truly special in terms of its low acceleration efficiency. Additionally, systematical analyses of radio halos in clusters of low and moderate mass will lead to a better understanding of the halo power and the spectral index distributions in this mass range.

Acknowledgements

We thank the referee for the useful comments which helped to improve the manuscript. LOFAR is the Low Frequency Array designed and constructed by ASTRON. It has observing, data processing, and data storage facilities in several countries, which are owned by various parties (each with their own funding sources), and which are collectively operated by the ILT foundation under a joint scientific policy. The ILT resources have benefited from the following recent major funding sources: CNRS-INSU, Observatoire de Paris and Université d'Orléans, France; BMBF, MIWF-NRW, MPG, Germany; Science Foundation Ireland (SFI), Department of Business, Enterprise and Innovation (DBEI), Ireland; NWO, The Netherlands; The Science and Technology Facilities Council, UK; Ministry of Science and Higher Education, Poland; The Istituto Nazionale di Astrofisica (INAF), Italy. This research made use of the Dutch national e-infrastructure with support of the SURF Cooperative (e-infra 180169) and NWO (grant 2019.056). The Jülich LOFAR Long Term Archive and the German LOFAR network are both coordinated and operated by the Jülich Supercomputing Centre (JSC), and computing resources on the supercomputer JUWELS at JSC were provided by the Gauss Centre for Supercomputing e.V. (grant CHTB00) through the John von Neumann Institute for Computing (NIC). This research made use of the University of Hertfordshire high-performance computing facility and the LOFAR-UK computing facility located at the University of Hertfordshire and supported by STFC [ST/P000096/1], and of the Italian LOFAR IT computing infrastructure supported and operated by INAF, and by the Physics Department of Turin university (under an agreement with Consorzio Interuniversitario per la Fisica Spaziale) at the C3S Supercomputing Centre, Italy. The data are published via the SURF Data Repository service which is

4 *A1033: Radio halo and GReET*

supported by the EU funded DICE project (H2020-INFRAEOSC-2018-2020 under Grant Agreement no. 101017207). This project is funded by the Deutsche Forschungsgemeinschaft (DFG, German Research Foundation) under project number 427771150. FdG acknowledges support from the Deutsche Forschungsgemeinschaft under Germany's excellence strategy - EXEC2121 "Quantum Universe" - 390833306. V.C. acknowledges support from the Alexander von Humboldt Foundation. RJvW acknowledges support from the ERC Starting Grant ClusterWeb 804208. AB acknowledges support from the VIDI research program with project number 639.042.729, which is financed by the Netherlands Organisation for Scientific Research (NWO), and from the ERC-StG DRANOEL n. 714245. AD acknowledges support by the BMBF Verbundforschung under the grant 05A20STA.

5 Investigating LOFAR 2.0 with Simulations

H. W. Edler, F. de Gasperin, D. Rafferty. *Astronomy & Astrophysics*, 652, p.A37 (2021)

Abstract

Context. There are a number of hardware upgrades for the Low-Frequency Array (LOFAR) currently under development. These upgrades are collectively referred to as the LOFAR 2.0 upgrade. The first stage of LOFAR 2.0 will introduce a distributed clock signal and allow for simultaneous observations using all the low-band and high-band antennas of the array. *Aim.* Our aim is to provide a tool for obtaining accurate simulations for LOFAR 2.0.

Methods. We present our software for simulating LOFAR and LOFAR 2.0 observations, which includes realistic models for all important systematic effects such as the first- and second-order ionospheric corruptions, time-variable primary-beam attenuation, station-based delays, and bandpass response. The ionosphere is represented as a thin layer of frozen turbulence. Furthermore, thermal noise can be added to the simulation at the expected level. We simulate a full eight-hour simultaneous low- and high-band antenna observation of a calibrator source and a target field with the LOFAR 2.0 instrument. The simulated data are calibrated using readjusted LOFAR calibration strategies. We examine novel approaches of solution-transfer and joint calibration to improve direction-dependent ionospheric calibration for LOFAR.

Results. We find that the calibration of the simulated data behaves very similarly to a real observation and reproduces certain characteristic properties of LOFAR data, such as realistic solutions and image quality. We analyze strategies for direction-dependent calibration of LOFAR 2.0 and find that the ionospheric parameters can be determined most accurately when combining the information of the high-band and low-band in a joint calibration approach. In contrast, the transfer of total electron content solutions from the high-band to the low-band shows good convergence but is highly susceptible to the presence of non-ionospheric phase errors in the data.

5.1 Introduction

The Low-Frequency Array (LOFAR) is an interferometer working at low (< 1 GHz) and ultra-low (< 100 MHz) radio frequencies. Most of its stations are located in the Netherlands and it has been operational since 2010 (van Haarlem et al. 2013). It conducts observations in a spectral band close to the low-frequency edge of the radio window, which has received reinforced attention in the last decade. Together with other new generation instruments, such as the Murchison Widefield Array (MWA, Tingay et al. 2013) and the Long Wavelength Array (LWA, Taylor et al. 2012), LOFAR

5 Investigating LOFAR 2.0 with Simulations

pioneers the technological ground for the ambitious plans on the Square Kilometer Array (SKA, Dewdney et al. 2009), which include the low-frequency interferometer SKA-low.

Among the most important research prospects in low-frequency radio astronomy are deep surveys, where phenomena such as the extended emission in galaxy clusters and high-redshift radio galaxies are studied. These sources oftentimes remain undetectable at higher frequencies due to their steep spectral energy distribution. Further science cases include the search for the epoch of reionization hydrogen line, cosmic magnetism, radio detection of exoplanets, mapping of the star-formation history of the universe as well as the observation of pulsars and radio transients.

A challenging limitation for the scientific value of wide-field images is imposed by the direction-dependent corruptions introduced by the ionosphere for Earthbound measurements of cosmic radio signals. This is especially problematic at ultra-low frequencies, where the impact of the ionosphere becomes increasingly dramatic. To accurately account for ionospheric effects during calibration, the development of a new generation of direction-dependent calibration strategies together with the corresponding software environment was initiated during the last decade (Tasse et al. 2021; de Gasperin et al. 2020; Albert et al. 2020; van Weeren et al. 2016). Nevertheless, excellent image fidelity is still hard to achieve with LOFAR for complex fields (e.g. towards the Galactic plane), during exceptionally active ionospheric conditions, and for the lowest part of the frequency band ($\lesssim 40$ MHz).

This has motivated the implementation of the LOFAR 2.0 upgrade, which is going to increase system performance, especially for the low-band antenna (LBA) part of the array (Hessels et al. in prep.). This upgrade will allow for simultaneous observations with the low-band and high-band antennas (HBA), and thus enable novel calibration algorithms that combine information from both antennas.

To make efficient use of the upgraded hardware, it is important to examine new calibration strategies for LOFAR 2.0 prior to the deployment of the upgraded hardware. We developed the *LOFAR Simulation Tool* (LoSiTo) to simulate a full 8 h simultaneous calibrator and target field observations with the upgraded LOFAR 2.0 system. First, we calibrated the simulated data for instrumental and direction-independent effects, relying mostly on standard LOFAR tools. Then, we investigated novel approaches for direction-dependent calibration with the aim of improving the ionospheric calibration of the LBA system.

This paper is arranged as follows. In Sect. 5.2, we discuss the current limitations of LOFAR and the improvements that will be introduced by LOFAR 2.0. In Sect. 5.3, we present models for the instrumental and ionospheric systematic errors in LOFAR 2.0 observations and estimate the noise level of the upgraded array. The implementation of these models in a simulation software as well as the setup of the simulated observation is described in Sect. 5.4. Next, in Sect. 5.5, we proceed with the calibration of the simulated data and investigate how the direction-dependent calibration for LBA could be improved by solution-transfer or joint calibration.

5.2 LOFAR and future upgrades

LOFAR is an array consisting of 55 stations spread across Europe. Three different station types with different hardware configurations exist: the central part of the array is composed of 24 core stations (CS); these are spread across an area in the northeast of the Netherlands that is less than 4 km wide. Another 16 stations are also located in the Netherlands, further away from the core, they are called remote stations (RS). The international part of the array consists of 15 more stations in eight European countries. Each LOFAR station hosts a field of dipoles operating as a phased array, with two drastically different dipole designs that are employed. The LBA are sensitive in the frequency

range of 10 MHz – 90 MHz. Additionally, the upper part of the frequency bandwidth of LOFAR is covered by the HBA, which are sensitive to the range from 110 MHz to 240 MHz. Each Dutch station is equipped with 96 LBA dipoles and 2×24 (CS) respectively 48 (RS) HBA tiles. The antenna signals are locally digitized in receiver units (RCUs), there are a total of 48 RCUs per Dutch station. Hence, operation is limited to either all 48 HBA tiles or 48 out of the 96 LBA dipoles (van Haarlem et al. 2013). Consequently, with regard to LBA, not all the existing dipoles are utilized and the potential sensitivity has not been reached.

Currently, the clock signals for all remote and international stations are provided by GPS-synchronized rubidium clocks. These clocks show the presence of a $O(10 \text{ ns h}^{-1})$ clock drift which causes non-negligible phase errors in the data (de Gasperin et al. 2019; van Weeren et al. 2016).

The LOFAR 2.0 upgrade is designed to overcome these limitations and consists of multiple projects (Hessels et al. in prep). In this work, we focus on the changes introduced by the *Digital Upgrade for Premier LOFAR Low-band Observing* (DUPLLO). DUPLLO is a funded project (Dutch Research Council (NWO) 2018), with its main focus based on improving the performance of the LBA system. Among the key components of DUPLLO is the deployment of improved station electronics. The number of RCUs per station will be tripled, this is going to allow for simultaneous observations with all 96 LBA dipoles as well as the 48 HBA tiles. The consequences of this move will be an increase of sensitivity and field of view (FoV) in LBA observations and the possibility of innovative calibration algorithms that can exploit the simultaneous observations to derive more accurate direction-dependent calibration solutions. The second improvement introduced by DUPLLO will be a new clock system. A “White Rabbit” ethernet-based timing distribution system (Lipiński et al. 2011) will be employed to synchronize all Dutch stations with a single clock (van Cappellen 2019). The roll-out of the first stage of LOFAR 2.0, which includes DUPLLO, is anticipated for April 2022 and full operation is expected for December 2023 (van Cappellen 2019).

5.3 Model corruptions

To accurately simulate LOFAR observations, realistic models for the corrupting effects present in the observations are required. Systematic effects related to physical and instrumental phenomena may be extracted from calibration solutions due to their characteristic properties and dependencies. In de Gasperin et al. (2019), measurements of the bright calibrator source *3C196* were analyzed and all major corrupting effects present in LOFAR observations could be isolated from the calibration solutions. We take these effects as a reference for the systematics that need to be included in realistic simulations. A summary of these effects together with the dominant noise components is presented in Tab. 5.1.

The mathematical framework of radio-interferometry is given by the radio interferometer measurement equation (hereinafter RIME; see Hamaker et al. 1996; Smirnov, O. M. 2011). The RIME connects the complex visibility \mathbf{V} , which is the quantity measured at the interferometer, to the sky brightness distribution \mathbf{B} . Systematic effects enter the RIME as *Jones-matrices* \mathbf{J}_a . Jones matrices are 2×2 matrices defined on the linear (or equivalently, circular) polarization basis of the electromagnetic field. If multiple effects are present, the total Jones matrix is the matrix product of the individual matrices. The order for matrix-multiplication is given by the order in which the effects occur along the signal path: $\mathbf{J}_{total} = \mathbf{J}_1 \cdot \dots \cdot \mathbf{J}_n$. The shape of the Jones-matrix is determined by the polarization-dependence of the underlying effect. A full formulation of the RIME is given by:

$$\mathbf{V}_{ab} = \iint \mathbf{J}_a(l, m) \mathbf{B}(l, m) \mathbf{J}_b^\dagger(l, m) e^{-2\pi i(ul+vm+wn)} \frac{dl dm}{n}, \quad (5.1)$$

Table 5.1: Systematic effects and noise components in LOFAR observations.

Effect	Type of Jones matrix	Phase or Amplitude?	Frequency dependence	Direction dependent?	Time dependent?
Clock drift	scalar	phase	$\propto \nu$	✗	✓(min.)
Polarization alignment	diagonal	phase	$\propto \nu$	✗	✗
Ionosphere 1st ord.	scalar	phase	$\propto \nu^{-1}$	✓	✓(sec.)
Ionosphere 2nd ord.	rotation	both	$\propto \nu^{-2}$	✓	✓(sec.)
Ionosphere 3rd ord.	scalar	phase	$\propto \nu^{-3}$	✓	✓(sec.)
Iono. scintillations	diagonal	amplitude	-	✓	✓(sec.)
Dipole beam	full-Jones	both	complex	✓	✓(min.)
Array factor	scalar	both	complex	✓	✓(min.)
Bandpass	diagonal	amplitude	complex	✗	✗
Sky noise	additive	both	$\propto \nu^{-2.57}$ ^a	✓	✓
Instrumental noise	additive	both	complex	✗	✓

^aSky noise spectral index from Guzmán et al. (2011) and valid for the North Galactic Pole.

Notes. This table is an extended version of the one in de Gasperin et al. (2019) and contains the noise components discussed in van Haarlem et al. (2013).

where l, m and $n = \sqrt{1 - l^2 - m^2}$ are the components of the source direction unit vector and u, v, w are the components of the baseline vector measured in wavelengths.

5.3.1 Ionosphere model

The ionized plasma of the upper atmosphere interferes with radioastronomic observations in a variety of ways. Series expansion of the refractive index $n(\nu)$ in ν^{-1} allows us to describe this interference by a few simple effects (Datta-Barua et al. 2008). The dominant ionospheric effect is a dispersive delay which expresses itself as a scalar phase error $\Delta\phi$ with a characteristic frequency dependence of $\propto \nu^{-1}$ (Mevius et al. 2016):

$$\Delta\phi = -84.48 \left[\frac{\text{dTEC}}{1 \text{ TECU}} \right] \left[\frac{100 \text{ MHz}}{\nu} \right] \text{ rad.} \quad (5.2)$$

This phase error depends on the line of sight integrated electron density N_e , which is referred to as the total electron content (TEC):

$$\text{TEC} = \int N_e dl. \quad (5.3)$$

The TEC is most commonly measured in total electron content units (TECU, $1 \text{ TECU} = 10 \times 10^{16} \text{ m}^{-2}$). Since the RIME is insensitive to a global scalar phase, only the differential TEC between the stations is relevant for the dispersive delay.

Another ionospheric effect that is non-negligible at the frequency range of LOFAR is Faraday rotation. This effect is of second order in ν^{-1} and hence, especially problematic at the lowest frequencies. It manifests itself as rotation in the plane of linear polarization. The line-of-sight contribution to the Faraday rotation depends on the magnetic field \vec{B} and the free electron density and can be summarized into the rotation measure (RM):

$$\text{RM} = \frac{e^3}{8\pi^2 \epsilon_0 m_e^2 c^3} \int N_e(l) \|\vec{B}\| \cos(\theta) dl. \quad (5.4)$$

Here, e is the electron charge, m_e the electron mass, c the speed of light in vacuum, ϵ_0 the vacuum permittivity, and θ the angle between the magnetic field vector and the line-of-sight. The corresponding rotation angle β is given by:

$$\beta = \text{RM} \cdot \left(\frac{c}{\nu}\right)^2. \quad (5.5)$$

Ionospheric rotation does also affect unpolarized signals: the magnetic flux density and the free electron number density vary between signal paths. This introduces a relative rotation angle between different stations and source directions. This effect is known as differential Faraday rotation and can, on the basis of linear polarization, be described by a rotational Jones matrix. This differential rotation causes amplitude and phase errors and may de-correlate the signal in extreme cases. The impact of this effect becomes important for frequencies below 80 MHz and baselines longer than 10 km (Mevisius 2018).

The next important higher order effect is of third order in ν^{-1} and manifests as dispersive delay, similar to the first order effect. In de Gasperin et al. (2018), it was found that this effect is only important for frequencies below 40 MHz. Since the effect is negligible for most of the frequency range observed by LOFAR and also quadratic in the free electron density and hence, harder to model compared to the first and second order effects, we have chosen to not include it in the simulation.

To obtain a realistic model of the ionosphere, a number of characteristic properties have to be considered. The scale and structure of the electron content must be in reasonable agreement with reality. Furthermore, the electron distribution must be spatially and temporally coherent. We employ the thin-layer model to describe the free electron density of the ionosphere. It represents the ionosphere as two-dimensional spherical shell at a height of h_{ion} around the Earth. This approximation is motivated by the vertical structure of the ionosphere. The majority of the free electrons are constrained within the ionospheric F -layer between 200 km and 450 km. Contracting the three-dimensional structure onto a two-dimensional sphere drastically reduces the complexity of the model while maintaining many of the important characteristics, such as spatial coherency and to some accuracy, the elevation dependence of the projected electron content (see Martin et al. 2016).

In the thin-layer approximation, the ionosphere is fully parameterized by a two-dimensional distribution of the vertical total electron content (vTEC). This distribution is hereinafter referred to as a TEC-screen. The TEC value corresponding to a specific signal path is evaluated at the ionospheric pierce point, which is defined as the point where the source direction vector pierces the TEC-screen.

For sources which are not directly at the zenith, an air-mass factor has to be taken into account to derive the slant TEC (sTEC) along the line of sight. Projection leads to an increase of the TEC for directions further away from the zenith:

$$\text{sTEC} = \frac{\text{vTEC}}{\cos(\theta_{ion})}, \quad (5.6)$$

where θ_{ion} is the pierce angle. Since we model the Earth as a sphere of radius R_E , the pierce angle can be calculated from the source elevation θ' according to the law of sines (Martin et al. 2016):

$$\sin(\theta_{ion}) = \frac{R_E}{R_E + h_{ion}} \sin(\theta'), \quad (5.7)$$

which allows us to derive the corresponding sTEC for any direction:

$$\text{sTEC} = \frac{\text{vTEC}}{\sqrt{1 - \frac{R_E}{R_E + h_{ion}} \sin(\theta')}}. \quad (5.8)$$

5 Investigating LOFAR 2.0 with Simulations

A substantial fraction of ionospheric inhomogeneity can be attributed to turbulent phenomena (Materassi et al. 2019; Giannattasio et al. 2018). Ionospheric turbulence can be approximately described by a process where energy is injected into a system with high Reynolds number at large spacial scales and iteratively distributed to smaller scales (Thompson et al. 2017). This self-similarity leads to a refractive-index power spectrum $\Phi(k)$ that follows a power-law shape:

$$\Phi(k) \propto k^{-\beta}, \quad (5.9)$$

where k is the spatial frequency. In case of pure Kolmogorov turbulence, the spectral index $\beta = 11/3$ (Tatarski 1961, 1971). Taking the finite outer scale L_0 of the turbulence into consideration yields:

$$\Phi(k) \propto (k^2 + L_0^{-2})^{-\beta}, \quad (5.10)$$

which in the $\beta = 11/3$ case describes the von Kármán spectrum (von Karman 1948).

Previous studies with LOFAR have confirmed the power-law shape, but found a slightly steeper spectrum of $\beta = 3.89 \pm 0.01$ (Mevius et al. 2016; de Gasperin et al. 2019)¹. We adopt this empirically derived value for our ionospheric model.

To generate a turbulent screen in LoSiTo, the algorithm described in Buscher (2016) is employed. This algorithm follows an approach based on the fast Fourier transform method and treats large and small spatial frequencies separately to increase computational performance. Furthermore, it makes use of the frozen turbulence approximation. In this approximation, the change of the turbulent structure is assumed to be negligible with respect to the bulk velocity of the ionosphere. Therefore, the ionosphere is modeled as a static grid moving across the LOFAR stations. To optimize performance, the extent of the screen is constrained to the outermost pierce-points for each time-step. We scale the dTEC sampled from the TEC-screen such that the maximum dTEC across all stations, directions, and times is 0.25 TECU. We add a homogeneous component of the TEC at 7.0 TECU. The daily ionospheric variation is included using a simple sinusoidal pattern: The total electron content peaks at 3:00 p.m. and drops to a level of 10% at 3:00 a.m.

We place our model-ionosphere at a height of $h_{ion} = 250$ km, around the typical location of the peak electron density at the latitude of LOFAR as modeled by the international reference ionosphere (Bilitza 2018). The ionospheric grid is simulated at an angular resolution of 1 arcmin (≈ 72 m) and moves from West to East at a velocity of 20 m s^{-1} .

One snapshot of such a TEC-screen is shown in Fig. 5.1. We show the pierce-points of five selected LOFAR stations. It is apparent that all the CS observe a similar ionosphere, the dTEC between different directions dominates compared to the dTEC between different CS. The most distant RS observe a different part of the ionosphere.

For each pierce-point and at every time-step, the vTEC-values of the closest grid points are linearly interpolated and converted to sTEC according to Eq. 5.8. These values are stored in the h5parm format introduced in de Gasperin et al. (2019). To derive the Faraday rotation from the ionospheric model, we apply the thin-layer approximation to Eq. 5.4:

$$\text{RM} = 2.62 \times 10^{-13} \text{ T}^{-1} \text{ TEC} \hat{d} \cdot \vec{B} \Big|_{\text{pierce-point}}. \quad (5.11)$$

For the calculation of the RM, the magnetic field vector \vec{B} projected onto the source-direction \hat{d} and evaluated at the pierce-point is required. As magnetic field model, the implementation of the World Magnetic Model (Chulliat et al. 2015) in the RMExtract library (Mevius 2018) is employed.

¹Derived from the phase structure function spectral index α as $\beta = \alpha - 2$ according to Boreman & Dainty (1996)

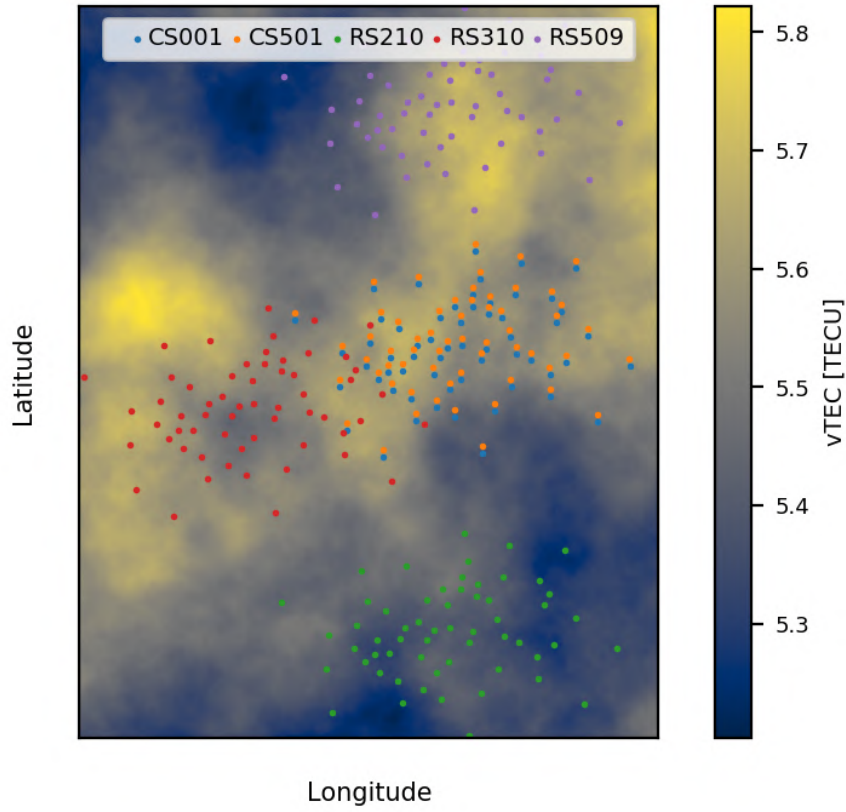


Figure 5.1: Snapshot of a simulated turbulent TEC-screen with the parameters $\beta = 3.89$ and $h_{iono} = 250$ km. Each circle marks one pierce-point, circles of the same color show pierce-points for different directions belonging to the same station. Only pierce-points belonging to one of the centermost stations (CS001), the most distant central station (CS501) as well as the three outermost remote stations (RS210, RS310, RS509) are displayed.

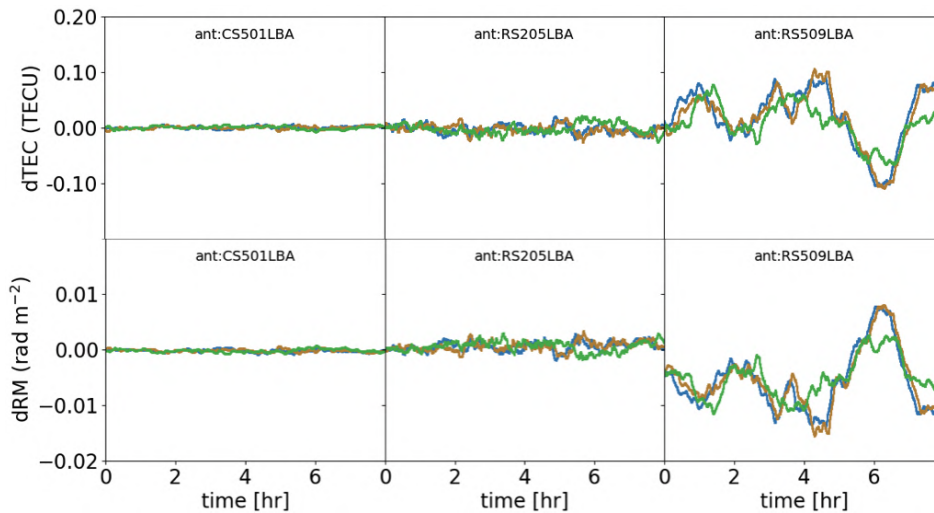


Figure 5.2: Simulated dTEC (top panels) and dIRM (bottom panels) for three stations for a source in the phase center (orange) and for sources separated from the phase center by 1.75° (blue) and 4.51° (green). The stations are at distances of 1.7 km (CS501), 6.3 km (RS205) and 55.7 km (RS509) to CS001. The values of each direction are referenced with respect to the same direction in CS001LBA.

5 Investigating LOFAR 2.0 with Simulations

The *FARADAY*-operation in LoSiTo derives the RM from this magnetic model and the sTEC values stored in the h5parm file. The RM values are added to the h5parm-file in a new table. The simulated dTEC and dRM-values for three stations and three directions are displayed in Fig. 5.2. As expected from Eq. 5.11, the dTEC and dRM values are highly correlated. From our experience, the ionospheric conditions of this simulation are representative for low solar activity.

5.3.2 Primary beam

The primary beam characterizes the directional sensitivity for the interferometer components, in the case of LOFAR for the individual stations. Since LOFAR does not simply consist of single dish antennas, but follows a phased array design, the treatment of the primary beam is more complex compared to classical interferometers. For LOFAR, the primary beam can be split into two components, the element beam and the array-factor. The element beam characterizes the directional sensitivity of a single antenna element. An LBA element consist of one dipole pair, while for HBA, tiles of 16 pairs are grouped together to form one element (van Haarlem et al. 2013). The element beam varies only slowly across the sky and in time. The element beam is always pointed towards the local horizon, leading to a decline of sensitivity for low elevations. In contrast, the array-factor is a Jones-scalar, which describes the influence of the beam-forming (that is, the superposition of the element signals) on the directional sensitivity. The array factor determines the size of the instrument FoV. LoSiTo uses the LOFARBeam² library to include both the element beam and the array factor in the simulations. This library uses results of electromagnetic simulations of the dipoles to calculate the primary beam Jones-matrices (Hamaker 2011).

Since the LOFAR 2.0 LBA system will utilize 96 dipoles per station instead of just 48, the shape of the array-factor will change. In Fig. 5.3, we show a comparison of the array-factor amplitude between a current LBA station, a LOFAR 2.0 LBA station, and an HBA station. We note that the LOFAR 2.0 upgrade will not just increase the size of the FoV, but also significantly reduce the side-lobe structure. The size of the primary beam at 54 MHz (full-width at half-maximum) will increase to 5.6° from 4.3° in *LBA_outer*. For comparison, the HBA beam in mode *Dual_inner* at 144 MHz is 4.8° wide.

5.3.3 Bandpass response

The bandpass describes the frequency dependence of the system's amplitude response. Therefore, it is constant in time and does not affect the phases. It is an instrumental effect which is largely shaped by the dipole response. In reality, variations in the dipole shapes and electronics cause deviations of the bandpass between the different stations and polarizations and might also introduce a slow time-variation. This variation may be caused by changes in environmental conditions that affect dipole properties, such as humidity. The bandpass can be described by a station dependent, real diagonal matrix.

LoSiTo includes a straightforward model for the bandpass, using the average bandpass that was determined in an empirical study of the instrument in van Haarlem et al. (2013). The model for both antenna types is shown in Fig. 5.4. LOFAR features three HBA bandpass modes with different spectral windows. We will only consider the mode *HBA-low*, since in practice, this mode is used almost exclusively. While the HBA dipole response is rather flat, the response of the LBA dipoles features a prominent peak at 58 MHz with a full width at half maximum (FWHM) of 15 MHz, causing a sharp decline of sensitivity below and above the peak frequency.

²github.com/lofar-astron/LOFARBeam

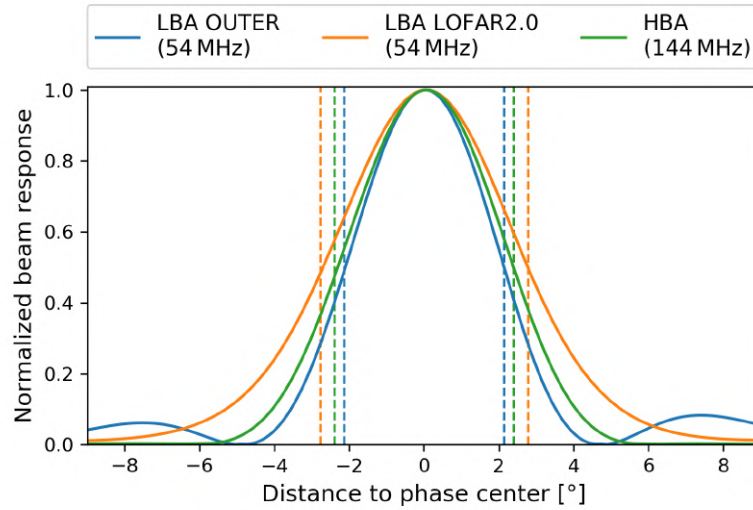


Figure 5.3: Normalized LOFARBeam beam response (y -axis) as a function of phase center separation (x -axis) for the current 48 dipole LBA system in mode outer, the 96 dipole LOFAR 2.0 LBA system and the HBA system. The dashed vertical lines mark the primary beam FWHM of the respective system.

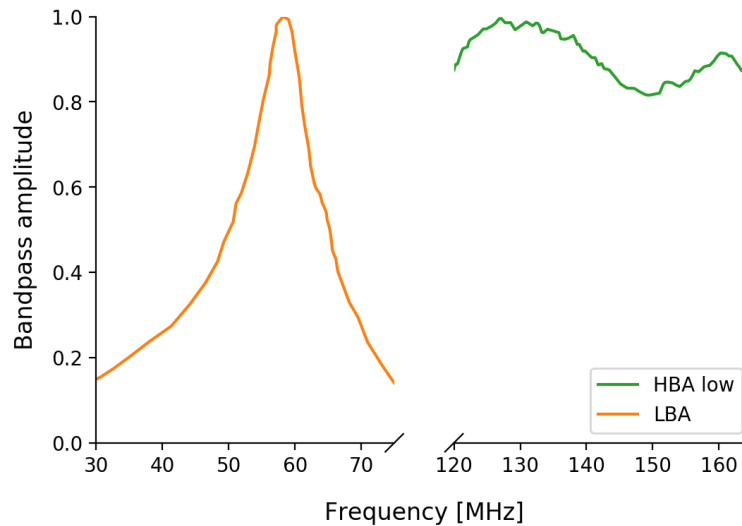


Figure 5.4: Normalized bandpass amplitudes (y -axis) for the LBA and the most common HBA bandpass setup *HBA-low* as a function of frequency (x -axis). The values are adopted from an empirical study of the instrument in van Haarlem et al. (2013).

Table 5.2: Numeric values for the widths of the Gaussian distributions used to construct the LOFAR 2.0 clock model.

Station type	$\Delta t_{\text{rms,max}}$ [ns]	σ_{offset} [ns]	$\sigma_{\text{amplitude}}$ [ns]
Core station	0.20	0.047	0.067
Remote station	0.35	0.083	0.117

5.3.4 Station based delays

An omnipresent systematic effect in radio interferometry is given by offsets in the signal timing between the interferometer stations or antennas. This is, for instance, caused by asynchronous clocks and improper calibration of electronics. Especially for long baseline instruments, the issue of accurate clock calibration across large physical distances arises.

A time delay Δt between two baseline elements introduces a phase-offset of $\Delta\phi$ in the *RIME*:

$$\Delta\phi = 2\pi\nu\Delta t. \quad (5.12)$$

While this phase error follows a linear frequency dependence and is therefore a greater issue at higher frequencies, it is still non-negligible in present-day LOFAR observations. Currently, the remote and international stations receive a time signal from GPS-synchronized rubidium clocks (van Haarlem et al. 2013). The signal of these clocks drifts slowly in time, causing a $O(10 \text{ ns})$ clock error with smooth temporal behavior. This translates to a phase-error in the order of 2π at 100 MHz. The LOFAR 2.0 upgrade will introduce a new system for the time synchronization, utilizing a distributed signal from a single clock for all Dutch stations. The requirements for the distributed single-clock signal are as follows (Bassa 2020, priv. comm.). First, the timing reference signal at Core Stations shall have a clock error of $\Delta t_{\text{rms}} < 0.20 \text{ ns}$ over a one-hour period. Second, the timing reference signal at Core and Remote Stations shall have a clock error of $\Delta t_{\text{rms}} < 0.35 \text{ ns}$ over an eight-hour period. We use a simple model consisting of a sinusoidal variation on top of a constant offset to include the clock drift in the simulation:

$$\Delta t_i = t_{\text{amp},i} \sin(2\pi\omega_{\text{clock},i}(t - t_{\text{shift}})) + t_{\text{offset}}. \quad (5.13)$$

The drift amplitude t_{amp} , drift frequency ω_{clock} and the clock offset t_{offset} are drawn from Gaussian distributions independently for each station. The widths σ_{offset} and $\sigma_{\text{amplitude}}$ are determined such that the root-mean-square (rms) error of the clock signal is one third of the maximum allowed rms in the system requirements. Furthermore, the total standard deviation should be caused in equal parts by the constant offset and the sine function. The corresponding parameters are displayed in Tab. 5.2.

The resulting clock offset from this model is shown in Fig. 5.5 for three selected stations. The corruptions are shared between the LBA and HBA parts of each station.

In addition to the station dependent clock delay, LOFAR data shows the presence of a nanosecond-scale time delay between the *X* and *Y* polarization of the station output. This delay, referred to as polarization misalignment, is constant in time and attributed to an inaccurate station-calibration (de Gasperin et al. 2019). We assume that this effect will be present at a similar magnitude in LOFAR 2.0. To replicate this effect, a random time offset between the polarizations is drawn from a Gaussian distribution with a width of 1 ns for each station. We sampled this effect independently for the LBA and HBA parts of a station.

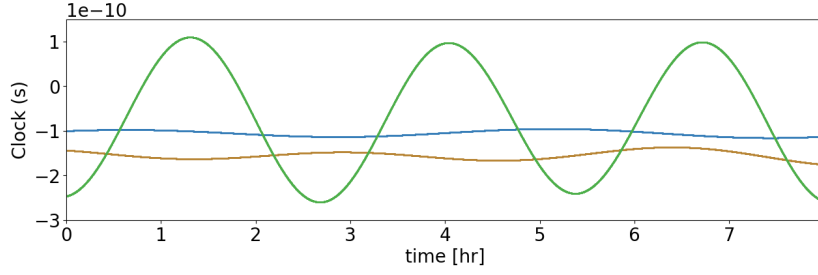


Figure 5.5: Simulated clock delay for CS501 (blue), RS205 (orange), and RS210 (green), referenced to the clock of CS001.

5.3.5 Thermal noise

The achievable sensitivity of a perfectly calibrated radio interferometer is limited by the presence of noise. There are two primary noise sources: instrumental noise, for example, from the receiver and amplifier system; and sky noise, which is of cosmic origin. While for radio observations at mid and high frequencies, the instrumental component is by far dominant, this changes in the low-frequency regime, where the sky noise becomes increasingly important.

The sky noise has an ultra-steep spectrum. Assuming a power-law shape $I_{sky} \propto \nu^{-\alpha}$, the study in Guzmán et al. (2011) found a spectral index of $\alpha = 2.57$ between 45 MHz and 408 MHz. This spectral index varies across the sky, increasing strongly towards the Galactic plane. Towards the Galactic center, the brightness of the sky noise is a factor of ≈ 10 higher compared to the Galactic poles. For LOFAR, the sky noise is, in fact, the dominant source of noise below 65 MHz (van Haarlem et al. 2013).

The noise of a radio astronomical instrument can be expressed in terms of system equivalent flux density (SEFD). The SEFD is the flux density of a hypothetical source which induces a power in the system that is equal to the power induced by the noise. It can be calculated from the system temperature T_{sys} , the antenna efficiency η and the effective collection area A_{eff} :

$$SEFD = \frac{2k_B T_{sys}}{\eta A_{eff}}. \quad (5.14)$$

An empirical study in van Haarlem et al. (2013) determined the SEFD for the LOFAR LBA and HBA. For the LBA system, the SEFD was measured independently for the two observation modes *Inner* and *Outer*, where only the 48 inner- or outermost of the 96 dipoles are used. To estimate the SEFD for the LOFAR 2.0 LBA, we take the mean of the two modes as reference. Additionally, we scale this mean value to account for the double dipole number. The anti-proportionality to the effective collection area in Eq. 5.14 suggests that a doubling of the dipoles reduces the SEFD by a factor of 2. However, we adopt a more conservative scaling factor of $\frac{1}{\sqrt{2}} \approx 0.71$ for two reasons: First, overlap in the effective areas of the dipoles leads to a decrease in the total area. Second, we compare the SEFD of the different HBA station types displayed in Fig. 5.6. The HBA arrays in the CS host 24 tiles, while the RS host 48 tiles, so they can give an idea on how a doubling of the dipoles affects the SEFD. The average SEFD of the 48 tile stations is lower by a factor of 0.75. Due to the different station layouts, this ratio cannot be transferred to LBA directly. Nevertheless, this comparison motivates our slightly more conservative value of 0.71. Our estimate for the LOFAR 2.0 LBA SEFD as well as the values adopted from van Haarlem et al. (2013) are displayed in Fig. 5.6.

The noise in visibility space follows a Gaussian distribution with a frequency dependent standard deviation. This standard deviation for a frequency channel of bandwidth $\Delta\nu$ can be computed from the

5 Investigating LOFAR 2.0 with Simulations

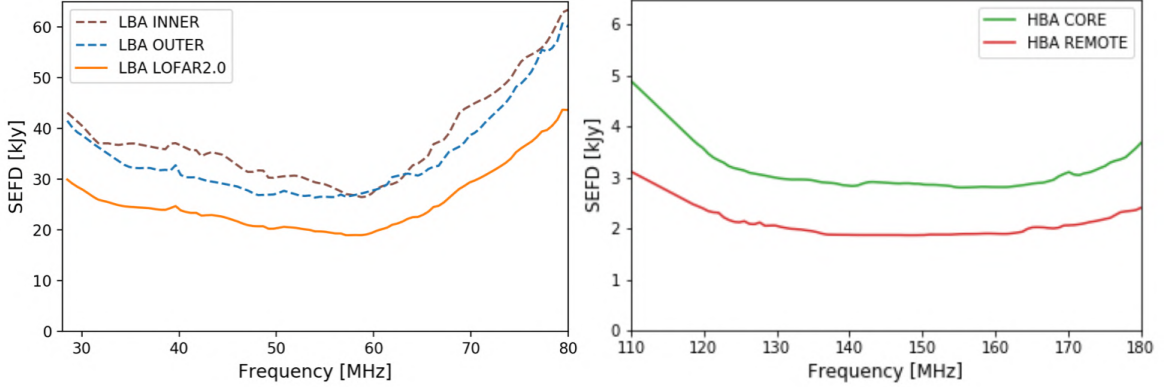


Figure 5.6: Frequency dependence of the SEFD for different configurations of the LBA (left) and two differently equipped HBA station types (right). The y-axes differ by a factor of 10. The estimate for the LOFAR 2.0 LBA SEFD is derived from the mean of the modes *Inner* and *Outer*.

SEFD of the two stations which form the baseline, the total system efficiency η_{sys} and the exposure τ (Taylor et al. 1999):

$$\Delta S_{ij}(\nu) = \frac{1}{\eta_{sys}} \sqrt{\frac{\text{SEFD}_i(\nu)\text{SEFD}_j(\nu)}{2\Delta\nu\tau}}. \quad (5.15)$$

We assume a system efficiency of $\eta_{sys} = 0.95$. Using these standard deviations, the simulated complex visibilities are corrupted with independent Gaussian noise in real and imaginary part for each frequency channel, baseline, time, and polarization.

5.4 Simulation software

We implemented the models for the corrupting effects presented in Sect. 5.3 in a code called the *LOFAR simulation tool* (LoSiTo)³. This software is a command-line program written in the Python programming language and build on top of existing LOFAR software. In the following, we provide a brief overview of the program. The main configuration file is the parameter set for which the user specifies the corrupting effects that should be included in the simulation and at which scale. Two more input files are required: one is the input sky model, where properties of the sources such as position, flux density, angular extension, spectral shape, and polarization properties are set. Such a sky model may be obtained from a source catalog or a radio image. Alternatively, it can be randomly generated using a script in LoSiTo. As last input for the simulation, a measurement set file (Schoenmaker & Renting 2011) is required. This file is the template for the simulated visibilities; furthermore, it stores the metadata of the observation, such as the observation time, frequency bands as well as location and status of the LOFAR stations. A LoSiTo simulation is composed of individual operations, each model corruption of Sect. 5.3 is implemented as one such operation. The simulated corruptions are stored in the h5parm data format. The central part of a simulation is the prediction. In this step, the visibilities corresponding to each source (or each patch of sources) are calculated in a Fourier-transformation from image-space to visibility-space. The Jones-matrices of the direction-dependent effects (DDE), such as the ionospheric effects and the primary beam, are calculated from the h5parm file content and multiplied with the predicted visibility matrices for the source(s). The resulting DDE corrupted visi-

³github.com/darafferty/losito

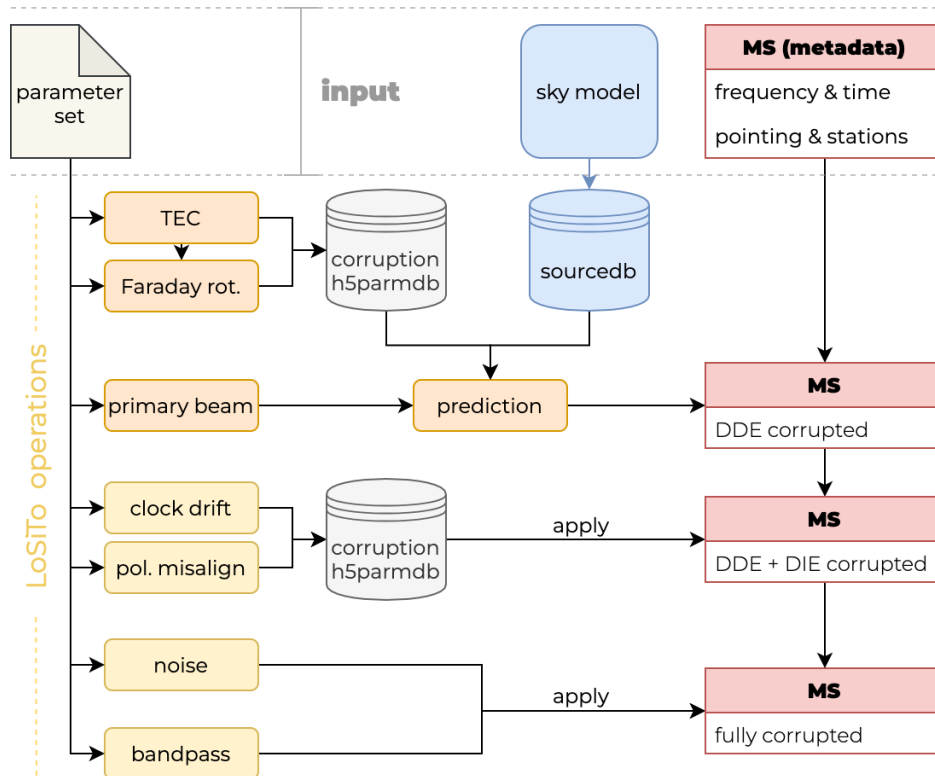


Figure 5.7: Diagram of LoSiTo. As input, a parameter set, a sky model, and a template measurement set are required. Orange boxes represent DDE, while yellow boxes represent DIE.

bilites for all directions are added. The Jones-matrices of the direction-independent effects (DIE) are multiplied with the visibility matrices afterwards to save computation time. This is possible because the DDE are prior to the DIE on the signal path. Lastly, noise is added to the visibilities and they are multiplied by the average bandpass response. The final product of the simulation is a measurement set file which obeys the same format as a real LOFAR observation, and thus, can be further processed with the same software. LoSiTo makes use of the software DPPP for the prediction and the application of the corruptions stored in *h5parm* files (van Diepen et al. 2018). The diagram in Fig. 5.7 presents a visualization of the architecture of LoSiTo.

5.4.1 Full simulation setup

We simulate a full eight-hour LOFAR 2.0 observation of a calibrator source and a target field using the Dutch LBA and HBA stations simultaneously. For the LBA system, multi-beam observing allows to point in parallel at both target and the calibrator during the whole observation. This is not possible for HBA, where we simulate a short calibrator scan of ten minutes at the beginning of the observation. The setup of the simulated observation is shown in Tab. 5.3. Since target and calibrator field are usually located at large angular separation, they were simulated using independent ionospheric models. The station-dependent instrumental effects of bandpass, clock, and polarization alignment are shared between the calibrator and target data set.

We extracted the sky model for the target from a real LOFAR LBA observation of the field around the galaxy cluster *Abell 1033* using the software PyBDSF (Mohan & Rafferty 2015). We corrected the

Table 5.3: Setup of the simulated observation.

Start time	2018-06-30 11:00:02
Observation time	8 h ^a
Time resolution	4 s
Frequency range (LBA)	30-78 MHz
Frequency range (HBA)	120-168 MHz
Frequency resolution	48.8 kHz
Target RA	10 ^h :31 ^m :41 ^s
Target Dec	+35°04'38"
Calibrator RA	08 ^h 13 ^m 35 ^s
Calibrator Dec	+48°13'02"

^aTen minutes for the HBA calibrator scan.

sky model for the primary beam attenuation and set the spectral shape of all sources to a power law with a typical radio-spectral index of 0.8 (Mahony et al. 2016). We manually adjusted the flux density of the bright, resolved source in the center of the field to make it less dominant. Furthermore, we discarded all sources fainter than 0.2 Jy to decrease computational cost. Lastly, to further improve computational efficiency, we grouped sources in close proximity into patches. The DDE are not applied to each individual source but to each patch of sources, taking the flux-weighted centroid of the source locations as reference. Further away than 2.5° from the phase center, sources are grouped into larger patches. The resulting sky model is displayed in Fig. 5.8, it contains 340 sources in 59 patches, the total flux density is 225.8 Jy at 54 MHz. For the calibrator observation, we use an existing model of the standard LOFAR calibrator source *3C196* which has a total flux density of 138.8 Jy at 54 MHz. We create the input measurement sets using a script available in LoSiTo. This way, we receive measurement sets for LBA and HBA with identical time-steps and pointing information. To take into account the changes introduced in the LOFAR 2.0 upgrade, we set all 96 LBA dipoles for each station to active.

We ran the simulation including all the corruptions discussed in Sect. 5.3. The full computation time for the simulation was 53 hours using eight compute nodes equipped with *Intel Xeon E5-1650* six-core processors. The primary bottleneck in terms of computation time is the prediction which depends on the number of patches and sources present in the sky model. The simulated data have been made publicly available⁴.

5.5 Calibration

Simultaneous LBA and HBA observations will offer new prospects for ionospheric calibration. Since the same region of the ionosphere will be observed in both parts of the array, the underlying parameters describing the ionospheric corruption in the data are identical. Consequently, combining the information of the low- and high-band observations could allow us to determine the ionospheric parameters more accurately and hence, derive more exact calibration solutions. This strategy is possible since both dipole systems have a comparable primary beam size which allows us to observe a sufficient number of calibrator sources in both parts of the array. It could especially benefit the LBA where the calibration of DDE is made more difficult due to the increased noise level and severity of ionospheric errors.

⁴<https://www.fdr.uni-hamburg.de/record/8587>

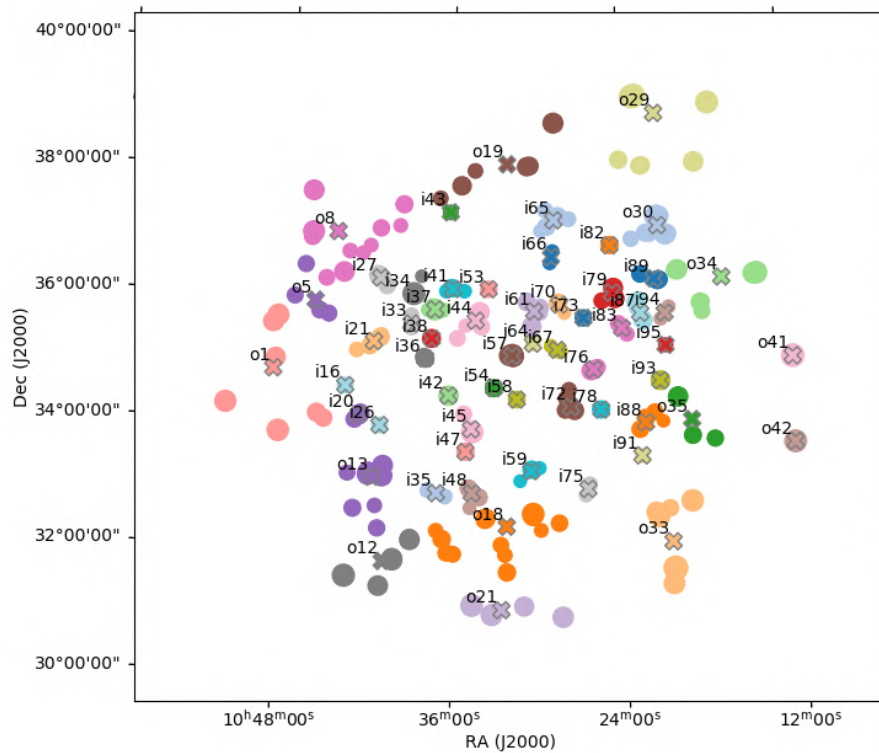


Figure 5.8: Input sky model of the simulation. The model is extracted from a real LOFAR observation of the target field. It contains 340 sources grouped into 59 patches, the total flux density is 226 Jy at 56 MHz. Circles correspond to source locations. Sources are color-coded according to their patch membership, patch centers are marked by an "X" and labeled.

5 Investigating LOFAR 2.0 with Simulations

Currently, calibration of DDE for LOFAR mostly follows a brute-force attempt: it is solved for effective Jones matrices which are assumed to be constant for small domains of time and frequency (Tasse et al. 2021; de Gasperin et al. 2020). However, to exploit the simultaneous observation, we must obtain parameters describing the underlying physical effects, such as TEC and RM, since only these values are frequency-independent and can be meaningfully translated between LBA and HBA. This drastically reduces the number of free parameters during calibration compared to the effective-Jones approach, but requires a sufficient S/N and data that is clean of other systematic errors to converge towards the correct solutions.

We focus on two approaches to exploit the simultaneous observation for calibration of the direction-dependent dTEC. One approach is the application of ionospheric solutions found in HBA to the LBA data, we will refer to this method as "solution transfer." This idea is based on the assumption that it is easier to converge towards correct calibration solutions in HBA, since there is significantly less noise compared to LBA (see Fig. 5.6). However, while the HBA stations are less affected by noise, they also observe a smaller fractional bandwidth (≈ 0.33) compared to LBA (≈ 0.89) which could make it harder to fit the ν^{-1} spectral dependency (see Eq. 5.2) of the dispersive delay. Therefore, it is not fully clear how much more accurate TEC-extraction is in HBA. In addition, we emphasize that, when applying HBA-derived solutions to LBA, it is crucial to minimize the presence of jumps in dTEC solutions. These jumps are a consequence of the local minima present in the χ^2 cost function which may be almost as deep as the global minimum, depending on the bandwidth (van Weeren et al. 2016). In the case of HBA, the jumps to a local minimum might still provide accurate calibration for a significant part of the HBA bandwidth, they cause substantially stronger phase-errors when transferred to LBA since the location of the local minima shifts with frequency.

The second method of exploiting the simultaneous observations that we consider in our analysis is joint calibration. In this scenario, it is solved for dTEC using data from both LBA and HBA together to leverage the large bandwidth observed by LOFAR and improve the S/N. This approach contains more information on a larger domain and thus, carries a greater potential for calibration, at the cost of a more complex algorithm, however.

The data reduction of the simulated observation is split into three parts, if not stated otherwise, data reduction steps are carried out independently for the LBA and HBA observations. First, the instrumental systematics are derived from the calibrator observation using the strategy described in de Gasperin et al. (2019). The second step is the calibration of DIE employing an adjusted version of the pipeline presented in de Gasperin et al. (2020). The final step is the direction-dependent calibration; here, we compare the LOFAR 2.0-specific calibration strategies to the independent calibration of the LBA system.

5.5.1 Calibrator data reduction

To find the solutions for the calibrator observation, we assume that the model of the calibrator source is fully accurate and calibrate against the same model we used as simulation input. First, solving against this model, the polarization alignment was derived by fitting a diagonal and a rotational matrix. The phase solutions from the diagonal matrix were averaged in time to extract the relative delay between the polarizations for each station. We corrected the data for these delays. Next, the LOFAR beam model was applied and a second diagonal and rotational fit was performed to extract the Faraday rotation solutions. The Faraday rotation solutions are applied to the data. Subsequently, a diagonal Jones-matrix was fitted and the resulting amplitude solutions were averaged in time to derive the bandpass responses. From here, the calibrator pipeline in de Gasperin et al. (2019) performs additional solution steps to derive the time-dependent clock delay from phase solutions. In a procedure called

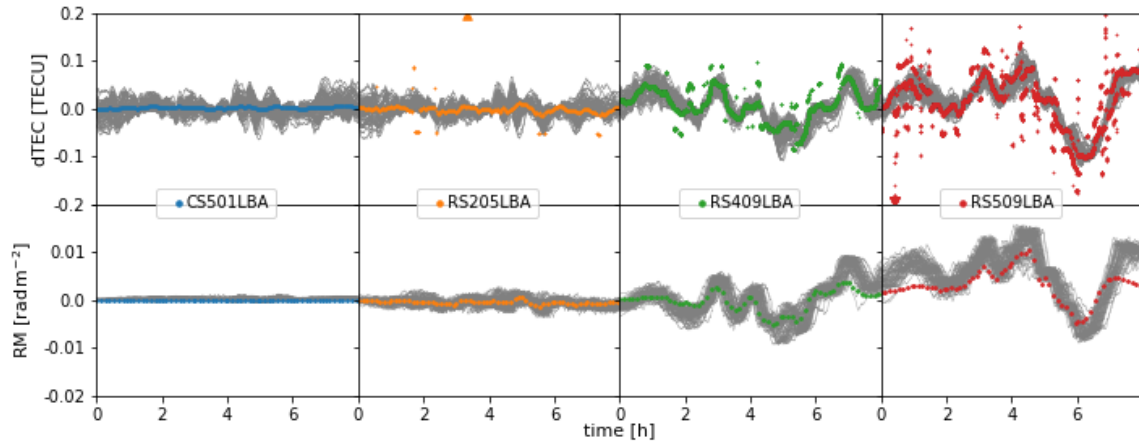


Figure 5.9: Direction-independent ionospheric solutions towards the target field for four LBA stations. The top panels show $dTEC$, the bottom panels dRM . The gray curves in the background show the input corruptions towards the 59 patches. The calibration solutions are referenced to station CS001LBA and the input corruptions are referenced to the phase center direction of CS001LBA. Triangles mark solutions outside of the graph's scale. We note that the missing variation of the input-RM for CS001 is caused by a referencing error present in the data. Simulated RM values were referenced for each direction individually instead of referencing to a single direction. However, we do not expect this to affect our analysis.

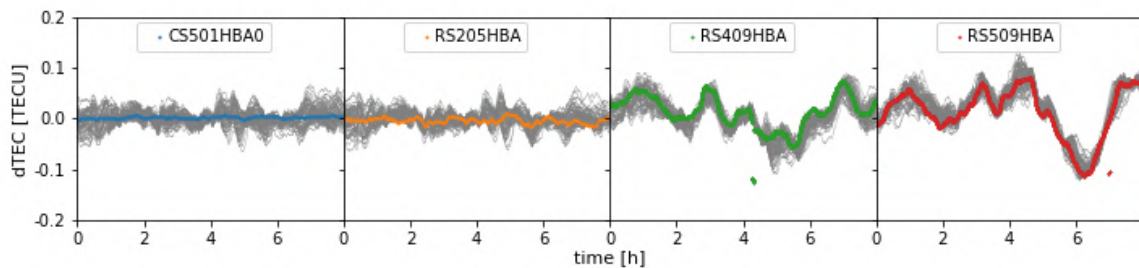


Figure 5.10: Direction-independent TEC solutions for four HBA stations. The gray curves in the background show the input corruptions towards the 59 patches. The calibration solutions are referenced to station CS001HBA0. The input corruptions are referenced to the phase center direction of CS001HBA0.

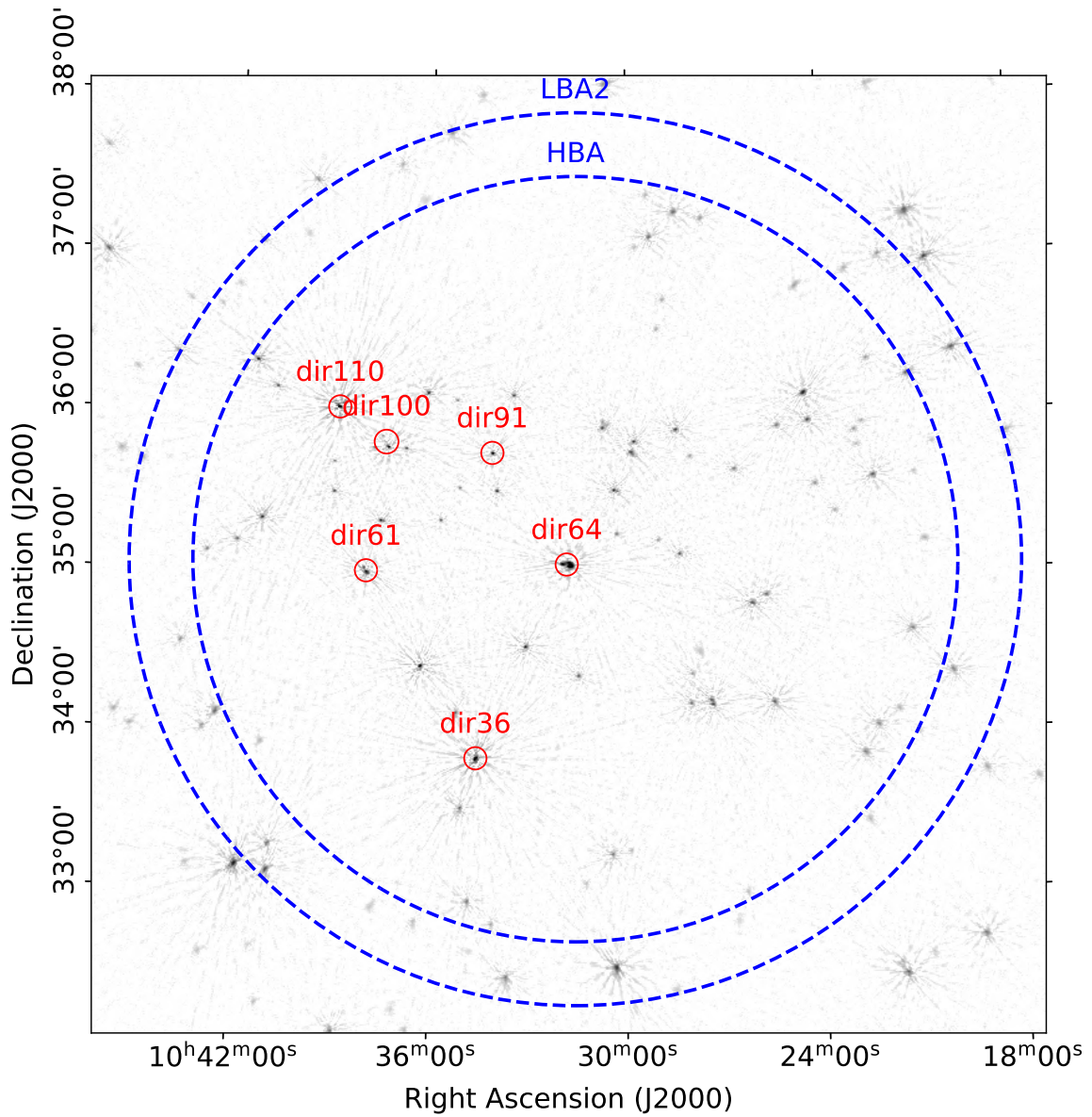


Figure 5.11: LBA wide-field image after DIE calibration. The rms background noise is $\approx 2.0 \text{ mJy beam}^{-1}$ at a resolution of $42'' \times 30''$. The DDE calibrator directions are highlighted in red, the blue dashed circles show the primary beam FWHM of the LOFAR 2.0 LBA at 54 MHz and the HBA at 144 MHz. The background color scale shows the logarithmic surface brightness in arbitrary units.

clock-TEC-separation, a clock term proportional to ν and a TEC term proportional to ν^{-1} are fitted to the phase solutions simultaneously to separate the effects by their characteristic frequency dependence (van Weeren et al. 2016). For HBA, calibrator observations are usually not simultaneous to the target observation due to limitations imposed by the tile beam. Therefore, we skip this step for the HBA data set. For LBA, additional smoothing was required to account for the significantly smaller clock error of our LOFAR 2.0 clock model. A benefit of testing the data reduction strategy on simulated data is that we can quantify the accuracy of the calibration solutions: for LBA, the frequency-averaged relative rms error of the bandpass solutions is 1.8% and the rms error of the polarization alignment and clock delay is 7.7 ps respectively 37 ps. For HBA, the frequency-averaged relative rms error of the bandpass solutions derived from the ten minute calibrator observation is 0.3% and the rms error of the polarization alignment delays is 1.9 ps. The bandpass, polarization alignment and clock solutions were transferred to the target data and the primary beam in direction of the phase center was applied. We exploit the simultaneity of the LOFAR 2.0 observations and transfer the LBA clock solutions to the HBA observation.

5.5.2 Direction-independent calibration

Next, we calibrated the target field data sets, starting with direction-independent self-calibration based on the procedure described in de Gasperin et al. (2020). The aim of this is to correct for the average ionospheric effects per station and to derive a robust source model for further direction-dependent calibration. For real observations, a catalog model of the target field is used as initial model for self-calibration. To replicate this incomplete first model, we use a sparse, corrupted version of the simulation input sky model. This model was obtained by selecting only the sources within the primary beam FWHM which are brighter than 0.5 Jy at 54 MHz. Flux density errors at a standard deviation of 10% were introduced to the remaining sources, which were 70 for LBA respectively 39 for HBA.

First, we find solutions for the differential Faraday rotation: we transform the data to circular polarization basis and consider only the phase differences of the XX and YY correlations. This eliminates all contributions of scalar phase errors such as the TEC or clock drift given that for unpolarized sources, they are equally present in both diagonal entries and cancel out. We fit these circular phase differences to a model with a phase of $\phi = 0$, extract the RM from the phase solutions and apply it to the data. Next, the pipeline solves for the direction-averaged dTEC in two sub-steps: first, only for the CS and the inner RS, these solutions are then applied to the data. Second, only for the outer RS, constraining all other stations to the same value. This improves the S/N when determining the large TEC-variations of the most distant stations. The solver estimates the dTEC by fitting the $1/\nu$ term of the dispersive delay phase error. In Fig. 5.9, the direction-independent dTEC and RM solutions for four LBA stations are displayed on top of the corresponding input corruptions. The direction-independent solutions trace a weighted average of the input corruptions towards the different directions. For the most distant stations, the solver sometimes converged towards neighboring minima due to the presence of noise. The RM solutions are less noisy since we chose a significantly longer solution interval of 8 min instead of 4 s, however, for a few stations (such as RS509), they sometimes show a systematic deviation from the input corruptions.

The HBA dTEC solutions are shown in Fig. 5.10; due to the lower noise level, they have significantly fewer jumps. The corrected data are imaged using the WSCLEAN multi-scale algorithm (Offringa et al. 2014; Offringa & Smirnov 2016). The *CLEAN*-components found during imaging are used as improved model for direction-dependent calibration.

For LBA, the image is displayed in Fig. 5.11, the rms background noise is $2.0 \text{ mJy beam}^{-1}$ at a resolution of $42'' \times 30''$, for HBA, the noise level is $200 \mu\text{Jy beam}^{-1}$ at a resolution of $18'' \times 14''$.

5 Investigating LOFAR 2.0 with Simulations

For comparison, typical values for the rms background noise of real LOFAR observations are around 5 mJy beam^{-1} for LBA (de Gasperin et al. 2021), respectively, $380 \mu\text{Jy beam}^{-1}$ for HBA (Shimwell et al. 2019). The lower noise can be attributed to the improved sensitivity of LOFAR 2.0 for LBA and a reduced source density of our simulated sky model compared to a fully realistic source distribution.

One point that must be accounted for in LOFAR 2.0 calibration is the difference in the FoV of the low- and high band (see Fig. 5.11). The LBA beam at the center of the frequency band covers a 36% larger area compared to HBA. This discrepancy could be compensated for by using multiple simultaneous HBA pointings to cover one LBA pointing. Alternatively, the greater sensitivity of the HBA could justify to use regions outside of the FWHM for simultaneous calibration.

5.5.3 Direction-dependent calibration

The last data-reduction step is the calibration for DDE which is necessary to correct for TEC-variation across the FoV. We identify DDE-calibrators from the DIE calibrated LBA image, using the source finder PyBDSF to isolate islands of emission. We employ a grouping algorithm to merge sources in close proximity. To avoid faint and very extended sources, we place a threshold on the flux density to source area ratio and discard all sources fainter than 0.8 Jy at 60 MHz . This procedure resulted in six calibrator directions with apparent flux densities of 0.9 to 2.8 Jy , the locations of which are shown in Fig. 5.11. We note that for sufficient calibration of the full FoV, more calibrator directions are necessary, depending on the ionospheric conditions. However, our sample contains point-like, multi-component and complex sources, and can thus give a good indication of the convergence for different morphologies. Expanding our strategy to more directions is straightforward as long as they are sufficiently bright.

We pursue an approach based on the peeling-strategy (van Weeren et al. 2016): We start by time-averaging the DIE-corrected data set to a resolution of 8 s and subtract all CLEAN-components from the DIE calibrated image. This creates a data set which is empty up to model inaccuracies and calibration residuals. We then iterate on our calibrator sources, starting with the brightest direction. We add the visibilities corresponding to the model of sources in this calibrator direction back to the measurement set. We create a measurement set for this specific direction by phase-shifting the data to the calibration direction and further averaging a factor of four in time and eight in frequency. Based on this data, we estimate the direction-dependent Faraday rotation from the circular-base $XX - YY$ phase difference, as described in Sect. 5.5.2. After applying these solutions, we perform several rounds of self-calibration, solving for scalar phases in time intervals of down to 32 s for each channel. We employ a station constraint, forcing all core stations to the same solution, and for these stations, a direction-dependent variation of the ionosphere is negligible. The resulting phases are smoothed, using a Gaussian kernel with a standard deviation of 5 MHz at 54 MHz . The kernel-size varies as ν^{-1} in frequency to allow for more smoothing in frequencies less affected by the ionospheric errors. The self-iteration loop is discontinued once the rms background noise of the calibrator region reduces for less than one percent. The phase solutions and source model of the iteration with the lowest background rms are used to re-subtract the calibrator sources from the data, reducing remaining artifacts. This improved empty data set is used as starting point for the next calibrator direction. This cycle is repeated for all eight calibration directions for both LBA and HBA. The resulting phase solutions for two stations and two directions are shown in Fig. 5.12. Temporal correlation of the solutions between LBA and HBA is visible, they are dominated by the ionospheric DDE.

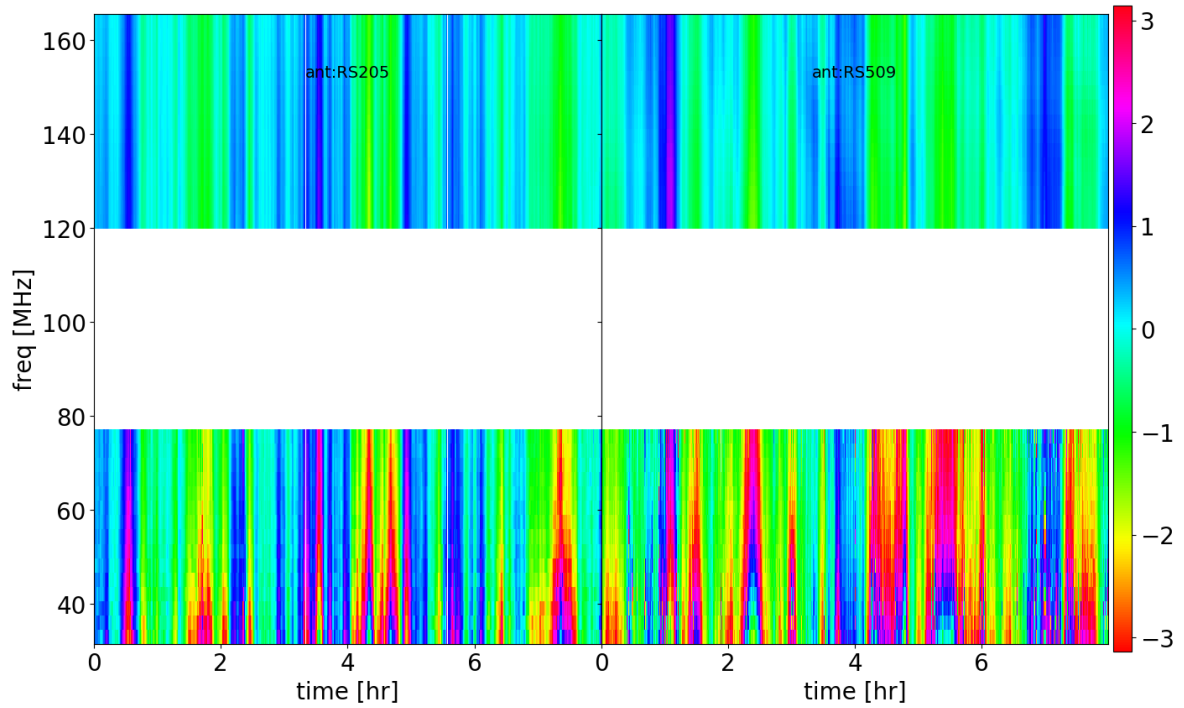
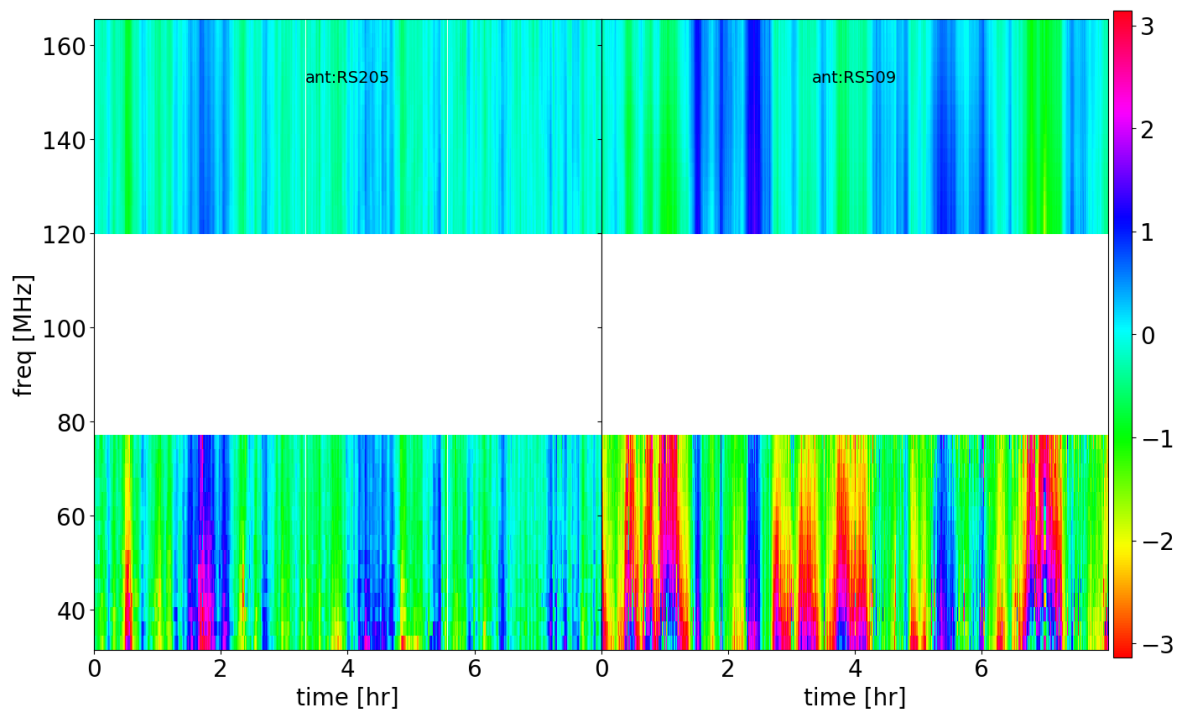
(a) Phase solutions towards *dir36*.(b) Phase solutions towards *dir100*.

Figure 5.12: Phase solutions ϕ in radians in LBA and HBA for the two stations RS205 and RS509 as a function of time (x -axis) and frequency (y -axis). The top figure (a) shows solutions towards calibrator direction *dir36*, the lower figure (b) towards *dir100*.

5 Investigating LOFAR 2.0 with Simulations

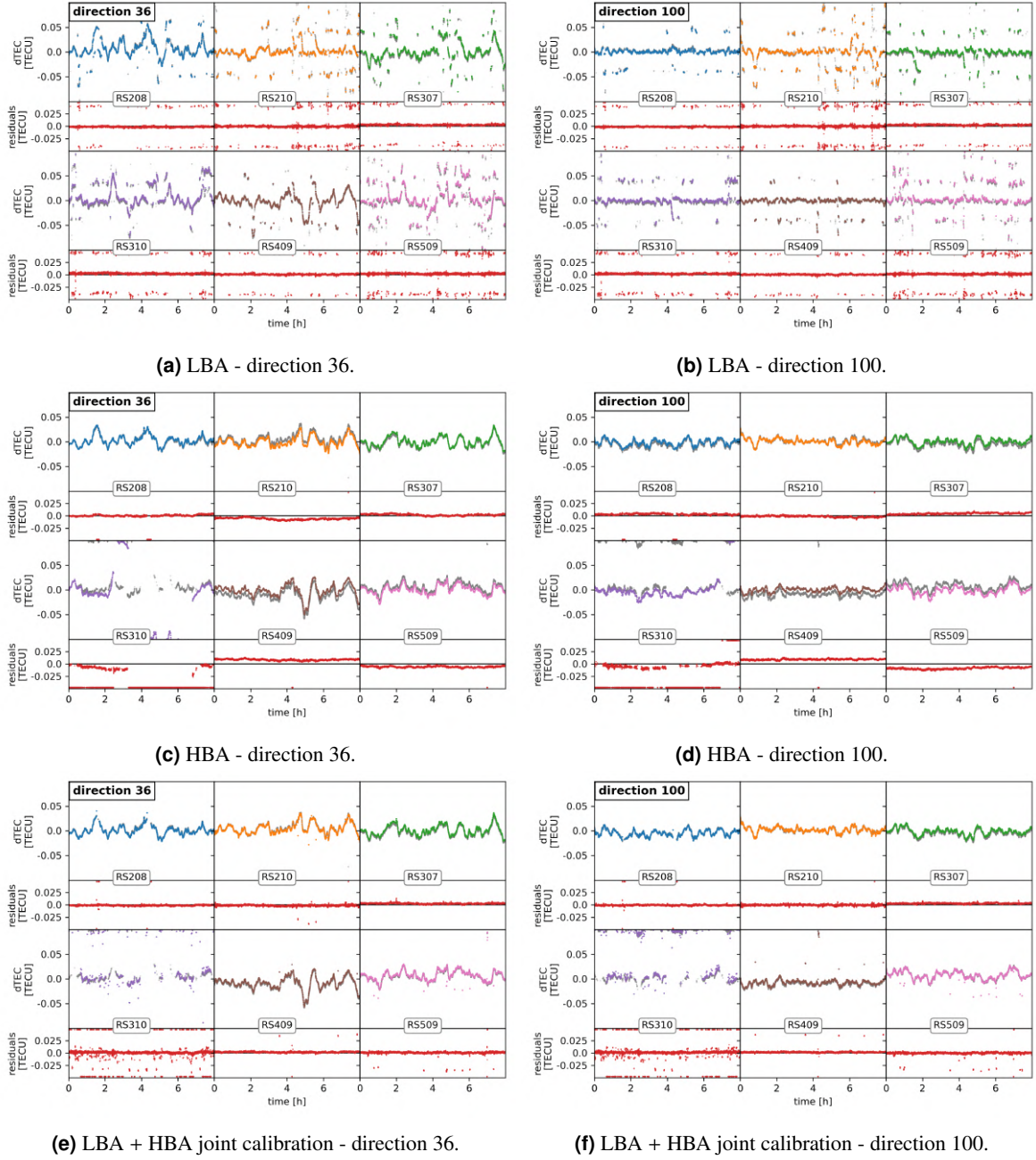
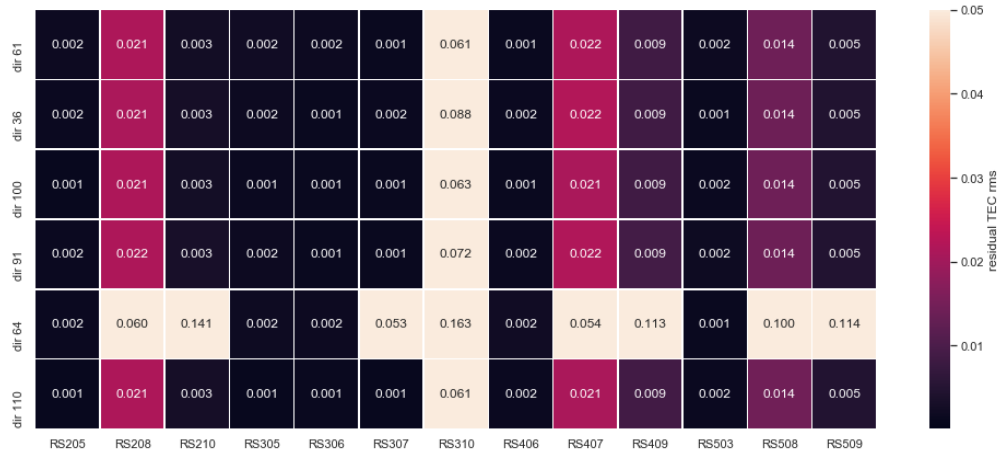


Figure 5.13: Direction-dependent TEC-solutions (colors except red) and residuals with respect to the simulation input (red) shown in each of the six panels (a) to (f) for six distant RS. Residuals outside of the displayed range are indicated by arrows. Figures (a), (c) and (e) in the left column show solutions towards *dir36*, whereas figures (b), (d), and (f) in the right column show solutions towards *dir100*. In the two figures in the top row, only LBA phase solutions were used to extract the dTEC, while for the center row, only HBA was considered. The figures in the bottom row show joint calibration solutions derived from LBA and HBA combined. The gray lines in the background of the dTEC panels show the difference between input dTEC and direction-independent dTEC solutions for this station and direction, these values were used to calculate the residuals as $dTEC_{residual} = dTEC_{DDE} - (dTEC_{input} - dTEC_{DIE})$. All values are referenced to CS001LBA and CS001HBA0, respectively.



(a) LBA TEC-solutions



(b) HBA TEC-solutions



(c) LBA + HBA joint calibration TEC-solutions

Figure 5.14: Each of the three plots (a) - (c) shows the direction-dependent TEC rms error as a function of direction (y-axis) and station (x-axis). The TEC was extracted from phase solutions derived from LBA (a), HBA, (b) or both (c).

5 Investigating LOFAR 2.0 with Simulations

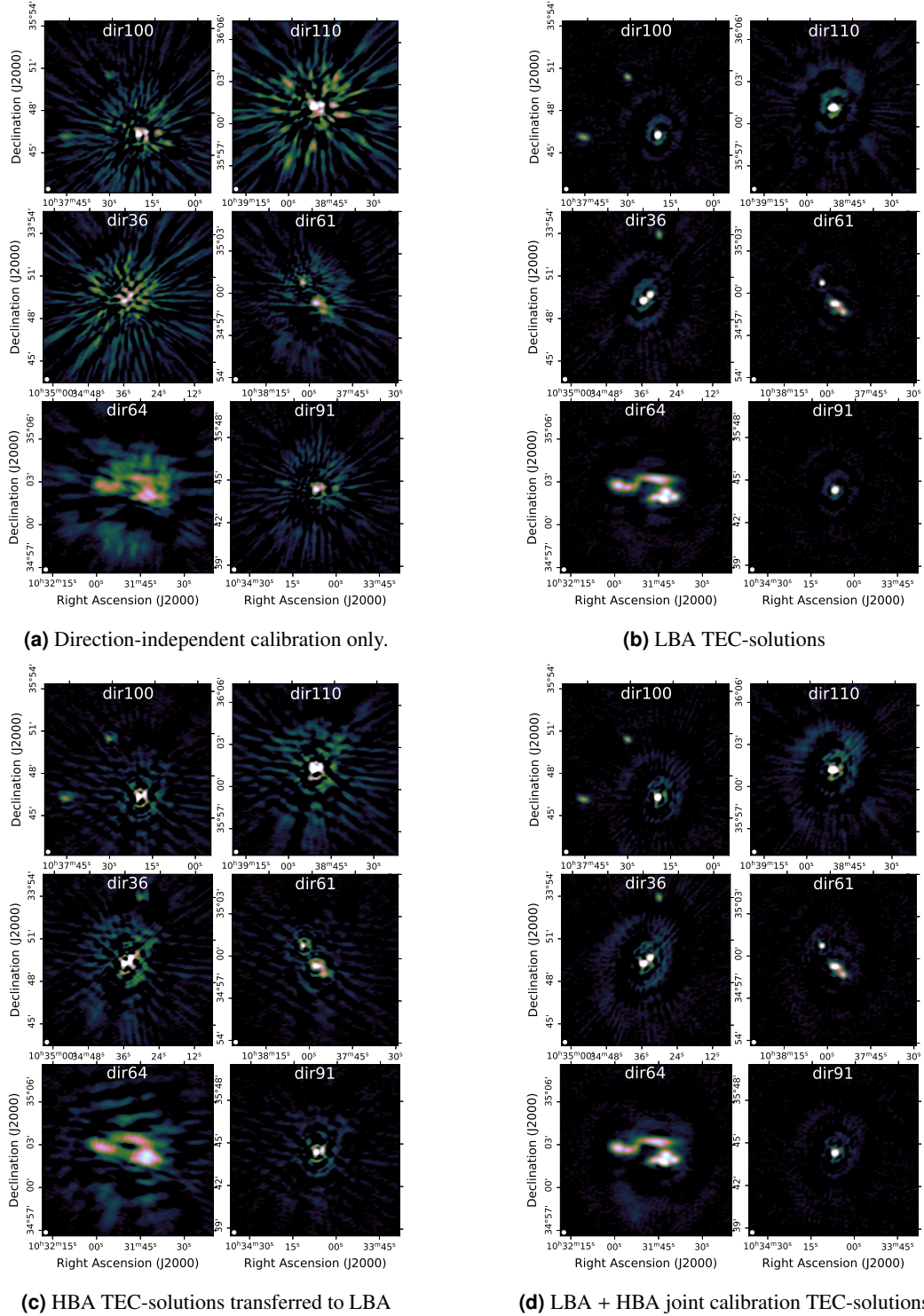


Figure 5.15: 12''-region around the six calibrator directions used in the analysis with different calibration solutions applied shown in panels (a) - (d). All images share the same color scale and show LBA data centered at 54 MHz. Panel (a) is corrected only for direction-independent effects, panels (b) and (c) are corrected using TEC-solutions derived from only LBA or only HBA, and panel (d) shows the joint-calibration case.

5.5.4 Calibration scenarios for LOFAR 2.0

To study possible scenarios of direction-dependent calibration in LOFAR 2.0, we rely on strategies which extract the TEC from the direction-dependent phase solutions. We use the software LoSoTo (de Gasperin et al. 2019) to fit the dispersive-delay term (see Eq. 5.2). To reduce the local minima problem, a grid-search is performed to determine the initial guess of the optimization. We assign a weight to the LBA phase solutions according to $w(\nu) = \min(\text{SEFD})/\text{SEFD}(\nu)$, the HBA phase solutions are assigned a constant weight of $w = 1$. We compare three different approaches to extract dTEC from the phase-solutions: First, using only the LBA solutions, as shown in Fig. 5.13a,b. Second, using only the HBA solutions, as shown in Fig. 5.13c,d. This scenario is the case of solution-transfer. Third, testing joint calibration - we combine LBA and HBA solutions to extract TEC over a broad frequency range, see Fig. 5.13e,f.

Due to the different beam sizes, the direction-independent TEC-solution of LBA and HBA differ slightly. Therefore, the direction-dependent solutions will also be slightly different to account for this offset. Thus, direction-independent solutions obtained with one antenna type cannot directly be combined with direction-dependent solutions obtained with the other. We take this into account by applying the HBA direction-independent solutions for the remote stations to the LBA data in the first and second case. For the third case, we also add the phases corresponding to the difference between the HBA and LBA direction-independent TEC solutions to the direction-dependent phase solutions in LBA to establish a common ground for direction-dependent TEC-extraction. The results of all three approaches as well as the residuals with respect to the simulation input are displayed in Fig. 5.13 for the calibrators *dir36* and *dir100*. In Fig. 5.14, we show the rms error of the TEC solutions for the six calibration directions and all remote stations. In the LBA only case, while many of the residuals are close to zero, a substantial fraction converged towards neighboring minima, leading to a rms error which is, in most cases, higher than in the competing approaches. This can be explained with the low S/N of the LBA. For the HBA observation, most stations and directions reach a mTECU-scale rms error but show a small systematic offset in the residuals. This offset appears to be present in most directions to a similar extent, pointing towards a direction-independent phase error in the data which is not fully corrected. One negative exception is the complex source *dir64*, where no sufficiently accurate model could be derived in HBA, leading to significantly noisier solutions. Further parameter fine-tuning could potentially improve solutions for this direction. Furthermore, for station RS310, improper solutions were found during direction-independent calibration. This issue propagates to direction-dependent calibration. In the joint-calibration approach, the mean rms of the solutions is the lowest and the aforementioned issues are partially solved. The TEC-jumps are considerably less frequent than in the LBA-only case, the systematic drifts present in the HBA residuals are attenuated and the solutions for the problematic station RS310 are substantially improved compared to the HBA-only case.

In Fig. 5.15, we show LBA images of the six calibrators, comparing image quality without direction-dependent corrections to the three different direction-dependent calibration strategies of our analysis. In all cases, the image quality improved compared to the direction-independently calibrated image. The best image quality is achieved using either LBA or joint-calibration TEC solutions, both approaches result in a noise level of $0.9 \text{ mJy beam}^{-1}$. The characteristic star-like patterns around the sources caused by the ionospheric dispersive delay are removed almost completely. However, extended, spiral-shaped artifacts remain. The image quality using only the LBA stations for calibration is equally good and for some directions even slightly better than the joint calibration despite the joint-calibration solutions being more accurate. This can be explained by two points: first, the jumps in LBA-extracted TEC lead to a high rms of the residuals while still providing a decent calibration for

5 Investigating LOFAR 2.0 with Simulations

part of the frequency band, and second, remaining corruptions in the LBA data might not be fully described by a TEC-term.

Image quality is worse in the solution-transfer scenario: noticeable calibration artifacts are present, revealing that multiple stations are not well calibrated. This gives rise to the question of why the image quality in this scenario is inferior if the solutions show fewer jumps than the ones obtained from LBA. The explanation for this must lie in the systematic offsets which can be observed in the HBA residuals in Fig. 5.13. The likely cause of these offsets comes from a phase error in HBA that was not fully corrected by our calibration strategy; however, the root of this issue could not be determined. While the HBA TEC-solutions will certainly improve if the phase offset can be solved, this also highlights an intrinsic disadvantage of the solution-transfer approach: while the presence of small phase errors in HBA data can still lead to satisfying results using TEC-calibration at HBA frequencies, transferring the solutions to LBA can strongly amplify any phase errors from TEC-offsets. Even if there were no residual errors in the simulated data, minor systematic effects which are not present in the simulation could cause similar problems in real observations. Therefore, solution-transfer is only viable if the HBA data are free of non-ionospheric phase errors.

A more refined calibration strategy could improve the solutions obtained during direction-dependent calibration. Most notably, we emphasize that there are further points where the simultaneity of the observations could be exploited. It would be possible to jointly calibrate the first, second, and possible third order ionospheric term as well as clock delays during direction-independent calibration. Additionally, the spectral properties of the model components could be estimated more accurately by a unified model for the low and high band, possibly obtained by joint de-convolution.

To use joint calibration strategies in application in the future, the development of specialized software will be necessary. Possible advancements include the implementation of a solution algorithm which can solve for TEC and further frequency-dependent effects on LBA and HBA data together, bypassing the intermediate phase-solution. Furthermore, joint calibration could enable the leap from facet-based towards TEC-screen based calibration as proposed in Albert et al. (2020) in LOFAR 2.0 by increasing the robustness of the TEC-estimates towards residual phase errors.

5.5.5 Limitations

A number of points must be considered when evaluating the accuracy of LoSiTo simulations. First of all, only the first and second order ionospheric effects are implemented in the simulation. Higher-order effects are non-negligible at the lowest frequencies observed by LOFAR ($\nu \lesssim 40$ MHz). Additionally, in real LOFAR observations, the presence of ionospheric scintillation can affect the coherency of celestial radio signals under special ionospheric conditions. These scintillations, together with artificial radio-frequency interference (RFI), can render data unusable for periods of time, but are not accounted for in LoSiTo. Second, while we do not expect the thin-layer and frozen turbulence assumptions to interfere with facet-based calibration strategies, we need to be cautious in using the simulations when working with approaches that enforce spatial coherency across multiple stations, since the phase error from projecting the three-dimensional structure onto a two-dimensional layer is not represented. Third, the simulated sky cannot recreate the complexity of the real radio sky due to limitations in computing power. The sky model used in this work underestimates the number density especially of faint sources. Furthermore, it does not contain emission in side lobes or on very large angular scales, both of which are known to interfere with calibration (de Gasperin et al. 2020; Shimwell et al. 2019). Fourth, the beam model employed in the simulation is the product of semi-analytic simulations. It is known that the real beam response deviates from this model to some extent (de Gasperin et al. 2019). This deviation is not included in the simulation. Last, real LOFAR data can contain subdominant sys-

tematic effects that are not well understood at present and hence, cannot be modeled in simulations.

5.6 Conclusions

In this paper, we present models for a comprehensive list of systematic effects in LOFAR and LOFAR 2.0 observations and the LoSiTo code in which we embedded them. These models include a turbulent thin-layer representation of the ionosphere which is used to derive the first and second order ionospheric effect. Furthermore, LoSiTo features the systematic effects of clock error, polarization misalignment, the primary beam and bandpass responses as well as an estimate of the LOFAR 2.0 noise level based on empirically determined values for the LOFAR SEFD. The product of a simulation is a "measurement set," which can be further processed with standard radio astronomy tools. The code was developed with the aim to assist the progression of current and future LOFAR calibration strategies and has been made publicly available.

We used LoSiTo to simulate a full eight-hour calibrator and target field observation using the LOFAR 2.0 system. We presented the analysis of the simulated data, where we performed data reduction of the calibrator observation and direction-dependent calibration of the target field using adjusted LOFAR calibration pipelines. As a proof-of-concept, we investigated new strategies for direction-dependent calibration of the data. We compared ionospheric solutions derived from LBA and HBA separately to solutions derived jointly from both systems. We found that the ionospheric parameters of the simulation can be determined most accurately in the joint calibration approach, where we reach a mTEC-scale rms error in 90% of the cases. When we use only LBA data for calibration, the solutions are more noisy; nevertheless, the resulting image quality is very similar to the joint calibration approach with an rms noise of $0.9 \text{ mJy beam}^{-1}$ away from bright sources and artifacts in the vicinity of the calibrators. This indicates that while we managed to determine the TEC accurately, our image-space results are still limited by the presence of systematic errors which could be resolved by an improvement of the strategy. For the case of solution transfer, where the ionospheric solutions found in the HBA calibration are applied to the LBA data, we find good convergence and very little noise in the solutions. However, they show systematic offsets at a scale of $\approx 5 \text{ mTECU}$ which create strong artifacts in image-space. While further development of the calibration procedure could improve the image quality, this result reveals a central downside of the solution-transfer approach: errors in the HBA data are strongly amplified when the solutions are applied to LBA data. Therefore, solution transfer can only be an option if all non-ionospheric effects in HBA are corrected to a high level of accuracy.

Acknowledgements

We thank the anonymous referee and the editor for their constructive remarks on this work. This project is funded by the Deutsche Forschungsgemeinschaft (DFG, German Research Foundation) under projet number 427771150. The authors thank J. Hessels, C. Bassa, T. Shimwell and the LOFAR 2.0 developing team for their help.

5 Investigating LOFAR 2.0 with Simulations

6 Conclusion and Outlook

In this thesis, I presented my research on the environmental effects in the galaxy clusters Virgo and A 1033. For this, I employed LOFAR observations to probe the radio emission of star-forming galaxies, radio galaxies and the ICM.

After introducing the basic astrophysical and observational concepts of this thesis in Chap. 1, I present the LOFAR Survey of the Virgo Cluster in Chap. 2. This cluster is a classical testbed for studies of the interaction between galaxies and the ICM. This survey is the deepest wide-field radio survey of Virgo and allowed me to conduct a radio census of galaxies in the Virgo cluster, resulting in a catalog of 111 LOFAR-detected galaxies. In the survey images, I discovered previously unknown radio tails of the massive early type galaxy M 49. These are clearly shaped by the ram pressure they experience during the infall of the M 49 sub-cluster onto the Virgo center. Furthermore, I found that 19/97 of the LOFAR-detected late-type galaxies in Virgo show a radio morphology that is indicative of RPS. Thus, **RPS as a mechanism that deprives galaxies of their ISM is a widespread phenomenon in Virgo**. Further, I showed that radio observations are suited to trace RPS events even in low-luminosity dwarf galaxies. The imaging data and the catalog of the survey are made available to the community¹ and carry a large legacy value.

Based on this survey data and additional LoTSS observations, I compiled a sample of Virgo Cluster RPS galaxies in Chap. 3. I then compared their properties to a control sample of LOFAR-detected nearby galaxies from the Herschel Reference Survey and derived the radio-SFR relations for these two samples using SFRs based on H α and FUV measurements. The radio-SFR relations I found for the control sample are in agreement with the relations reported in the literature. However, the RPS sample shows a clear radio-excess of a factor of 2-3 compared to the control sample. While it was known that galaxies suffering from RPS oftentimes show excess radio emission, it is now apparent how common this excess is. Almost 90% of the RPS galaxies in the Virgo cluster have a higher radio luminosity than the radio-SFR-relation for the control sample would suggest. Furthermore, I investigated the radio spectral indices of the galaxies using archival 1.4 GHz data. **I reported for the first time evidence that RPS galaxies have not only higher radio luminosities, but also steeper spectral indices compared to non-perturbed objects of the same mass.**

I considered two models which could explain both of these differences, a scenario with rapid SFR-quenching due to RPS, and a scenario where the magnetic field in RPS galaxies is enhanced by the environmental interaction. **The rapid-quenching model can only explain the multi-frequency data for the three galaxies with the highest radio excess and only in the case of short quenching times below 100 Myr. An enhanced magnetic field provides a better explanation for the general properties of RPS galaxies**, and I find that an increase of the magnetic field of a factor of ~ 1.5 – 2 can approximately reproduce the observed radio emission and spectral steepening. To further probe the nature of the radio excess, I constructed spatially resolved maps of the expected radio emission based on the SFR surface density and isotropic CRe diffusion. I compared the ratio between the observed and the expected emission of the RPS galaxies. In general, the radio excess is present not just in the tails, but also across the disks. Only for NGC 4501 and NGC 4330 the excess is dominantly at the

¹https://lofar-surveys.org/virgo_data.html

6 Conclusion and Outlook

leading edge of the galaxy, as it would be expected from the magnetic field compression scenario. Therefore, magnetic field compression is either not the only mechanism at play or projection effects make the signature of the compression challenging to identify. Follow-up simulations are necessary to further investigate the expected radio morphology of galaxies suffering from RPS.

RPS affects not only star-forming galaxies, but also radio galaxies by stripping and bending their radio lobes. Under certain circumstances, the interaction between the stripped plasma and the ICM can re-accelerate the CRe in the plasma. A particularly puzzling case where such a mechanism is at work is the GReET in A 1033, which is among the steepest-spectrum radio sources known with a 144-323 MHz spectral index of $\alpha \sim -4$. In Chap. 4, I presented new ultra-low frequency LOFAR LBA observations of the system, where I find that **the spectrum of this peculiar source is extremely curved and flattens between 54-144 MHz to $\alpha \sim -2$** . This implies the presence of a cut-off in the CRe energy spectrum of the GReET, **in agreement with re-acceleration of an old CRe population by a low-efficiency process**. A suggested mechanism for this is turbulence that is forced into the tail by the interactions with the ICM. I also carried out a multi-frequency spectral aging analysis of the tail, **finding a maximum age of the tail of 800 Myr**.

A 1033 also hosts a radio halo. I analyzed the spectrum of the halo and found an ultra-steep spectral index of $\alpha \sim -1.7$ between 54 and 144 MHz. USSRHs are expected in moderately massive clusters like A 1033. However, the total radio power of the halo is a factor 7 higher than expected, given the mass of A 1033. Possible reasons for this are either a particularly energetic merger or a strong enrichment with mildly relativistic CRe in the cluster due to the various powerful radio sources present.

These scientific results of my thesis were enabled by technical developments of the calibration and imaging strategies for LOFAR. My work proved that LOFAR HBA can reach quasi-thermal noise even in the presence of extremely bright sources. The *peeling*-approach I developed for M 87 can be transferred to other regions of the sky which are plagued by the presence of bright *A-Team* or calibrator sources, for example in LoTSS. At the start of my doctoral project, direction-dependent calibration for LOFAR LBA was still in its infancy, and not a single published observation reached the thermal noise level of the instrument. The calibration strategies for LOFAR LBA were improved also in context of the work presented in Chap. 4, and by now, the full direction-dependent calibration of LOFAR LBA observations is routinely achieved.

To further advance our understanding of the radio sky, we need to improve our observational capabilities. Fortunately, the ongoing LOFAR 2.0 upgrade will bring this required progress, in particular in the low-band. This update will, among other improvements, allow us to simultaneously observe with the high- and low-band antennas, thereby enabling new calibration strategies that leverage the large combined bandwidth. In Chap. 5, I investigated these future calibration strategies based on simulated LOFAR 2.0 observations. I found that the transfer of ionospheric calibration solutions from the high-signal-to-noise HBA to the low-signal-to-noise LBA is susceptible to any residual errors present in the HBA data. These residual errors will be strongly amplified when transferred across frequency. Therefore, a combined calibration approach, where solutions are simultaneously derived from LBA and HBA data, proved more stable. Such a strategy will in particular be helpful for faint sources, where the signal in LBA is not sufficient to independently derive the ionospheric parameters.

6.1 Further projects

In this dissertation, I presented a large part of the research I conducted during my doctoral studies, which I collected in the form of four publications. However, I took part in further research projects, a

few of which I would like to highlight here with the aim of drawing a connection to the work of this thesis. First of all, I was involved in the technical development of the *Library for Low-Frequencies* (LiLF), the default calibration framework for interferometric observations with the LOFAR LBA. In this context, I contributed to the data releases of the LoLSS survey (de Gasperin et al. 2021; de Gasperin et al. 2023). This survey is the most sensitive and highest resolution survey in the ultra-low frequency regime, the current and future data releases will allow us to systematically investigate the spectral properties of star-forming galaxies down to the ultra-low frequencies where ionization losses and absorption effects become relevant (Gajović et al. in prep.). Furthermore, LoLSS is crucial to detect and model steep-spectrum emission, which oftentimes cannot be detected above the frequency range of LOFAR. Examples for such sources are (ultra steep-spectrum) radio halos, ancient or gently re-energized radio galaxy tails and radio phoenixes.

The work that we published in Pasini et al. (2022) represents a sneak-peek of the results that will be possible for large samples with LoLSS and LoTSS in the future. In this publication, we present a study of the A 1550 cluster, which hosts a USSRH, a radio relic and a peculiar re-energized radio galaxy tail. A follow-up study of 11 galaxy clusters in the data release 1 of LoLSS and the data release 2 of LoTSS (Shimwell et al. 2022) is on the way, it represents the first dedicated analysis of the low-frequency spectral indices of a sample of radio halos (Pasini et al. submitted).

In Cuciti et al. (2022), the combination of LOFAR LBA and HBA also allowed us to detect highly extended emission in four massive galaxy clusters. This proves that galaxy clusters are enveloped by CRe out to a significant distance (> 1 Mpc). This new category of sources is called *Megahalo*. Furthermore, in Biava et al. (2021), we unveiled ultra-steep spectrum emission surrounding the cool-core of the galaxy cluster RXJ1720.1+2638. We attributed this radio emission to re-acceleration of CRe by turbulence which was injected into the ICM by a minor merger event. This shows that radio halo-like emission is not only limited to strong mergers.

6.2 The next steps

I presented the LOFAR HBA Virgo Cluster Survey, the deepest wide-field survey of the cluster to date. This represents the first data release of the ViCTORIA project. The second sub-projects of ViCTORIA is the LOFAR LBA Virgo Cluster Survey (PI: Edler), which consists of 66 h of observation time in multi-beam mode, i.e. observing three target fields in parallel for an effective exposure of 198 h at 54 MHz. This survey covers the same pointings as the HBA counterpart and it will be crucial to interpret the diffuse extended emission that we detect for M49 and the W'-filament. Furthermore, we will be able to probe the spectral index properties of the RPS galaxies, perform spectral aging analyses of the tails and probe the presence of leading-edge ISM compression which would imprint in an ultra-low frequency flattening due to ionization losses.

The third ViCTORIA sub-project is the MeerKAT Virgo Cluster Survey (PI: de Gasperin), which consists of 287 h of MeerKAT L-band (900–1700 MHz) observations that cover the cluster with 320 pointings in full polarization. This survey will enable us to match the resolution of the LOFAR HBA survey for resolved spectral index studies at sub-kpc scale. We will be able to probe even fainter RPS tails due to the $\sim 7 \mu\text{Jy beam}^{-1}$ resolution reached by the survey. The polarized data will allow us to infer the magnetic field structure in the RPS galaxies, thereby allowing us to test the presence of magnetic field draping or compression. In addition, we will also be able to probe the magnetic field within the ICM using Faraday rotation studies of polarized background sources. Since the frequency band covers the 21 cm-line at 25 kHz resolution, we will not just receive a full H I-census of the cluster, which presents an independent tool to trace RPS events, but also be able to infer the ISM dynamics

6 Conclusion and Outlook

of perturbed galaxies. The first pilot fields of the MeerKAT survey are already processed and we published them in Boselli et al. (2023b). In this work, we discovered a new H I-tail of the star-forming galaxy NGC 4523, which is on its first infall onto the Virgo cluster and in an early phase of stripping.

The ViCTORIA data will also be used to study interacting radio galaxies in the early-type galaxies. We are working on a sample of 11 elliptical galaxies which are detected in the LOFAR HBA and MeerKAT Virgo Cluster Surveys (Spasic et al. in prep.). In this work, we will analyze the properties of the AGN as a function of the surroundings and present a detailed study of the stripped radio galaxy tails of M49, which was first detected in the publications presented in this thesis.

To study the impact of the cluster environment on the evolution of galaxies, it is important to infer the properties of the ICM itself. To date, the most sensitive X-ray survey published that covers the full Virgo cluster is still from ROSAT. With the advance of eROSITA, we will be able to probe the ICM properties and dynamics at a greatly improved sensitivity and spatial resolution (McCall et al. in prep.).

Next, while we are vastly accelerating our understanding of the environmental effects at play in Virgo, further nearby galaxy clusters, most notably Coma and A 1367, are also of great importance to obtain the full picture of RPS in clusters of different mass and dynamical state. Imaging campaigns of these systems, also including the ultra-low frequency LOFAR LBA part, are in preparation. The last step after detailed studies of nearby galaxies will be to extend these studies to clusters of mid and high redshift to estimate the importance of RPS across cosmic time. In this context, higher resolution instruments are required. For LOFAR, imaging with the HBA international stations is by now routinely possible and allows us to achieve the sub-arcsecond resolution required to probe stripped tails in distant clusters, while for the LBA international stations, first proof-of-concepts were conducted and the LOFAR 2.0 upgrade will further amplify these endeavors.

7 Acknowledgments

During the three years of my doctoral studies, I had the chance to meet many interesting people, learn about the universe, take part in exciting projects and travel across Europe. I greatly enjoyed this time with all its challenges and changes, and I would like to express my gratitude to the following people:

First and foremost, I want to thank my supervisor Francesco de Gasperin for his support during my PhD. I am privileged to have had him as a supervisor, colleague and friend and I greatly enjoyed our scientific and non-scientific discussions, travels and our exciting joint projects. It is thanks to Francesco that I discovered my passion for radio astronomy. Next, I want to thank my supervisor Marcus Brüggemann for the support and advice I received in the last years and for building such a vivid research group. It is due to Marcus' dedication that Hamburg Observatory plays an active role in radio astronomy with LOFAR and beyond.

Next, I thank Joe Liske, Dieter Horns and Peter Hauschildt for being part of the examination commission of my doctoral defense.

A special thanks to my friends and partners in crime science Kathrin, Marco and Giulia for their friendship, support, their pleasant distraction, their sweets and the scientific discussion and travel company during my PhD. I also want to thank Volker, Antonio, Thomas, Virginia, Angelina, Gabriella, Jörg, Lovorka, and all the others for making my time at the Observatory so enjoyable.

Outside of the academic world, I want to thank Thomas, Lena, Ali, Andras, my dad, Nicole and my sisters Emma, Meike and Verena for their support, friendship, love or a combination thereof. Finally, my greatest thanks goes to Lena for her love and support through the various phases of my career, from school to my Bachelor's and Master's studies and now finally my PhD. Thanks for always being there for me and caring for me.

7 Acknowledgments

8 Bibliography

- Abazajian, K. N., Adelman-Mccarthy, J. K., Agüeros, M. A., et al. 2009, *ApJ Suppl.*, 182, 543
- Abdo, A. A., Ackermann, M., Ajello, M., et al. 2010a, *ApJ*, 723, 649
- Abdo, A. A., Ackermann, M., Ajello, M., et al. 2010b, *ApJ*, 708, 1254
- Abdollahi, S., Ackermann, M., Ajello, M., et al. 2017, *Phys. Rev. D*, 95, 082007
- Adami, C., Slezak, E., Durret, F., et al. 2005, *A&A*, 429, 39
- Ade, P. A., Aghanim, N., Arnaud, M., et al. 2016, *A&A*, 594, 79
- Adriani, O., Akaike, Y., Asano, K., et al. 2017, *Phys. Rev. Lett.*, 119, 181101
- Aguerri, J. A. L., Gerhard, O. E., Arnaboldi, M., et al. 2005, *AJ*, 129, 2585
- Aguilar, M., Aisa, D., Alvino, A., et al. 2014, *Phys. Rev. Lett.*, 113, 121102
- Akritas, M. G. & Bershadsky, M. A. 1996, *ApJ*, 470, 706
- Alam, S., Albareti, F. D., Allende Prieto, C., et al. 2015, *ApJ Suppl.*, 219, 12
- Albert, J. G., van Weeren, R. J., Intema, H. T., & Röttgering, H. J. A. 2020, *A&A*, 635, A147
- Allen, S. W., Dunn, R. J. H., Fabian, A. C., Taylor, G. B., & Reynolds, C. S. 2006, *MNRAS*, 372, 21
- Arnaboldi, M., Gerhard, O., Aguerri, J. A. L., et al. 2005, *ApJL*, 614, L33
- Astropy Collaboration, Price-Whelan, A. M., Lim, P. L., et al. 2022, *ApJ*, 935, 167
- Baade, W. & Zwicky, F. 1934, *Phys. Rev.*, 46, 76
- Baars, J. W. M., Genzel, R., Pauliny-Toth, I. I. K., & Witzel, A. 1977, *A&A*, Vol. 61, p. 99 - 106, 61, 99
- Baldwin, J. A., Phillips, M. M., & Terlevich, R. 1981, *PASP*, 93, 5
- Ballarati, B., Feretti, L., Ficarra, A., et al. 1981, *A&A*, 100, 323
- Bambic, C. J., Russell, H. R., Reynolds, C. S., et al. 2023, *MNRAS*, 522, 4374
- Bartels, R., Zandanel, F., & Ando, S. 2015, *A&A*, 582, A20
- Basu, A., Beck, R., Schmidt, P., & Roy, S. 2015, *MNRAS*, 449, 3879
- Beck, R. 2015, *A&A Rev.*, 24, 4
- Beck, R., Berkhuijsen, E. M., Gießübel, R., & Mulcahy, D. D. 2020, *A&A*, 633, A5

8 Bibliography

- Beck, R. & Krause, M. 2005, *Astronomische Nachrichten*, 326, 414
- Bell, A. R. 1978a, *MNRAS*, 182, 147
- Bell, A. R. 1978b, *MNRAS*, 182, 443
- Bell, E. F. 2003, *The Astrophysical Journal*, 586, 794
- Berkhuijsen, E. M., Beck, R., & Tabatabaei, F. S. 2013, *MNRAS*, 435, 1598
- Best, P. N. 2009, *Astronomische Nachrichten*, 330, 184
- Best, P. N., Kauffmann, G., Heckman, T. M., et al. 2005, *MNRAS*, 362, 25
- Best, P. N., Kondapally, R., Williams, W. L., et al. 2023, *MNRAS*, 523, 1729
- Biava, N., de Gasperin, F., Bonafede, A., et al. 2021, *MNRAS*, 508, 3995
- Bilitza, D. 2018, *Advances in Radio Science*, 16, 1
- Bilton, L. E. & Pimblet, K. A. 2018, *MNRAS*, 481, 1507
- Binggeli, B., Popescu, C. C., Tammann, G. A., et al. 1993, *A&A Suppl. Ser.*, 98, 275
- Binggeli, B., Sandage, A., & Tammann, G. A. 1985, *AJ*, 90, 1681
- Binggeli, B., Tammann, G. A., Sandage, A., et al. 1987, *AJ*, 94, 251
- Bîrzan, L., McNamara, B. R., Nulsen, P. E. J., Carilli, C. L., & Wise, M. W. 2008, *ApJ*, 686, 859
- Bîrzan, L., Rafferty, D. A., Cassano, R., et al. 2019, *MNRAS*, 487, 4775
- Bîrzan, L., Rafferty, D. A., McNamara, B. R., Wise, M. W., & Nulsen, P. E. J. 2004, *ApJ*, 607, 800
- Blandford, R. D. & Znajek, R. L. 1977, *MNRAS*, 179, 433
- Blumenthal, G. R., Faber, S. M., Primack, J. R., & Rees, M. J. 1984, *Nature*, 311, 517
- Böhringer, H., Briel, U. G., Schwarz, R. A., et al. 1994, *Nature*, Volume 368, Issue 6474, pp. 828-831 (1994)., 368, 828
- Böhringer, H., Chon, G., & Kronberg, P. P. 2016, *A&A*, 596, A22
- Bonafede, A., Brügger, M., Rafferty, D., et al. 2018, *MNRAS*, 478, 2927
- Bonafede, A., Brunetti, G., Rudnick, L., et al. 2022, *ApJ*, 933, 218
- Bonafede, A., Brunetti, G., Vazza, F., et al. 2021, *ApJ*, 907, 32
- Bonafede, A., Feretti, L., Murgia, M., et al. 2010, *A&A*, 513, A30
- Bonafede, A., Intema, H. T., Brügger, M., et al. 2014, *ApJ*, 785, 1
- Boreman, G. & Dainty, C. 1996, *Journal of the Optical Society of America A*, 13, 517
- Borlaff, A. S., Lopez-Rodriguez, E., Beck, R., et al. 2023, *ApJ*, 952, 4

- Boselli, A., Boissier, S., Cortese, L., et al. 2006, *ApJ*, 651, 811
- Boselli, A., Boissier, S., Heinis, S., et al. 2011, *A&A Suppl. Ser.*, Volume 528, id.A107, 19 pp., 528, A107
- Boselli, A., Cortese, L., & Boquien, M. 2014a, *A&A*, 564, A65
- Boselli, A., Cortese, L., Boquien, M., et al. 2014b, *A&A*, 564, A67
- Boselli, A., Cuillandre, J. C., Fossati, M., et al. 2016, *A&A Suppl. Ser.*, Volume 587, id.A68, 17 pp., 587, A68
- Boselli, A., Eales, S., Cortese, L., et al. 2010, *PASP*, 122, 261
- Boselli, A., Fossati, M., Consolandi, G., et al. 2018, *A&A*, 620, A164
- Boselli, A., Fossati, M., Cuillandre, J. C., et al. 2018a, *A&A*, 615, A114
- Boselli, A., Fossati, M., Ferrarese, L., et al. 2018b, *A&A*, 614, A56
- Boselli, A., Fossati, M., Gavazzi, G., et al. 2015, *A&A Suppl. Ser.*, 579, 102
- Boselli, A., Fossati, M., Roediger, J., et al. 2023a, *A&A*, 669, A73
- Boselli, A., Fossati, M., & Sun, M. 2022, *A&ARev.*, 30, 3
- Boselli, A. & Gavazzi, G. 2006, *PASP*, 118, 517
- Boselli, A., Hughes, T. M., Cortese, L., Gavazzi, G., & Buat, V. 2013, *A&A*, 550, A114
- Boselli, A., Lupi, A., Epinat, B., et al. 2021, *A&A*, 646, 139
- Boselli, A., Roehlly, Y., Fossati, M., et al. 2016, *A&A*, 596, A11
- Boselli, A., Serra, P., de Gasperin, F., et al. 2023b, *A&A*, 676, A92
- Boselli, A., Voyer, E., Boissier, S., et al. 2014, *A&A*, 570, A69
- Bothun, G. D. & Dressler, A. 1986, *ApJ*, 301, 57
- Botteon, A., Cassano, R., Eckert, D., et al. 2019, *A&A*, 630, 77
- Botteon, A., Cassano, R., Van Weeren, R. J., et al. 2021a, *ApJ Let.*, 914, L29
- Botteon, A., Giacintucci, S., Gastaldello, F., et al. 2021b, *A&A*, 649, 37
- Botteon, A., Shimwell, T. W., Cassano, R., et al. 2022, *A&A*, 660, A78
- Boxelaar, J. M., van Weeren, R. J., & Botteon, A. 2021, *Astronomy and Computing*, 35, 100464
- Boyd, T. J. M. & Sanderson, J. J. 1969, *Plasma dynamics* (London, Nelson)
- Brienza, M., Shimwell, T. W., de Gasperin, F., et al. 2021, *Nature Astron.*, 5, 1261
- Brosch, N., Almoznino, E., & Hoffman, G. L. 1998, *A&A*, 331, 873

8 Bibliography

- Brown, T., Wilson, C. D., Zabel, N., et al. 2021, *ApJ Suppl.*, 257, 21
- Brüggen, M., Bykov, A., Ryu, D., & Röttgering, H. 2012, *SSR*, 166, 187
- Brunetti, G., Blasi, P., Reimer, O., et al. 2012, *MNRAS*, 426, 956
- Brunetti, G., Giacintucci, S., Cassano, R., et al. 2008, *Nature*, 455, 944
- Brunetti, G. & Jones, T. W. 2014, *Rev. Mod. Phys.*
- Brunetti, G. & Lazarian, A. 2007, *MNRAS*, 378, 245
- Brunetti, G. & Lazarian, A. 2011, *MNRAS*, 412, 817
- Brunetti, G. & Lazarian, A. 2016, *MNRAS*, 458, 2584
- Brunetti, G., Setti, G., Feretti, L., & Giovannini, G. 2001, *MNRAS*, 320, 365
- Brunetti, G. & Vazza, F. 2020, *Phys. Rev. Lett.*, 124, 051101
- Brunetti, G., Zimmer, S., & Zandanel, F. 2017, *MNRAS*, 472, 1506
- Bruno, L., Brunetti, G., Botteon, A., et al. 2023, *A&A*, 672, A41
- Buscher, D. F. 2016, *Opt. Express*, 24, 23566
- Bykov, A. M., Marcowith, A., Amato, E., et al. 2020, *SSR*, 216, 42
- Byrd, G. & Valtonen, M. 1990, *ApJ*, 350, 89
- Calistro Rivera, G., Williams, W. L., Hardcastle, M. J., et al. 2017, *MNRAS*, 469, 3468
- Cantiello, M., Blakeslee, J. P., Ferrarese, L., et al. 2018, *ApJ*, 856, 126
- Capetti, A., Kharb, P., Axon, D. J., Merritt, D., & Baldi, R. D. 2009, *AJ*, 138, 1990
- Cassano, R. 2010, *A&A*, 517, A10
- Cassano, R., Brunetti, G., Norris, R. P., et al. 2012, *A&A*, 548, A100
- Cassano, R., Brunetti, G., & Setti, G. 2006, *MNRAS*, 369, 1577
- Cassano, R., Etori, S., Brunetti, G., et al. 2013, *ApJ*, 777, 141
- Cassano, R., Etori, S., Giacintucci, S., et al. 2010, *ApJ Lett.*, 721, 82
- Catinella, B., Schiminovich, D., Cortese, L., et al. 2013, *MNRAS*, 436, 34
- Cavagnolo, K. W., Donahue, M., Voit, G. M., & Sun, M. 2009, *ApJ Suppl.*, 182, 12
- Chabrier, G. 2003, *PASP*, 115, 763
- Chandra, P., Ray, A., & Bhatnagar, S. 2004, *ApJ*, 612, 974
- Chang, J. & Cooper, G. 1970, *Journal of Computational Physics*, 6, 1
- Chen, H., Sun, M., Yagi, M., et al. 2020, *MNRAS*, 496, 4654

- Chomiuk, L. & Povich, M. S. 2011, *AJ*, 142, 197
- Chulliat, A., Macmillan, S., Alken, P., et al. 2015, *BGS and NOAA*,
- Chung, A., Van Gorkom, J. H., Kenney, J. D., Crowl, H., & Vollmer, B. 2009, *AJ*, 138, 1741
- Chung, A., van Gorkom, J. H., Kenney, J. D. P., & Vollmer, B. 2007, *ApJ*, 659, L115
- Churazov, E., Forman, W., Vikhlinin, A., et al. 2008, *MNRAS*, 388, 1062
- Chyzy, K. T. 2008, *A&A*, 482, 755
- Chyzy, K. T., Ehle, M., & Beck, R. 2007, *A&A*, Volume 474, Issue 2, November I 2007, pp.415-429, 474, 415
- Chyzy, K. T., Soida, M., Bomans, D. J., et al. 2006, *A&A*, 447, 465
- Cid Fernandes, R., Stasińska, G., Mateus, A., & Vale Asari, N. 2011, *MNRAS*, 413, 1687
- Ciesla, L., Boselli, A., Elbaz, D., et al. 2016, *A&A*, 585, A43
- Clarke, T. E. 2004, *Journal of Korean Astronomical Society*, 37, 337
- Clemens, M. S., Scaife, A., Vega, O., & Bressan, A. 2010, *MNRAS*, 405, 887
- Cohen, A. S. & Clarke, T. E. 2011, *AJ*, 141, 149
- Condon, J. J. 1992, *Ann. Rev. A&A*, 30, 575
- Condon, J. J., Cotton, W. D., & Broderick, J. J. 2002, *AJ*, 124, 675
- Condon, J. J., Cotton, W. D., Greisen, E. W., et al. 1998, *AJ*, 115, 1693
- Contini, M. 2004, *Monthly Notices of the Royal Astronomical Society*, 354, 675
- Cordey, R. A. 1985, *MNRAS*, 215, 437
- Cortese, L., Boissier, S., Boselli, A., et al. 2012, *A&A*, 544, A101
- Cortese, L., Boselli, A., Franzetti, P., et al. 2008, *MNRAS*, 386, 1157
- Cortese, L., Catinella, B., & Smith, R. 2021, *PASA*, 38, e035
- Cortese, L., Fritz, J., Bianchi, S., et al. 2014, *MNRAS*, 440, 942
- Cote, P., Blakeslee, J. P., Ferrarese, L., et al. 2004, *ApJ Suppl.*, 153, 223
- Cowie, L. L. & Songaila, A. 1977, *Nature*, 266, 501
- Cramer, W. J., Kenney, J. D. P., Cortes, J. R., et al. 2020, *ApJ*, 901, 95
- Croston, J. H., Hardcastle, M. J., Harris, D. E., et al. 2005, *ApJ*, 626, 733
- Crowl, H. H., Kenney, J. D. P., van Gorkom, J. H., & Vollmer, B. 2005, *AJ*, Volume 130, Issue 1, pp. 65-72., 130, 65

8 Bibliography

- Cuciti, V., Brunetti, G., Van Weeren, R., et al. 2018, *A&A*, 609, A61
- Cuciti, V., Cassano, R., Brunetti, G., et al. 2021, *A&A*, 647
- Cuciti, V., Cassano, R., Brunetti, G., et al. 2015, *A&A*, 580, A97
- Cuciti, V., de Gasperin, F., Brüggen, M., et al. 2022, *Nature*, 609, 911
- Damas-Segovia, A., Beck, R., Vollmer, B., et al. 2016, *ApJ*, 824, 30
- DAMPE Collaboration, Ambrosi, G., An, Q., et al. 2017, *Nature*, 552, 63
- Datta-Barua, S., Walter, T., Blanch, J., & Enge, P. 2008, *Radio Science*, 43, n/a
- Davies, J. I., Baes, M., Bendo, G. J., et al. 2010, *A&A*, 518, 48
- de Gasperin, F. 2017, *MNRAS*, 467, 2234
- de Gasperin, F., Brunetti, G., Brüggen, M., et al. 2020, *A&A*, 642, A85
- de Gasperin, F., Dijkema, T. J., Drabent, A., et al. 2019, *A&A*, 622
- de Gasperin, F., Edler, H. W., Williams, W. L., et al. 2023, *A&A*, 673, A165
- de Gasperin, F., Intema, H. T., Shimwell, T. W., et al. 2017, *Science Advances*, 3
- de Gasperin, F., Intema, H. T., Van Weeren, R. J., et al. 2015, *MNRAS*, 453, 3483
- de Gasperin, F., Mevius, M., Rafferty, D. A., Intema, H. T., & Fallows, R. A. 2018, *A&A*, 615, A179
- de Gasperin, F., Orrú, E., Murgia, M., et al. 2012, *A&A*, 547
- de Gasperin, F., Rudnick, L., Finoguenov, A., et al. 2022, *A&A*, 659, A146
- de Gasperin, F., Vink, J., McKean, J. P., et al. 2020, *A&A*, 635
- de Gasperin, F., Williams, W. L., Best, P., et al. 2021, *A&A*, 648, A104
- de Vaucouleurs, G. 1961, *ApJ Suppl.*, vol. 6, p.213, 6, 213
- Deb, T., Verheijen, M. A. W., Poggianti, B. M., et al. 2022, *MNRAS*, 516, 2683
- Decarli, R., Gavazzi, G., Arosio, I., et al. 2007, *MNRAS*, 381, 136
- Dennison, B. 1980, *ApJ Let.*, 239, L93
- Dewdney, P. E., Hall, P. J., Schilizzi, R. T., & Lazio, T. J. L. W. 2009, *IEEE Proceedings*, 97, 1482
- Dey, A., Schlegel, D. J., Lang, D., et al. 2019, *AJ*, 157, 168
- Di Gennaro, G., Van Weeren, R. J., Cassano, R., et al. 2021, *A&A*, 654, A166
- Di Gennaro, G., van Weeren, R. J., Hoeft, M., et al. 2018, *ApJ*, 865, 24
- Donnert, J., Vazza, F., Brüggen, M., & ZuHone, J. 2018, *SSR*, 214, 122
- Dörner, J., Reichherzer, P., Becker Tjus, J., & Heesen, V. 2023, *A&A*, 669, A111

- Drinkwater, M. J., Gregg, M. D., & Colless, M. 2001, *ApJ Let.*, 548, L139
- Drury, L. O. 1983, *Reports on Progress in Physics*, 46, 973
- Duc, P.-A. & Bournaud, F. 2008, *ApJ*, 673, 787
- Duchesne, S. W., Johnston-Hollitt, M., Offringa, A. R., et al. 2021, *PASA*, 38, 26
- Dunn, R. J. H., Allen, S. W., Taylor, G. B., et al. 2010, *MNRAS*, 404, 180
- Dursi, L. J. & Pfrommer, C. 2008, *ApJ*, 677, 993
- Dutch Research Council (NWO) . 2018, NWO Investment Grant Large 2017 - 2018, [Online; accessed 12. Oct. 2020]
- Edler, H. W., de Gasperin, F., Brunetti, G., et al. 2022, *A&A*, 666, A3
- Edler, H. W., de Gasperin, F., & Rafferty, D. 2021, *A&A*, 652, A37
- Edler, H. W., de Gasperin, F., Shimwell, T. W., et al. 2023a, *A&A*, 676, A24
- Edler, H. W., Roberts, I. D., Boselli, A., et al. 2023b, arXiv e-prints, arXiv:2311.01904
- Engelbracht, C. W., Blaylock, M., Su, K. Y. L., et al. 2007, *PASP*, 119, 994
- Enßlin, T., Pfrommer, C., Miniati, F., & Subramanian, K. 2011, *A&A*, 527, A99
- Ensslin, T. A., Biermann, P. L., Klein, U., & Kohle, S. 1998, *A&A*, 332, 395
- Enßlin, T. A. & Brügger, M. 2002, *MNRAS*, 331, 1011
- Enßlin, T. A. & Gopal-Krishna. 2001, *A&A*, 366, 26
- Fabian, A. C. 1994, *Ann. Rev. A&A*, 32, 277
- Fabian, A. C. 2012, *ARA&A*, 50, 455
- Fanaroff, B. L. & Riley, J. M. 1974, *MNRAS*, 167, 31P
- Farber, R. J., Ruszkowski, M., Tonnesen, S., & Holguin, F. 2022, *MNRAS*, 512, 5927
- Farris, M. H. & Russell, C. T. 1994, *JGR*, 99, 17681
- Ferland, G. J., Fabian, A. C., Hatch, N. A., et al. 2009, *MNRAS*, 392, 1475
- Fermi, E. 1949, *Physical Review*, 75, 1169
- Ferrarese, L., Côté, P., Cuillandre, J.-C., et al. 2012, *ApJS*, 200, 4
- Ferrarese, L., Mould, J. R., Kennicutt, Robert C., J., et al. 2000, *ApJ*, 529, 745
- Field, G. B., Goldsmith, D. W., & Habing, H. J. 1969, *ApJ Let.*, 155, L149
- Finoguenov, A. & Jones, C. 2001, *ApJ*, 547, L107
- Finoguenov, A., Ruszkowski, M., Jones, C., et al. 2008, *ApJ*, 686, 911

8 Bibliography

- Fixsen, D. J. 2009, *ApJ*, 707, 916
- Forman, W., Jones, C., Churazov, E., et al. 2007, *ApJ*, 665, 1057
- Fossati, M., Fumagalli, M., Boselli, A., et al. 2016, *MNRAS*, 455, 2028
- Fossati, M., Mendel, J. T., Boselli, A., et al. 2018, *A&A*, 614, A57
- French, D. M., Fox, A. J., Wakker, B. P., et al. 2021, *ApJ*, 923, 50
- Fumagalli, M. & Gavazzi, G. 2008, *A&A*, 490, 571
- Fumagalli, M., Krumholz, M. R., Prochaska, J. X., Gavazzi, G., & Boselli, A. 2009, *ApJ*, 697, 1811
- Gabel, J. R. & Bruhweiler, F. C. 2002, *AJ*, 124, 737
- Gallo, E., Treu, T., Marshall, P. J., et al. 2010, *ApJ*, 714, 25
- Garon, A. F., Rudnick, L., Wong, O. I., et al. 2019, *AJ*, 157, 126
- Gaspari, M., Brighenti, F., & Temi, P. 2012, *MNRAS*, 424, 190
- Gaspari, M., Ruszkowski, M., & Sharma, P. 2012, *ApJ*, 746, 94
- Gatuzz, E., Sanders, J. S., Dennerl, K., et al. 2018, *MNRAS*, 000
- Gavazzi, G. 1978, *A&A*, 69, 355
- Gavazzi, G. & Boselli, A. 1999, *A&A*, v.343, p.93-99 (1999), 343, 93
- Gavazzi, G., Boselli, A., & Kennicutt, R. 1991, *AJ*, v.101, p.1207, 101, 1207
- Gavazzi, G., Boselli, A., Mayer, L., et al. 2001, *ApJ Let.*, 563, L23
- Gavazzi, G., Boselli, A., Scodreggio, M., Pierini, D., & Belsole, E. 1998, *MNRAS*, Volume 304, Issue 3, pp. 595-610., 304, 595
- Gavazzi, G., Consolandi, G., Belladitta, S., Boselli, A., & Fossati, M. 2018, *A&A*, 615, A104
- Gavazzi, G., Contursi, A., Carrasco, L., et al. 1995, *A&A*, 304, 325
- Gavazzi, G. & Jaffe, W. 1985, *ApJ Let.*, 294, L89
- Gendre, M. A., Best, P. N., Wall, J. V., & Ker, L. M. 2013, *MNRAS*, 430, 3086
- Gendron-Marsolais, M., Kraft, R. P., Bogdan, A., et al. 2017, *ApJ*, 848, 26
- George, L. T., Dwarakanath, K. S., Johnston-Hollitt, M., et al. 2017, *MNRAS*, 467, 936
- Geyer, F., Schmidt, K., Kummer, J., et al. 2023, *A&A*, 677, A167
- Giacintucci, S., Markevitch, M., Cassano, R., et al. 2017, *ApJ*, 841, 71
- Giacintucci, S., Markevitch, M., Cassano, R., et al. 2019, *ApJ*, 880, 70
- Giannattasio, F., de Michelis, P., Consolini, G., et al. 2018, *Annals of Geophysics*, 61, 1

- Gil de Paz, A., Boissier, S., Madore, B. F., et al. 2007, *ApJ Suppl.*, 173, 185
- Giovannini, G., Bonafede, A., Feretti, L., et al. 2009, *A&A*, 507, 1257
- Giroletti, M. & Panessa, F. 2009, *ApJ*, 706, 260
- Gitti, M., Brunetti, G., Feretti, L., & Setti, G. 2004, *A&A*, 417, 1
- Goldreich, P. & Sridhar, S. 1997, *ApJ*, 485, 680
- Göller, J., Joshi, G. D., Rohr, E., Zinger, E., & Pillepich, A. 2023, *MNRAS*, 525, 3551
- Gómez-López, J. A., Amram, P., Epinat, B., et al. 2019, *A&A*, 631, A71
- Gonzalez, A. H., Sivanandam, S., Zabludoff, A. I., & Zaritsky, D. 2013, *ApJ*, 778, 14
- Govoni, F. & Feretti, L. 2004, *International Journal of Modern Physics D*, 13, 1549
- Gressel, O., Elstner, D., Ziegler, U., & Rüdiger, G. 2008, *A&A*, 486, L35
- Groeneveld, C., van Weeren, R. J., Miley, G. K., et al. 2022, *A&A*, 658, A9
- Grossi, M., Corbelli, E., Bizzocchi, L., et al. 2016, *A&A*, 590, A27
- Grossová, R., Werner, N., Massaro, F., et al. 2022, *ApJ Suppl.*, 258, 30
- Gunn, J. E. & Gott, J. Richard, I. 1972, *ApJ*, 176, 1
- Gürkan, G., Hardcastle, M. J., Smith, D. J. B., et al. 2018, *MNRAS*, 475, 3010
- Gursky, H., Kellogg, E., Murray, S., et al. 1971, *ApJ Let.*, 167, L81
- Guzmán, A. E., May, J., Alvarez, H., & Maeda, K. 2011, *A&A*, 525, A138
- Hales, S. E. G., Baldwin, J. E., & Warner, P. J. 1988, *MNRAS*, 234, 919
- Hamaker, J. P. 2011, *Mathematical-physical analysis of the generic dual-dipole antenna*, Tech. rep., ASTRON
- Hamaker, J. P., Bregman, J. D., & Sault, R. J. 1996, *A&A Suppl. Ser.*, 117, 137
- Hardcastle, M. J. 2013, *MNRAS*, 433, 3364
- Hardcastle, M. J. & Croston, J. H. 2020, *NARev*, 88, 101539
- Harwood, J. J., Hardcastle, M. J., & Croston, J. H. 2015, *MNRAS*, 454, 3403
- Harwood, J. J., Hardcastle, M. J., Croston, J. H., & Goodger, J. L. 2013, *MNRAS*, 435, 3353
- Harwood, J. J., Hardcastle, M. J., Morganti, R., et al. 2017, *MNRAS*, 469, 639
- Haynes, M. P., Giovanelli, R., & Chincarini, G. L. 1984, IN: *Annual review of astronomy and astrophysics*. Volume 22. Palo Alto, CA, Annual Reviews, Inc., 1984, p. 445-470., 22, 445
- Haynes, M. P., Giovanelli, R., & Kent, B. R. 2007, *ApJ*, 665, L19

8 Bibliography

- Heald, G. H., Pizzo, R. F., Orrú, E., et al. 2015, *A&A*, 582, 123
- Heckman, T. M. 1980, *A&A*, 87, 152
- Heesen, V., Buie, E., Huff, C. J., et al. 2019, *A&A*, 622, A8
- Heesen, V., de Gasperin, F., Schulz, S., et al. 2023a, *A&A*, 672, A21
- Heesen, V., Klocke, T. L., Brügggen, M., et al. 2023b, *A&A*, 669, A8
- Heesen, V., Krause, M., Beck, R., et al. 2018, *MNRAS*, 476, 158
- Heesen, V., Staffehl, M., Basu, A., et al. 2022, *A&A*, 664, A83
- Hess, V. F. 1913, *Phys. Zeit.*, 14, 612
- Hester, J. A., Seibert, M., Neill, J. D., et al. 2010, *ApJ Let.*, 716, L14
- Hindson, L., Kitchener, G., Brinks, E., et al. 2018, *ApJ Suppl.*, 234, 29
- Hoang, D. N., Shimwell, T. W., Osinga, E., et al. 2021, *MNRAS*, 501, 576
- Hoang, D. N., Shimwell, T. W., Van Weeren, R. J., et al. 2019a, *A&A*, 622, 20
- Hoang, D. N., Shimwell, T. W., Van Weeren, R. J., et al. 2019b, *A&A*, 622, 21
- Hofmann, W. & Hinton, J. A. 2020, *Cosmic Particle Accelerators* (Cham: Springer International Publishing), 827–863
- Hota, A., Saikia, D. J., & Irwin, J. A. 2007, *MNRAS*, 380, 1009
- Hubble, E. P. 1926, *ApJ*, 64, 321
- Hummel, E. & Saikia, D. J. 1991, *A&A*, 249, 43
- Hurley-Walker, N., Callingham, J. R., Hancock, P. J., et al. 2017, *MNRAS*, 464, 1146
- Ignesti, A., Brunetti, G., Shimwell, T., et al. 2022a, *A&A*, 659, A20
- Ignesti, A., Vulcani, B., Botteon, A., et al. 2023, *A&A*, 675, A118
- Ignesti, A., Vulcani, B., Poggianti, B. M., et al. 2022b, *ApJ*, 937, 58
- Ignesti, A., Vulcani, B., Poggianti, B. M., et al. 2022c, *ApJ*, 924, 64
- Intema, H. T., Jagannathan, P., Mooley, K. P., & Frail, D. A. 2017, *A&A*, 598, A78
- Jacobs, D. C., Aguirre, J. E., Parsons, A. R., et al. 2011, *ApJ Let.*, 734, L34
- Jaffe, W. J. & Perola, G. C. 1973, *A&A*, 26, 423
- Jones, R. C. 1941, *J. Opt. Soc. Am.*, 31, 488
- Kale, R. & Dwarakanath, K. S. 2011, *ApJ*, 744, 46
- Kang, H., Ryu, D., & Jones, T. W. 2012, *ApJ*, 756, 97

- Kantharia, N. G., Rao, A. P., & Sirothia, S. K. 2008, MNRAS, 383, 173
- Kardashev, N. S. 1962, SOVAST, 6, 317
- Kenney, J. D. P., Geha, M., Jáchym, P., et al. 2014, ApJ, 780, 119
- Kenney, J. D. P. & Koopmann, R. A. 1999, AJ, 117, 181
- Kenney, J. D. P., Tal, T., Crowl, H. H., Feldmeier, J., & Jacoby, G. H. 2008, ApJ Let., Volume 687, Issue 2, pp. L69 (2008)., 687, L69
- Kenney, J. D. P., van Gorkom, J. H., & Vollmer, B. 2004, AJ, 127, 3361
- Kennicutt, R. C., J. 1983, AJ, 88, 483
- Kennicutt, Robert C., J. 1998, ApJ, 498, 541
- Kennicutt, R. C. & Evans, N. J. 2012, Ann. Rev. A&A, 50, 531
- Kerszberg, D. 2017, in ICRC 2017
- Kharb, P., O’Dea, C. P., Tilak, A., et al. 2012, ApJ, 754, 1
- Kierdorf, M., Beck, R., Hoeft, M., et al. 2017, A&A, 600, A18
- Kim, S., Rey, S.-C., Jerjen, H., et al. 2014, ApJ Suppl., 215, 22
- Kolokythas, K., O’Sullivan, E., Giacintucci, S., et al. 2015, MNRAS, 450, 1732
- Köppen, J., Jáchym, P., Taylor, R., & Palouš, J. 2018, MNRAS, 479, 4367
- Kotera, K. & Olinto, A. V. 2011, Ann. Rev. A&A, 49, 119
- Kraft, R. P., Forman, W. R., Jones, C., et al. 2011, ApJ, 727, 41
- Kraft, R. P., Roediger, E., Machacek, M., et al. 2017, ApJ, 848, 27
- Kraichnan, R. H. & Nagarajan, S. 1967, Physics of Fluids, 10, 859
- Kronberg, P. P., Lesch, H., & Hopp, U. 1999, ApJ, 511, 56
- Kroupa, P. 2001, MNRAS, 322, 231
- Kulsrud, R. M. & Ostriker, E. C. 2006, Physics Today, 59, 58
- Kuo, P., Hwang, C., & Ip, W. 2003, ApJ, 594, 732
- Lacy, M., Baum, S. A., Chandler, C. J., et al. 2020, PASP, 132, 035001
- Laing, R. A., Bridle, A. H., Parma, P., et al. 2008, MNRAS, 386, 657
- Laing, R. A., Guidetti, D., Bridle, A. H., Parma, P., & Bondi, M. 2011, MNRAS, 417, 2789
- Lal, D. V., Lyskova, N., Zhang, C., et al. 2022, ApJ, 934, 170
- Lane, W. M., Cotton, W. D., van Velzen, S., et al. 2014, MNRAS, 440, 327

8 Bibliography

- Large, M. I., Mathewson, D. S., & Haslam, C. G. T. 1959, *Nature*, 183, 1663
- Larson, R. B., Tinsley, B. M., & Caldwell, C. N. 1980, *ApJ*, 237, 692
- Lazarian, A. & Yan, H. 2014, *ApJ*, 784, 38
- Lequeux, J., Maucherat-Joubert, M., Deharveng, J. M., & Kunth, D. 1981, *A&A*, 103, 305
- Leroy, A. K., Bigiel, F., de Blok, W. J. G., et al. 2012, *AJ*, 144, 3
- Leroy, A. K., Sandstrom, K. M., Lang, D., et al. 2019, *ApJ Suppl.*, 244, 24
- Li, J.-T., Beck, R., Dettmar, R.-J., et al. 2016, *MNRAS*, 456, 1723
- Lipiński, M., Włostowski, T., Serrano, J., & Alvarez, P. 2011, in 2011 IEEE International Symposium on Precision Clock Synchronization for Measurement, Control and Communication, 25–30
- Lobanov, A. P. 1998, *A&A*, 330, 79
- Loi, F., Murgia, M., Govoni, F., et al. 2017, *MNRAS*, 472, 3605
- Longair, M. S. 2011, *High Energy Astrophysics*, 3rd edn. (Cambridge University Press)
- Lynden-Bell, D. 1969, *Nature*, 223, 690
- Macario, G., Markevitch, M., Giacintucci, S., et al. 2011, *ApJ*, 728, 82
- Macario, G., Venturi, T., Intema, H. T., et al. 2013, *A&A*, 551, 141
- Machacek, M., Nulsen, P. E. J., Jones, C., & Forman, W. R. 2006, *ApJ*, 648, 947
- Madau, P. & Dickinson, M. 2014, *Ann. Rev. A&A*, 52, 415
- Magliocchetti, M. 2022, *A&A Rev.*, 30, 6
- Mahony, E. K., Morganti, R., Prandoni, I., et al. 2016, *MNRAS*, 463, 2997
- Martin, D. C., Fanson, J., Schiminovich, D., et al. 2005, *ApJ Let.*, 619, L1
- Martin, P. L., Bray, J. D., & Scaife, A. M. 2016, *MNRAS*, 459, 3525
- Materassi, M., Forte, B., Coster, A., & Skone, S. 2019, *The Dynamical Ionosphere - A Systems Approach to Ionospheric Irregularity* (1st ed.) (Netherlands: Elsevier), 301–310
- Matsushita, K., Belsole, E., Finoguenov, A., & Böhringer, H. 2002, *A&A*, 386, 77
- McConnell, D., Hale, C. L., Lenc, E., et al. 2020, *PASA*, 37, e048
- Meekins, J. F., Fritz, G., Chubb, T. A., & Friedman, H. 1971, *Nature*, 231, 107
- Mei, S., Blakeslee, J., Cote, P., et al. 2007, *ApJ*, 655, 144
- Merloni, A., Predehl, P., Becker, W., et al. 2012, arXiv e-prints, arXiv:1209.3114
- Merritt, D. 1984, *ApJ*, 276, 26

- Messier, C. 1781, Catalogue des Nébuleuses et des Amas d'Étoiles (Catalog of Nebulae and Star Clusters), *Connaissance des Temps ou des Mouvements Célestes*, for 1784, p. 227-267
- Mevius, M. 2018, in *Low Frequency Radio Astronomy and the LOFAR Observatory*, ed. J. M. George Heald & R. Pizzo (Springer), 103–117
- Mevius, M. 2018, RMextract: Ionospheric Faraday Rotation calculator
- Mevius, M., van der Tol, S., Pandey, V. N., et al. 2016, *Radio Science*, 51, 927
- Miley, G. K., Perola, G. C., van der Kruit, P. C., & van der Laan, H. 1972, *Nature*, 237, 269
- Miller, N. A. & Owen, F. N. 2001, *AJ*, Volume 121, Issue 4, pp. 1903-1914., 121, 1903
- Million, E. T., Werner, N., Simionesc, A., et al. 2010, *MNRAS*, 407, 2046
- Mingo, B., Croston, J. H., Hardcastle, M. J., et al. 2019, *MNRAS*, 488, 2701
- Miniati, F. 2015, *ApJ*, 800
- Mohan, N. & Rafferty, D. 2015, PyBDSF: Python Blob Detection and Source Finder
- Molnár, D. C., Serra, P., van der Hulst, T., et al. 2022, *A&A*, 659, A94
- Moore, B., Katz, N., Lake, G., Dressler, A., & Oemler, A. 1996, *Nature*, 379, 613
- Müller, A., Pfrommer, C., Ignesti, A., et al. 2021, *MNRAS*, 000, 1
- Müller, A., Poggianti, B. M., Pfrommer, C., et al. 2021, *Nature Astronomy*, 5, 159
- Murgia, M., Govoni, F., Markevitch, M., et al. 2009, *A&A*, 499, 679
- Murphy, E. J., Bremseth, J., Mason, B. S., et al. 2012, *ApJ*, 761, 97
- Murphy, E. J., Condon, J. J., Schinnerer, E., et al. 2011, *ApJ*, 737, 67
- Murphy, E. J., Kenney, J. D., Helou, G., Chung, A., & Howell, J. H. 2009, *ApJ*, 694, 1435
- Nemmen, R. S., Georganopoulos, M., Guiriec, S., et al. 2012, *Science*, 338, 1445
- Niklas, S., Klein, U., & Wielebinski, R. 1997, *A&A*, 322, 19
- O'Dea, C. P. 1998, *PASP*, 110, 493
- Offringa, A. R., McKinley, B., Hurley-Walker, N., et al. 2014, *MNRAS*, 444, 606
- Offringa, A. R. & Smirnov, O. 2016, *MNRAS*, 000, 1
- Offringa, A. R., Van De Gronde, J. J., & Roerdink, J. B. 2012, *A&A Suppl. Ser.*, 539, A95
- Ogrean, G. A., Brügger, M., van Weeren, R., et al. 2014, *MNRAS*, 440, 3416
- Oosterloo, T. & van Gorkom, J. 2005, *A&A*, Volume 437, Issue 1, July I 2005, pp.L19-L22, 437, L19
- Osinga, E., Van Weeren, R. J., Boxelaar, J. M., et al. 2021, *A&A*, 648, A11

8 Bibliography

- O'Sullivan, E., Worrall, D. M., Birkinshaw, M., et al. 2011, *A&A Suppl. Ser.*, 100, 47
- Owen, E. R., Wu, K., Inoue, Y., Yang, H. Y. K., & Mitchell, A. M. W. 2023, *Galaxies*, 11, 86
- Owen, F. N., Eilek, J. A., & Kassim, N. E. 2000, *ApJ*, 543, 611
- Owen, F. N., Hardee, P. E., & Cornwell, T. J. 1989, *ApJ*, 340, 698
- Owen, F. N. & Rudnick, L. 1976, *ApJ Let.*, 205, L1
- Pacholczyk, A. G. 1970, *Radio astrophysics. Nonthermal processes in galactic and extragalactic sources* (W.H.Freeman & Co Ltd)
- Paggi, A., Fabbiano, G., Kim, D. W., et al. 2014, *ApJ*, Volume 787, Issue 2, article id. 134, 12 pp. (2014)., 787, 134
- Pasini, T., Edler, H. W., Brüggén, M., et al. 2022, *A&A*, 663, A105
- Perley, R. A. & Butler, B. J. 2017, *ApJ Suppl.*, 230, 7
- Peterson, J. R. & Fabian, A. C. 2006, *Phys. Rep.*, 427, 1
- Petrosian, V. 2001, *ApJ*, 557, 560
- Pfrommer, C. & Dursi, L. J. 2010, *Nature Physics*, 6, 520
- Pfrommer, C. & Enßlin, T. A. 2004, *MNRAS*, 352, 76
- Pinjarkar, S., Hardcastle, M. J., Harwood, J. J., et al. 2023, *MNRAS*, 523, 620
- Pinzke, A., Oh, S. P., & Pfrommer, C. 2017, *MNRAS*, 465, 4800
- Poggianti, B. M., Fasano, G., Bettoni, D., et al. 2009, *ApJ Let.*, 697, L137
- Poggianti, B. M., Moretti, A., Gullieuszik, M., et al. 2017, *ApJ*, 844, 48
- Predehl, P., Andritschke, R., Arefiev, V., et al. 2021, *A&A*, 647, A1
- Predehl, P., Sunyaev, R. A., Becker, W., et al. 2020, *Nature* 2020 588:7837, 588, 227
- Quilis, V., Planelles, S., & Ricciardelli, E. 2017, *MNRAS*, 469, 80
- Rajpurohit, K., Hoeft, M., van Weeren, R. J., et al. 2018, *ApJ*, 852, 65
- Rajpurohit, K., Hoeft, M., Vazza, F., et al. 2020, *A&A*, 636, A30
- Rebusco, P., Churazov, E., Böhringer, H., & Forman, W. 2005, *MNRAS*, 359, 1041
- Rebusco, P., Churazov, E., Böhringer, H., & Forman, W. 2006, *MNRAS*, 372, 1840
- Rengelink, R. B., Tang, Y., de Bruyn, A. G., et al. 1997, *A&A Suppl. Ser.*, 124, 259
- Roberts, I. D., Lang, M., Trotsenko, D., et al. 2022a, *ApJ*, 941, 77
- Roberts, I. D. & Parker, L. C. 2020, *MNRAS*, 495, 554

- Roberts, I. D., van Weeren, R. J., Lal, D. V., et al. 2023, arXiv e-prints, arXiv:2310.20417
- Roberts, I. D., Van Weeren, R. J., Mcgee, S. L., et al. 2021a, A&A, 650
- Roberts, I. D., van Weeren, R. J., McGee, S. L., et al. 2021b, A&A, 652, A153
- Roberts, I. D., van Weeren, R. J., Timmerman, R., et al. 2022b, A&A, 658, A44
- Roediger, E. & Brüggen, M. 2006, MNRAS, 369, 567
- Roediger, E. & Brüggen, M. 2007, MNRAS, 380, 1399
- Roediger, E., Kraft, R., Nulsen, P., et al. 2014, The Astrophysical Journal, 806
- Roediger, E., Kraft, R. P., Nulsen, P. E. J., et al. 2015a, ApJ, 806, 103
- Roediger, E., Kraft, R. P., Nulsen, P. E. J., et al. 2015b, ApJ, 806, 104
- Roger, R. S., Costain, C. H., & Bridle, A. H. 1973, AJ, Vol. 78, p. 1030 (1973), 78, 1030
- Rudnick, L. & Owen, F. N. 1976, ApJ Let., 203, L107
- Ruszkowski, M., Brüggen, M., Lee, D., & Shin, M. S. 2014, ApJ, 784, 75
- Ruszkowski, M. & Pfrommer, C. 2023, arXiv e-prints, arXiv:2306.03141
- S. Niklas, U. Klein, R. W. 1995, A&A, 293, 56
- Saikia, D. J. 2022, Journal of Astrophysics and Astronomy, 43, 97
- Salpeter, E. E. 1955, ApJ, 121, 161
- Salter, C. J. 1983, BASI V.11:1, P. 1, 1983, 11, 1
- Sanders, J. S., Dennerl, K., Russell, H. R., et al. 2020, A&A, 633, A42
- Sarazin, C. L. 1986, Rev. Mod. Phys., 58, 1
- Sarazin, C. L. 1999, ApJ, 520, 529
- Sarazin, C. L. 2008, Gas Dynamics in Clusters of Galaxies (Dordrecht: Springer Netherlands), 1–30
- Sardaneta, M. M., Amram, P., Boselli, A., et al. 2022, A&A, 659, A45
- Savini, F., Bonafede, A., Brüggen, M., et al. 2019, A&A, 622
- Savini, F., Bonafede, A., Brüggen, M., et al. 2018, MNRAS, 478, 2234
- Scaife, A. M. M. & Heald, G. H. 2012, MNRAS, 423, 30
- Schindler, S., Binggeli, B., & Böhringer, H. 1999, Astron. Astrophys, 343, 420
- Schleicher, D. R. G. & Beck, R. 2013, A&A, 556, A142
- Schlickeiser, R., Sievers, A., Thiemann, H., et al. 1987, A&A, 182, 21
- Schmidt, M. 1963, Nature, 197, 1040

8 Bibliography

- Schoenmaker, A. P. & Renting, G. A. 2011, MS2 description for LOFAR
- Serra, P., de Blok, W. J. G., Bryan, G. L., et al. 2016, in *MeerKAT Science: On the Pathway to the SKA*, 8
- Serra, P., Maccagni, F. M., Kleiner, D., et al. 2023, *A&A*, 673, A146
- Shibata, R., Matsushita, K., Yamasaki, N. Y., et al. 2001, *ApJ*, 549, 228
- Shimwell, T. W., Hardcastle, M. J., Tasse, C., et al. 2022, *A&A*, 659, A1
- Shimwell, T. W., Röttgering, H. J. A., Best, P. N., et al. 2017, *A&A*, 598, 104
- Shimwell, T. W., Tasse, C., Hardcastle, M. J., et al. 2019, *The LOFAR Two-metre Sky Survey: II. First data release*
- Shurkin, K., Dunn, R. J. H., Gentile, G., Taylor, G. B., & Allen, S. W. 2007, *MNRAS*, 383, 923
- Simionescu, A., Allen, S. W., Mantz, A., et al. 2011, *Science*, 331, 1576
- Simionescu, A., Werner, N., Mantz, A., Allen, S. W., & Urban, O. 2017, *MNRAS*, 469, 1476
- Smartt, S. J., Eldridge, J. J., Crockett, R. M., & Maund, J. R. 2009, *MNRAS*, 395, 1409
- Smirnov, O. M. 2011, *A&A*, 527
- Smirnov, O. M. 2011, *A&A*, 527, A106
- Sofue, Y. 2000, *ApJ*, 540, 224
- Soria, R., Kolehmainen, M., Graham, A. W., et al. 2022, *MNRAS*, 512, 3284
- Srivastava, S. & Singal, A. K. 2020, *MNRAS*, 493, 3811
- Stein, Y., Bomans, D. J., Kamphuis, P., et al. 2018, *A&A*, 620, A29
- Stevens, I. R., Acreman, D. M., & Ponman, T. J. 1999, *MNRAS*, 310, 663
- Steyrleithner, P., Hensler, G., & Boselli, A. 2020, *MNRAS*, 494, 1114
- Stroe, A., Harwood, J. J., Hardcastle, M. J., & Röttgering, H. J. 2014, *MNRAS*, 445, 1213
- Su, Y., Kraft, R. P., Nulsen, P. E. J., et al. 2019, *AJ*, 158, 6
- Subramanian, K. 2016, *Reports on Progress in Physics*, 79, 076901
- Sun, M., Ge, C., Luo, R., et al. 2021, *Nature Astronomy*, 6, 270
- Sunyaev, R. A. & Zeldovich, Y. B. 1972, *Comments on Astrophysics and Space Physics*, 4, 173
- Tabatabaei, F. S., Schinnerer, E., Krause, M., et al. 2017, *ApJ*, 836, 185
- Tasse, C. 2014a, *arXiv e-prints*, arXiv:1410.8706
- Tasse, C. 2014b, *A&A*, 566, A127

- Tasse, C., Hugo, B., Mirmont, M., et al. 2018, *A&A*, 611, 87
- Tasse, C., Shimwell, T., Hardcastle, M. J., et al. 2021, *A&A*, 648, A1
- Tatarski, V. I. 1961, Translated by R. A. Silverman. McGraw-Hill, New York
- Tatarski, V. I. 1971, Nauka Press, Moscow (in Russian; English translation: National Technical Information Service, Springfield, Va., 1971)
- Taylor, G. B., Carilli, C. L., Perley, R. A., & (U.S.), N. R. A. O. 1999, *Synthesis imaging in radio astronomy II* (Astronomical Society of the Pacific), 170–180
- Taylor, G. B., Ellingson, S. W., Kassim, N. E., et al. 2012, *Journal of Astronomical Instrumentation*, 1, 1250004
- Thompson, A. R., Moran, J. M., & Swenson, G. W. 2017, *Interferometry and Synthesis in Radio Astronomy*, 3rd edn. (Springer Open)
- Tingay, S. J., Goeke, R., Bowman, J. D., et al. 2013, *PASA*, 30, e007
- Tonnesen, S. & Stone, J. 2014, *ApJ*, 795, 148
- Tribble, P. C. 1993, *MNRAS*, 261, 57
- Urban, O., Werner, N., Simionescu, A., Allen, S. W., & Böhringer, H. 2011, *MNRAS*, 414, 2101
- Urbanik, M., Klein, U., & Graeve, R. 1986, *A&A*, Vol. 166, p. 107-114 (1986), 166, 107
- Vacca, V., Feretti, L., Giovannini, G., et al. 2014, *A&A*, 561, A52
- van Cappellen, W. 2019, LOFAR 2.0 Stage 1 development, Talk at LOFAR science workshop 2019
- van der Kruit, P. C., Kruit, v. d., & C., P. 1971, *A&A*, 15, 110
- van der Kruit, P. C., Kruit, v. d., & C., P. 1973, *A&A*, 29, 263
- van der Tol, S., Veenboer, B., & Offringa, A. R. 2019, *A&A*, 616, 27
- van Diepen, G., Dijkema, T. J., & Offringa, A. 2018, *DPPP: Default Pre-Processing Pipeline*
- van Haarlem, M. P., Wise, M. W., Gunst, A. W., et al. 2013, *A&A*, 556, A2
- van Weeren, R. J., Andrade-Santos, F., Dawson, W. A., et al. 2017, *Nature Astron.*, 1, 0005
- van Weeren, R. J., de Gasperin, F., Akamatsu, H., et al. 2019, *Space Sci. Rev.*, 215, 16
- van Weeren, R. J., Röttgering, H. J., Rafferty, D. A., et al. 2012, *A&A*, 543, 43
- van Weeren, R. J., Röttgering, H. J. A., Brüggén, M., & Hoeft, M. 2010, *Science*, 330, 347
- van Weeren, R. J., Shimwell, T. W., Botteon, A., et al. 2021, *A&A Suppl. Ser.*, 651, A115
- van Weeren, R. J., Williams, W. L., Hardcastle, M. J., et al. 2016, *ApJ Suppl.*, 223, 2
- Vazza, F., Angelinelli, M., Jones, T. W., et al. 2018, *MNRAS*, 481, L120

8 Bibliography

- Vazza, F., Brüggén, M., Gheller, C., & Wang, P. 2014, *MNRAS*, 445, 3706
- Vazza, F., Wittor, D., Brüggén, M., & Brunetti, G. 2023, *Galaxies*, 11, 45
- Voelk, H. J. 1989, *A&A*, 218, 67
- Voit, G. M. 2005, *Reviews of Modern Physics*, 77, 207
- Völk, H. J. & Atoyan, A. M. 2000, *ApJ*, 541, 88
- Völk, H. J. & Xu, C. 1994, *Infrared Physics and Technology*, 35, 527
- Vollmer, B. 2003, *A&A*, 398, 525
- Vollmer, B., Beck, R., Kenney, J. D. P., & van Gorkom, J. H. 2004, *AJ*, 127, 3375
- Vollmer, B., Braine, J., Combes, F., & Sofue, Y. 2005, *A&A*, 441, 473
- Vollmer, B., Cayatte, V., Balkowski, C., & Duschl, W. J. 2001, *ApJ*, 561, 708
- Vollmer, B., Cayatte, V., Boselli, A., Balkowski, C., & Duschl, W. J. 1999, *A&A*, 349, 411
- Vollmer, B., Fossati, M., Boselli, A., et al. 2021, *A&A*, 645, A121
- Vollmer, B., Huchtmeier, W., & Van Driel, W. 2005, *A&A*, 439, 921
- Vollmer, B., Soida, M., Beck, R., et al. 2013, *A&A*, 553, A116
- Vollmer, B., Soida, M., Beck, R., et al. 2007, *A&A Suppl. Ser.*, 464, L37
- Vollmer, B., Soida, M., Braine, J., et al. 2012, *A&A*, 537, A143
- Vollmer, B., Soida, M., Chung, A., et al. 2010, *A&A*, Volume 512, id.A36, 15 pp., 512, A36
- Vollmer, B., Soida, M., Chung, A., et al. 2009, *A&A*, 496, 669
- Vollmer, B., Soida, M., Chung, A., et al. 2008, *A&A*, 483, 89
- Vollmer, B., Wong, O. I., Braine, J., Chung, A., & Kenney, J. D. P. 2012, *A&A*, 543, A33
- von Karman, T. 1948, *Proceedings of the National Academy of Sciences*, 34, 530
- Vulcani, B., Poggianti, B. M., Gullieuszik, M., et al. 2018, *The Astrophysical Journal Letters*, 866, L25
- Wang, J., Staveley-Smith, L., Westmeier, T., et al. 2021, *ApJ*, 915, 70
- Watts, A. B., Cortese, L., Catinella, B., et al. 2023, *PASA*, 40, e017
- Weżgowiec, M., Urbanik, M., Beck, R., Chyży, K. T., & Soida, M. 2012, *A&A*, 545, A69
- Weżgowiec, M., Urbanik, M., Vollmer, B., et al. 2007, *A&A*, 471, 93
- Wilber, A., Brüggén, M., Bonafede, A., et al. 2018, *MNRAS*, 473, 3536
- Williams, W. L., Van Weeren, R. J., Röttgering, H. J., et al. 2016, *MNRAS*, 460, 2385

- Willson, M. A. G. 1970, MNRAS, 151, 1
- Wilson, R. W., Jefferts, K. B., & Penzias, A. A. 1970, ApJ Let., 161, L43
- Wing, J. D. & Blanton, E. L. 2011, AJ, 141, 88
- Yagi, M., Yoshida, M., Komiyama, Y., et al. 2010, AJ, 140, 1814
- Yoshida, M., Yagi, M., Okamura, S., et al. 2002, ApJ, 567, 118
- Young, L. M., Rosolowsky, E., van Gorkom, J. H., & Lamb, S. A. 2006, ApJ, 650, 166
- Yun, K., Pillepich, A., Zinger, E., et al. 2019, MNRAS, 483, 1042
- Zhu, J., Tonnesen, S., & Bryan, G. L. 2023, arXiv e-prints, arXiv:2309.07037
- Zibetti, S., Charlot, S., & Rix, H.-W. 2009, MNRAS, 400, 1181
- ZuHone, J. & Su, Y. 2022, *The Merger Dynamics of the X-Ray-Emitting Plasma in Clusters of Galaxies* (Singapore: Springer Nature Singapore), 1–44

8 *Bibliography*

A Images of Virgo cluster galaxies

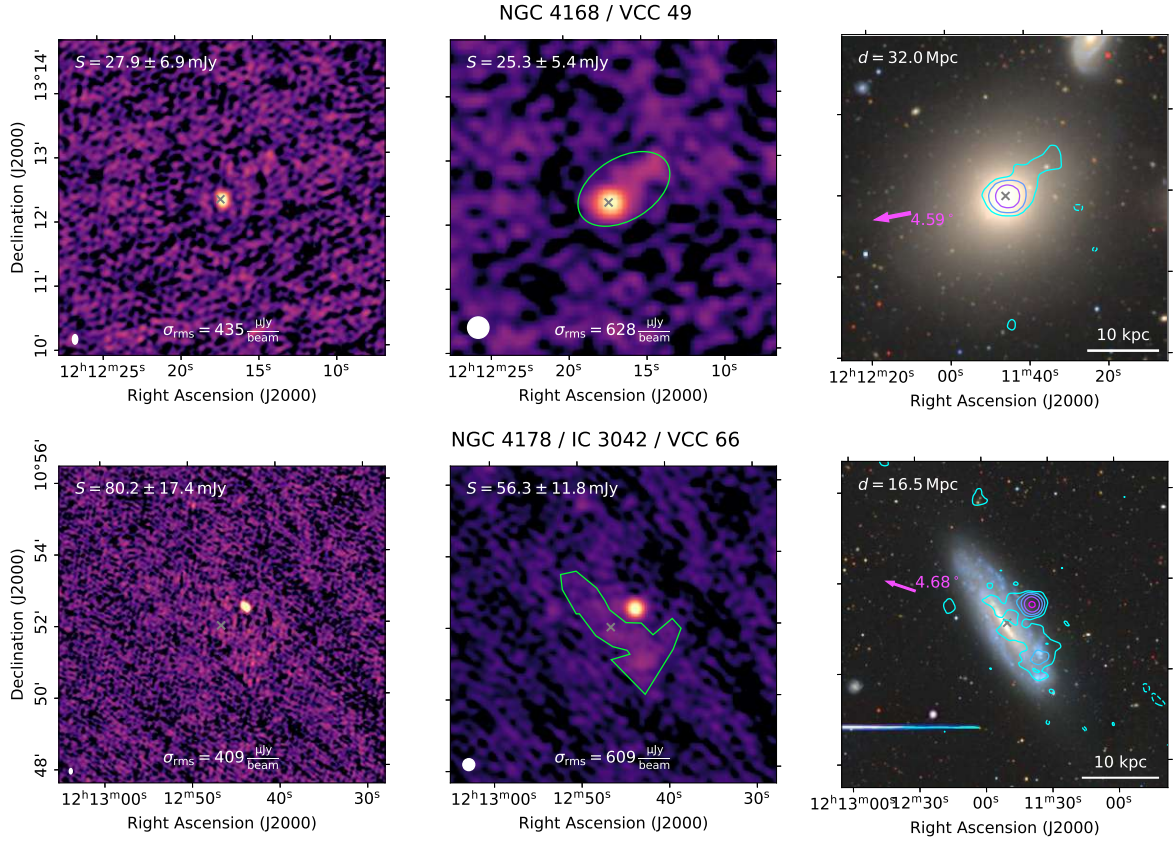


Figure A.1: LOFAR images of the galaxy VCC 144 at resolutions of $9'' \times 5''$ (left panel) and $20''$ (center panel), and the corresponding optical image of the DESI Legacy Imaging Survey DR9 (Dey et al. 2019) with the $20''$ LOFAR contours starting from 3σ and increasing in powers of two (right panel). The region outlined in green in the central panel marks the area used for the flux density measurement at high- and low-resolution. The measured flux density is displayed in the top left corner and the background RMS σ_{rms} of the maps at the bottom. In the right panel, the pink arrow marks the direction of and distance to the cluster center (M87), and the redshift-independent distance d is reported in the top left.

A Images of Virgo cluster galaxies

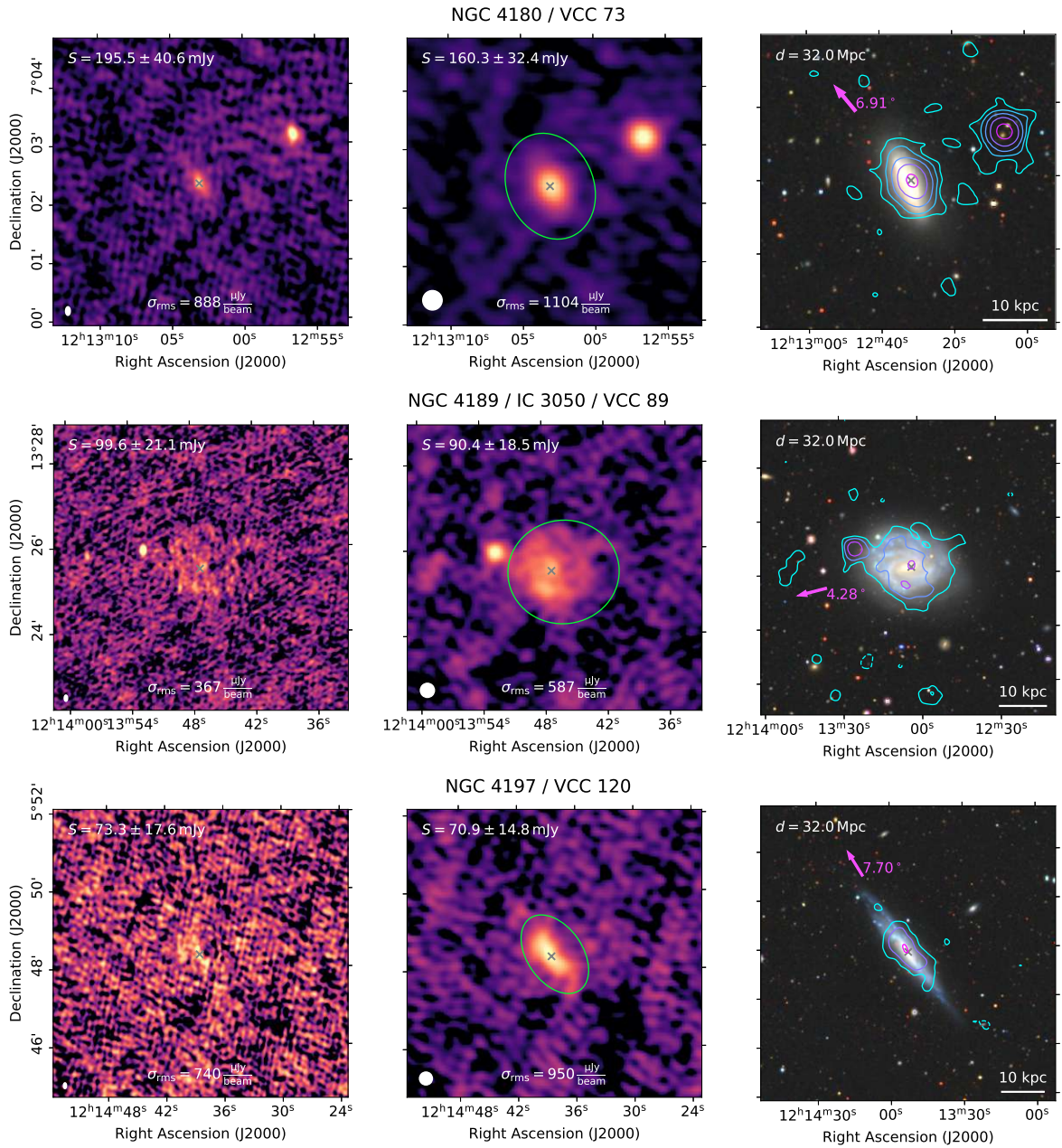


Figure A.1: Continued.

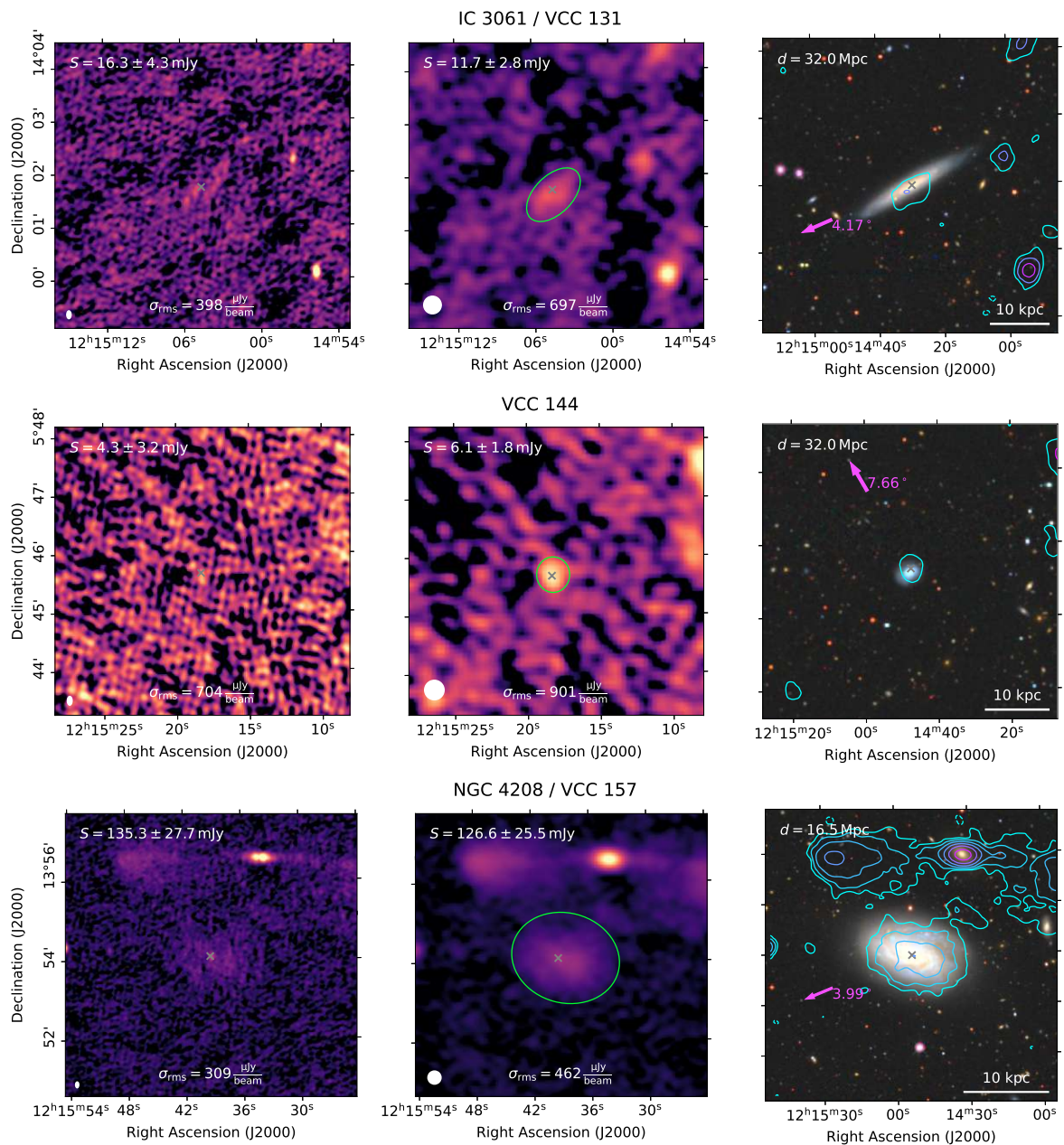


Figure A.1: Continued.

A Images of Virgo cluster galaxies

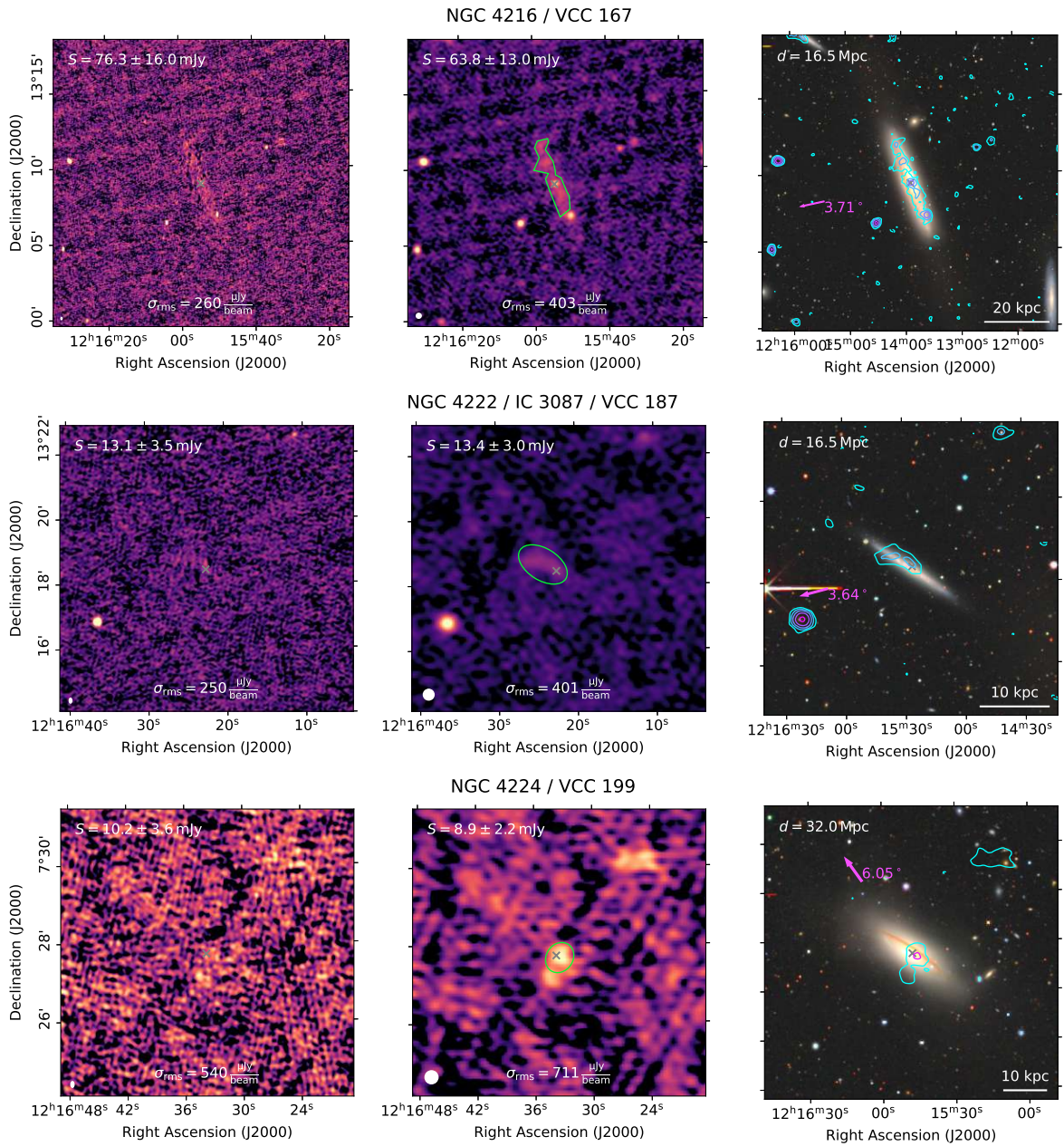


Figure A.1: Continued.

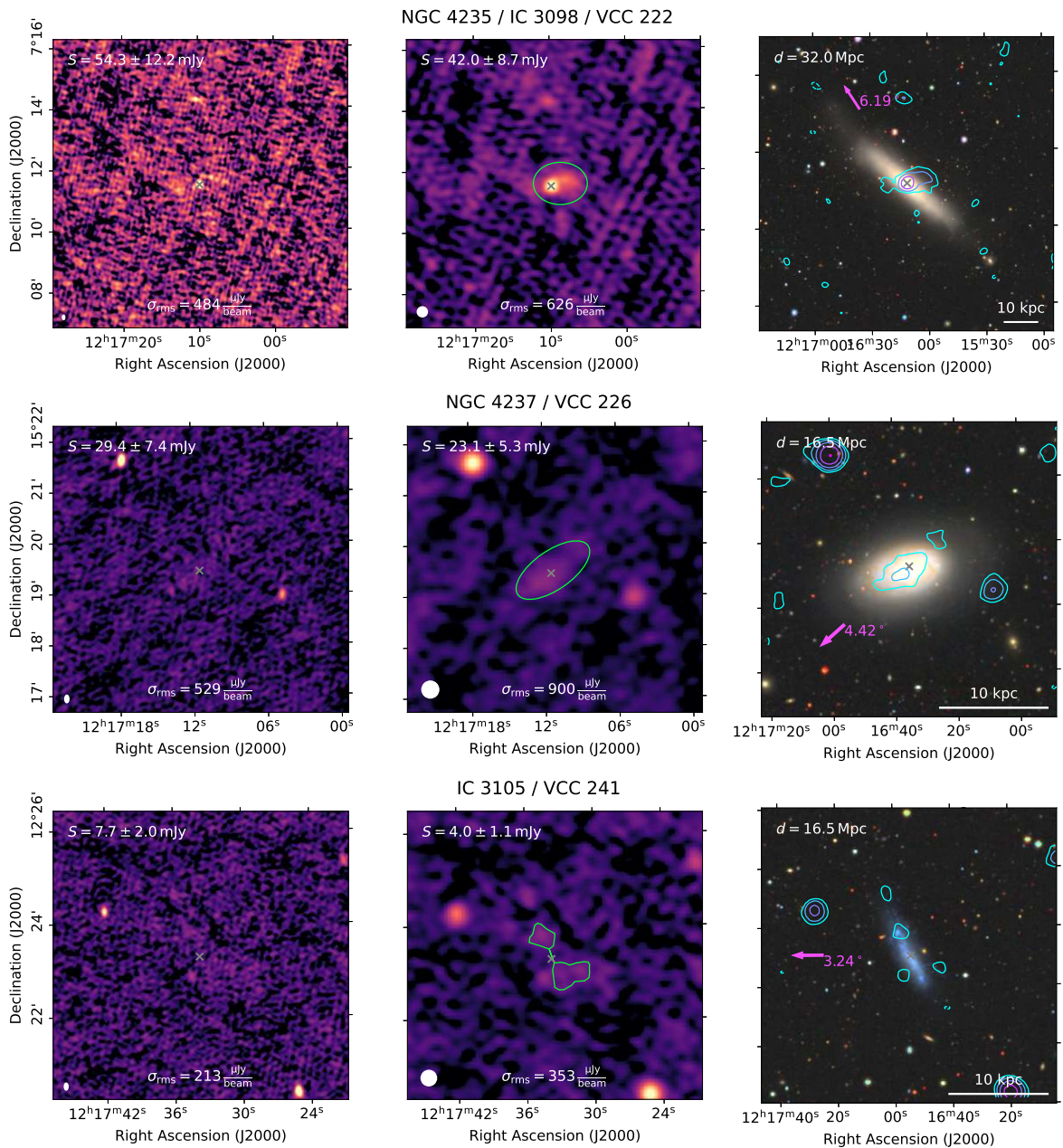


Figure A.1: Continued.

A Images of Virgo cluster galaxies

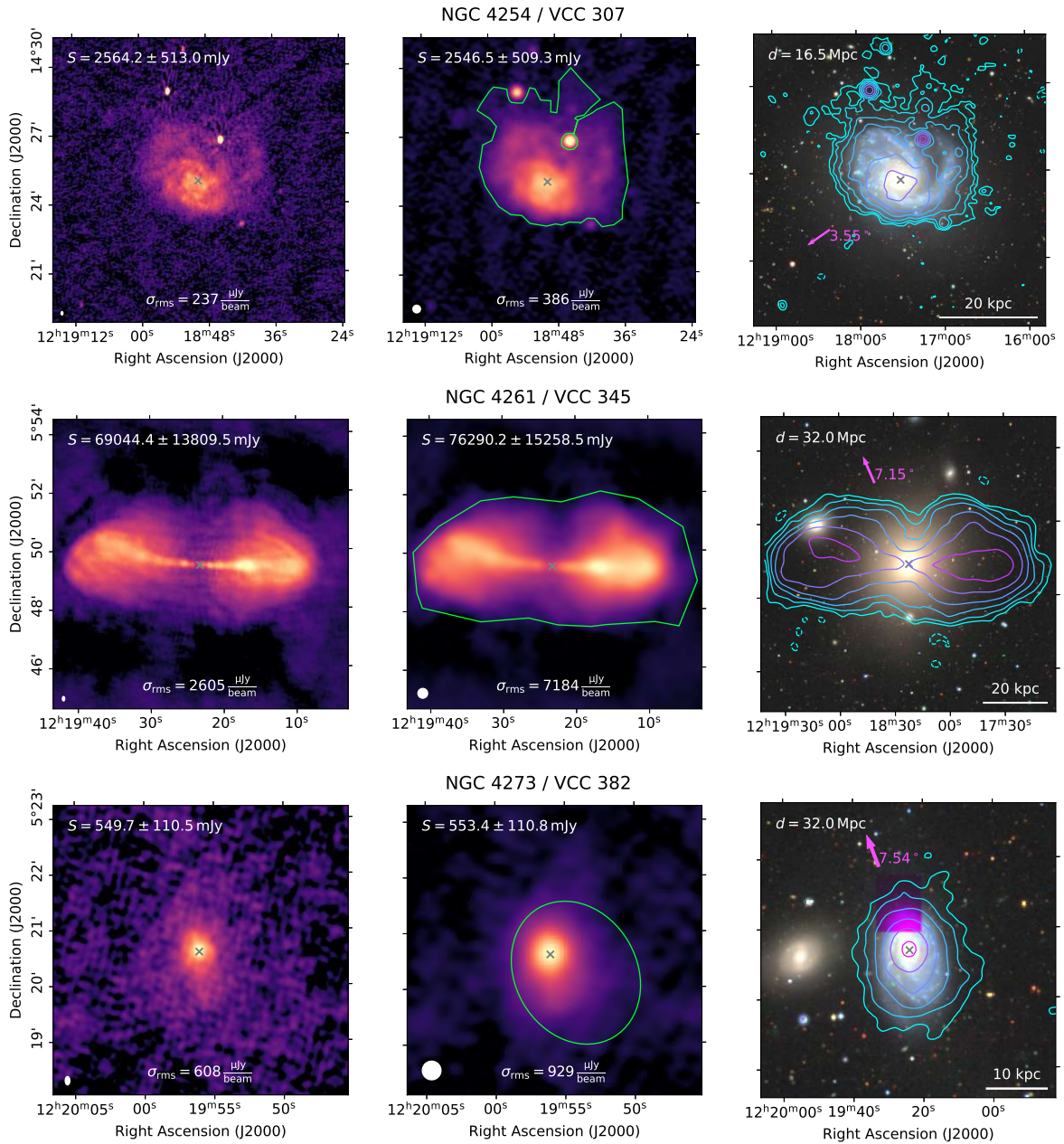


Figure A.1: Continued.

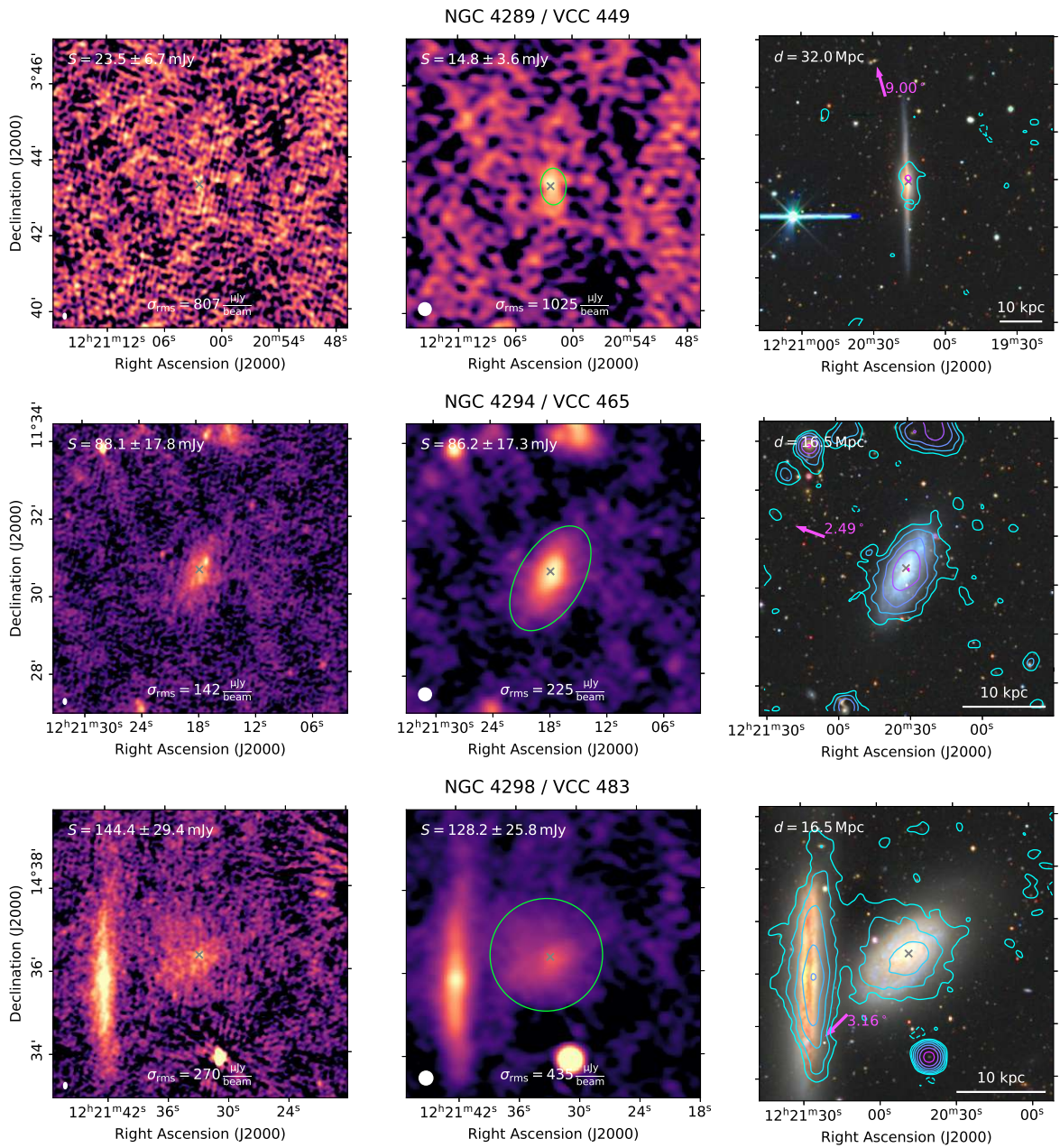


Figure A.1: Continued.

A Images of Virgo cluster galaxies

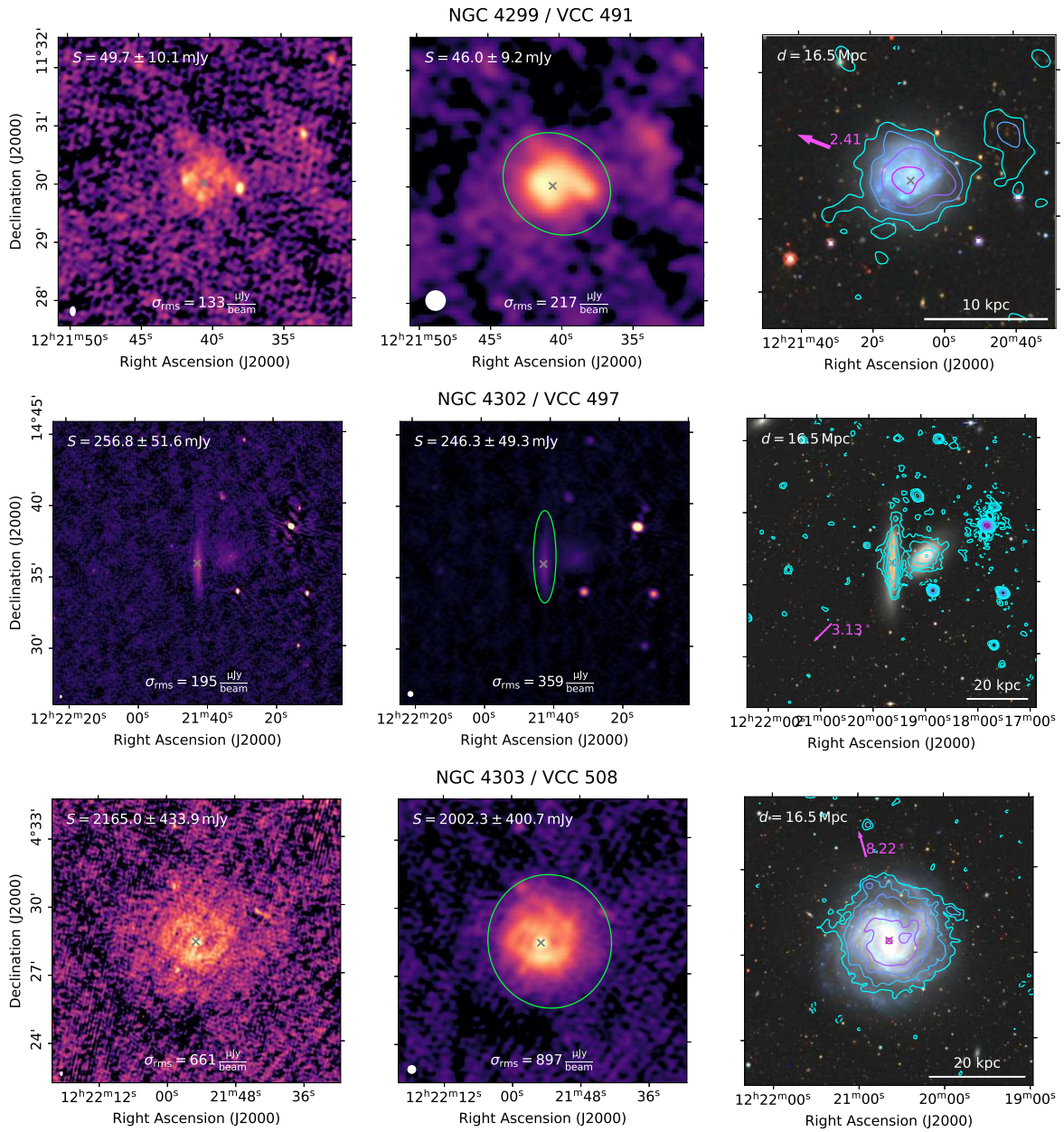


Figure A.1: Continued.

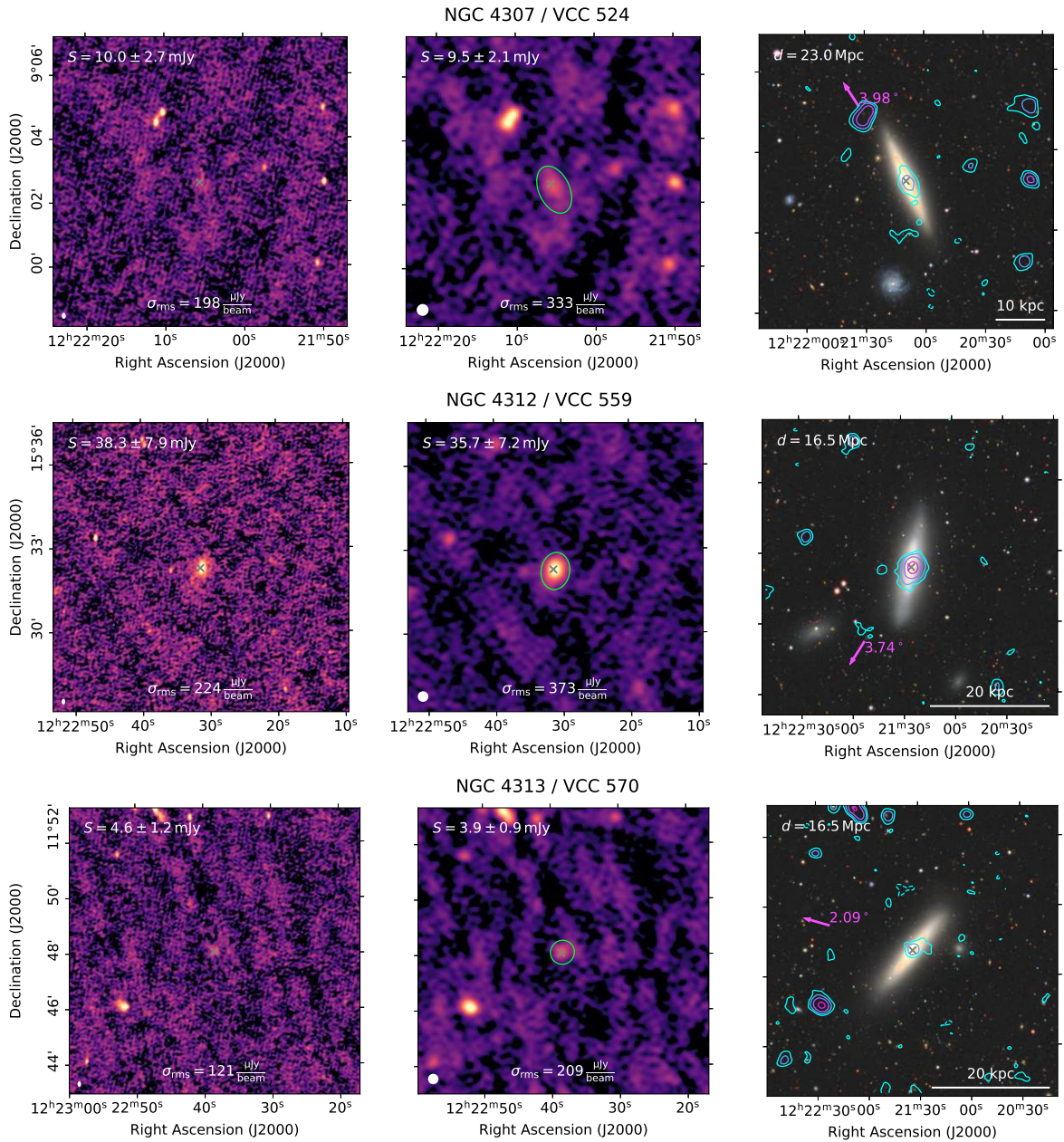


Figure A.1: Continued.

A Images of Virgo cluster galaxies

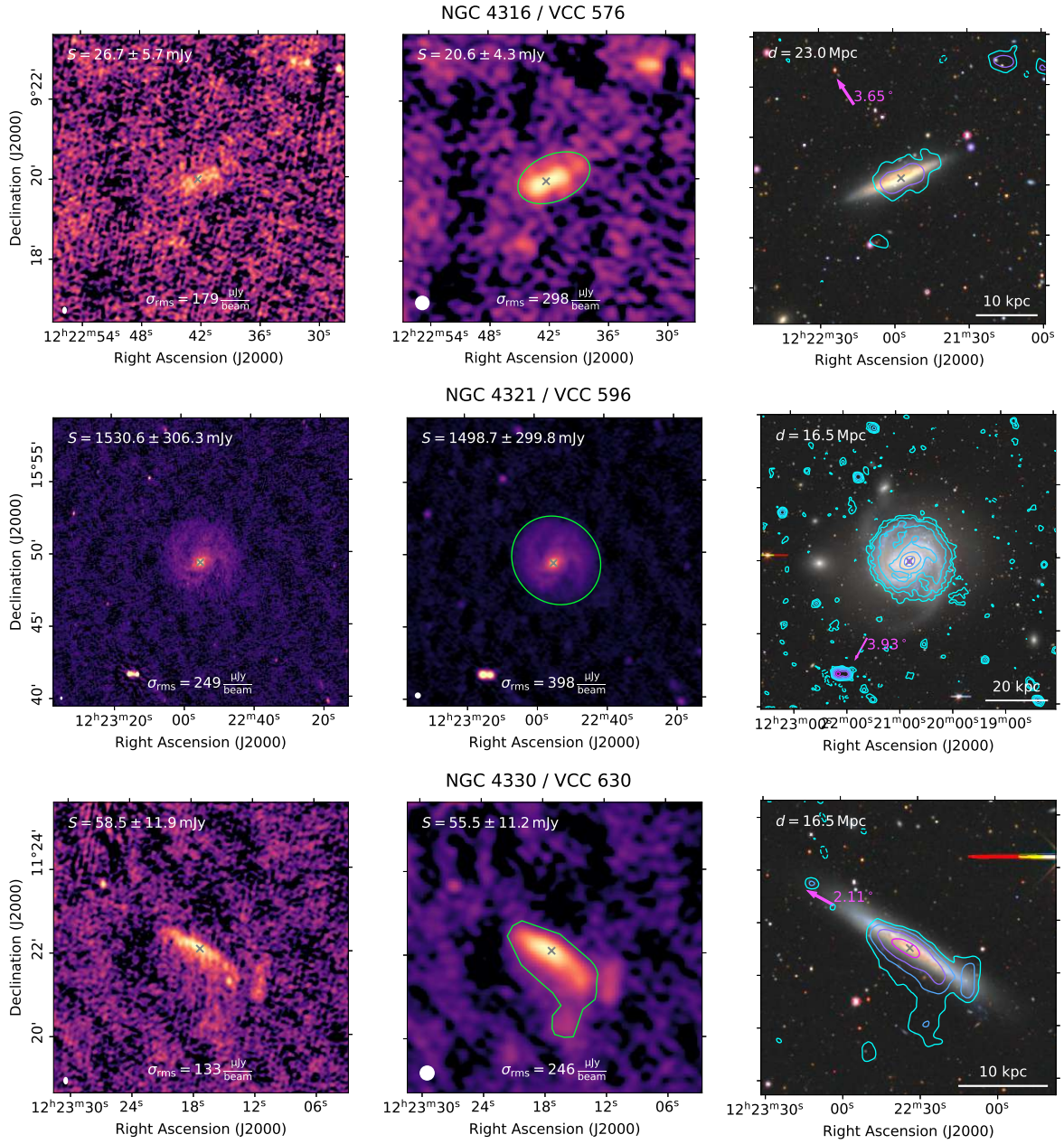


Figure A.1: Continued.

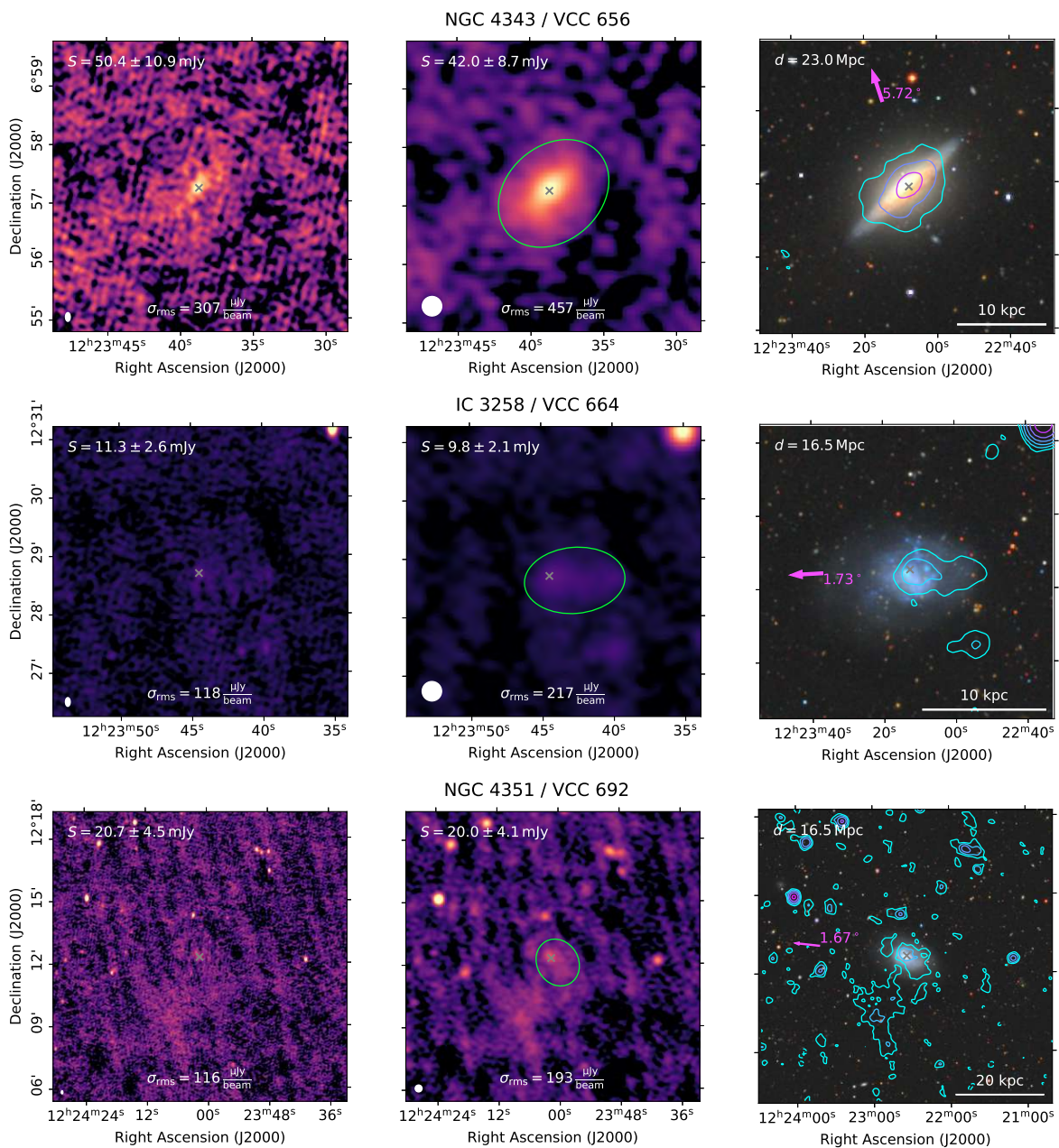


Figure A.1: Continued.

A Images of Virgo cluster galaxies

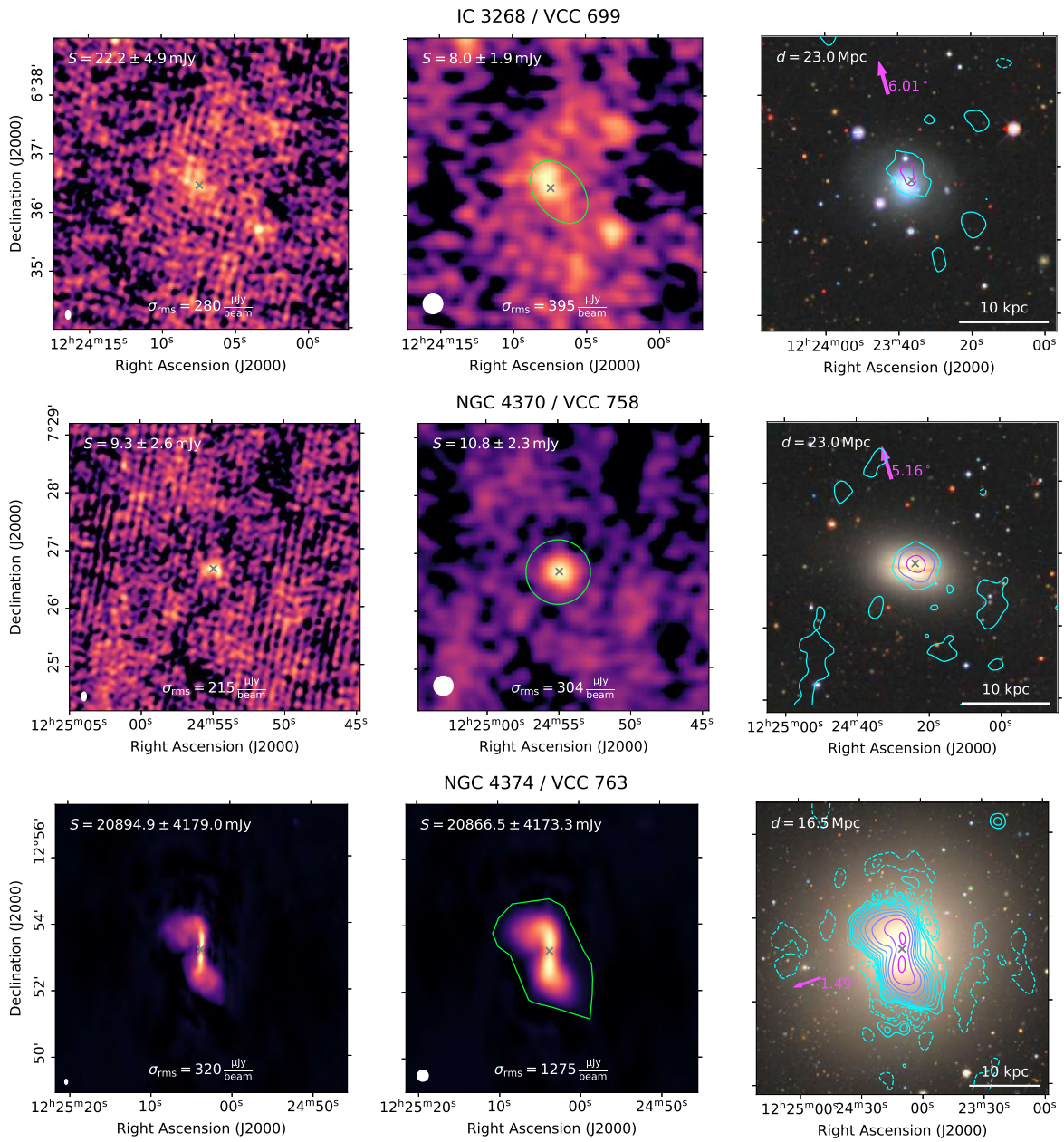


Figure A.1: Continued.

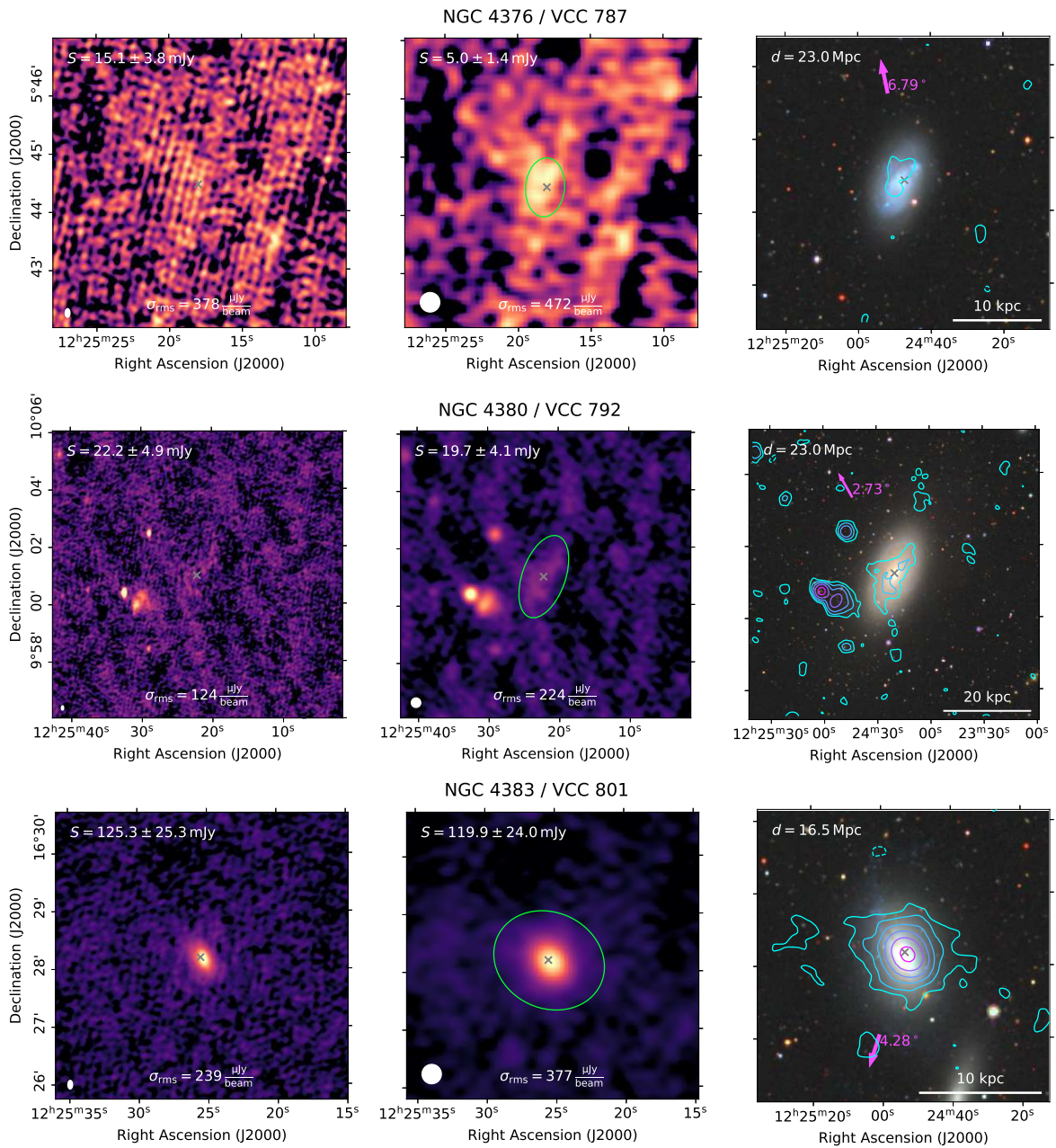


Figure A.1: Continued.

A Images of Virgo cluster galaxies

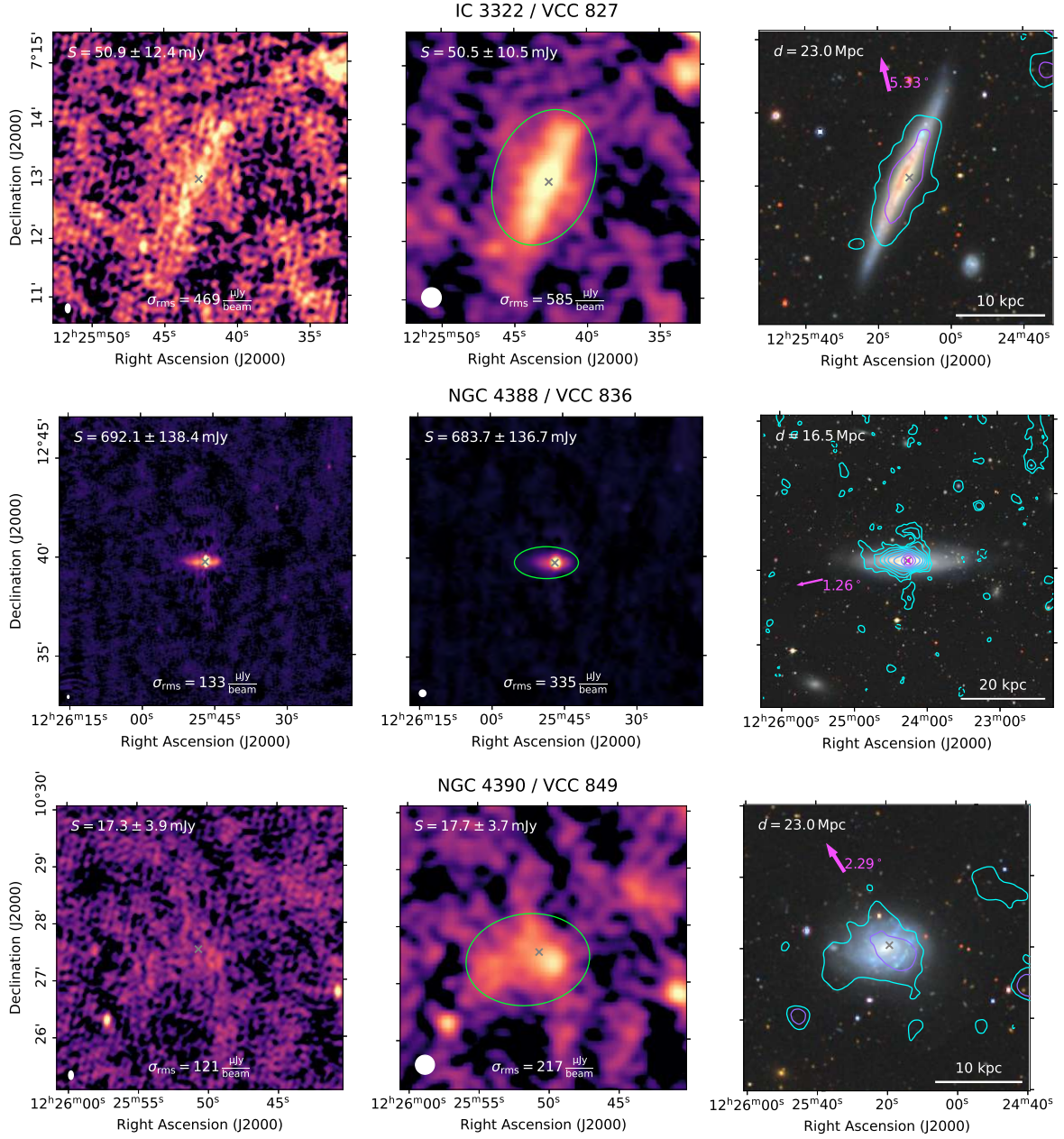


Figure A.1: Continued.

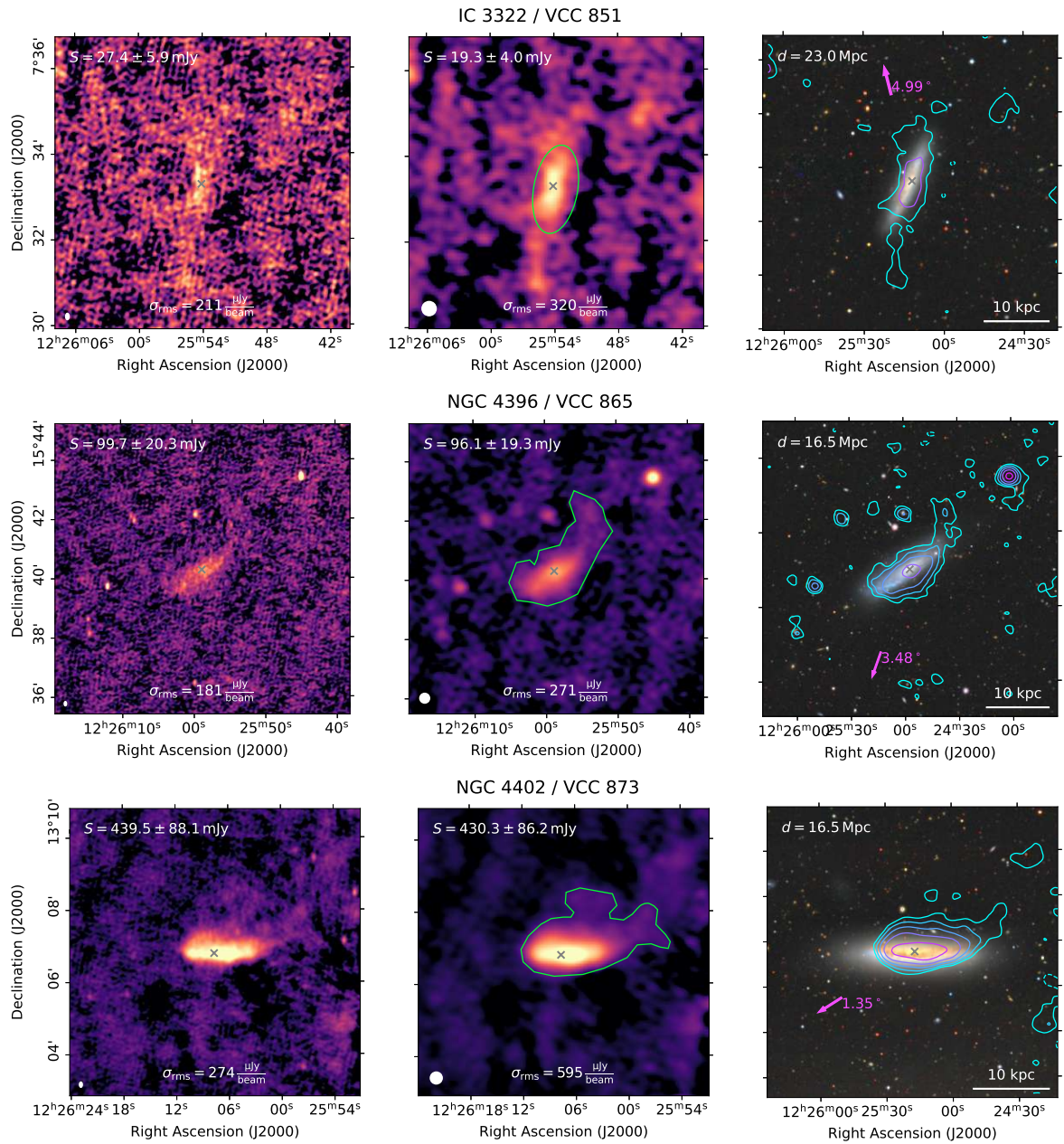


Figure A.1: Continued.

A Images of Virgo cluster galaxies

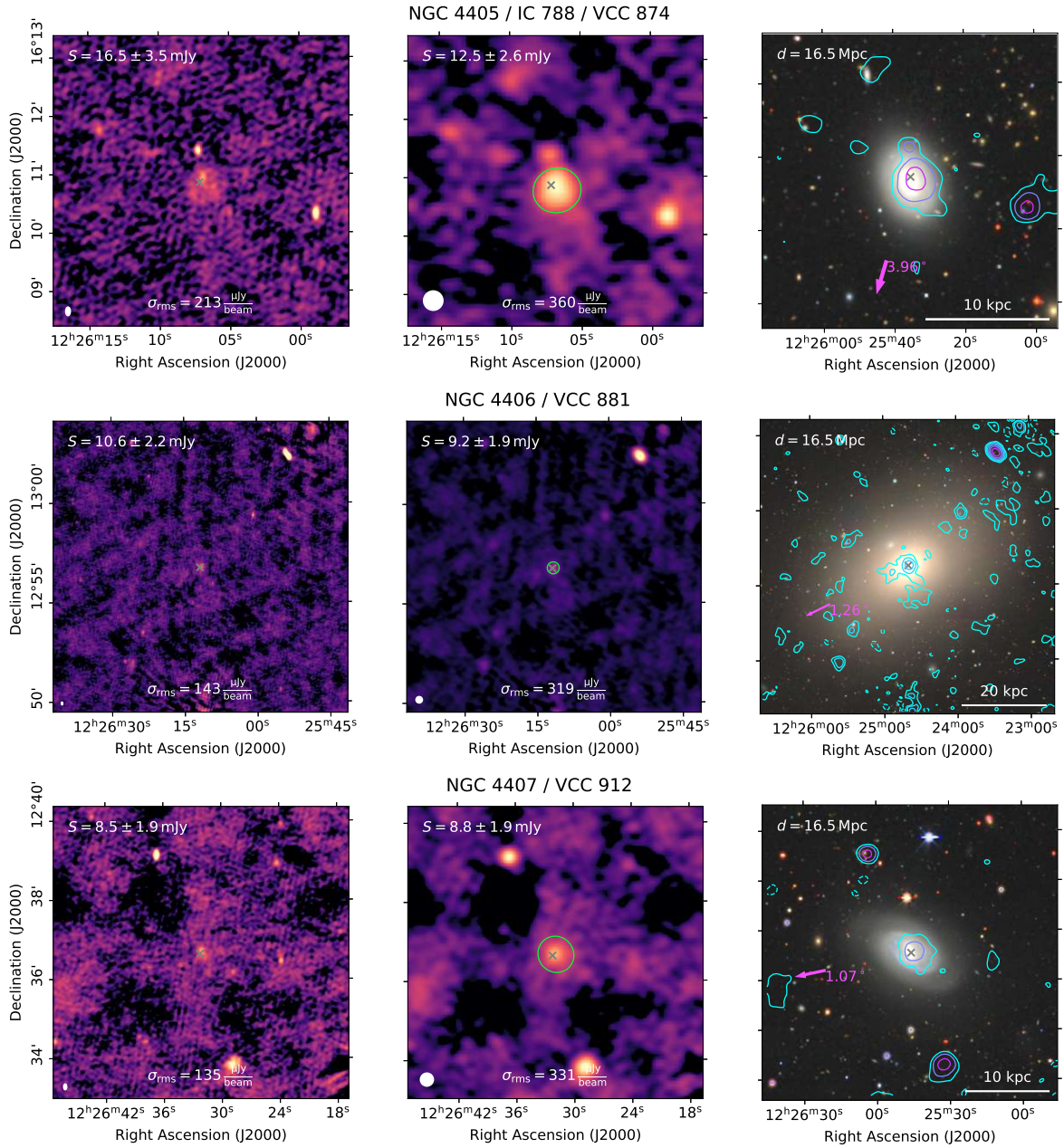


Figure A.1: Continued.

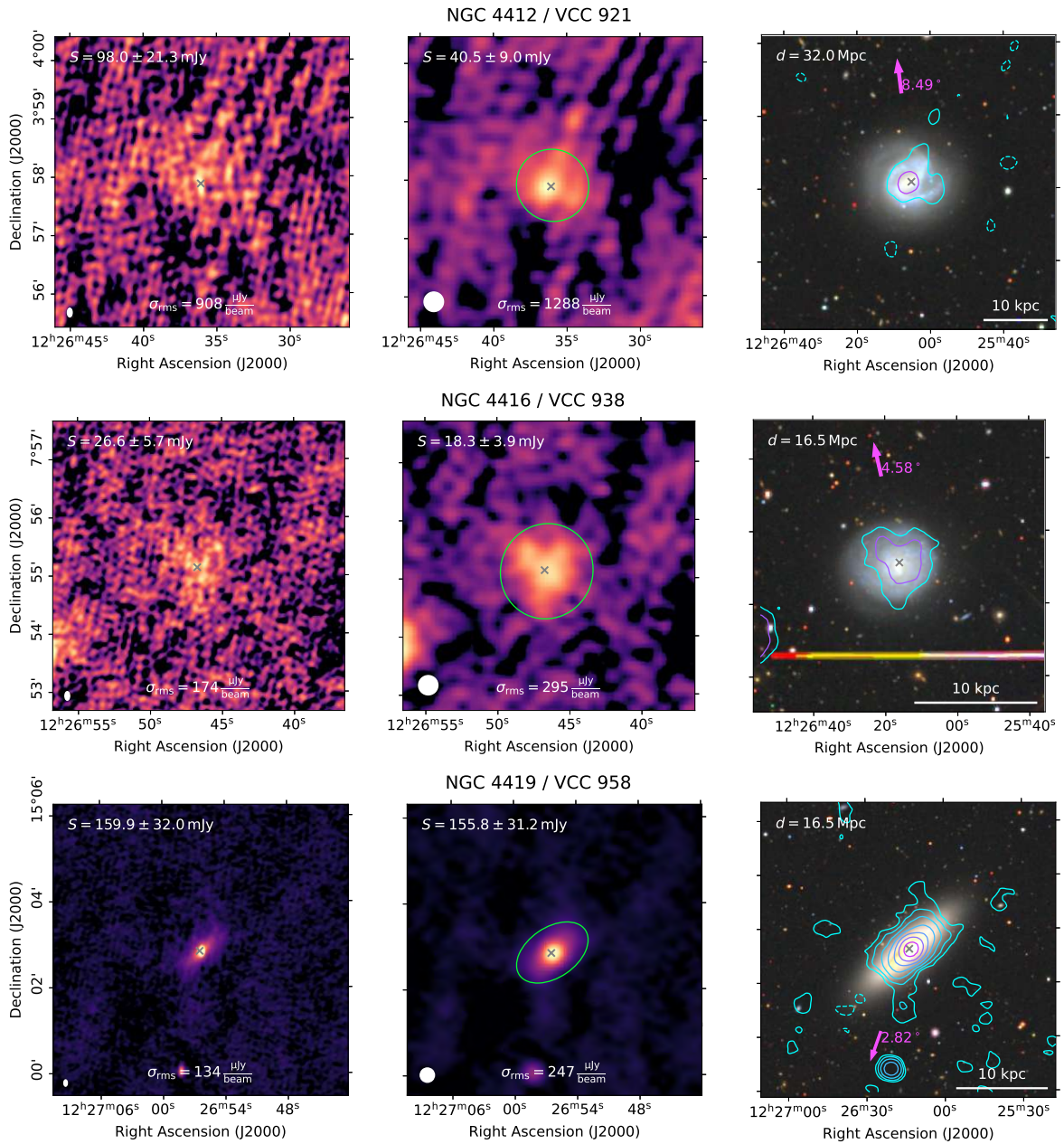


Figure A.1: Continued.

A Images of Virgo cluster galaxies

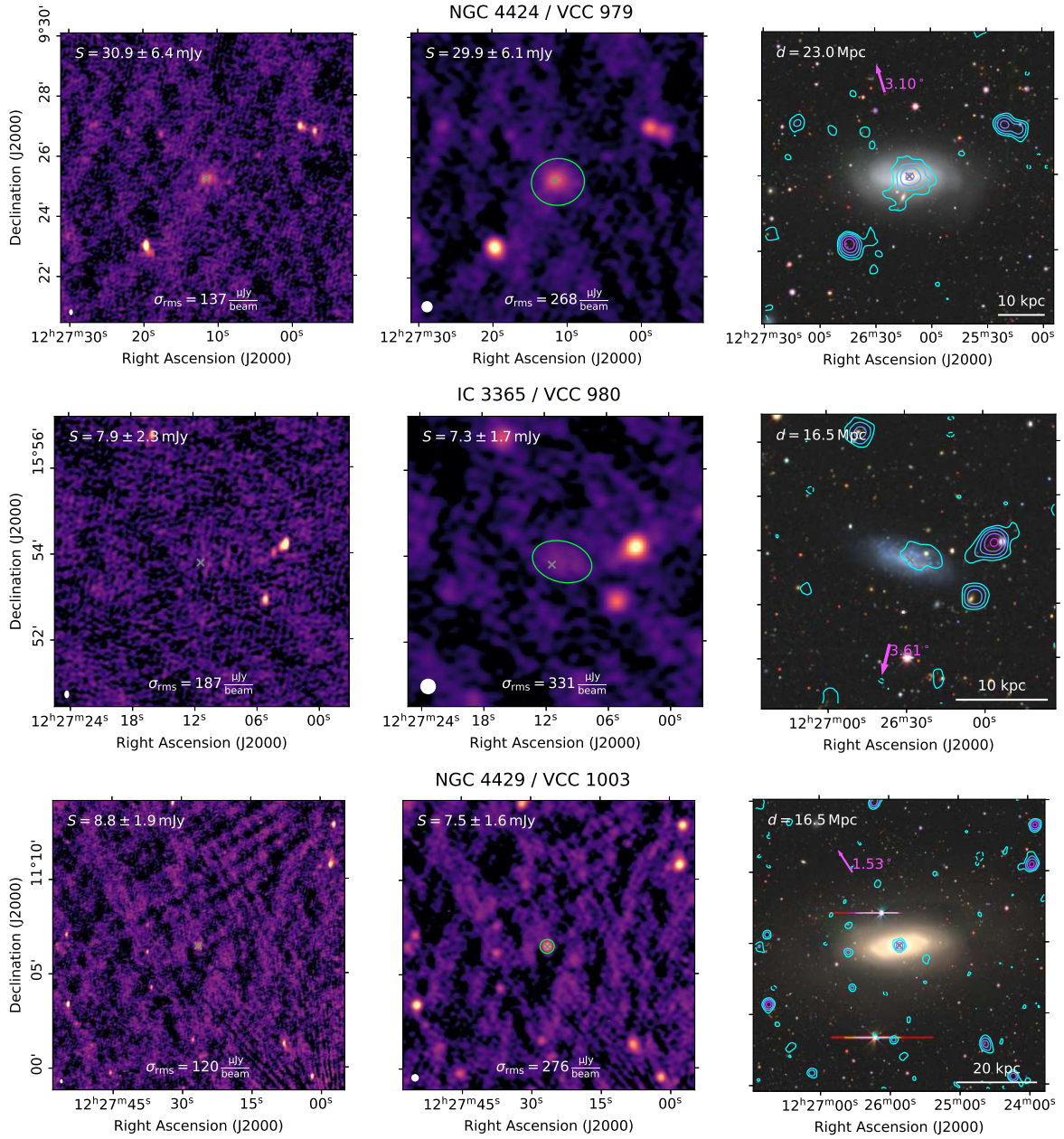


Figure A.1: Continued.

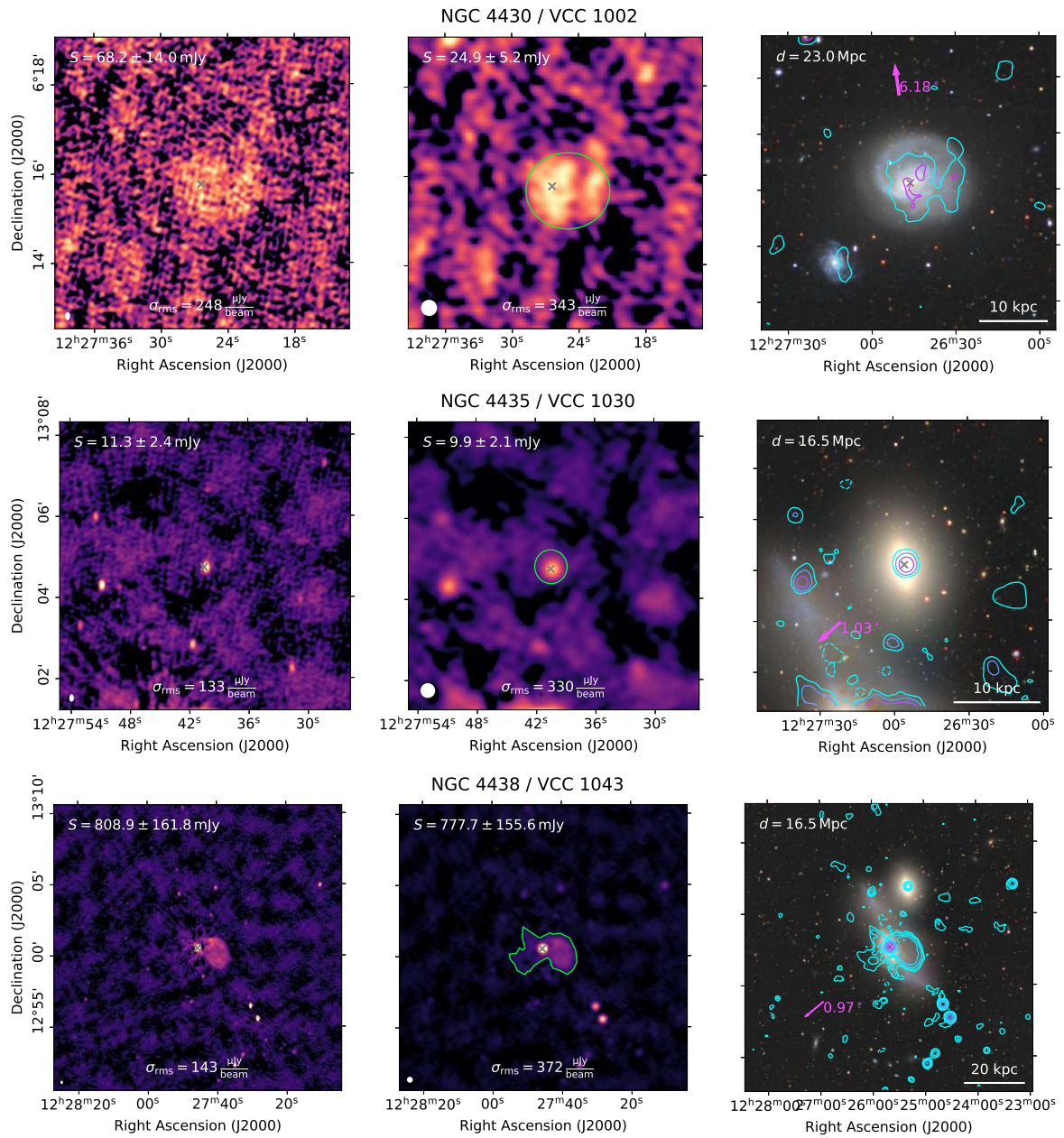


Figure A.1: Continued.

A Images of Virgo cluster galaxies

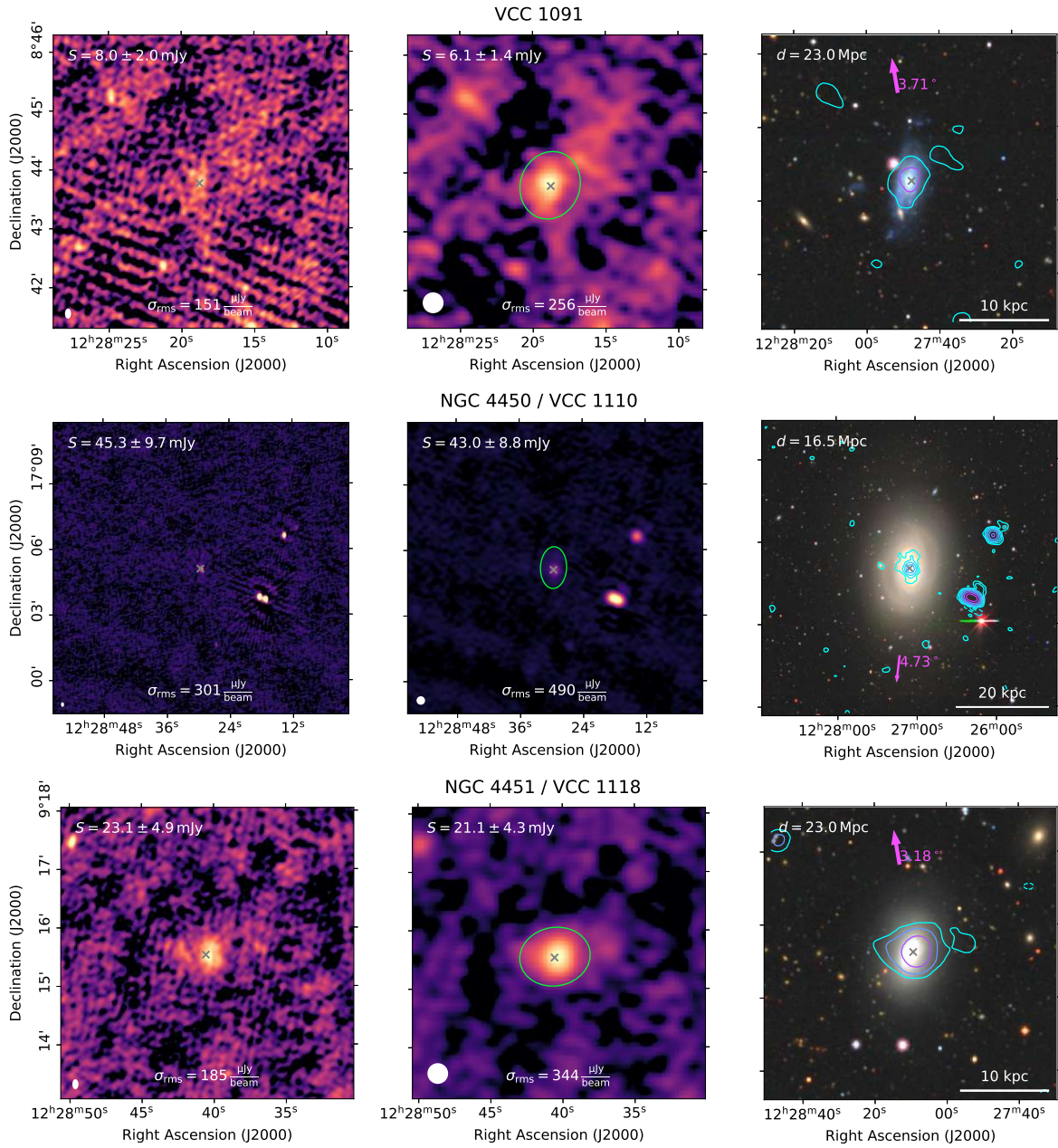


Figure A.1: Continued.

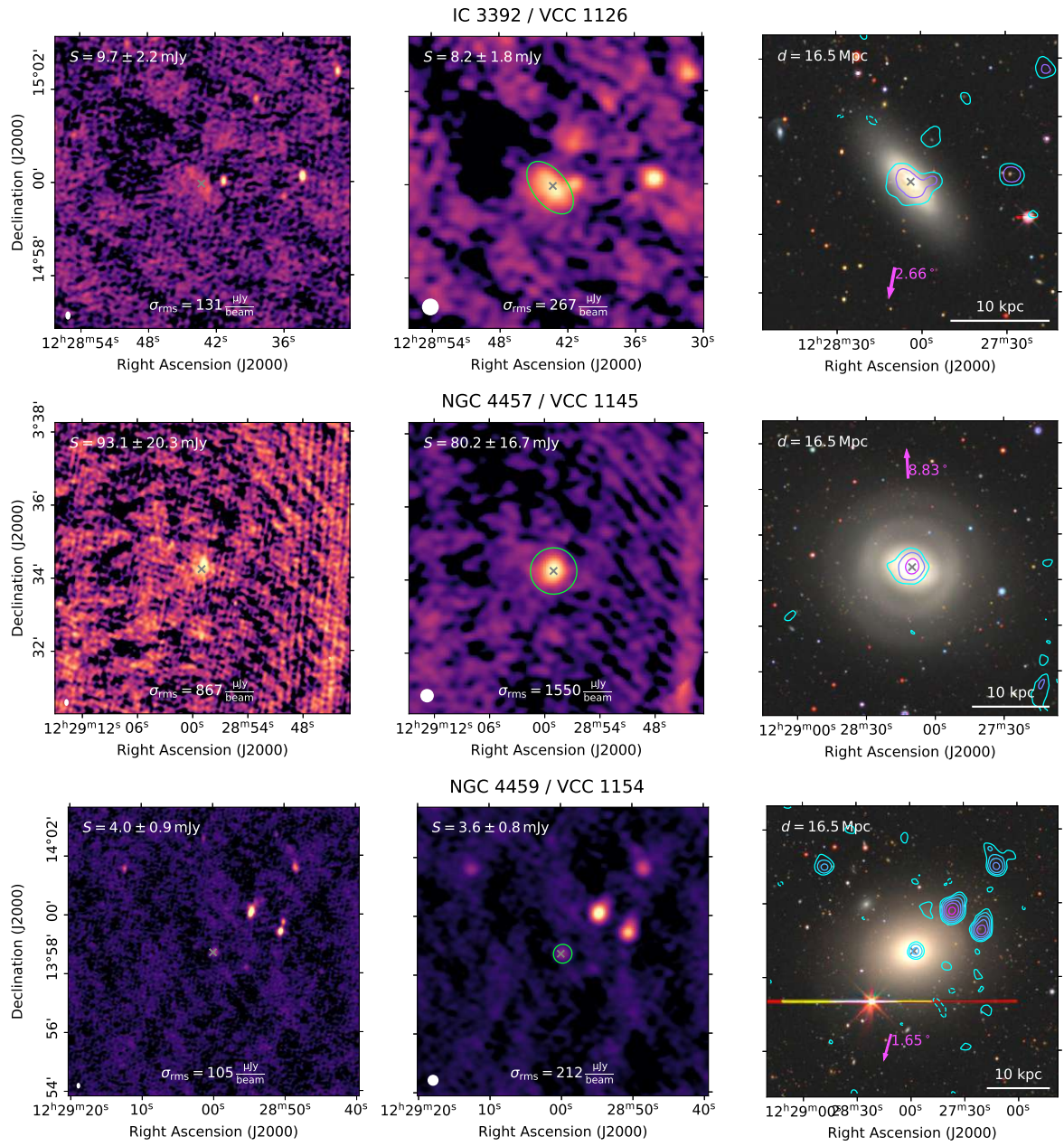


Figure A.1: Continued.

A Images of Virgo cluster galaxies

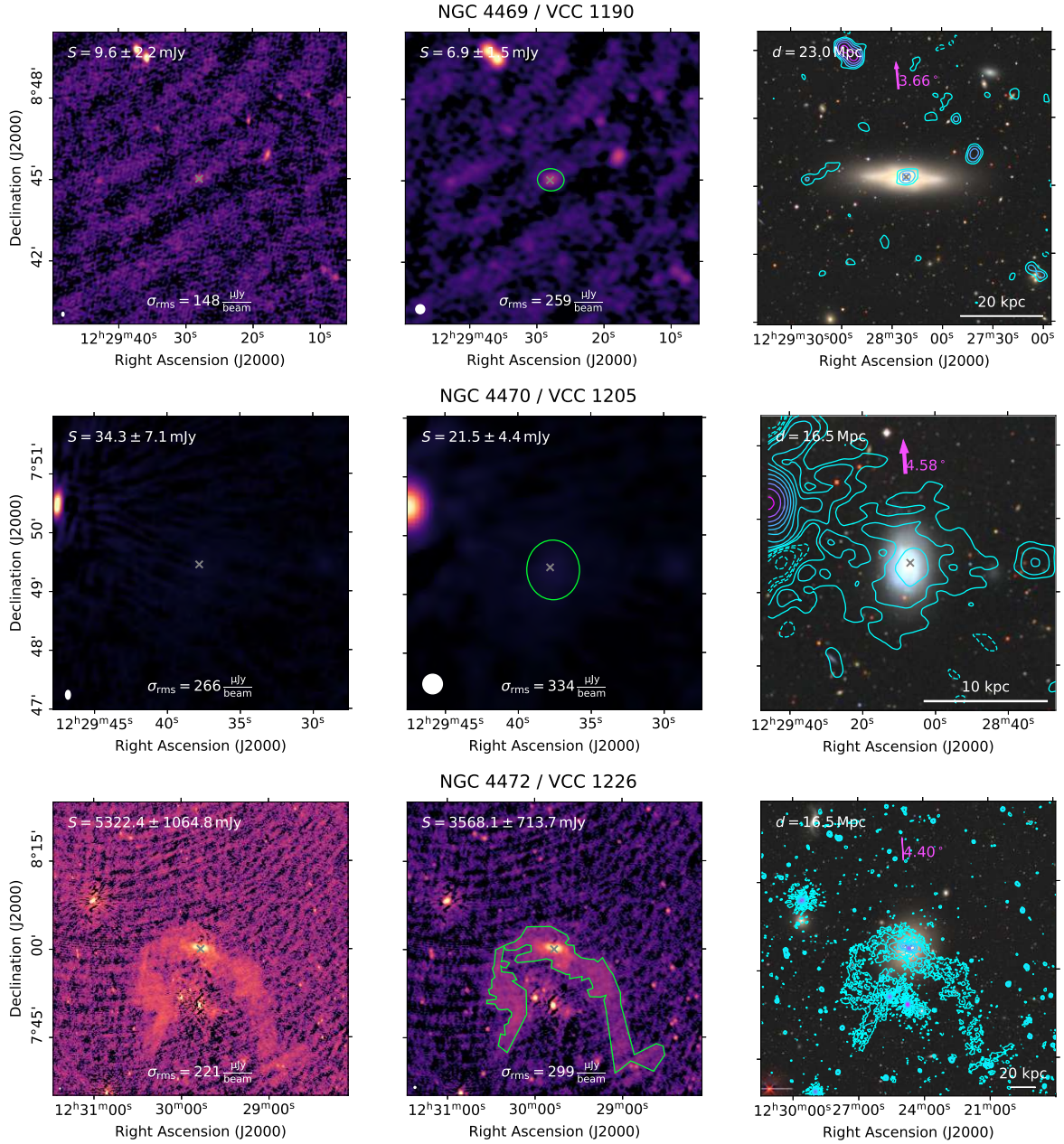


Figure A.1: Continued.

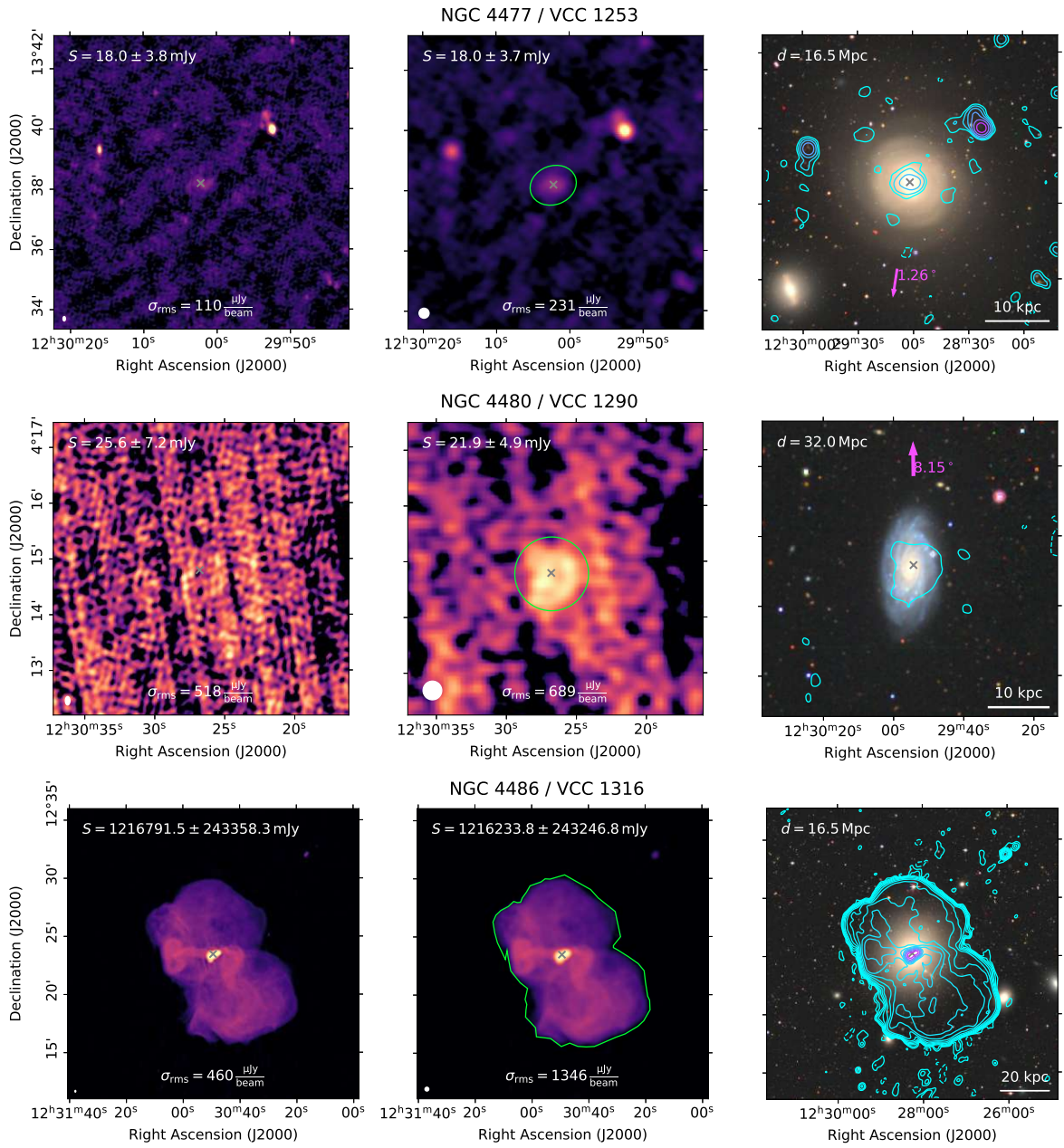


Figure A.1: Continued.

A Images of Virgo cluster galaxies

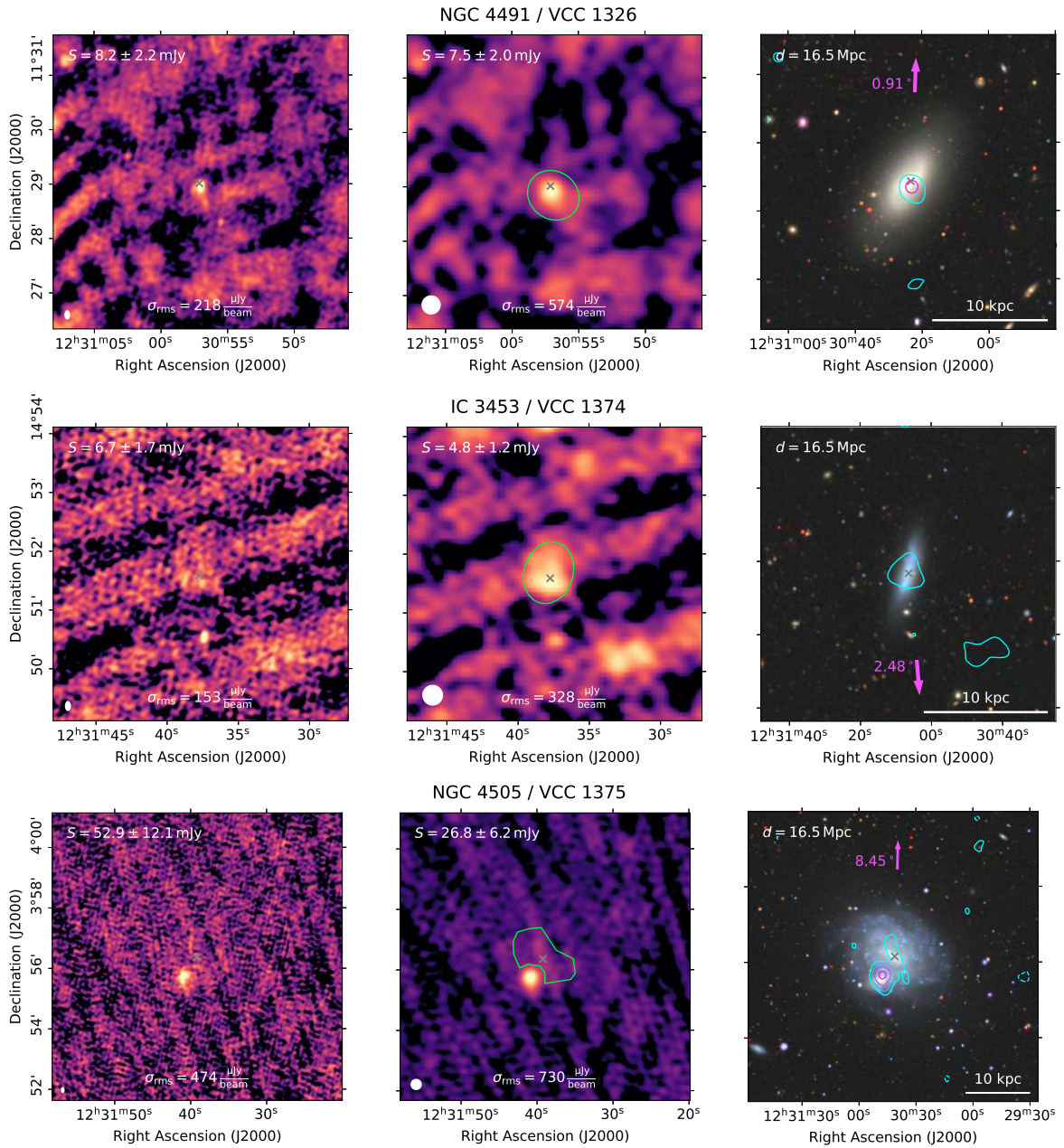


Figure A.1: Continued.

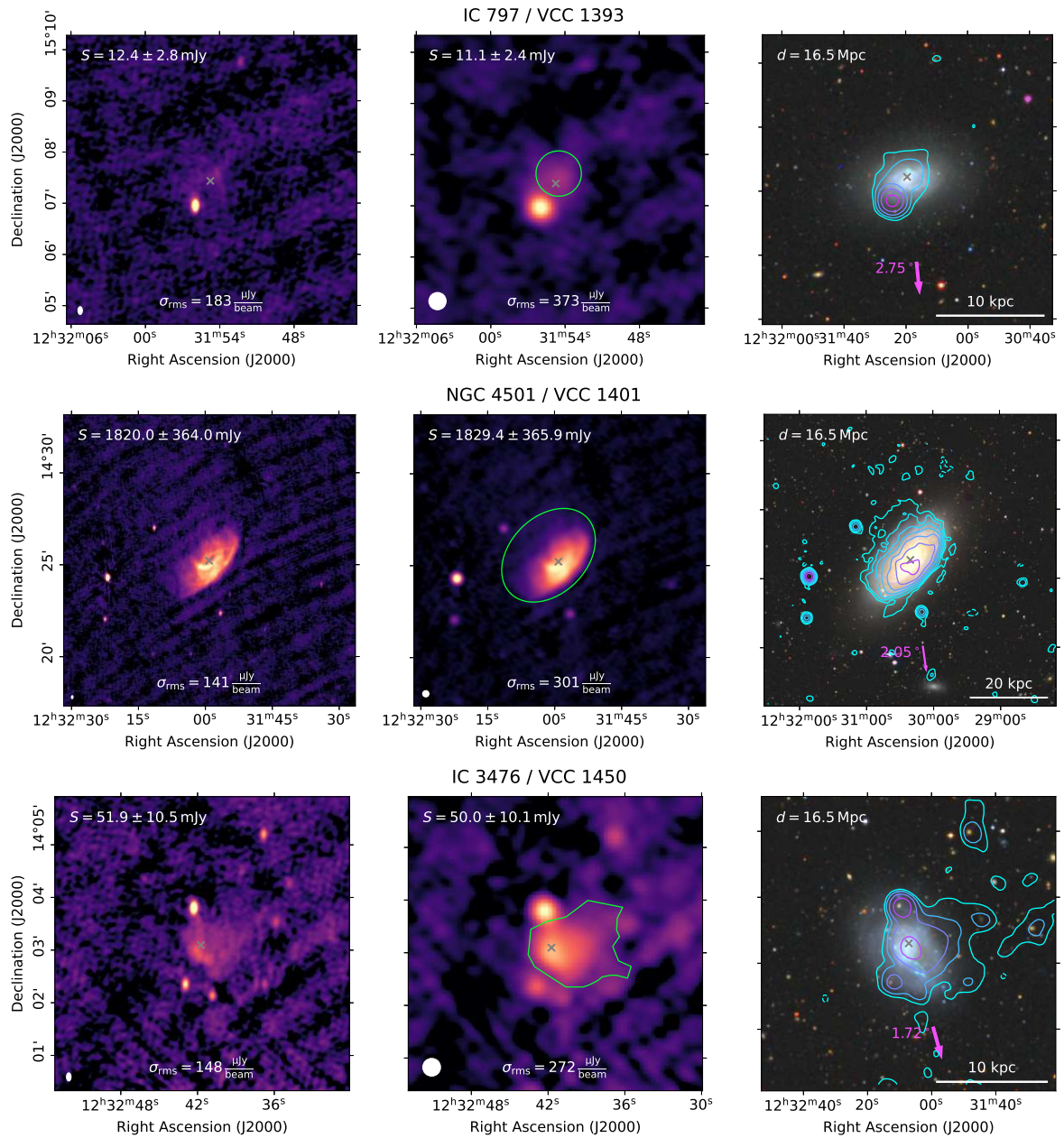


Figure A.1: Continued.

A Images of Virgo cluster galaxies

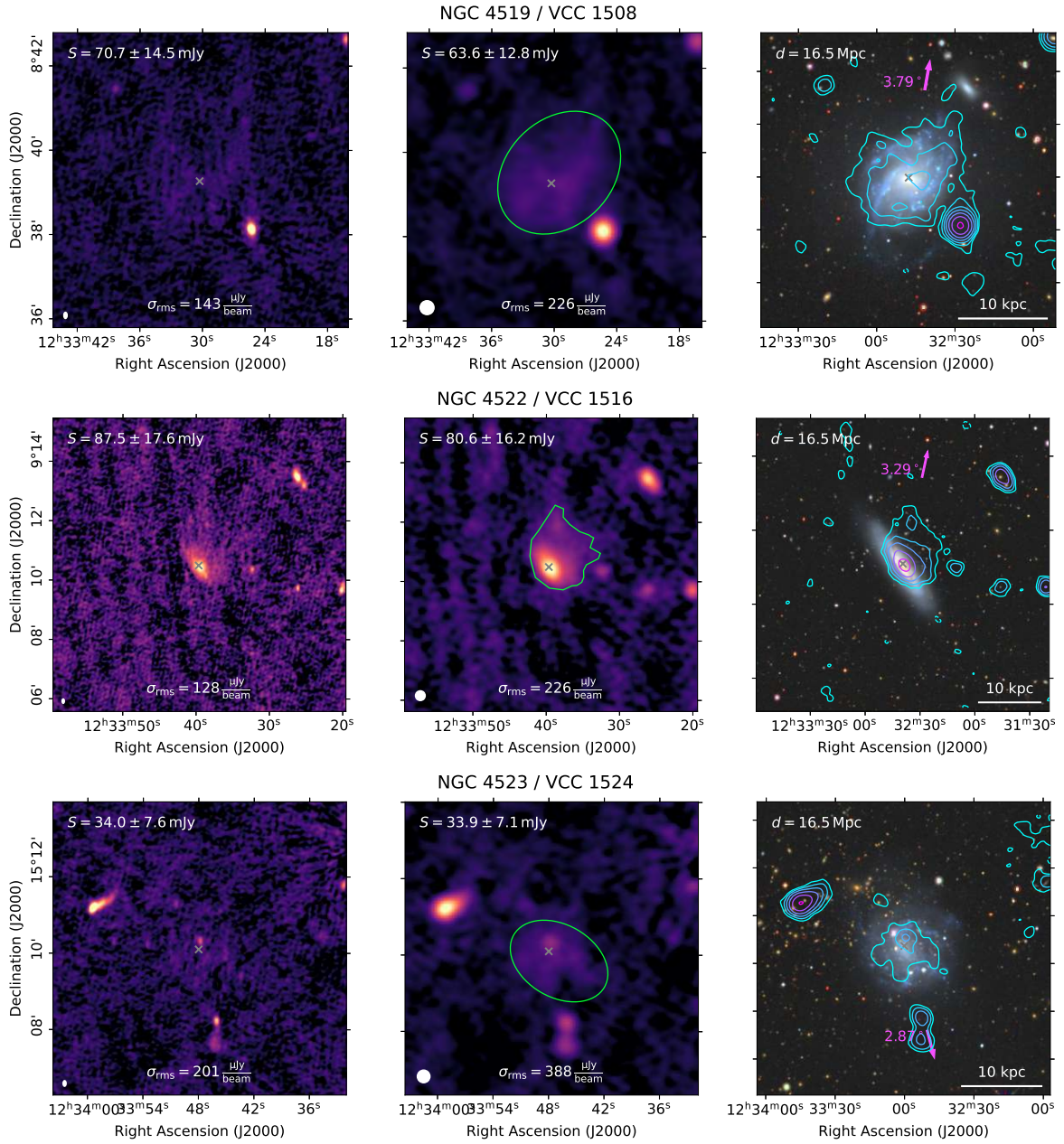


Figure A.1: Continued.

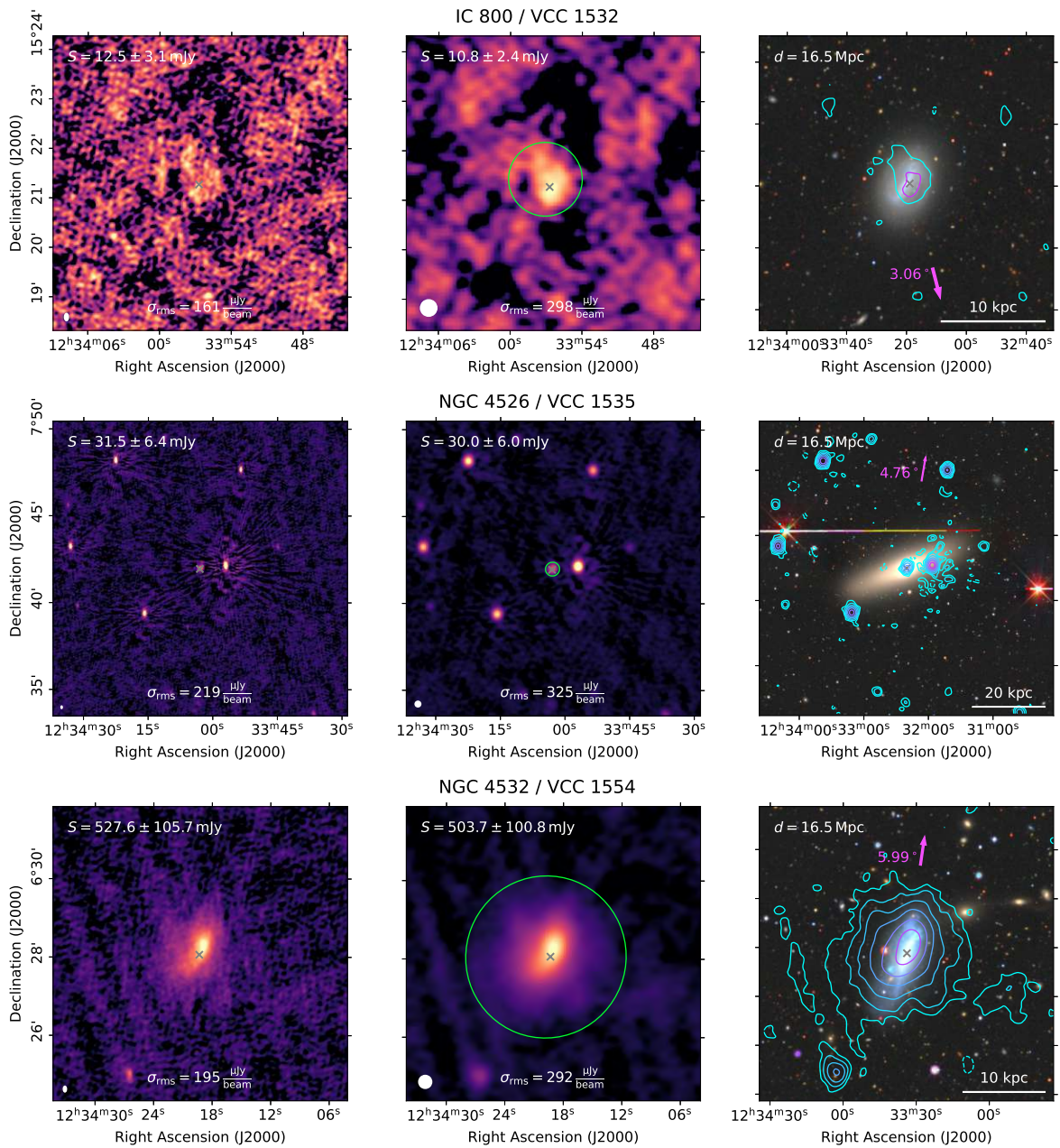


Figure A.1: Continued.

A Images of Virgo cluster galaxies

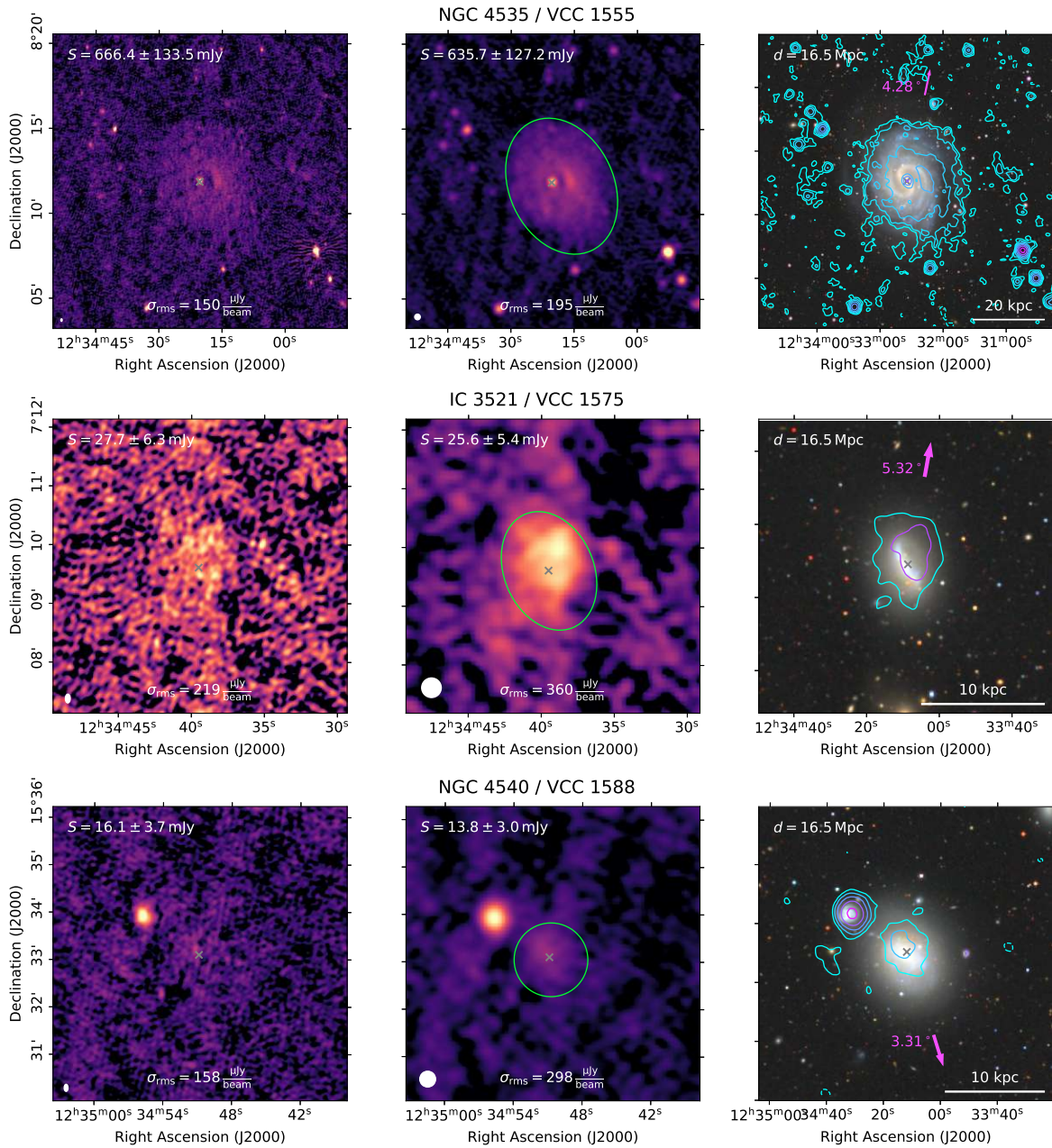


Figure A.1: Continued.

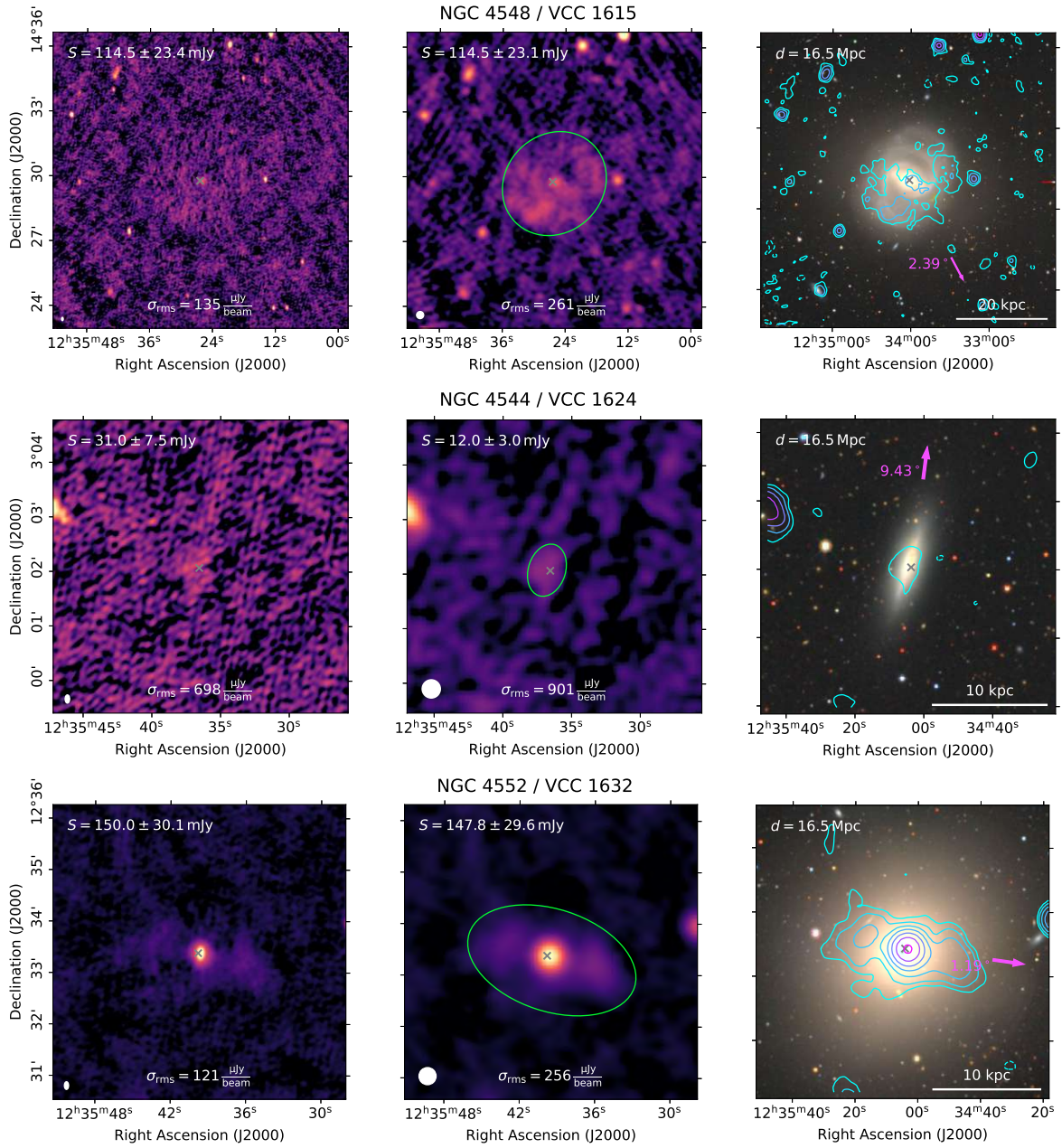


Figure A.1: Continued.

A Images of Virgo cluster galaxies

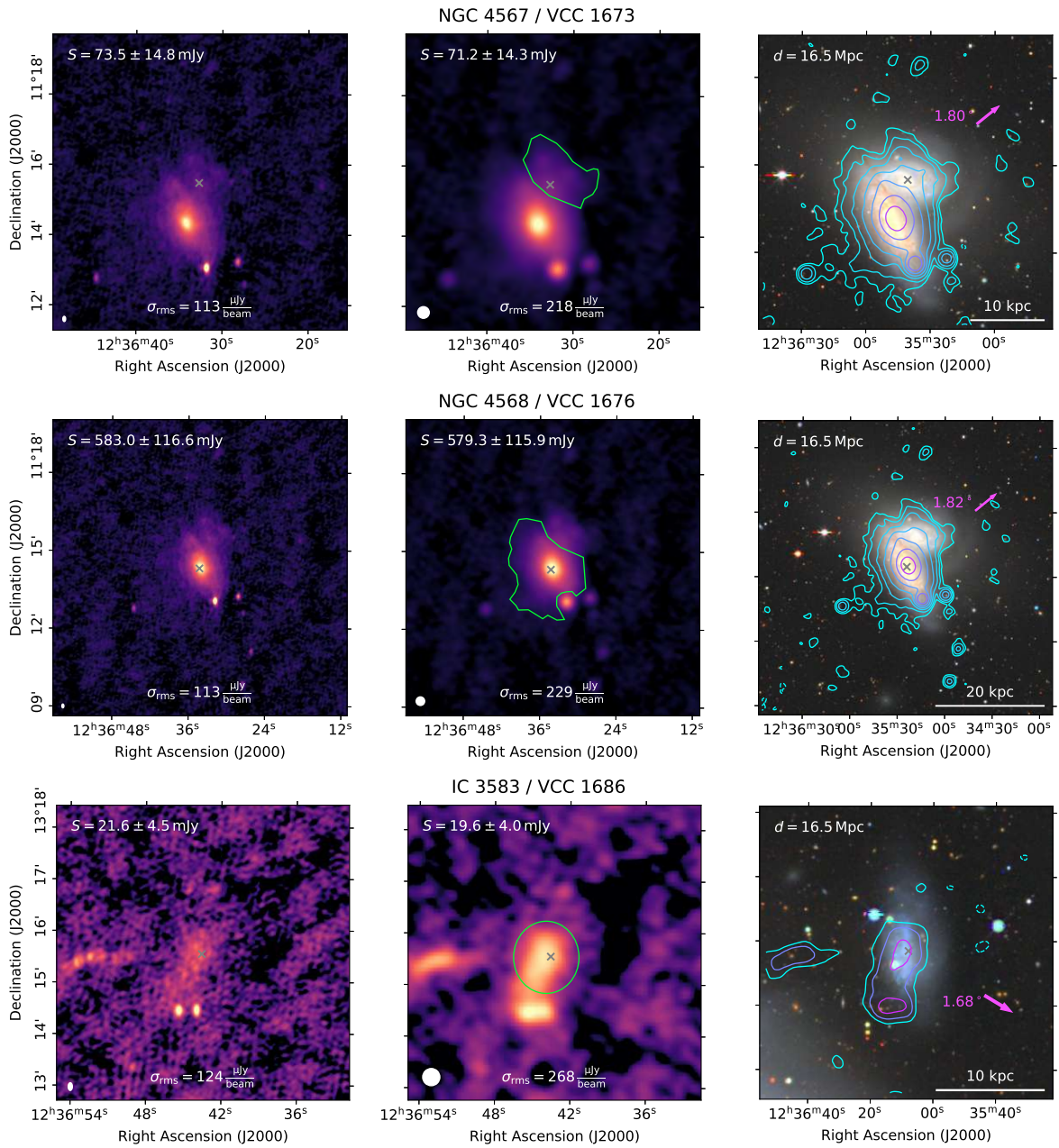


Figure A.1: Continued.

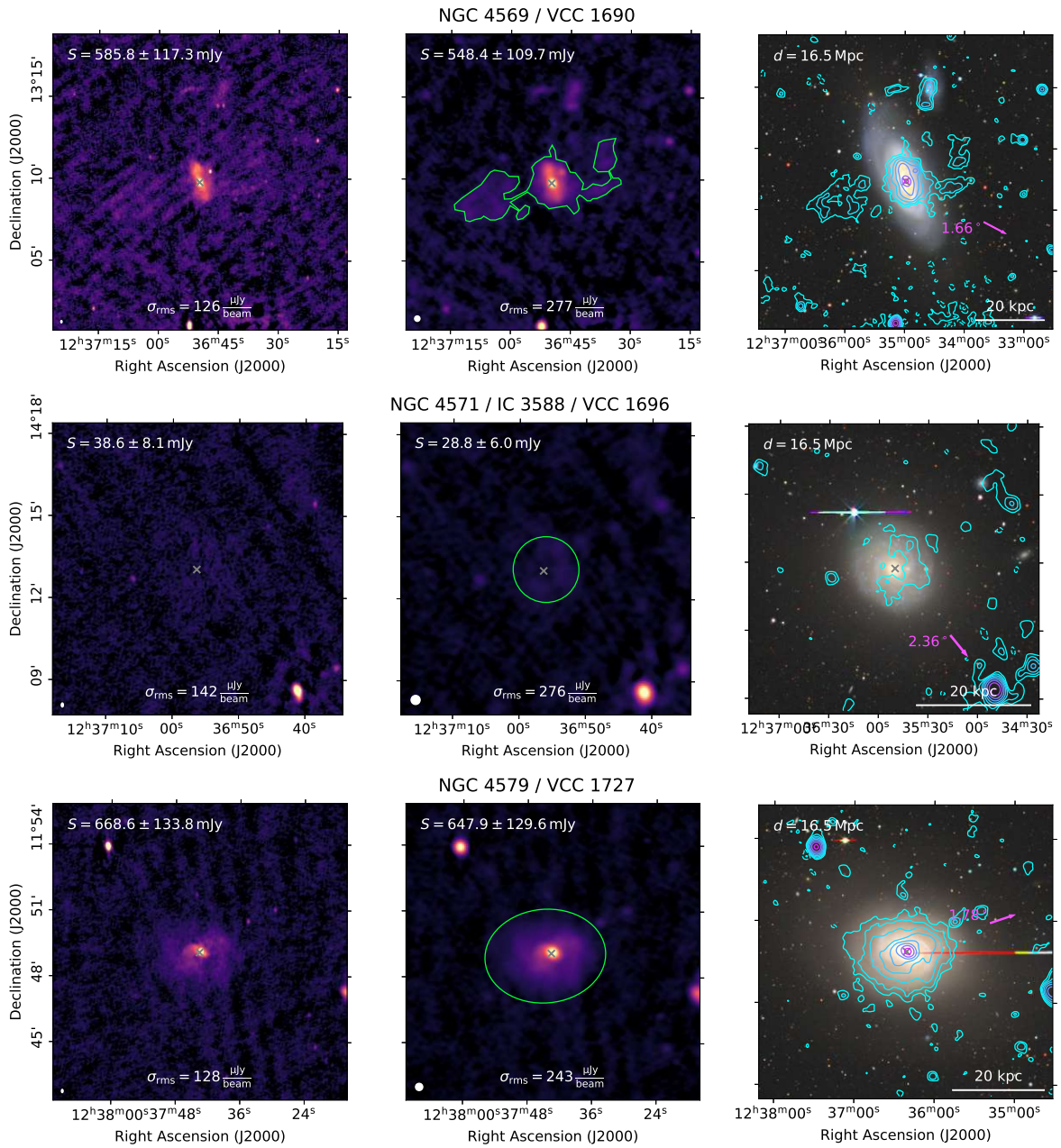


Figure A.1: Continued.

A Images of Virgo cluster galaxies

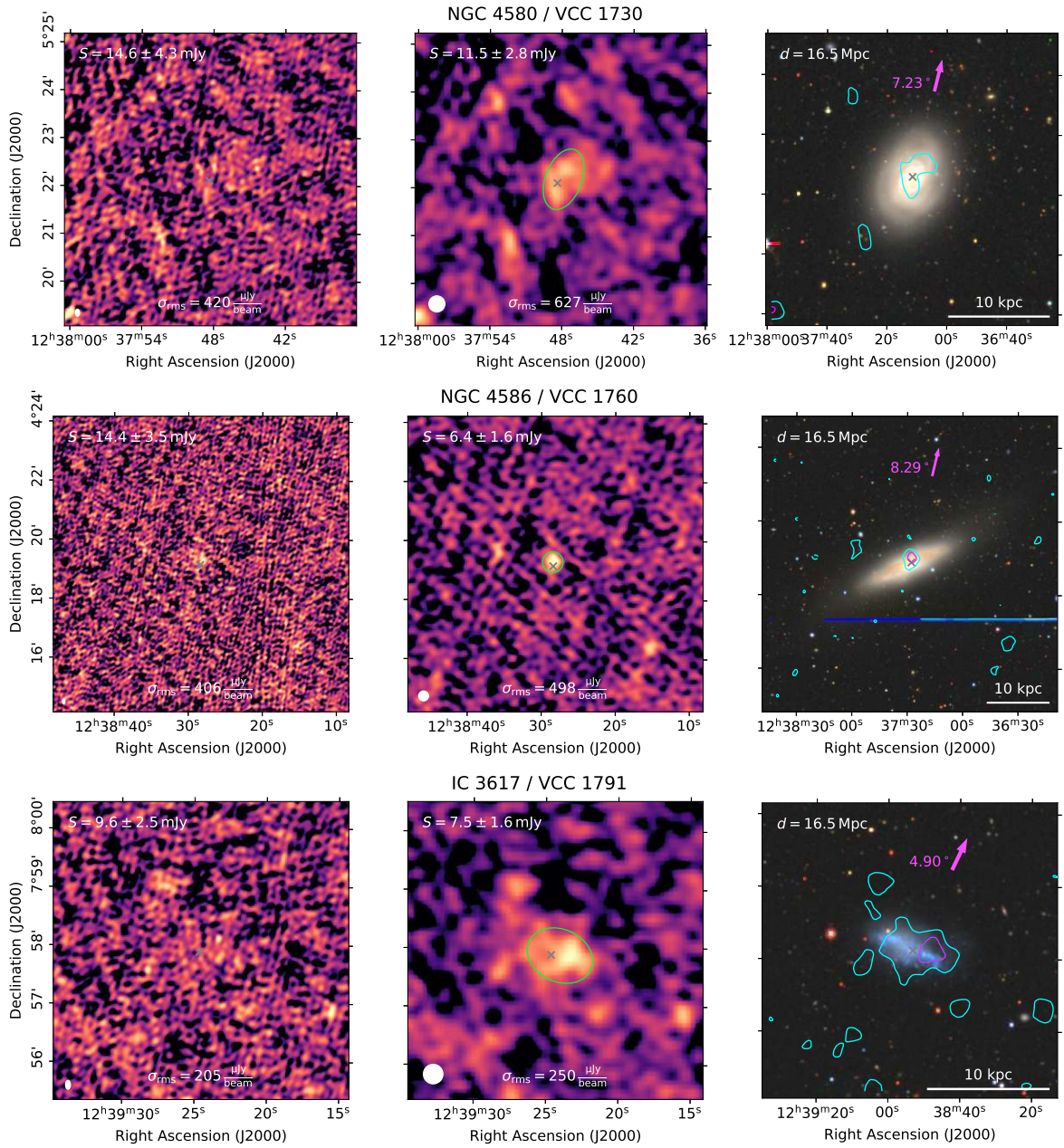


Figure A.1: Continued.

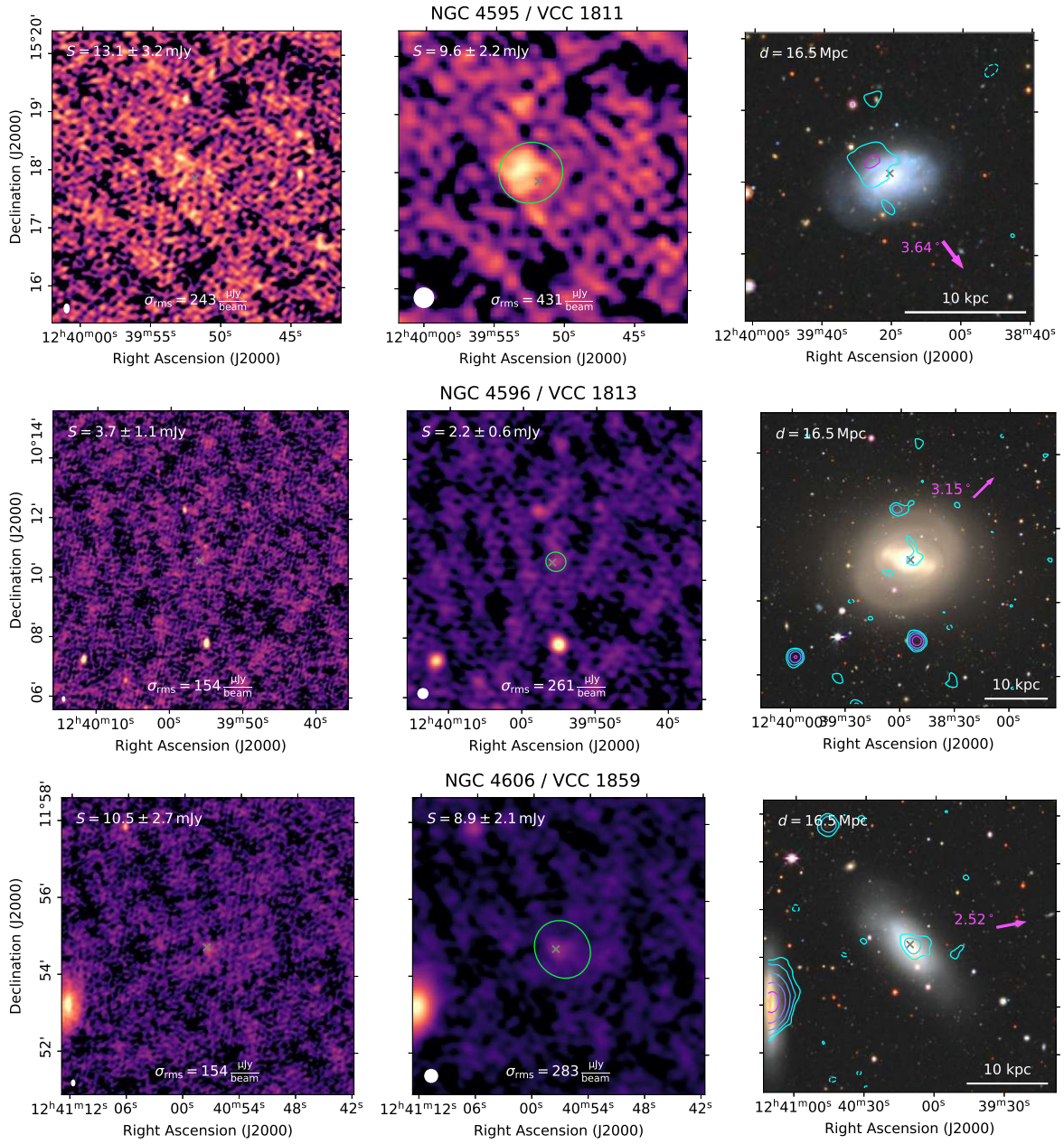


Figure A.1: Continued.

A Images of Virgo cluster galaxies

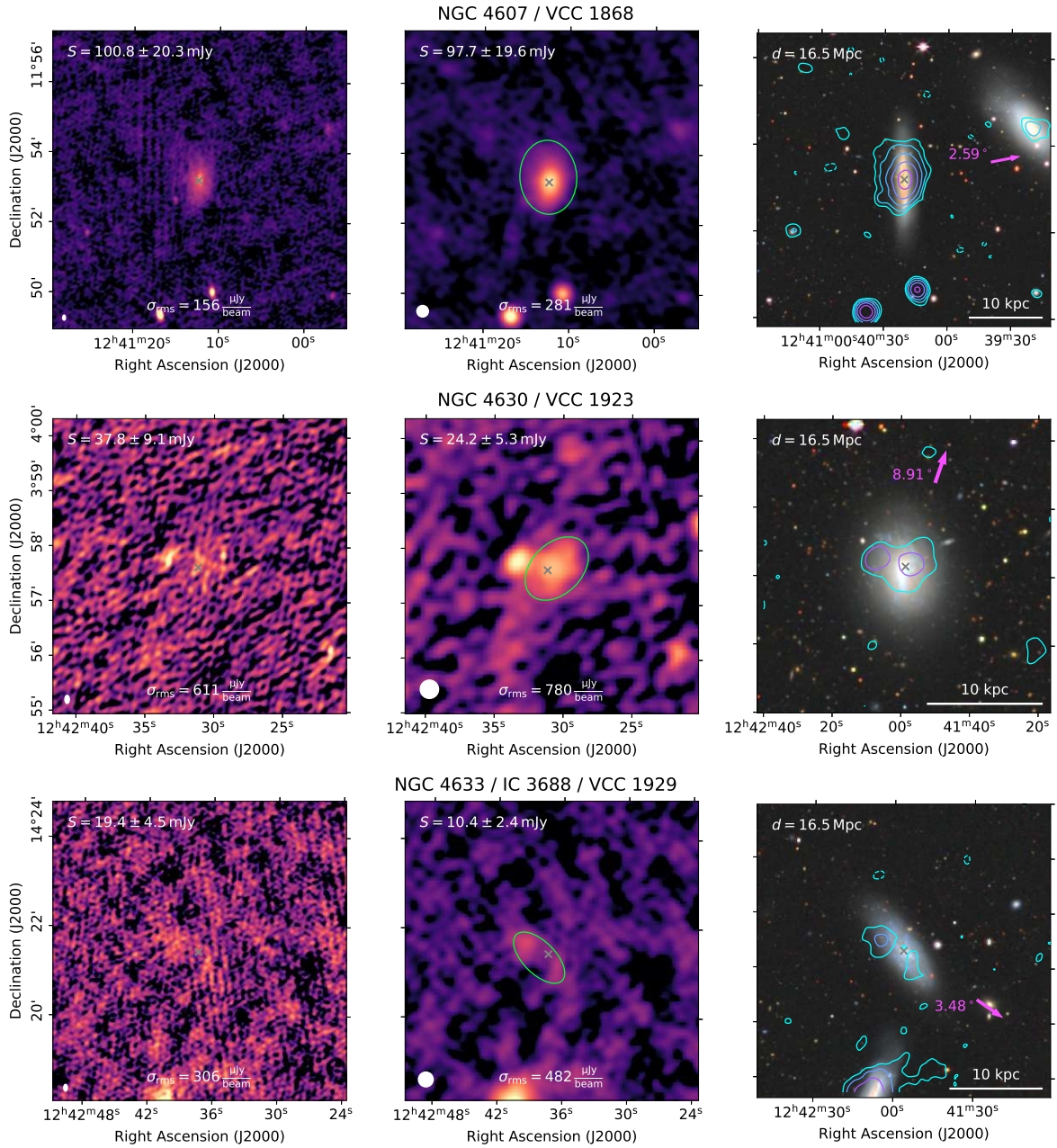


Figure A.1: Continued.

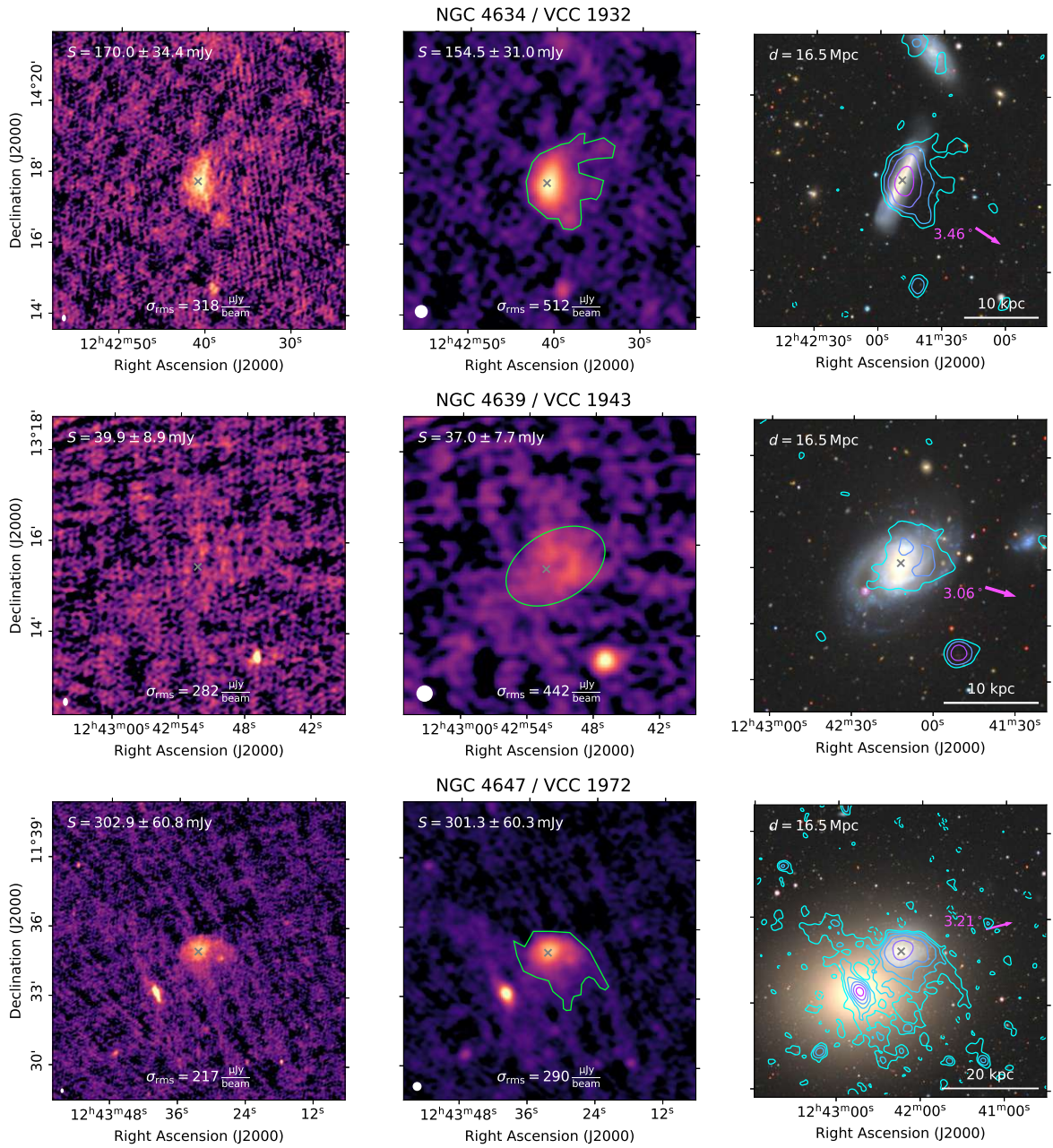


Figure A.1: Continued.

A Images of Virgo cluster galaxies

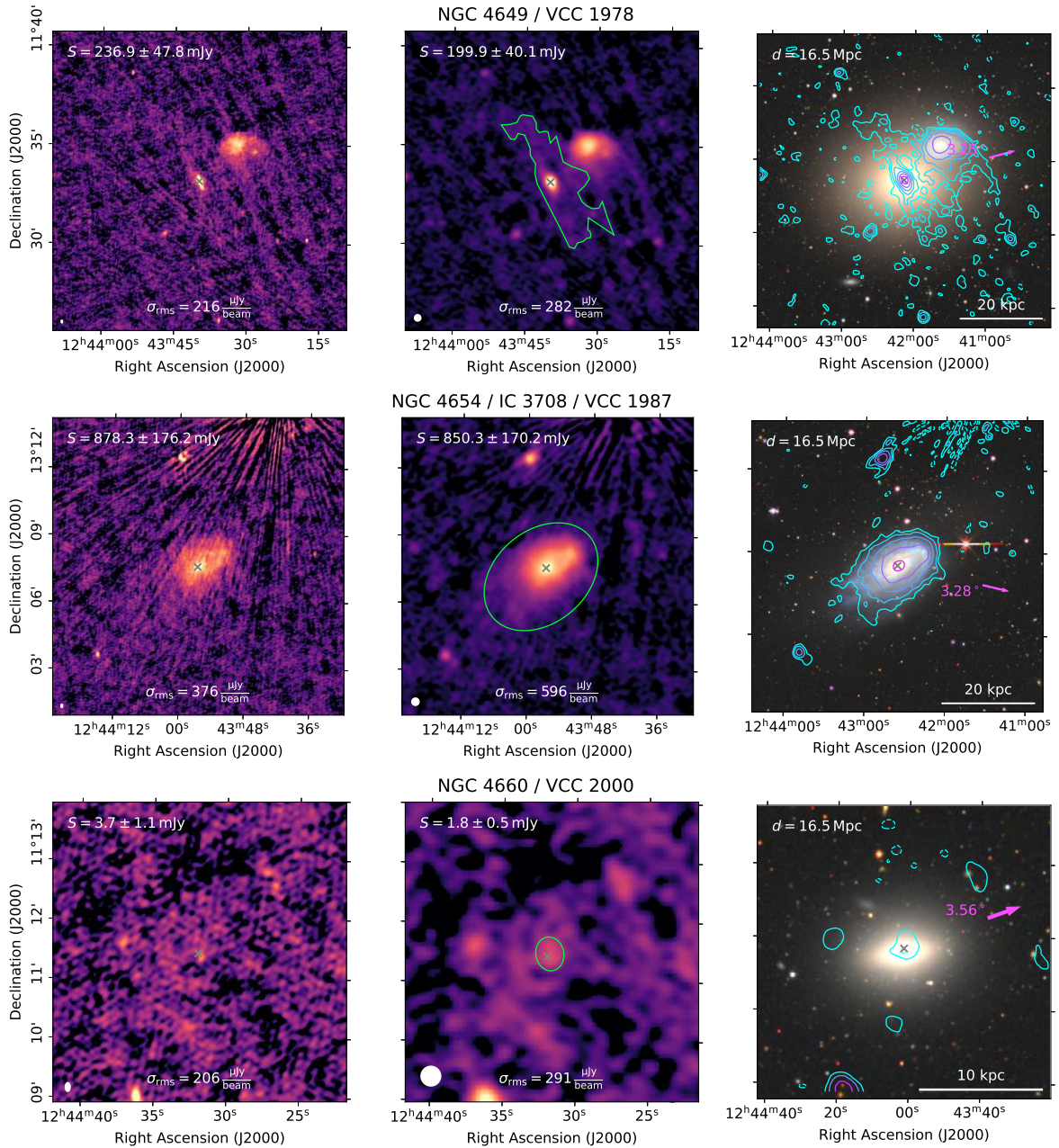


Figure A.1: Continued.

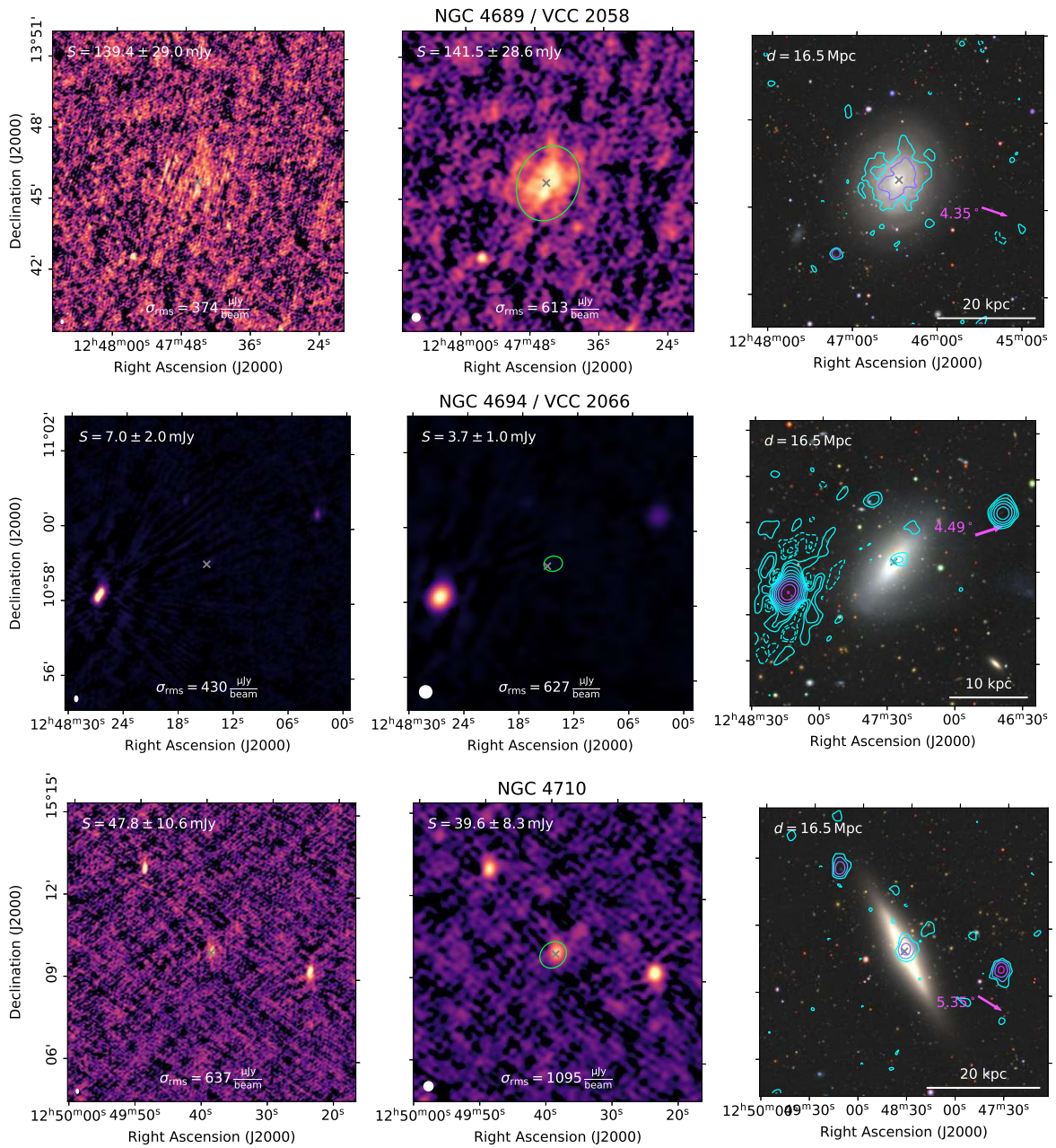


Figure A.1: Continued.

A Images of Virgo cluster galaxies

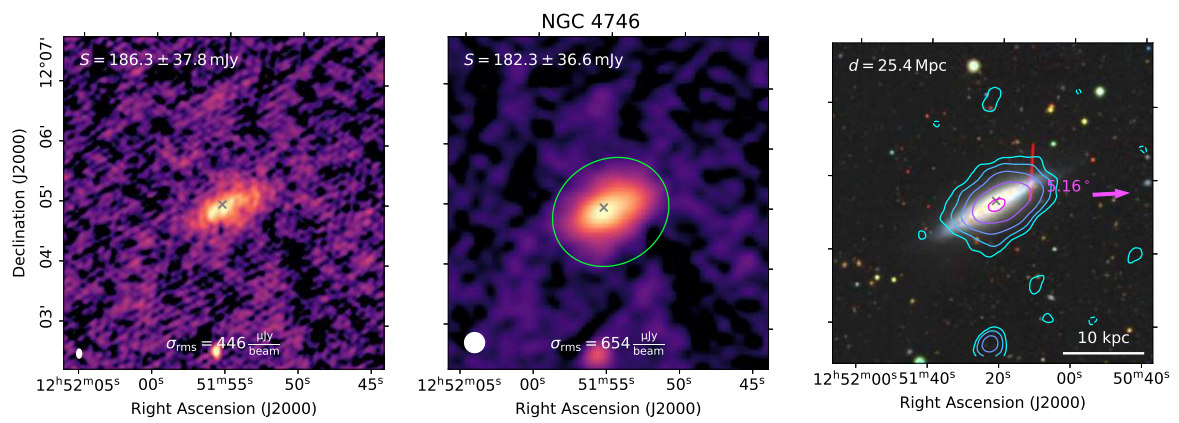


Figure A.1: Continued.

B LOFAR data

Table B.1: LOFAR data.

Name	S_{144} [Jy]	d [Mpc]	L_{144} [W Hz ⁻¹]	α_{144}^{1400}
(1)	(2)	(3)	(4)	(5)
HRS 2	(1.5±0.3)e-2	18.44	(6.1±1.3)e+20	-0.47 ± 0.11 ^a
IC 610	(2.0±0.4)e-2	16.71	(6.5±1.3)e+20	-0.58 ± 0.11 ^a
NGC 3254	(3.4±0.5)e-2	19.37	(1.5±0.2)e+21	< -1.25 ^a
NGC 3277	(1.8±0.3)e-2	20.21	(8.8±1.4)e+20	-0.58 ± 0.09 ^a
HRS 10	(8.2±1.3)e-3	21.66	(4.6±0.8)e+20	-0.56 ± 0.13 ^a
NGC 3287	(2.8±0.6)e-2	18.93	(1.2±0.2)e+21	-0.39 ± 0.10 ^a
HRS 12	(3.4±0.8)e-3	19.89	(1.6±0.4)e+20	< -0.27 ^a
NGC 3294	(2.3±0.3)e-1	22.47	(1.4±0.2)e+22	-0.70 ± 0.08 ^a
NGC 3338	(7.1±1.4)e-2	18.57	(2.9±0.6)e+21	-0.40 ± 0.10 ^a
NGC 3346	(3.0±0.6)e-2	18.0	(1.2±0.2)e+21	-0.34 ± 0.10 ^a
NGC 3380	(1.1±0.2)e-2	22.91	(7.1±1.2)e+20	-0.68 ± 0.12 ^a
NGC 3381	(2.9±0.4)e-2	23.29	(1.9±0.3)e+21	-0.70 ± 0.09 ^a
NGC 3395	(3.9±0.6)e-1	23.1	(2.5±0.4)e+22	-0.64 ± 0.08 ^a
NGC 3424	(3.0±0.4)e-1	21.44	(1.6±0.2)e+22	-0.75 ± 0.08 ^a
NGC 3430	(1.4±0.2)e-1	22.64	(8.7±1.3)e+21	-0.68 ± 0.08 ^a
NGC 3437	(2.6±0.5)e-1	18.24	(1.0±0.2)e+22	-0.59 ± 0.10 ^a
HRS 26	(4.8±0.8)e-3	22.41	(2.9±0.5)e+20	< -0.42 ^a
NGC 3442	(4.6±0.7)e-2	24.77	(3.4±0.5)e+21	-0.56 ± 0.08 ^a
NGC 3451	(3.0±0.6)e-2	19.03	(1.3±0.3)e+21	-0.43 ± 0.10 ^a
NGC 3448	(1.9±0.3)e-1	19.63	(8.6±1.3)e+21	-0.54 ± 0.08 ^a
NGC 3504	(8.8±1.3)e-1	21.94	(5.1±0.8)e+22	-0.51 ± 0.08 ^a
NGC 3512	(3.8±0.6)e-2	19.61	(1.7±0.3)e+21	-0.56 ± 0.08 ^a
NGC 3596	(5.8±1.2)e-2	17.04	(2.0±0.4)e+21	-0.51 ± 0.10 ^a
NGC 3629	(2.1±0.4)e-2	21.53	(1.2±0.2)e+21	-0.46 ± 0.10 ^a
NGC 3631	(4.3±0.6)e-1	16.5	(1.4±0.2)e+22	-0.72 ± 0.08 ^a
NGC 3655	(1.6±0.3)e-1	21.43	(8.6±1.7)e+21	-0.43 ± 0.10 ^a
NGC 3657	(9.1±1.4)e-3	17.2	(3.2±0.5)e+20	-0.39 ± 0.10 ^a
NGC 3666	(5.1±1.0)e-2	15.14	(1.4±0.3)e+21	-0.45 ± 0.10 ^a
NGC 3684	(6.4±1.6)e-2	16.54	(2.1±0.5)e+21	-0.64 ± 0.11 ^a
NGC 3683	(4.9±0.7)e-1	24.4	(3.5±0.5)e+22	-0.69 ± 0.08 ^a
NGC 3686	(8.7±1.8)e-2	16.51	(2.8±0.6)e+21	-0.74 ± 0.10 ^a
NGC 3729	(6.8±1.0)e-2	15.14	(1.9±0.3)e+21	-0.51 ± 0.08 ^a
HRS 61	(4.3±0.7)e-3	17.39	(1.6±0.3)e+20	< -0.37 ^a
NGC 3755	(3.2±0.5)e-2	22.44	(2.0±0.3)e+21	-0.57 ± 0.08 ^a

Table B.1: continued.

Name	S_{144} [Jy]	d [Mpc]	L_{144} [W Hz ⁻¹]	α_{144}^{1400}
(1)	(2)	(3)	(4)	(5)
NGC 3756	(2.8±0.4)e-2	18.41	(1.1±0.2)e+21	-0.81 ± 0.09 ^a
NGC 3795	(3.7±0.6)e-3	17.33	(1.3±0.2)e+20	< -0.31 ^a
NGC 3794	(1.0±0.2)e-2	19.76	(4.8±0.8)e+20	< -0.74 ^a
NGC 3813	(3.4±0.5)e-1	20.97	(1.8±0.3)e+22	-0.57 ± 0.08 ^a
HRS 67	(6.2±1.0)e-3	20.51	(3.1±0.5)e+20	-0.34 ± 0.11 ^a
HRS 68	(1.1±0.2)e-2	20.17	(5.6±0.8)e+20	-0.49 ± 0.10 ^a
NGC 3898	(3.9±0.6)e-2	16.73	(1.3±0.2)e+21	-0.78 ± 0.08 ^a
NGC 3953	(2.4±0.4)e-1	15.0	(6.4±1.0)e+21	-0.75 ± 0.08 ^a
NGC 3982	(2.5±0.4)e-1	15.83	(7.6±1.1)e+21	-0.61 ± 0.08 ^a
HRS 76	(4.7±0.8)e-3	15.27	(1.3±0.2)e+20	-0.18 ± 0.11 ^a
NGC 4100	(2.1±0.3)e-1	15.31	(6.0±0.9)e+21	-0.60 ± 0.08 ^a
NGC 4178	(5.6±1.2)e-2	16.5	(1.8±0.4)e+21	-0.38 ± 0.10 ^a
IC 3061	(1.2±0.3)e-2	16.5	(3.8±0.9)e+20	< -0.80 ^a
NGC 4207	(3.4±0.7)e-2	16.5	(1.1±0.2)e+21	-0.25 ± 0.10 ^a
NGC 4212	(1.3±0.3)e-1	16.5	(4.1±0.8)e+21	-0.72 ± 0.10 ^a
NGC 4216	(6.4±1.3)e-2	16.5	(2.1±0.4)e+21	-0.72 ± 0.10 ^b
NGC 4222	(1.3±0.3)e-2	16.5	(4.4±1.0)e+20	-0.58 ± 0.12 ^a
NGC 4237	(2.3±0.5)e-2	16.5	(7.5±1.7)e+20	-0.58 ± 0.11 ^a
IC 3105 [†]	(4.0±1.1)e-3	16.5	(1.3±0.4)e+20	< -0.36 ^c
NGC 4254 [†]	(2.5±0.5)e+0	16.5	(8.3±1.7)e+22	-0.77 ± 0.10 ^a
NGC 4289	(1.5±0.4)e-2	16.5	(4.8±1.2)e+20	-0.53 ± 0.12 ^b
NGC 4294	(8.6±1.7)e-2	16.5	(2.8±0.6)e+21	-0.51 ± 0.10 ^b
NGC 4298	(1.3±0.3)e-1	16.5	(4.2±0.8)e+21	-0.88 ± 0.10 ^d
NGC 4302 [†]	(2.5±0.5)e-1	16.5	(8.0±1.6)e+21	-0.77 ± 0.10 ^a
NGC 4303	(2.0±0.4)e+0	16.5	(6.5±1.3)e+22	-0.67 ± 0.10 ^a
NGC 4307	(9.5±2.1)e-3	23.0	(6.0±1.4)e+20	-0.57 ± 0.14 ^a
NGC 4312	(3.6±0.7)e-2	16.5	(1.2±0.2)e+21	-0.50 ± 0.10 ^a
NGC 4316	(2.1±0.4)e-2	23.0	(1.3±0.3)e+21	-0.54 ± 0.10 ^c
NGC 4321	(1.5±0.3)e+0	16.5	(4.9±1.0)e+22	-0.74 ± 0.10 ^d
NGC 4330 [†]	(5.6±1.1)e-2	16.5	(1.8±0.4)e+21	-0.63 ± 0.11 ^a
NGC 4343	(4.2±0.9)e-2	23.0	(2.7±0.5)e+21	-1.01 ± 0.11 ^b
IC 3258 [†]	(9.8±2.1)e-3	16.5	(3.2±0.7)e+20	< -0.74 ^a
NGC 4351	(2.0±0.4)e-2	16.5	(6.5±1.3)e+20	< -1.03 ^a
IC 3268	(8.0±1.9)e-3	23.0	(5.1±1.2)e+20	-0.26 ± 0.12 ^a
NGC 4359	(1.1±0.2)e-2	17.9	(4.2±0.7)e+20	< -0.77 ^a
NGC 4370	(1.1±0.2)e-2	23.0	(6.8±1.5)e+20	< -0.77 ^a
NGC 4376	(5.0±1.4)e-3	23.0	(3.1±0.9)e+20	< -0.43 ^b
NGC 4380	(2.0±0.4)e-2	23.0	(1.2±0.3)e+21	< -0.68 ^a
NGC 4383	(1.2±0.2)e-1	16.5	(3.9±0.8)e+21	-0.45 ± 0.10 ^a
VCC 827	(5.1±1.1)e-2	23.0	(3.2±0.7)e+21	-0.59 ± 0.10 ^a
NGC 4390	(1.8±0.4)e-2	23.0	(1.1±0.2)e+21	< -0.98 ^d
IC 3322	(1.9±0.4)e-2	23.0	(1.2±0.3)e+21	-0.79 ± 0.12 ^d

Table B.1: continued.

Name	S_{144} [Jy]	d [Mpc]	L_{144} [W Hz ⁻¹]	α_{144}^{1400}
(1)	(2)	(3)	(4)	(5)
NGC 4396 [†]	(9.6±1.9)e-2	16.5	(3.1±0.6)e+21	-0.79 ± 0.10 ^a
NGC 4402 [†]	(4.3±0.9)e-1	16.5	(1.4±0.3)e+22	-0.81 ± 0.10 ^a
NGC 4413	(8.8±1.9)e-3	16.5	(2.9±0.6)e+20	< -0.68 ^a
NGC 4412	(4.0±0.9)e-2	16.5	(1.3±0.3)e+21	-0.44 ± 0.11 ^d
NGC 4416	(1.8±0.4)e-2	16.5	(6.0±1.3)e+20	-0.57 ± 0.11 ^a
NGC 4424 [†]	(3.0±0.6)e-2	23.0	(1.9±0.4)e+21	-0.67 ± 0.11 ^a
NGC 4430	(2.5±0.5)e-2	23.0	(1.6±0.3)e+21	-0.57 ± 0.10 ^b
VCC 1091	(6.1±1.4)e-3	23.0	(3.9±0.9)e+20	-0.25 ± 0.12 ^a
NGC 4450	(4.3±0.9)e-2	16.5	(1.4±0.3)e+21	-0.71 ± 0.10 ^a
NGC 4451	(2.1±0.4)e-2	23.0	(1.3±0.3)e+21	-0.52 ± 0.10 ^b
IC 3392	(8.2±1.8)e-3	16.5	(2.7±0.6)e+20	-0.44 ± 0.13 ^a
NGC 4457	(8.0±1.7)e-2	16.5	(2.6±0.5)e+21	-0.45 ± 0.10 ^a
NGC 4470	(2.1±0.4)e-2	16.5	(7.0±1.4)e+20	-0.14 ± 0.10 ^a
NGC 4480	(2.2±0.5)e-2	16.5	(7.1±1.6)e+20	-0.86 ± 0.13 ^a
NGC 4491	(7.5±2.0)e-3	16.5	(2.4±0.7)e+20	< -0.61 ^a
NGC 4505	(2.7±0.6)e-2	16.5	(8.7±2.0)e+20	< -1.15 ^d
IC 797	(1.1±0.2)e-2	16.5	(3.6±0.8)e+20	< -0.78 ^a
NGC 4501 [†]	(1.8±0.4)e+0	16.5	(6.0±1.2)e+22	-0.75 ± 0.10 ^a
IC 3476 [†]	(5.0±1.0)e-2	16.5	(1.6±0.3)e+21	-0.81 ± 0.10 ^c
NGC 4519	(6.4±1.3)e-2	16.5	(2.1±0.4)e+21	-0.83 ± 0.10 ^a
NGC 4522 [†]	(8.1±1.6)e-2	16.5	(2.6±0.5)e+21	-0.48 ± 0.10 ^a
NGC 4525	(2.1±0.4)e-3	16.77	(7.2±1.4)e+19	< -0.07 ^d
IC 800 [†]	(1.1±0.2)e-2	16.5	(3.5±0.8)e+20	< -0.76 ^b
NGC 4532	(5.0±1.0)e-1	16.5	(1.6±0.3)e+22	-0.63 ± 0.10 ^a
NGC 4535	(6.4±1.3)e-1	16.5	(2.1±0.4)e+22	-0.96 ± 0.10 ^a
IC 3521	(2.6±0.5)e-2	16.5	(8.3±1.7)e+20	-0.84 ± 0.12 ^b
NGC 4540	(1.4±0.3)e-2	16.5	(4.5±1.0)e+20	-0.64 ± 0.12 ^a
NGC 4548 [†]	(1.1±0.2)e-1	16.5	(3.7±0.8)e+21	-1.32 ± 0.10 ^b
NGC 4565	(8.6±1.7)e-1	17.61	(3.2±0.6)e+22	-0.80 ± 0.10 ^b
NGC 4567	(7.1±1.4)e-2	16.5	(2.3±0.5)e+21	-0.76 ± 0.10 ^c
NGC 4568	(5.8±1.2)e-1	16.5	(1.9±0.4)e+22	-0.60 ± 0.10 ^c
NGC 4569 [†]	(5.5±1.1)e-1	16.5	(1.8±0.4)e+22	-0.55 ± 0.10 ^c
NGC 4579	(6.5±1.3)e-1	16.5	(2.1±0.4)e+22	-0.59 ± 0.10 ^a
NGC 4580	(1.2±0.3)e-2	16.5	(3.8±0.9)e+20	< -0.79 ^b
NGC 4595	(9.6±2.2)e-3	16.5	(3.1±0.7)e+20	-0.31 ± 0.12 ^b
NGC 4606	(8.9±2.1)e-3	16.5	(2.9±0.7)e+20	< -0.68 ^a
NGC 4607 [†]	(9.8±2.0)e-2	16.5	(3.2±0.6)e+21	-0.70 ± 0.10 ^a
NGC 4630	(2.4±0.5)e-2	16.5	(7.9±1.7)e+20	-0.28 ± 0.10 ^a
NGC 4634 [†]	(1.5±0.3)e-1	16.5	(5.0±1.0)e+21	-0.66 ± 0.10 ^a
NGC 4639	(3.7±0.8)e-2	16.5	(1.2±0.3)e+21	-0.68 ± 0.10 ^b
NGC 4647	(3.0±0.6)e-1	16.5	(9.8±2.0)e+21	-0.92 ± 0.10 ^a
NGC 4654 [†]	(8.5±1.7)e-1	16.5	(2.8±0.6)e+22	-0.87 ± 0.10 ^a

B LOFAR data

Table B.1: continued.

Name	S_{144} [Jy]	d [Mpc]	L_{144} [W Hz ⁻¹]	α_{144}^{1400}
(1)	(2)	(3)	(4)	(5)
NGC 4689	(1.4±0.3)e-1	16.5	(4.6±0.9)e+21	-1.15 ± 0.10 ^a
NGC 4725	(1.8±0.3)e-1	17.27	(6.4±1.0)e+21	-0.79 ± 0.08 ^a
NGC 4747	(1.6±0.3)e-2	16.84	(5.4±0.9)e+20	-0.33 ± 0.08 ^a
NGC 4746	(1.8±0.4)e-1	16.5	(5.9±1.2)e+21	-0.52 ± 0.10 ^a
NGC 4758	(6.7±1.5)e-3	16.5	(2.2±0.5)e+20	-0.34 ± 0.13 ^a
NGC 4779	(2.6±0.5)e-2	16.5	(8.4±1.8)e+20	-0.49 ± 0.10 ^a
NGC 5014	(3.2±0.5)e-2	16.23	(10.0±1.5)e+20	-0.44 ± 0.08 ^a
NGC 5145	(1.3±0.2)e-1	17.5	(4.7±0.7)e+21	-0.58 ± 0.08 ^a
IC 902	(2.1±0.3)e-2	22.97	(1.3±0.2)e+21	-0.46 ± 0.08 ^a
NGC 5248	(5.4±1.1)e-1	16.46	(1.8±0.4)e+22	-0.58 ± 0.10 ^a
NGC 5301	(7.2±1.1)e-2	21.54	(4.0±0.6)e+21	-0.63 ± 0.08 ^a
NGC 5303	(7.4±1.1)e-2	20.27	(3.6±0.5)e+21	-0.46 ± 0.08 ^a
HRS 300	(3.0±0.6)e-3	19.34	(1.4±0.3)e+20	< -0.22 ^a
NGC 5372	(5.2±0.8)e-2	24.53	(3.7±0.6)e+21	-0.51 ± 0.08 ^a
NGC 5486	(9.5±1.5)e-3	19.76	(4.4±0.7)e+20	< -0.71 ^a
HRS 315	(3.2±0.7)e-3	20.57	(1.6±0.4)e+20	< -0.24 ^a
NGC 5645	(4.1±0.9)e-2	19.57	(1.9±0.4)e+21	-0.44 ± 0.10 ^a
NGC 5669	(2.6±0.5)e-2	19.54	(1.2±0.2)e+21	-0.38 ± 0.10 ^a
NGC 5692	(3.0±0.6)e-2	22.59	(1.8±0.4)e+21	-0.68 ± 0.10 ^a

Notes. Column (1) lists the galaxy names, objects that are marked with a dagger symbol are in the RPS sample. Column (2) shows the LOFAR flux density measured at 20'' resolution, column (3) the distance (taken from Boselli et al. 2010 for objects outside the Virgo cluster, otherwise assumed to be 16.5 Mpc), column (4) the 144 MHz luminosity and column (5) the spectral index between 144 MHz and 1.4 GHz. The 1.4 GHz flux densities (or upper limits) are taken from ^a Boselli et al. (2015); ^b measured from the maps of Chung et al. (2009); ^c Murphy et al. (2009) and ^d Vollmer et al. (2010).

C Radio-SFR maps

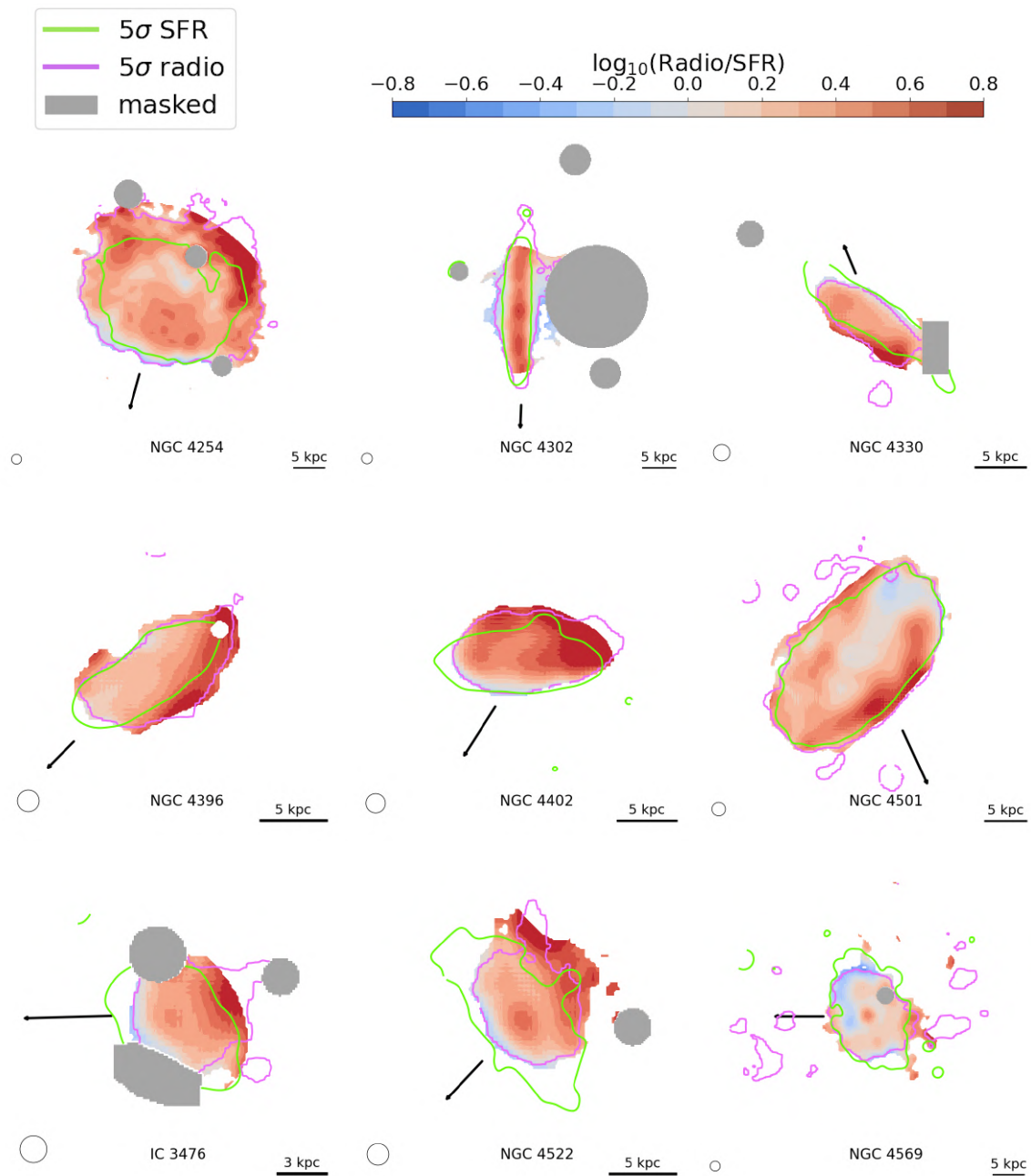


Figure C.1: Logarithmic ratio between the observed and modeled radio emission. The figure is identical to Fig. 3.8, except that we only show the images based on the $20''$ radio maps which were not displayed previously.

C Radio-SFR maps

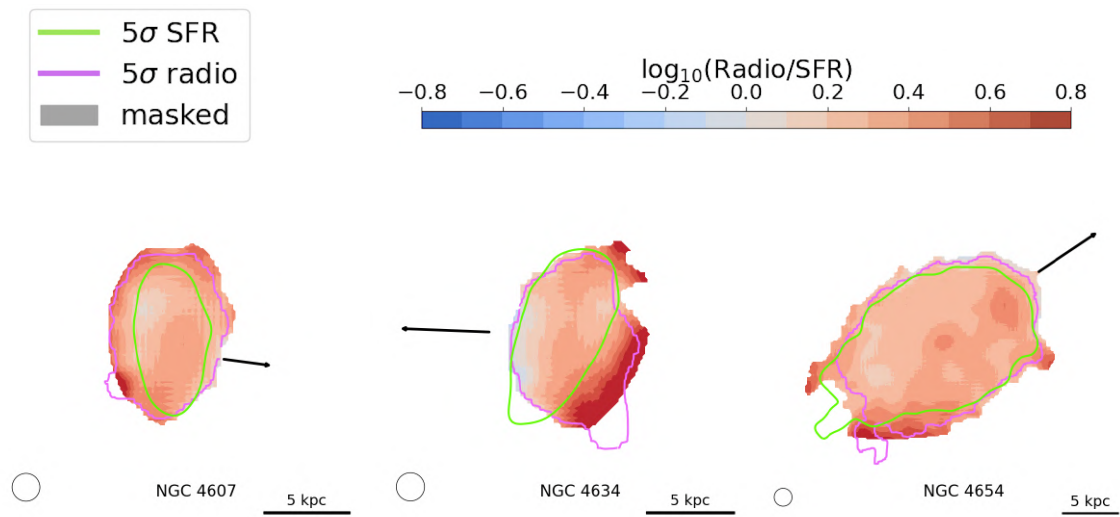


Figure C.1: Continued.

D Synchrotron emission model

To numerically solve Eq. 3.9, we use the Chang-Cooper discretization scheme (Chang & Cooper 1970) implemented in the `pychangcooper`¹ library. We extend this code to include an escape term $N(E, t)/t_{\text{esc}}$, a time-dependent injection term $Q(E, t) = qE^{-2} \exp(-t/t_{\text{quench}})$ and the relevant loss processes, i.e. Synchrotron radiation, inverse Compton scattering, ionization and Bremsstrahlung. Those are described by (Longair 2011):

$$b(E) = b_0 E^2 + N_{\text{gas}} \left(b_1 \left(3 \log \frac{E}{m_e c^2} + 19.8 \right) + b_2 E \right), \quad (\text{D.1})$$

with $b_0 = 3.2 \times 10^{-6} (B^2/2\mu_0 + u_{\text{rad}}) \text{ m}^3 \text{ MeV}^{-2} \text{ Myr}^{-1}$, $b_1 = 2.4 \times 10^{-7} \text{ MeV m}^3 \text{ Myr}^{-1}$, and $b_2 = 1.2 \times 10^{-8} \text{ m}^3 \text{ Myr}^{-1}$. Here, m_e is the electron rest mass, c the speed of light and N_{gas} the gas density. For the latter, we assume that only the H I content contributes and approximate a typical mean density $N_{\text{gas}} = 4.4 \times 10^5 \text{ m}^{-3}$ assuming the H I mass of NGC 4396 $M_{\text{HI}} = 8.6 \times 10^8 M_{\odot}$ (Chung et al. 2009) is distributed in a cylinder with a radius of 5 kpc and a height of 1 kpc.

We split the energy domain into 100 logarithmically spaced points ranging from 1 MeV to 100 GeV. The time domain is discretized in steps of 0.1 Myr. For the initial electron spectrum, we use the source term $Q(E)$ for constant injection and let the spectrum evolve for $t \gg t_{\text{esc}}$ until it reaches a steady state. This spectrum is then either subject to a time-dependent decrease of the source term on a scale t_{quench} or to an increase of the magnetic field by a factor of f_B and evolved in time.

The flux density of the corresponding synchrotron emission at a frequency ν and after a time t is given by (Harwood et al. 2013):

$$S(\nu, B, t) = S_0 B \int_0^\pi d\delta \sin(\delta)^2 \int dE F(x) N(E, B, t), \quad (\text{D.2})$$

where δ is the pitch angle, S_0 a normalization constant and $F(x)$ the following integral of the Bessel function of order 5/3:

$$F(x) = x \int_x^\infty K_{5/3}(z) dz. \quad (\text{D.3})$$

The variable $x = \nu/\nu_c$ is the ratio of the frequency ν and the critical frequency ν_c , which is given by:

$$\nu_c = \frac{3E^2 e B \sin(\delta)}{4\pi m_e^3 c^4}. \quad (\text{D.4})$$

Here, e is the electron charge.

For the electron spectrum and the corresponding synchrotron emission, we include a 10 Myr delay between the star formation and the CRE injection due to the lifetime of the massive O and B stars. The FUV and H α emission will also be delayed compared to the star formation, although less severely. We define $I_{\text{burst}}(t)$ as the time-dependent intensity after an instantaneous burst of star formation, where we

¹<https://github.com/grburgess/pychangcooper>

D Synchrotron emission model

use the distribution provided in Leroy et al. (2012). To take into account the contribution of the prior SFR history to the intensity $I(t)$, we use the convolution:

$$I(t) = \int \text{SFR}(\tau) I_{\text{burst}}(t - \tau) d\tau. \quad (\text{D.5})$$

In the scenario of reducing SFR due to RPS, the SFR is given by:

$$\text{SFR}(t) = \begin{cases} \text{SFR}_0, & \text{if } t \leq 0 \\ \text{SFR}_0 e^{-\frac{t}{t_{\text{quench}}}}, & \text{otherwise.} \end{cases} \quad (\text{D.6})$$

E Uncertainty maps

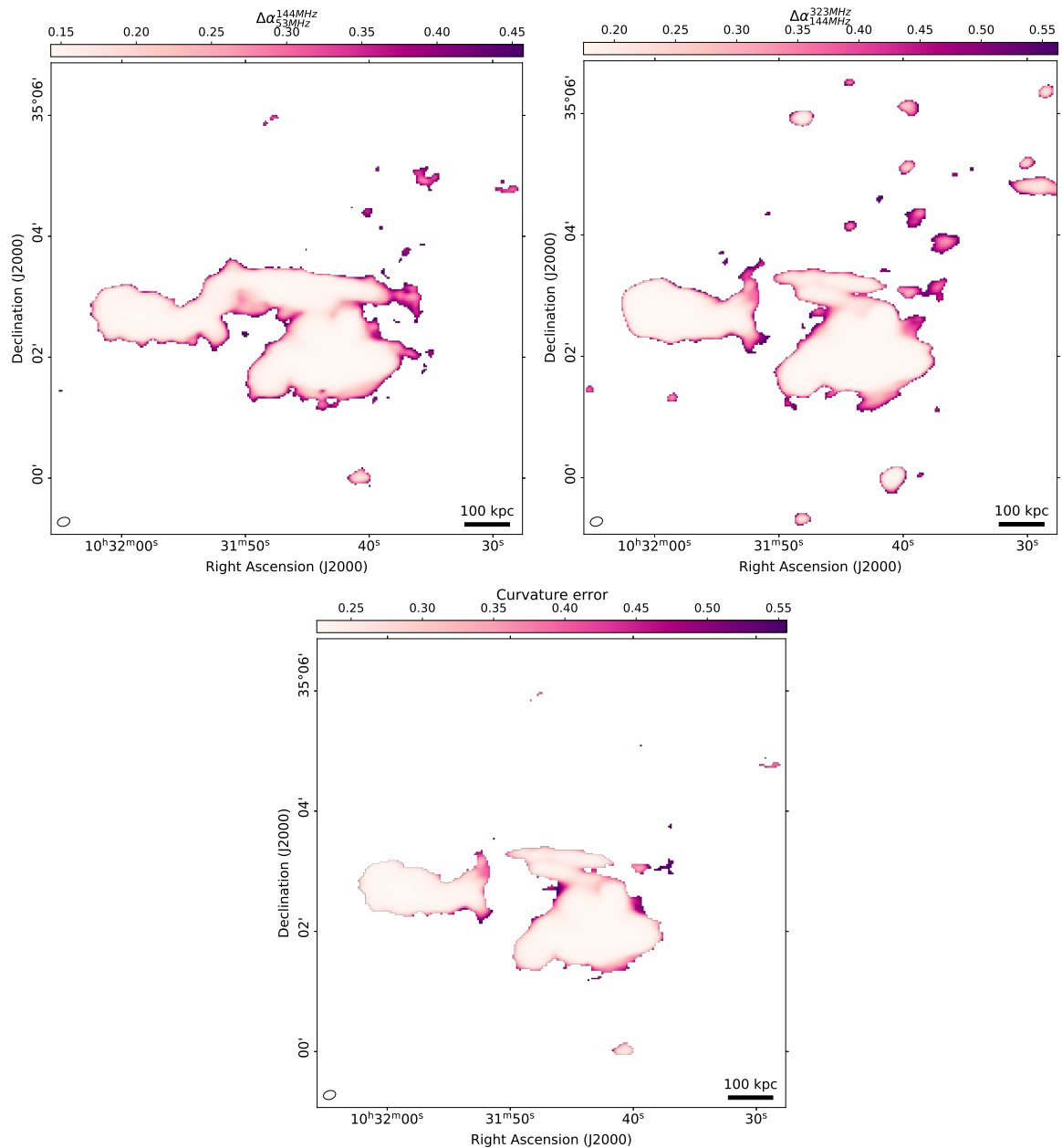


Figure E.1: Uncertainty maps to Fig. 4.3. The top left and top right figure show the spectral index uncertainties between 54-144 MHz (left) and 144-323 MHz (right). The bottom image shows the uncertainty of the curvature map.

E Uncertainty maps

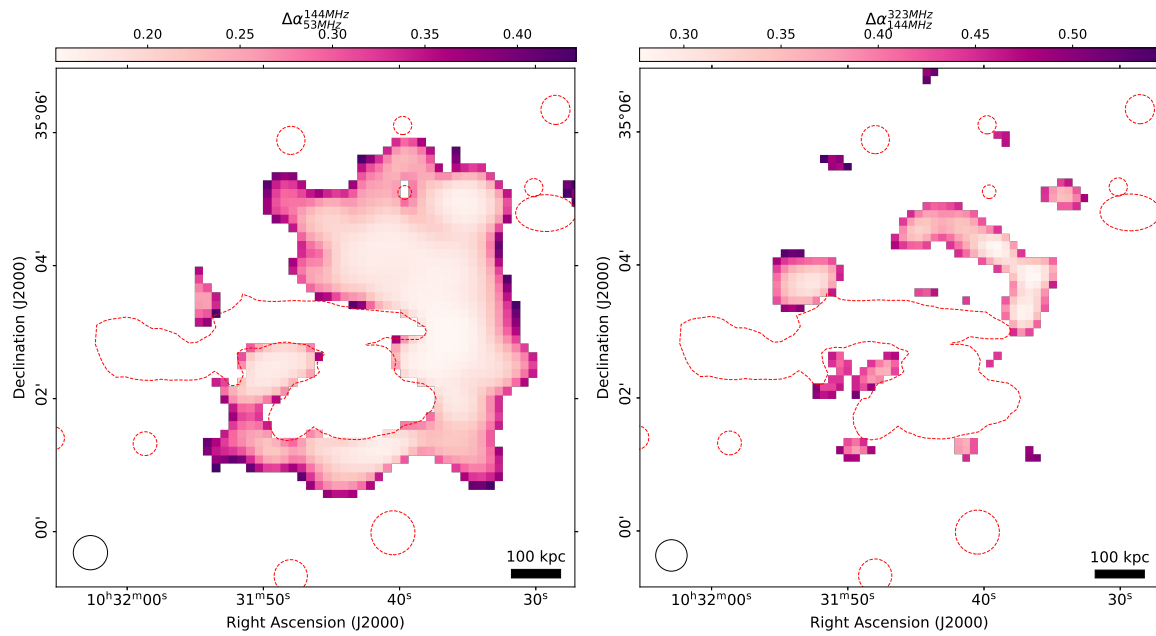


Figure E.2: Source-subtracted spectral index uncertainty maps at a spatial resolution of $30''$. The two figures are for the frequency ranges 54-144 MHz (left) and 144-323 MHz (right). Dashed red lines highlight the regions from which sources are subtracted.

F Spectral aging model

We employed the standard JP spectral aging model to describe the aging in the first section of the WAT radio galaxy. The flux density of this model at a frequency ν and after a time t is given by (Harwood et al. 2013)

$$S_{\text{JP}}(N_0, \nu, B, t, z, \alpha_{\text{inj}}) = N_0 \frac{\sqrt{3} \ln(10) e^3 B}{16\pi \epsilon_0 m_e (z+1)^2} \int_0^\pi d\delta \sin(\delta)^2 \int d\log(E) E F(x) n_e(E, B, t, z, \alpha_{\text{inj}}), \quad (\text{F.1})$$

where e and m_e are the electron charge and mass, ϵ_0 is the vacuum permittivity, δ is the pitch angle, and $F(x)$ is the following function:

$$F(x) = x \int_x^\infty K_{5/3}(z) dz. \quad (\text{F.2})$$

The variable $x = \nu/\nu_c$ is the ratio of the frequency ν and the critical frequency ν_c , which is given by

$$\nu_c = \frac{3E^2 e B \sin(\delta)}{4\pi m_e^3 c^4}. \quad (\text{F.3})$$

In Eq. F.1, the energy-integration is performed in log-space for numerical efficiency. We first fit a spectral index model to the observed spectral index values α to remove the dependence on the normalizations N_0 . The spectral index model is calculated as

$$\alpha_{\text{JP},i}(\nu_1, \nu_2, B, t, z, \alpha_{\text{inj}}) = \frac{\log \frac{S_{\text{JP}}(\nu_1, B, t, z, \alpha_{\text{inj}})}{S_{\text{JP}}(\nu_2, B, t, z, \alpha_{\text{inj}})}}{\log \frac{\nu_1}{\nu_2}}. \quad (\text{F.4})$$

The uncertainty for the observed spectral index values σ_α is obtained from the uncertainties of the flux densities σ_S according to Gaussian propagation of uncertainty,

$$\sigma_\alpha = \frac{1}{\log(\nu_1/\nu_2)} \sqrt{\frac{\sigma_{S_1, \text{stat.}}^2 + (0.1 \times S_1)^2}{S_1^2} + \frac{\sigma_{S_2, \text{stat.}}^2 + (0.1 \times S_2)^2}{S_2^2}}. \quad (\text{F.5})$$

Here we take into account the 10% systematic uncertainty on the flux scales. We fit the WAT projected velocity v_\perp by minimizing the standard χ^2 statistics assuming a minimum aging magnetic field B_{min} and a linear motion $t = d_\perp/v_\perp$,

$$\chi^2 = \sum_{i=0}^9 \sum_{j=0}^1 \left(\frac{\alpha_i(\nu_j, \nu_{j+1}) - \alpha_{\text{JP},i}(\nu_j, \nu_{j+1}, B_{\text{min}}, d_\perp/v_\perp, z, \alpha_{\text{inj}})}{\sigma_{\alpha_i}(\nu_j, \nu_{j+1})} \right)^2. \quad (\text{F.6})$$

Subsequently, a normalization factor $N_{0,i}$ is fitted in log-space for each beam-sized region along the WAT/GReET.

F Spectral aging model

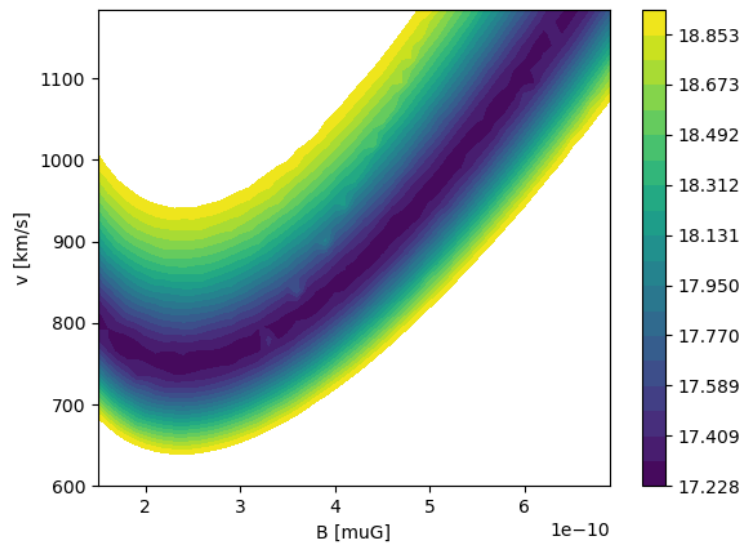


Figure F.1: Aging model merit function against magnetic field (x -axis) and projected velocity (y -axis) in arbitrary units.

G Halo fit results

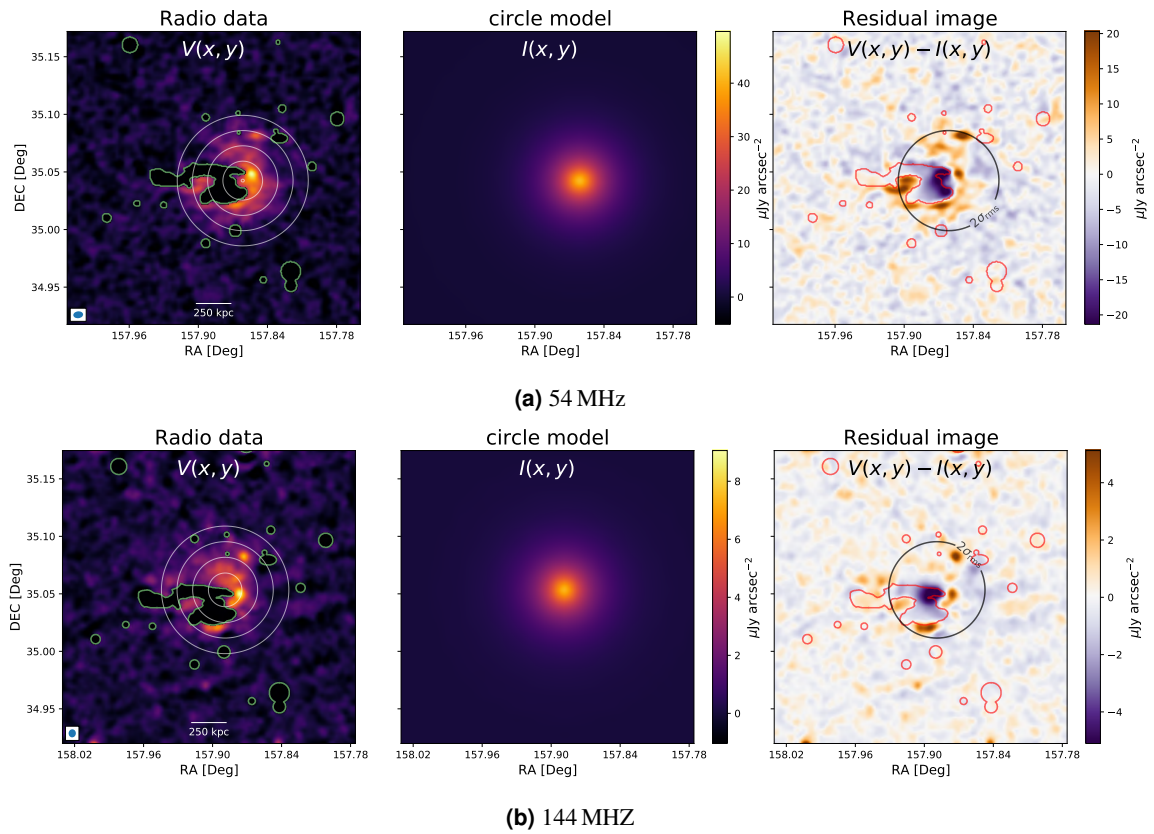


Figure G.1: Results of the halo fitting in LBA (a) and HBA (b). The circles in the left panels indicate the position of the best-fit halo on top of the flux density maps. The center panels show the model, and the right panels present the residual. The green and red regions are excluded from the fitting.